milliKelvin ESR of rare-earth doped crystals using superconducting resonators

Gavin Patrick Dold

A thesis submitted for the degree of

Doctor of Philosophy

London Centre for Nanotechnology
Electronic and Electrical Engineering
University College London

London, 11th May 2020

I, Gavin Patrick Dold, confirm that the work presented in this thesis is my own. Where information has been derived from other sources, I confirm that this has been indicated in the thesis.

London, 11th May 2020 Gavin Patrick Dold

milliKelvin ESR of rare-earth doped crystals using superconducting resonators

Gavin Patrick Dold

Abstract

Rare-earth doped crystals have proven to be of considerable interest for quantum information processing, with demonstrations of quantum memories and the potential for coherent microwave–optical conversion as part of a quantum network. By interfacing these rare-earth based technologies with superconducting devices, they can complement existing technologies — which form the basis of many state-of-the-art quantum computers — forming a hybrid quantum information processing architecture exhibiting the advantages of fast superconducting processors alongside the extended coherence time and frequency conversion available from rare-earths.

This thesis demonstrates the suitability of a widely used rare-earth doped crystal, yttrium orthosilicate (Y_2SiO_5 or YSO) doped with ^{145}Nd or with ^{171}Yb, as a substrate for fabrication of superconducting resonators. Designs for these resonators are presented with simulations of their electromagnetic modes, and their fabrication detailed. These devices are cooled to milliKelvin temperatures in a dilution refrigerator in order to investigate properties of the device and its coupling to electron spin transitions within the substrate where a coupling rate of the order $g_{\mathrm{ens}}/2\pi$ =1.2–7.1 MHz is observed. Dielectric loss due to two-level systems is measured with a loss-tangent $\tan\delta = 4 \times 10^{-6}$, and a coupling between resonator and spins is observed to have a high cooperativity $C \approx 8$–250.

The superconducting resonator is then used to perform pulsed spectroscopy of electron spin resonance (ESR) transitions in the high-cooperativity regime, measuring two-pulse coherence times of $T_2 = (409 \pm 14)\,\mu\mathrm{s}$ for 200 ppm ^{145}Nd:Y_2SiO_5 and $T_2 = (1170 \pm 90)\,\mu\mathrm{s}$ for 50 ppm ^{171}Yb:Y_2SiO_5. Chirped pulses are used to invert spin magnetisation and drive arbitrary rotations, enabling the measurement of relaxation dynamics and Rabi oscillations. Dynamical decoupling sequences are explored as a method for extending coherence time. Experiments exploiting coherence-enhancing 'near-ZEFOZ' transitions in ^{171}Yb are proposed, and continuous-wave measurements are used to demonstrate the working principle of such a scheme.

Impact statement

This thesis describes an investigation into the suitability of yttrium orthosilicate Y_2SiO_5 as a substrate for superconducting device fabrication, and uses superconducting resonators fabricated on Y_2SiO_5 to drive ESR transitions in rare-earth ions doped within the crystal while measuring physical parameters of the device and rare-earth spin ensemble.

The immediate impact is primarily academic, as further work is needed to produce a commercially viable device. A new methodology is presented in the fabrication of devices on Y_2SiO_5; measurements of dielectric loss and device quality indicate this new approach can yield low-loss devices. Experiments coupling the resonator to ESR transitions show these transitions can be driven with continuous and pulsed excitations, enabling parameters quantifying the phase-coherence of electron spins to be extracted as a function of environmental properties such as temperature. These demonstrate an enhancement of coherence with decreased temperature. Simulations of ESR transitions also confirm the existence of specific magnetic fields with properties capable of enhancing the coherence time of ^{171}Yb:Y_2SiO_5, and an experiment to measure these properties is proposed.

In the greater context, this work demonstrates an interface between planar superconducting devices and an ensemble of electron spins. By using rare-earth doped crystals as the substrate and spin ensemble, their optical properties and long coherence times can be exploited to store quantum states as a quantum memory, or convert quantum states from microwave to optical frequencies as a quantum transducer. The device can additionally couple to superconducting qubits, a technology at the forefront of approaches toward scalable quantum computers. As such this work is a step toward two quantum technologies which when combined can extend the capabilities of quantum computers, by providing a storage medium for quantum infomation, or allowing quantum states to be sent between quantum computers in the form of a photon along an optical fibre.

Such a device would have wide-ranging impact, by providing an additional element which a quantum computer could utilise as part of computational algorithms, or by providing a vital component for communication between distant nodes of a

quantum network. This technology would transform some commercial sectors by enabling calculations that are otherwise infeasible using classical technology, by enabling simulation of complex quantum systems (with benefits to the chemical industry and healthcare), secure communication via quantum repeaters (impacting finance and governmental services), and by extending the computational capability available to enable otherwise impossible calculations.

Acknowledgements

This thesis, as with every PhD, would not have been possible without the contribution of many people I have had the pleasure of working with. Their teaching, assistance, advice, guidance, support, and company have been invaluable in realising this project and its results. I wish to thank:

My supervisors *John Morton* and *Tobias Lindström*, without whose trust, encouragement, and patience throughout the past three and a half years this project would never have been possible. They provided the knowledge and equipment necessary to explore and develop this project, and maintained an open door for discussion and advice whenever it was needed.

Christoph Zollitsch, whose guidance and expertise has been indispensable in developing my experimental skills from the cleanroom to the dilution fridge, and who helped me understand the intricacies involved in device fabrication and electron spin resonance.

Oscar Kennedy who has been a fountain of knowledge, and whose wisdom, kindness, and awful puns were deeply welcome during the many hours spent writing this thesis.

James O'Sullivan and *Joe Alexander*, whose support and presence in the lab helped me through many long hours listening to the never-ending hiss of pulse tubes.

My colleagues *Leonid Abdurakhimov*, *Hee-Jin Lim*, *Mantas Šimėnas*, *Sebastian de Graaf*, and *Siddharth Dhomkar*, whose advice and assistance in spin resonance, microwave engineering, and quantum optics have been indispensable in planning and developing the equipment for this project.

Philippe Goldner, *Sacha Welinski*, and *Alban Ferrier* for growing and polishing the rare-earth doped crystals used throughout this work.

Steve Etienne Vijayalakshmi Krishnan, and *Lorella Rossi* for their help and advice in the cleanroom, and *Rohit Khanna* whose electronics and soldering skills are the envy of everyone in the department.

Chang-Min Lee and *Jason Robinson*, for generously providing superconducting NbN film at a critical time when our cleanroom was not.

Sebastian Probst and *Alexey Tiranov* for open and fruitful discussions at conferences, and *Yui Kubo* for graciously accommodating us after our post-conference plans were (predictably) scuppered by typhoon season.

The *QSD group*, my *CDT colleagues*, as well as *Shaun Geaney* and *Ailsa Keyser* at NPL, for the camaraderie — as well as the copious time spent at the pub — that we shared.

My friends and housemates over the past four years, who provided a much-needed balance by openly sharing their company, tea, music, stories, and board games.

Most of this thesis was written to a soundtrack of the Canadian ambient drone duo *Nadja*, Polish black metal band *Mgła*, or American post-metal band *Deafheaven*.

Finally, I am grateful to the *Centre for Doctoral Training in Delivering Quantum Technologies* and the *National Physical Laboratory* for providing this opportunity and funding my PhD programme.

Contents

Chapter 1

Introduction

Worldwide demand for data and computational power is growing year-on-year. 88 % of the UK population has access to a smartphone. Intensive algorithms are driving the development of artificial intelligence, diagnosing cancers more accurately than clinicians and putting autonomous cars on the road. Global internet traffic has just exceeded 3 zettabytes per year while data centres and cloud computing burn an estimated 660 TWh worldwide[1]. This technological uprising has been driven by silicon processors, fuelled by Moore's law [1], performing computation with the fundamental binary unit of classical information represented by the states 0 or 1 — the *bit*.

Despite the computing power currently available, there are classes of problems which remain infeasible by classical computers — this poses challenges for large optimisation problems and underpins the security of many classical cryptographic protocols based on the difficulty of prime factorisation. This limitation, alongside the predicted death of Moore's law in the 2020s [2], drives research into another paradigm of computing which exploits quantum mechanics. The quantum computer was proposed in the 1980s by Paul Benioff and Richard Feynman [3] as the natural framework for simulating a quantum system, and formalised by David Deutsch [4] to describe a universal quantum computer using a series of quantum gates analogous to classical logic gates.

Quantum computing uses a generalisation of the classical bit using the quantum eigenstates $|0\rangle$ and $|1\rangle$ as the logical states of a *qubit*. The state $|\psi\rangle$ of a qubit is represented by an arbitrary superposition of these two eigenstates

$$|\psi\rangle = \cos\tfrac{\theta}{2}\,|0\rangle + \mathrm{e}^{\mathrm{i}\phi}\sin\tfrac{\theta}{2}\,|1\rangle$$

where $0 \leq \theta \leq \pi$ and $0 \leq \phi < 2\pi$. These variables θ and ϕ invoke an obvious analogy to spherical polar coordinates whereby any pure quantum state $|\psi\rangle$ can be

[1]This is approximately double the electrical power consumption of the United Kingdom.

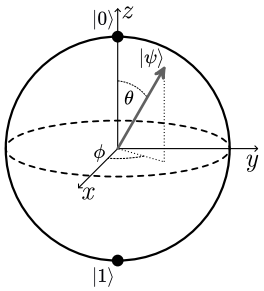

Figure 1.1: In the Bloch sphere picture, the state $|\psi\rangle$ of a single qubit can be described by a position on the surface of the a unit sphere using the spherical coordinates θ and ϕ.

described as a point on the surface of a unit sphere, in a representation known as the Bloch sphere [5] shown in Fig. 1.1.

It is immediately obvious that a quantum state $|\psi\rangle$ encodes more information than a classical bit with strictly two possible states, but when measured the qubit state collapses to one of two states — typically the computational basis $|0\rangle$, $|1\rangle$ — causing the quantum nature of the information to be lost. The real power of a quantum computer arises when multiple qubits are used concurrently and allowed to entangle, maintaining the integrity of the quantum information during the computation (provided the qubits are not measured by the user or the environment).

Several routes toward the experimental realisation of a quantum computer have been explored. In 2012, the Nobel prize in physics was awarded "for ground-breaking experimental methods that enable measuring and manipulation of individual quantum systems", shared jointly between Serge Haroche and David Wineland [6, 7], for pioneering experiments coupling atoms to light confined within a reflective cavity in a field known as cavity quantum electrodynamics (cavity QED). However, the most recent breakthroughs in quantum computing have been demonstrated using superconductors.

Superconducting qubits are constructed using Josephson junctions, formed of two superconducting electrodes separated by an insulating (or non-superconducting) tunnel barrier. This forms a component with nonlinear inductance, which as part of a circuit forms a nonlinear resonator, of which two energy levels can be used as a qubit. This type of qubit was developed following theoretical predictions by Brian Josephson [8], for which he was awarded the Nobel prize in physics in 1973. This artificially made qubit effectively substitutes the natural qubit in cavity QED, creating a new field of *circuit* QED [9].

Following decades of academic interest, and developments in the microwave instrumentation and millikelvin cryogenic apparatus required to operate these super-

conducting devices, industrial funding has driven substantial growth in the field. Large organisations including Google, IBM, and Intel, as well as companies started-up around quantum computing such as D-Wave, Oxford Quantum Circuits, Rigetti, IQM, and Seeqc, are each pursuing their own approach to developing superconducting computers.

With industrial backing, superconducting quantum computing has made rapid progress. State-of-the-art machines can incorporate 50–100 qubits with fast 10 ns–100 ns two-qubit gate operations with ~99.5 % fidelity and coherence times ~100 µs [10]. While this is not enough to perform error-correction, it is nonetheless sufficient for Google's quantum research group, while led by John Martinis, to have demonstrated a quantum speedup with a 53-qubit processor, taking 200 s to calculate a result they claim a classical supercomputer would take 10 000 years [11]. These types of devices — too small and noisy for universal computation, but nonetheless advantageous over classical algorithms — are typically referred to as *noisy intermediate-scale quantum* (NISQ) technologies.

While circuit QED shows potential as a route towards quantum computing, the best artificial qubits typically suffer far shorter coherence times 0.1 ms–1 ms [10] than have been seen in cavity QED where coherence times can be orders of magnitude longer [12–15]. However, gate operations in cavity QED tend to be correspondingly longer as natural atoms couple more weakly to applied microwave fields. This has led to the proposal of the *hybrid quantum system* [16–21], combining superconducting qubits for fast gate operations with solid-state spin qubits via a superconducting resonator to act as a bus between the two and drive electron spin resonance (ESR) transitions.

This hybrid system enables the storage of quantum states within a solid-state spin ensemble. They could be later retrieved as part of a computation [21, 22], but if the quantum state is stored in an optically active medium this also enables the conversion of a quantum state from being encoded over a transition at ~GHz as is typical for superconducting qubits, to an optical transition ~100s of THz. The quantum state can then be sent as a photon down an optical fibre to a distant location or distant computer, forming an interface between stationary and flying qubits as required for an eventual 'quantum internet'.

A promising solid-state medium for storage and conversion of quantum states is found in crystals doped with rare-earth elements. These offer long coherence times [13, 14] as well as interfaces to optical transitions [23–25], and their properties and decoherence mechanisms are an active area of research [26–29].

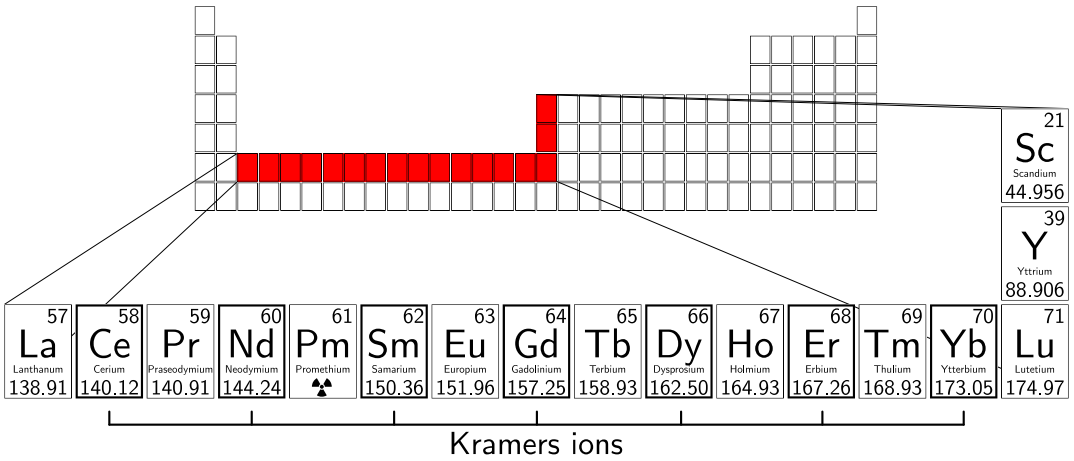

Figure 1.2: The rare-earth elements within the periodic table. Of particular interest are the ESR-active Kramers ions whose 3+ charge states have half-integer total spin, yielding a degenerate ground spin state which can be split by applying a magnetic field.

1.1 Rare-earth doped crystals

The rare-earth elements[2] consist of the elements lanthanum though to lutetium La–Lu in the periodic table, along with elements scandium Sc and yttrium[3] Y. Additional electrons are added to the 4f sub-shell along the lanthanide series, leaving the outer orbitals with similar configurations $[Xe]4f^{[0-14]}5d^{[0-1]}6s^2$. This gives these elements very similar chemical and physical properties, but substantially different hyperfine spectra between different isotopes due to differing nuclear structures.

All rare-earths have optical or near-optical transitions, but only half of the rare-earths have accessible microwave transitions. These are the so-called Kramers ions with half-integer total spin. This results in a degenerate ground spin state, which can be split with application of a magnetic field. The 4f subshell penetrates more deeply toward the nucleus than the 5s and 5p subshells, providing an element of protection from the environment that gives rare-earth ions excellent coherence properties.

Rare-earth elements usually appear as tripositive RE^{3+} ions, and their extremely similar chemical properties make them readily interchangeable in compounds and crystals. As a result rare-earths are also well-suited for solid-state applications through doping in solid-state crystals.

[2]Despite their name, the rare-earth elements are actually quite plentiful in the Earth's crust with cerium having a greater natural abundance than copper. The apparent misnomer is due to the presumed scarcity of mineral deposits upon their identification in 1794 [30].

[3]Yttrium, along with the elements Terbium, Erbium, and Ytterbium, were named after the Swedish village of Ytterby where the first rare-earth mineral was unearthed in 1788.

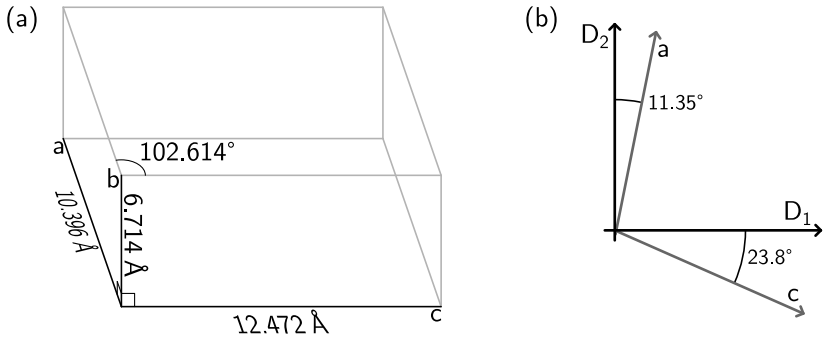

Figure 1.3: (a) Dimensions of Y_2SiO_5 unit cell [31]. (b) Relation between (a, c) crystal axes and (D_1, D_2) optical indicatrix axes [32].

1.1.1 Yttrium orthosilicate

This work focuses on the crystal yttrium orthosilicate Y_2SiO_5, sometimes shortened to YSO, a material widely used as a solid-state laser medium that has been appropriated by the field of quantum technologies. It has a high optical depth [33], low dielectric losses [34], yields long spectral hole lifetimes, and achieves narrow homogeneous linewidths [35]. This is largely due to the low abundance of nuclear magnetic moments in its component atoms, as the abundant ^{89}Y has $\mu = -0.137\mu_N$ and the other constituents have low abundances of isotopes with nuclear spin, with 4.7 % ^{29}Si and 0.038 % ^{17}O. This reduces the magnitude of magnetic fluctuations in the nuclear spin bath providing a stable magnetic environment for doped spins.

Y_2SiO_5 is grown as a boule by the Czochralski method [32] making it possible in principle to fabricate on a large scale. Rare-earth ions RE^{3+} can be introduced by adding impurities to the melt, substituting for yttrium Y^{3+} during the growth process causing minimal perturbation to the lattice. Typical doping concentrations are 10–200 ppm, with $1\,\text{ppm} \equiv 1.883 \times 10^{16}\,\text{cm}^{-3}$.

The Y_2SiO_5 crystal belongs in the monoclinic C2/c space group, having a conventional unit cell of dimensions [31] $a = 10.396\,\text{Å}$, $b = 6.714\,\text{Å}$, $c = 12.472\,\text{Å}$, and an angle $\beta = 102.614°$ between a and c as illustrated in Fig. 1.3(a). To more conveniently represent the Y_2SiO_5 coordinate system an orthogonal frame (D_1, D_2, b) is defined by the optical extinction axes D_1 and D_2, both in the a–c plane and perpendicular to b related by the transformation in Fig. 1.3(b) [32]. The Y_2SiO_5 unit cell contains two inequivalent Y lattice sites where doped rare-earth ions can substitute referred to as site 1 and site 2, with site 1 conventionally referring to the site with larger volume. In addition, the crystal symmetry introduces two orientations in the lattice for each site, related by a 180° rotation around the b axis and a mirror plane perpendicular to b, referred to as sub-sites. The sub-sites are

magnetically equivalent for magnetic fields parallel with b, or perpendicular to b in the D_1–D_2 plane. Several views of the Y_2SiO_5 crystal unit cell are rendered in Fig. 1.4, showing the different sites and sub-sites.

Studies into the dielectric properties of Y_2SiO_5 determine its permittivity to be anisotropic, with principal values ($\epsilon_x = 9.36$, $\epsilon_y = 10.90$, $\epsilon_z = 10.21$) with a mean $\epsilon = 10.16$ [38]. In addition to bulk doping during Czochralski growth, FIB (focused ion beam) doping of Er^{3+} into undoped Y_2SiO_5 has been performed [39] though ESR measurements show a 5–10 times greater spin linewidth than bulk-doped Er:Y_2SiO_5 [19] indicating a larger inhomogeneity in the spin environment.

1.1.2 Applications of rare-earth doped crystals

Y_2SiO_5 initially found widespread use as a laser medium prior to the interest for quantum information, and as such has well studied optical properties [33, 40], in particular Er:Y_2SiO_5 which has a transition in the telecom band at 1538 nm [41], enabling the use of existing fibre infrastructure for transmission of coherent quantum information. Alongside the rare-earths' optical transitions, the Kramers ions exhibit an effective electron spin $S = \frac{1}{2}$ resulting in transitions at microwave frequencies. To drive these transitions a cavity is typically employed to increase the strength of the B_1 oscillating magnetic field and enhance the collection efficiency of emitted photons.

Microwave experiments using doped Y_2SiO_5 employ a variety of cavities to drive ESR transitions: 3D cavities can take various geometries such as sapphire cylinders [42] and loop-gap resonators [25, 43]; whispering-gallery modes in Y_2SiO_5 cylinders [38] have been used to observe ESR transitions of iron-group impurities [44]; and planar superconducting resonators have been used to drive ESR transitions in FIB-implanted sapphire [45] and in Er:Y_2SiO_5 [46].

Optical cavities have also been fabricated in Y_2SiO_5, with the demonstration of Purcell-enhanced photoemission with a nanoresonator in Nd:Y_2SiO_5 [47]. This may eventually enable wholly on-chip frequency conversion using both microwave and optical microcavities, though spatial mode-matching between the resonators will be challenging.

Solid-state spin ensembles coupled via a superconducting resonator have been proposed as a quantum memory [16] and investigated for a variety of spin species including ruby [48], NV centres in diamond [17], N@C_{60} [49], group V donors in silicon [50, 51], and rare-earth doped crystals [34, 45, 52]. Such a memory would

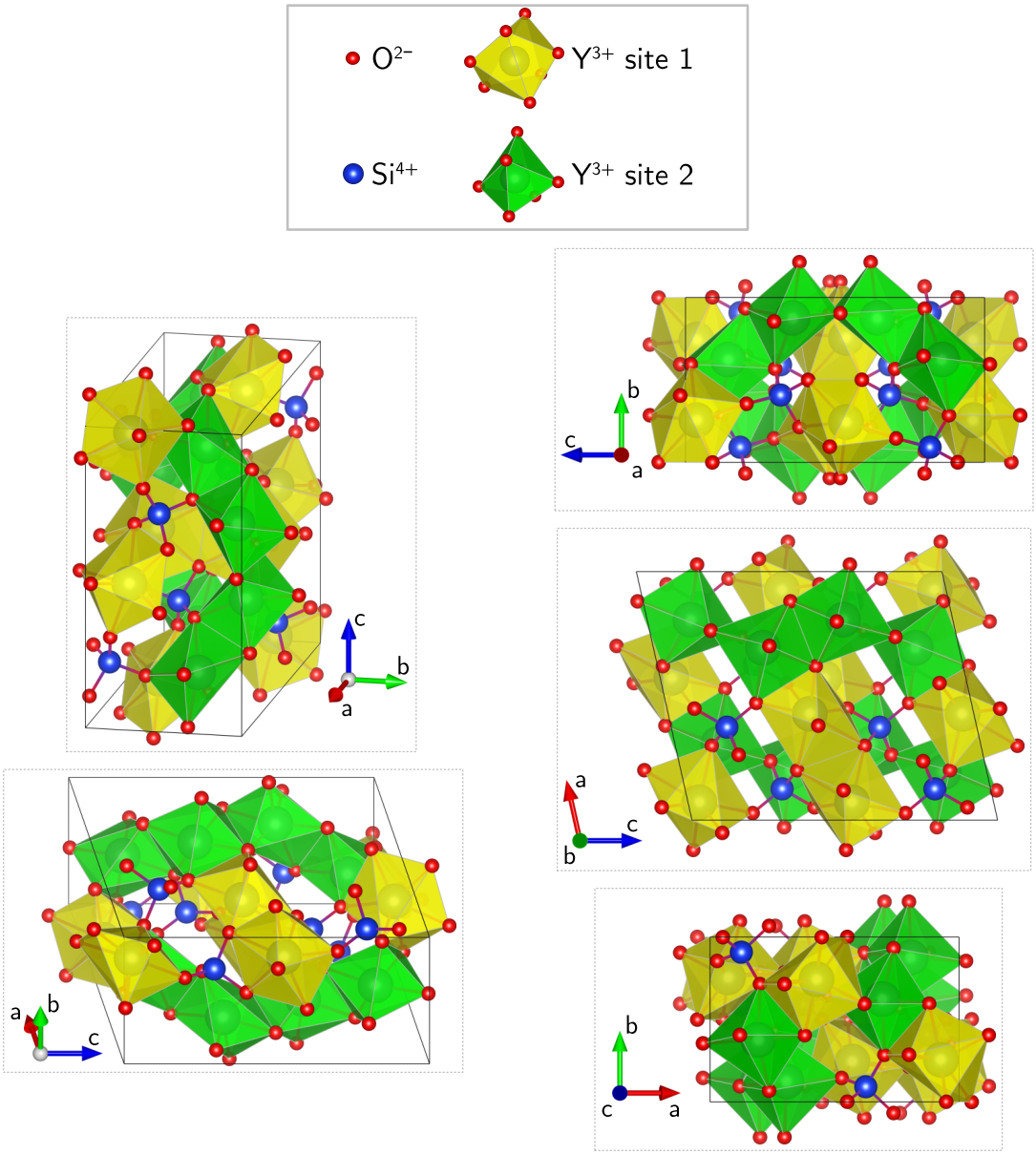

Figure 1.4: Y_2SiO_5 unit cell viewed from several angles. Left: perspective views; Right: views along each of the crystal axes (a, b, c). Yttrium atoms are enclosed by a polygon with vertices at the nearest neighbours. The two inequivalent Y sites have different coordination numbers, and are differentiated by colour with the larger site 1 in yellow and the smaller site 2 in green. The C2/c symmetry duplicates the Y_2SiO_5 unit and forms two sub-sites for each crystal site, related by a 180° rotation around the b axis and a mirror plane perpendicular to b. Crystallographic data from ICSD collection code 291362 [31, 36] rendered using VESTA [37].

be used to extend the storage time available for a quantum computer, and as such achieving a long coherence time T_2 is crucial for the effectiveness of such a device.

Proposals for frequency converters exploiting optical and spin transitions in rare-earth doped crystals have emerged [23, 24], with optical and microwave cavities mutually coupled via a rare-earth doped crystal. A strong coupling between the microwave field and spin ensemble is crucial for efficient conversion, so for these devices maximising the coupling strength g_{ens} between cavity and spin ensemble is beneficial. Demonstrations of such a frequency conversion scheme have shown its efficacy using a 3D microwave cavity [25] though the lack of an optical cavity in this setup limited the conversion efficiency.

In addition to its promise as a medium for frequency conversion, some rare-earths exhibit coherence-enhancing ZEFOZ (ZEro First-Order Zeeman) transitions, also known as clock transitions, where the transition frequency becomes insensitive to first-order changes in magnetic field $\frac{\mathrm{d}f}{\mathrm{d}B} = 0$. This property is discussed in detail in Section 2.1.5. One of the most remarkable results used a hyperfine ZEFOZ transition in Eu:Y_2SiO_5 to achieve an astonishing 6-hour coherence time at 2 K [13] by exploiting a frozen-core effect at 1.35 T and by applying dynamical decoupling sequences. Europium, however, is a non-Kramers ion so is not suitable for microwave applications. ZEFOZ transitions have also been found in Er:Y_2SiO_5 and Pr:YAG [53], and Yb:Y_2SiO_5 [14, 29] whose low-field first-order Zeeman properties are investigated by simulation in Section 2.3.3.

Exploiting such a ZEFOZ transition yields a solid-state spin ensemble with a coherence time extended beyond that observable by conventional ESR. Driving a ZEFOZ transition with a superconducting resonator would then provide an interface with a large coupling strength, by which excitations can be coherently stored from the resonator to within the spin ensemble, benefitting from the enhanced coherence time. This provides an additional advantage to using the solid-state spin ensemble as a quantum memory, enabling quantum information to be coherently stored for longer as part of a computation. As an element of a frequency converter, it would also serve to minimise the decoherence of the quantum state over the course of a conversion scheme, potentially improving the fidelity of the conversion process.

1.2 Thesis outline

The first four chapters of this thesis provide the necessary background and context to describe the current state of research in hybrid superconductor–spin devices and

rare-earth ESR, and detail important elements of this project including simulation and device fabrication, to support the later experimental chapters.

Chapter 2 outlines the theory of electron spin resonance and decoherence mechanisms in dilute solid-state spin ensembles. Hamiltonian parameters for ^{145}Nd and ^{171}Yb from the literature are used to calculate resonance conditions, simulating ESR spectra for experiments sweeping both magnetic field strength and angle. These simulations are then used to predict the existence of coherence-enhancing 'near-ZEFOZ' conditions where $\left|\frac{\mathrm{d}f}{\mathrm{d}B}\right| \to 0$ for magnetic field vectors compatible with the orientation of the superconducting resonator with respect to the Y_2SiO_5 crystal axes.

Chapter 3 describes the superconducting resonators used for this project, which are lumped-element resonators in a thin-ring or spiral configuration. The response of the resonator to microwave excitation is described analytically as a function of probe frequency and its interaction with resonant spins. The magnetic field dependence of a superconducting resonator is considered, as well as the resulting shift in resonant frequency with respect to applied magnetic field, a property which gives the resonator a degree of tunability. Designs of the thin-ring and spiral resonators are given, along with finite-element simulation of the B_1 magnetic field their resonant modes generate. Their fabrication by photolithography in the LCN cleanroom is summarised.

Chapter 4 details the equipment and experimental setups used for device measurements, cooling the fabricated chip to mK temperatures in a dilution refrigerator (whose operating principle is briefly outlined) and measuring its microwave response using continuous-wave excitation with a VNA or pulsed excitation using a custom ESR spectrometer along with a 2–4 GHz bridge which was designed and built specifically for this project.

The following three chapters describe the main experiments and results of this project, using the equipment from Chapter 4 to test the devices of Chapter 3 aiming to measure electron spin resonance of rare-earth spins as predicted in Chapter 2.

Chapter 5 describes an experiment using continuous-wave (CW) excitation of a thin-ring superconducting resonator in a dilution refrigerator at 10 mK. The zero-field frequency and quality factor of a resonator are measured as a function of applied CW power and dilution fridge temperature, to obtain the limiting quality factor at low powers, and to characterise the dielectric losses of this device due to interaction with two-level systems (TLS). Magnetic field is applied to bring ESR transitions of ^{145}Nd spins within the substrate in resonance with the resonator, resulting in the

measurement of ESR spectra and an angular-dependent roadmap, and analysis of an avoided crossing allows the linewidths and coupling strength to be determined.

Chapter 6 uses a thin-ring resonator to perform pulsed ESR spectroscopy of a ^{145}Nd spin ensemble in Y_2SiO_5, using a two-pulse sequence to generate a spin echo from which spin relaxation properties are determined. Spin coherence time T_2 is measured at various points of the avoided crossing and as a function of temperature. Longitudinal relaxation time T_1 is measured using adiabatic fast passage. Additional three-pulse stimulated echo and modified two-pulse echo sequences are used to attempt to extract information about the contribution of spectral and instantaneous diffusion to decoherence.

Chapter 7 performs pulsed ESR spectroscopy on Yb using a spiral resonator design. High-frequency avoided crossings of two isotopes are investigated, and T_2 measured for each using two-pulse and dynamical decoupling sequences. An experiment is devised for exploiting the near-ZEFOZ transitions of the $I = \frac{1}{2}$ isotope ^{171}Yb using a field-tunable resonator to couple to low-frequency transitions. The working principle of the experiment is demonstrated using CW measurements.

Chapter 8 summarises the thesis and its results, and proposes avenues for further research and development of the devices created by this project.

Chapter 2

Electron spin resonance

2.1 Principle of ESR

Electrons, along with other elementary particles, carry an intrinsic angular momentum known as spin [54]. This is a vector property denoted $\boldsymbol{S}$, with components in a Cartesian frame S_x, S_y, S_z, and magnitude[1] $|\boldsymbol{S}| = \sqrt{S(S+1)}$ determined by the spin quantum number S. The operators for these projections do not commute, so only one component can have a well-defined value within a set of quantised states ranging from $-S$ to $+S$ in integer steps. For an electron with $S = \frac{1}{2}$ this implies the spin projection has two possible values $S_{(x,y,z)} = \pm\frac{1}{2}$.

This spin angular momentum gives rise to a magnetic dipole [55, 56] $\boldsymbol{\mu}_\mathrm{e} = -g\mu_\mathrm{B}\boldsymbol{S}$ where for a free electron the Landé g-factor is $g \approx 2$, and the Bohr magneton $\mu_\mathrm{B} = \frac{e\hbar}{2m_\mathrm{e}}$. Classically, the energy of this dipole within a magnetic field $\boldsymbol{B}$ is $E = -\boldsymbol{\mu}_\mathrm{e} \cdot \boldsymbol{B} = g\mu_\mathrm{B}\boldsymbol{S} \cdot \boldsymbol{B}$. For a free electron the choice of coordinate frame is arbitrary, and conventionally chosen such that $\boldsymbol{B}$ aligns with the lab z-axis. In this case, only the $S_z = \pm\frac{1}{2}$ projection contributes to the energy, which can be written $E = g\mu_\mathrm{B}B_0S_z$ where B_0 is the magnetic field strength. The Hamiltonian operator can then be written

$$H = g\mu_\mathrm{B}B_0\hat{S}_z$$

with two eigenstates $|0\rangle$ and $|1\rangle$ separated in energy by $\Delta E = g\mu_\mathrm{B}B_0$. This breaking of degeneracy in the presence of a magnetic field is the Zeeman effect.

The states $|0\rangle$ and $|1\rangle$ are static under this Hamiltonian, but a superposition state $|\psi\rangle = a\,|0\rangle + b\,|1\rangle$ evolves in time[2] as

$$|\psi(t)\rangle = a\,|0\rangle + b\,\mathrm{e}^{-\mathrm{i}\omega_0 t}\,|1\rangle \tag{2.1}$$

[1] In units where $\hbar = 1$

[2] This arises from solving the time-dependent Schrödinger equation

corresponding to a precession around the z axis of the Bloch sphere at the Larmor frequency $\omega_0 = \gamma B_0$ determined by the gyromagnetic ratio[3] $\gamma = \frac{g\mu_\mathrm{B}}{\hbar}$.

In the case of an atom or ion, the electron spin S comes from an unpaired electron in an outer shell of the atom, and the influence of its nucleus typically cannot be neglected. In an atom the value of the electron g-factor typically differs from that of a free electron. The nucleus in general also has a spin angular momentum $\boldsymbol{I}$, which interacts with the external $\boldsymbol{B}$-field to add an additional term through the nuclear Zeeman effect

$$H = g\mu_\mathrm{B} B_0 \hat{S}_z + g_\mathrm{N}\mu_\mathrm{N} B_0 \hat{I}_z$$

where $\mu_\mathrm{N} = \frac{e\hbar}{2m_\mathrm{p}}$, with m_p the mass of a proton.

The nuclear spin $\boldsymbol{I}$ provides an additional contribution to the magnetic field experienced by the electron spin. This shift in energy due to the nucleus–electron interaction is the hyperfine effect, which adds another term depending on both electron and nuclear spins to the Hamiltonian

$$H = g\mu_\mathrm{B} B_0 \hat{S}_z + g_\mathrm{N}\mu_\mathrm{N} B_0 \hat{I}_z + A\hat{\boldsymbol{S}} \cdot \hat{\boldsymbol{I}}.$$

where the hyperfine constant A is a function of the intersection of the electron wavefuction within the nucleus. The hyperfine interaction splits each energy level from the Zeeman effect into $2I + 1$ components.

In general the environment of the spin system is not necessarily isotropic, as in the case of dopants in a complex crystal lattice such as Y_2SiO_5. This breaks the symmetry that allowed the choice of z-axis to align with the B-field direction, and the g-factor and hyperfine constant A become tensors $\boldsymbol{g}$ and $\boldsymbol{A}$. The more general form of the ESR Hamiltonian for anisotropic systems, including the Zeeman terms and hyperfine interaction, becomes

$$H = \mu_\mathrm{B} \boldsymbol{B}^\mathrm{T} \boldsymbol{g} \hat{\boldsymbol{S}} + \mu_\mathrm{N} \boldsymbol{B}^\mathrm{T} \boldsymbol{g}_\mathrm{N} \hat{\boldsymbol{I}} + \hat{\boldsymbol{S}}^\mathrm{T} \boldsymbol{A} \hat{\boldsymbol{I}}.$$

Typically the nuclear Zeeman term $\boldsymbol{g}_\mathrm{N}$ is small compared to that of the electron $\boldsymbol{g}$, and published analysis of ESR data for rare-earths often does not include this term. Hence the Hamiltonian used for simulations in this chapter and later is

$$H = \mu_\mathrm{B} \boldsymbol{B}^\mathrm{T} \boldsymbol{g} \hat{\boldsymbol{S}} + \hat{\boldsymbol{S}}^\mathrm{T} \boldsymbol{A} \hat{\boldsymbol{I}}. \tag{2.2}$$

[3] As written this is in units of $\mathrm{rad\,s^{-1}\,T^{-1}}$ but is often more usefully quoted in $\mathrm{MHz\,mT^{-1}}$. Confusingly, this term is also sometimes used to refer to $\frac{\mathrm{d}f}{\mathrm{d}B}$, a useful quantity when considering decoherence mechanisms and dipole coupling.

2.1.1 Driving ESR transitions

Now consider the effect of applying a weak microwave drive at frequency ω. For simplicity we consider the case of a free electron. With a static magnetic field B_0 along z and a weak microwave field $B_1\cos(\omega t)$ polarised along x, the Hamiltonian becomes

$$H' = \underbrace{g\mu_\mathrm{B}B_0\hat{S}_z}_{H_0} + \underbrace{g\mu_\mathrm{B}B_1\cos(\omega t)\hat{S}_x}_{V(t)}$$

where H_0 and $V(t)$ are the unperturbed and perturbation parts of the Hamiltonian.

We pre-emptively apply the rotating wave approximation by removing the terms from $V(t)$ that would become fast-rotating terms [5, 57], making the perturbation Hamiltonian

$$V(t) \approx \frac{g\mu_\mathrm{B}B_1}{2}\begin{pmatrix} 0 & \mathrm{e}^{+\mathrm{i}\omega t} \\ \mathrm{e}^{-\mathrm{i}\omega t} & 0 \end{pmatrix}$$

By writing the evolution of the quantum state as $|\psi(t)\rangle = a(t)\,|0\rangle + b(t)\,|1\rangle$, we can apply the time-dependent Schrödinger equation to arrive at two coupled differential equations for the state amplitudes

$$\begin{aligned}\dot{a} &= -\tfrac{\mathrm{i}}{2\hbar}g\mu_\mathrm{B}B_1\mathrm{e}^{+\mathrm{i}\omega t}\mathrm{e}^{-\mathrm{i}\omega_0 t}b \\ \dot{b} &= -\tfrac{\mathrm{i}}{2\hbar}g\mu_\mathrm{B}B_1\mathrm{e}^{-\mathrm{i}\omega t}\mathrm{e}^{+\mathrm{i}\omega_0 t}a\end{aligned}$$

which combine to give a second-order differential equation (substituting $\gamma = \frac{g\mu_\mathrm{B}}{\hbar}$)

$$\ddot{b} + \mathrm{i}(\omega-\omega_0)\dot{b} + \left(\tfrac{1}{2}\gamma B_1\right)^2 b = 0.$$

Starting in the ground state $b(0) = 0$ gives the solution for the amplitude $b(t)$ and probability of the system being found in the excited state $P_{a\to b}(t) = |b(t)|^2$ as

$$\begin{aligned} b(t) &= -\,\mathrm{i}\gamma B_1\mathrm{e}^{-\mathrm{i}(\omega-\omega_0)t/2}\frac{\sin(\omega_\mathrm{r}t/2)}{\omega_\mathrm{r}} \\ P_{a\to b}(t) &= (\gamma B_1)^2\,\frac{\sin^2(\omega_\mathrm{r}t/2)}{\omega_\mathrm{r}^2} = \frac{\omega_1^2}{\omega_r^2}\,\tfrac{1}{2}[1-\cos(\omega_\mathrm{r}t)] \end{aligned} \tag{2.3}$$

such that the probability of the excited state oscillates at the Rabi frequency $\omega_\mathrm{r} = \sqrt{(\omega-\omega_0)^2+\omega_1^2}$ which is $\omega_1 = \gamma B_1$ when on-resonance $\omega = \omega_0$. This is known as Rabi flopping, shown as a function of time and detuning in Fig. 2.1. Note the Rabi frequency is proportional to the strength of the driving field B_1 when on-resonance.

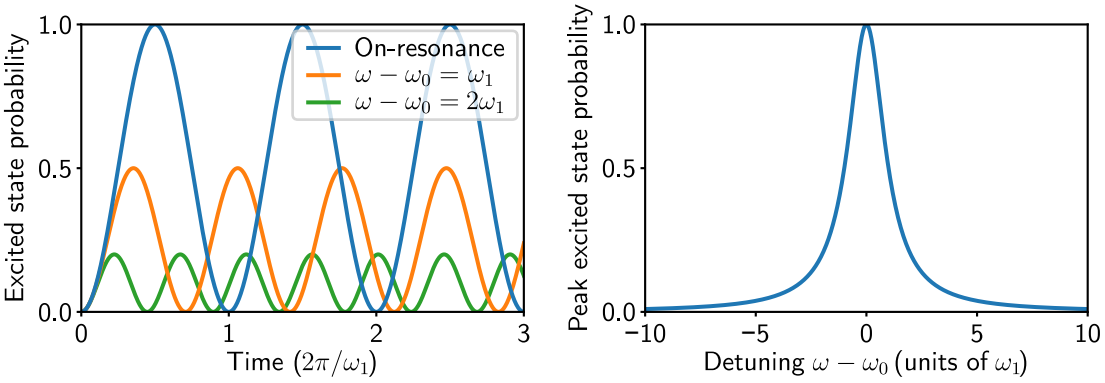

Figure 2.1: A weak oscillating field at frequency ω drives the ESR transition between the ground and excited state at the Rabi frequency ω_r in a phenomenon known as Rabi flopping (left). To maximise the probability of reaching the excited state, the drive should be on-resonance $\omega = \omega_0$ (right).

2.1.2 Pulsed ESR

As described in section 2.1, application of a static magnetic field B_0 to a spin causes its magnetic moment $\boldsymbol{\mu}$ to precess around the z-axis at the Larmor frequency $\omega_0 = \gamma B_0$. By transforming to a coordinate frame rotating around S_z at this frequency, this rapid motion disappears and the spin appears static, effectively subtracting the effect of the constant B_0 field.

We have shown in section 2.1.1 that a weak oscillating magnetic field $B_1 \cos(\omega t)$ can drive ESR transitions when $\omega = \omega_0$. In the rotating frame, this weak drive field becomes effectively static in time, directed along the x-axis of the Bloch sphere. This provides an intuitive way of visualising how the weak field drives the transition, as the effective B_1 field then causes Larmor precession around the x-axis at the Rabi frequency $\omega_1 = \gamma B_1$, rotating the spin vector from the ground state $|0\rangle$ along $+z$ toward the excited state $|1\rangle$ along $-z$.

The extent of this rotation can be controlled by applying short pulses, with either the duration or power of each pulse determining the rotation angle. Since the $\omega_1 \propto B_1$, the rotation angle is proportional to the pulse duration (at fixed power), or the *square*[4] of the pulse power[5] (for fixed duration). These pulses are typically referred to by their rotation angle with a π-pulse rotating from $+z$ to $-z$ and a $\frac{\pi}{2}$-pulse rotating $+z$ to $-y$.

ESR is typically performed not on a single spin but on an ensemble, where the magnetic dipole of each individual spin $\boldsymbol{\mu}$ contributes to an overall magnetisation

[4]This is because the energy density of a microwave field is $U = \frac{1}{2}\boldsymbol{B} \cdot \boldsymbol{H} \propto B_1^2$
[5]Since $P \propto V^2$, the rotation angle is therefore proportional to the rms voltage.

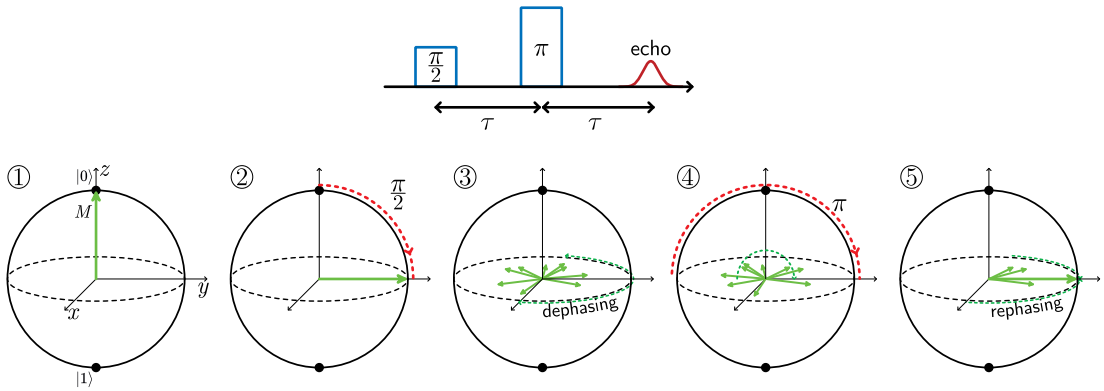

Figure 2.2: Two-pulse echo sequence. 1: Spin ensemble initially relaxed in ground state. 2: $\frac{\pi}{2}$-pulse rotates magnetisation onto x–y plane. 3: Inhomogeneity of Larmor frequency over spin ensemble causes dephasing. 4: π-pulse inverts phase on x–y plane. 5: Phase accrued by each spin prior to π-pulse is reversed as spin ensemble rephases, generating an overall magnetisation detected as a spin echo.

$\boldsymbol{M}$. Due to variation of the gyromagnetic ratio γ or the magnetic field strength B_0 over the spin ensemble, an inhomogeneous broadening of the Larmor frequency is present. This causes individual spins to precess at different rates following a $\frac{\pi}{2}$-pulse, causing dephasing and a free induction decay in the magnitude of $\boldsymbol{M}$ over a characteristic dephasing time T_2^*.

Dephasing induced by a static inhomogeneous broadening over a time τ can be corrected by reversing the time evolution of the spin ensemble. This is done by applying a π-pulse to rotate the spin ensemble around the x-axis, inverting the phase ϕ of the y-component of the magnetisation. The phase accrued by each spin over τ is then reversed over a further time τ, causing a refocusing of the magnetisation of the spin ensemble at time 2τ. The net alignment of magnetisation in the x–y plane emits electromagnetic radiation, creating a detectable signal referred to as a "spin echo". This process of refocusing a spin ensemble, illustrated in Fig. 2.2, is known as a two-pulse or "Hahn" echo sequence [58, 59], which forms the basis of many pulsed ESR methods.

2.1.3 Relaxation

For a spin to relax from an excited state to its ground state, in absence of a driving field, it must lose energy through interaction with the environment. This occurs over a characteristic relaxation time T_1 through several mechanisms, two of which are briefly described here.

Spin-lattice relaxation

In solids the dominant relaxation processes often arise due to interaction with phonons, mediated by fluctuations in local magnetic field due to lattice vibration, known as spin–lattice relaxation [59] (SLR).

Three main processes contribute to SLR [26], with dependence on the transition frequency f and temperature T: The direct process involving one phonon being absorbed or emitted with rate $R_\mathrm{d} = \alpha_\mathrm{D} g^{-2} (hf)^5 \coth\left(\frac{hf}{2k_\mathrm{B}T}\right)$; The Raman process which is a two-phonon process mediated by a virtual energy level $R_\mathrm{R} = \alpha_\mathrm{R} T^{-9}$; and the Orbach process exchanging two phonons with an actual excited energy level $R_\mathrm{O} = \alpha_\mathrm{O} \exp\left(-\frac{\Delta_\mathrm{O}}{k_\mathrm{B}T}\right)$. Here, α_D, α_R, α_O, and Δ_O are empirically determined constants that depend on the spin system in question, and the orientation of the magnetic field in anisotropic systems such as doped Y_2SiO_5.

These relaxation mechanisms exhibit a temperature dependence due to the suppression of lattice vibration at low temperature. The two-phonon Raman and Orbach processes are suppressed heavily at sub-Kelvin temperatures, while the direct process remains as spontaneous emission of a phonon does not require existing lattice vibrations.

Cross-relaxation

Another relaxation process occurs when two ensembles of spins are close enough in resonance to exchange energy with each other through their magnetic dipoles in a process known as cross-relaxation [59]. This can happen when two different types of paramagnetic ions, one excited (ensemble A) and one relaxed (ensemble B), are brought in resonance, or when the bandwidth of the measurement setup is narrower than the inhomogeneous spin linewidth in which case the excited ensemble A and relaxed ensemble B can be the same paramagnetic species. Dipolar coupling between A and B spins causes a resonant exchange of coherent magnetisation at rate ω_FF from A with incoherent magnetisation from B, via a flip-flop interaction $\omega_\mathrm{FF}(S_x^\mathrm{A} S_x^\mathrm{B} + S_y^\mathrm{A} S_y^\mathrm{B})$ [59]. This results in an observed relaxation rate $R_\mathrm{FF} = \alpha_\mathrm{FF} \frac{g^4 n^2}{\Gamma} \operatorname{sech}^2\left(\frac{hf}{2k_\mathrm{B}T}\right)$ where α_FF is an empirically determined constant, Γ is the inhomogeneous spin linewidth, and n the spin concentration [26].

2.1.4 Decoherence

The dephasing induced within a spin ensemble due to its inhomogeneous broadening cannot be refocused with perfect fidelity due to influence from the environment

and uncorrectable spin–spin interactions within the spin ensemble. This uncorrectable dephasing is known as decoherence, an irreversible loss of phase-coherence of quantum information, which occurs over a characteristic coherence time T_2.

Decoherence can arise due to non-static environmental conditions such as fluctuations or noise in the applied B_0 magnetic field, or due to spin–spin interactions between the magnetic fields generated by the precession of each individual spin which creates a different and time-dependent background magnetic environment for each spin. Two common spin–spin decoherence mechanisms present in many ESR experiments, namely spectral diffusion and instantaneous diffusion, are described here.

Spectral diffusion

When the bandwidth of the measurement setup is less than the inhomogeneous broadening of the spin ensemble, only a sub-ensemble A of the spins are excited leaving a sub-ensemble B of spins in thermal equilibrium and not directly affected by the measurement. Spin–spin relaxation processes within the B ensemble cause a change in the local magnetic environment of the A spins, which transfers some A spins out of the detection bandwidth. Similarly, some B spins experience a change in local field which brings them within the measurement bandwidth. The net effect is that some of the excited spin magnetisation is replaced by spins in thermal equilibrium, resulting in an apparent relaxation and a transfer of incoherent B spins into the coherent A sub-ensemble causing decoherence. This is known as spectral diffusion.

The dipolar interactions between the two sub-ensembles give rise to the spectral diffusion linewidth [28, 40]

$$\Gamma_{\mathrm{SD}} = \frac{\pi\mu_0 h}{9\sqrt{3}} n\gamma_{\mathrm{A}}\gamma_{\mathrm{B}} \operatorname{sech}^2\left(\frac{hf}{2k_{\mathrm{B}}T}\right) \tag{2.4}$$

where γ_{A} and γ_{B} are the gyromagnetic ratios (in $\frac{\mathrm{d}f}{\mathrm{d}B_0}$) of the two spin ensembles (typically $\gamma_{\mathrm{A}} \approx \gamma_{\mathrm{B}}$) and n the spin concentration. The $\operatorname{sech}^2\left(\frac{hf}{2k_{\mathrm{B}}T}\right)$ term creates a temperature dependence which heavily suppresses spectral diffusion below the Zeeman temperature $T_{\mathrm{Ze}} = \frac{hf}{k_{\mathrm{B}}}$.

Instantaneous diffusion

While spectral diffusion describes exchange of excited A spins out of the measurement bandwidth due to dynamics within the B spins, instantaneous diffusion arises

from interactions within the A sub-ensemble. The excitation of A spins causes a change in the local magnetic environment surrounding each excited spin. If an A spin is close enough to another for them to be dipole-coupled, the change in magnetic environment may shift the frequency of some A spins out of the detection bandwidth following the excitation pulse. This prevents these spins from being refocused by a two-pulse echo sequence so manifests as a contribution to the measured decoherence.

The proportion of A spins affected by instantaneous diffusion depends on the density of excited spins, as if the A sub-ensemble is sufficiently dilute the distance between nearest-neighbour spins will be large enough to suppress their dipole coupling. Hence the rate of instantaneous diffusion depends on the actual spin concentration n and the spin-flip probability of a microwave pulse of angle θ [59]

$$R_{\mathrm{ID}} = \frac{2\pi^2 \mu_0 h}{9\sqrt{3}} n\gamma^2 \sin^2\left(\frac{\theta}{2}\right). \tag{2.5}$$

where $\gamma = \frac{\mathrm{d}f}{\mathrm{d}B_0}$ is the gyromagnetic ratio of the ensemble being measured. This implies instantaneous diffusion can be suppressed by applying sufficiently weak microwave pulses, or by operating in a regime where $\frac{\mathrm{d}f}{\mathrm{d}B_0} \to 0$.

2.1.5 Zero first-order Zeeman (ZEFOZ)

Many of these decoherence effects arise due to the sensitivity of the spin's energy levels (and hence the spin transition frequencies) to fluctuations in magnetic field. These fluctuations can come from an external source, such as magnetic field noise from the magnet power supply or a stray field from a nearby lab, or they can come from sources within the spin lattice such as spin flips within the spin bath causing a tiny change in magnetic environment. If the sensitivity of the spin frequency to these magnetic fluctuations can be eliminated — i.e. $\frac{\mathrm{d}f}{\mathrm{d}B} = 0$ — then many of these decoherence mechanisms can be heavily suppressed and the coherence time extended by orders of magnitude.

This effect is variously referred to as a "ZEro First-Order Zeeman" (ZEFOZ) condition, or sometimes as a "clock transition" due to its applicability toward making atomic clocks insensitive to fluctuations in magnetic field. The clock transition term is widely used in atomic physics, and in solid-state materials is often used when referring to such effects in isotropic spin systems such as donors in Si. In anisotropic spin systems such as rare-earth doped crystals and in nuclear spin systems, the ZEFOZ term seems to be more common.

ZEFOZ points occur at specific magnetic fields and frequencies. In isotropic systems the orientation of magnetic field does not matter, and the condition for a clock transition $\frac{\mathrm{d}f}{\mathrm{d}B_z} = 0$ can be found for any $I \geq 1$ nucleus coupled to a $S = \frac{1}{2}$ electron. Bismuth-doped silicon with $I = \frac{9}{2}$ exhibits 4 ESR-like clock transitions, measurements at one of which have been shown to extend electron coherence time to 93 ms in $^{\mathrm{nat}}$Si and 2.7 s in isotopically purified ^{28}Si [12].

In anisotropic spin systems such as rare-earth doped Y_2SiO_5, the $\frac{\mathrm{d}f}{\mathrm{d}B_z} = 0$ condition is not sufficient, as the spin frequency must also be resilient to perturbations along x and y, i.e. $\frac{\mathrm{d}f}{\mathrm{d}B_x} = \frac{\mathrm{d}f}{\mathrm{d}B_y} = \frac{\mathrm{d}f}{\mathrm{d}B_z} = 0$; the occurrence of such a point, if it exists, arises from a complex interplay between the anisotropic $\boldsymbol{g}$ and $\boldsymbol{A}$ tensors. ZEFOZ points have been shown to exist across optical transitions in Pr:YAG and hyperfine transitions in Er:Y_2SiO_5 [53], with experimental measurements of nuclear spin coherence time in Er:Y_2SiO_5 combined with dynamical decoupling pulse sequences and a "frozen-core" effect to exhibit an astonishing coherence time of 6 hours [13]. ZEFOZ and near-ZEFOZ conditions have also been realised in ^{171}Yb:Y_2SiO_5 with ESR coherence times of up to 4.1 ms [14]. These ^{171}Yb ZEFOZ transitions are investigated in more detail in Section 2.3.3 and Chapter 7.

2.2 Cavity QED

To drive ESR transitions, an oscillating $B_1 \sin(\omega t)$ magnetic field is applied to the spin ensemble, in resonance with the spin transition frequency. This can be achieved by irradiating the sample with microwaves in free space, but to enhance the strength of the magnetic field a cavity with frequency f_c and linewidth Δf (FWHM) is typically employed to confine and enhance the EM field as photons linger within the cavity for a number of cycles equivalent to the cavity's quality factor $Q = \frac{f_c}{\Delta f}$.

The theory behind the interaction between the cavity and spin is known as cavity QED [6, 7]. Here we summarise its main results relevant to driving spin ensembles with a superconducting resonator and derive important metrics of the strength of the coupling, as well as some results relevant to performing ESR in a strongly coupled system.

2.2.1 Single-spin coupling

The coupling between a cavity and a two-level system such as the resonant transition in a spin is described by the Rabi Hamiltonian [60]

$$\hat{H}^{\mathrm{Rabi}} = \tfrac{1}{2}\hbar\omega_{\mathrm{s}}\hat{\sigma}_z + \hbar\omega_{\mathrm{c}}\left(\hat{a}^\dagger\hat{a} + \tfrac{1}{2}\right) + \tfrac{1}{2}\hbar g_0(\hat{a} + \hat{a}^\dagger)(\hat{\sigma}_+ + \hat{\sigma}_-).$$

where the first term describes the energy of the spin with level splitting ω_{s}, the second the energy of the light field of frequency ω_{c}, and the third the interaction between the cavity with photon number $|n\rangle$ and the spin with ground and excited states $|\downarrow\rangle$ and $|\uparrow\rangle$. $\hat{\sigma}_+ = |\uparrow\rangle\langle\downarrow|$ and $\hat{\sigma}_- = |\downarrow\rangle\langle\uparrow|$ represent the spin raising and lowering operators, and $\hat{a}^\dagger$ and $\hat{a}$ are the bosonic creation and annihilation operators representing the emission $\hat{a}\,|n\rangle = \sqrt{n}\,|n-1\rangle$ and absorption $\hat{a}^\dagger\,|n\rangle = \sqrt{n+1}\,|n+1\rangle$ of a photon in the cavity. In this notation the photon number operator can be written $n = \hat{a}^\dagger\hat{a}$.

Assuming the single-spin coupling strength $g_0 \ll \omega_{\mathrm{s}}, \omega_{\mathrm{c}}$, by applying the rotating wave approximation we arrive at the Jaynes–Cummings Hamiltonian [61]

$$\hat{H}^{\mathrm{JC}} = \tfrac{1}{2}\hbar\omega_{\mathrm{s}}\hat{\sigma}_z + \hbar\omega_{\mathrm{c}}\left(\hat{a}^\dagger\hat{a} + \tfrac{1}{2}\right) + \hbar g_0(\hat{a}\hat{\sigma}_+ + \hat{a}^\dagger\hat{\sigma}_-)$$

In addition to the coupling strength[6] g_0, the system also has loss rates from the cavity κ and the spin γ. In the ideal case for coherent exchange of information between cavity and spin the coupling strength should be much larger than these losses $g_0 \gg \kappa, \gamma$. This is the *strong coupling* regime where losses are negligible in the timescale of the interaction [62]. In this case the Hamiltonian commutes with the total excitation over both cavity and spin $\hat{n}_{\mathrm{tot}} = \hat{a}^\dagger\hat{a} + |e\rangle\langle e|$ and its eigenstates are no longer the states $|n\rangle$ of the cavity and $|g\rangle$, $|e\rangle$ of the spin, but states in the eigenspace of constant excitation number n_{tot} over both cavity and spin [63]

$$\begin{aligned} |+, n\rangle &= \quad \cos(\theta_n)\,|\uparrow, n\rangle + \sin(\theta_n)\,|\downarrow, n+1\rangle \\ |-, n\rangle &= -\sin(\theta_n)\,|\uparrow, n\rangle + \cos(\theta_n)\,|\downarrow, n+1\rangle \end{aligned}$$

with the mixing angle θ_{n} such that

$$\tan(2\theta_{\mathrm{n}}) = -2g_0\frac{\sqrt{n+1}}{\Delta}$$

[6] Not to be confused with the Zeeman g-factor in the ESR Hamiltonian.

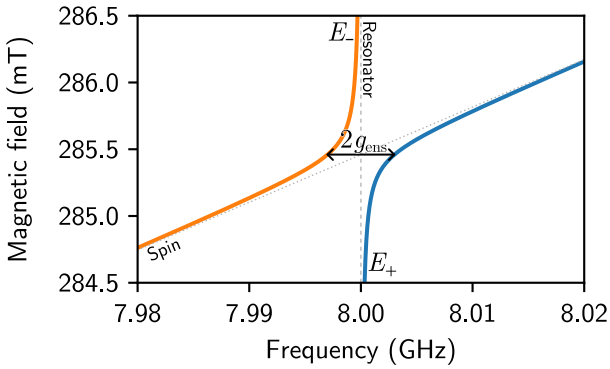

Figure 2.3: Eigenstates $E_\pm$ of the Tavis-Cummings Hamiltonian from Eqn. 2.7. Applied magnetic field is plotted on the y-axis, resonance frequency on the x-axis. Plot calculated for a $g = 2$ free electron with $\gamma = 28.025\,\mathrm{MHz\,mT^{-1}}$ coupling to a $f_\mathrm{c} = 8\,\mathrm{GHz}$ cavity at $g_\mathrm{ens} = 3\,\mathrm{MHz}$. The vacuum Rabi splitting of $2g_\mathrm{ens} = 6\,\mathrm{MHz}$ is visible at the centre of the avoided crossing at $B_0 = 285.5\,\mathrm{mT}$. The uncoupled modes of the resonator (vertical, dashed) and spin (diagonal, dotted) are also shown.

where $\Delta = \omega_\mathrm{s} - \omega_\mathrm{c}$ is the detuning between the photon energy and the spin energy levels. The eigenenergies of these states for a single excitation are [63]

$$E_\pm = \tfrac{1}{2}\hbar(\omega_\mathrm{c} + \omega_\mathrm{s}) \pm \tfrac{1}{2}\hbar\sqrt{\Delta^2 + 4g_0^2} \tag{2.6}$$

When the spin and cavity are on-resonance $|\Delta| \ll g_0$ we are in the resonant regime and the splitting between the two modes $E_+ - E_- = 2g_0$, known as the vacuum Rabi splitting. The coupling between the spin and the vacuum fluctuations of the cavity field causes spontaneous emission, and there is a periodic exchange between the spin and cavity. If at $t = 0$ the spin is excited and the cavity empty $|\uparrow, 0\rangle$, the probability of finding a photon in the resonator and the spin relaxed $|\downarrow, 1\rangle$ is

$$P(t) = \sin^2(g_0 t).$$

This phenomenon is referred to as *vacuum Rabi oscillations*.

The effect of being on-resonance is also observed in the eigenstates and energies of the Hamiltonian, where an avoided crossing of width $2g_0$ appears. This effect, shown in Fig. 2.3, is *vacuum Rabi splitting* and is characteristic of strong coupling.

2.2.2 Many-spin coupling

The Jaynes-Cummings model is not applicable when describing an ensemble of N spins, but by modifying the spin operators to describe excitation of a single spin k

of the N-spin ensemble [63] we arrive at the Tavis-Cummings Hamiltonian [64]

$$\hat{H}^{\mathrm{TC}} = \sum_{k=1}^{N} \tfrac{1}{2}\hbar\omega_{\mathrm{s}}\hat{\sigma}_k^z + \hbar\omega_{\mathrm{c}}\Big(\hat{a}^\dagger\hat{a} + \tfrac{1}{2}\Big) + \sum_{k=1}^{N} \hbar g_k(\hat{a}\hat{\sigma}_k^+ + \hat{a}^\dagger\hat{\sigma}_k^-)$$

where each of the N spins has a coupling strength to the resonator of g_k. Focusing now on a single excitation $n_{\mathrm{tot}} = 1$ the basis states in the eigenspace of constant excitation number over cavity and spin ensemble $\hat{n}_{\mathrm{tot}} = \hat{a}^\dagger\hat{a} + \sum_{k=1}^{N} |e\rangle_k\langle e|$ are $|\downarrow\cdots\downarrow, 1\rangle$ and all N states of one single spin excitation $|\downarrow\cdots\uparrow_k\cdots\downarrow, 0\rangle$. Diagonalisation of the Hamiltonian gives eigenstates similar to the Jaynes-Cummings case but with a *collective* excitation over the spin ensemble

$$\begin{aligned} |+\rangle &= \quad \cos(\theta)\sum_{k=1}^{N} |\downarrow\cdots\uparrow_k\cdots\downarrow, 0\rangle + \sin(\theta)\,|\downarrow\cdots\downarrow, 1\rangle \\ |-\rangle &= -\sin(\theta)\sum_{k=1}^{N} |\downarrow\cdots\uparrow_k\cdots\downarrow, 0\rangle + \cos(\theta)\,|\downarrow\cdots\downarrow, 1\rangle \end{aligned}$$

with eigenenergies

$$E_\pm = \tfrac{1}{2}\hbar(\omega_{\mathrm{c}} + \omega_{\mathrm{s}}) \pm \tfrac{1}{2}\hbar\sqrt{\Delta^2 + 4g_{\mathrm{ens}}^2} \tag{2.7}$$

where we introduce the collective coupling constant $g_{\mathrm{ens}} = \sqrt{\sum_k |g_k|^2}$.

Assuming each spin has the same coupling strength $g_k = g_0$, we can deduce an enhancement in coupling strength against a single spin of $g_{\mathrm{ens}} = \sqrt{N}\,g_0$. This is not a statistical phenomenon, but is due to a single coherent excitation being shared across all spins, referred to as a *spin wave*. This enhancement makes it possible to reach a strong coupling regime $g_{\mathrm{ens}} \gg \kappa, \gamma$ even if the single-spin coupling g_0 is small.

For low excitation numbers $1 < n_{\mathrm{tot}} \ll N$, the system behaves as two mutually coupled harmonic oscillators, and many excitations can be put into the spin wave before saturation becomes relevant [63].

2.2.3 Purcell effect

If the loss rate κ of the cavity is greater than the single-spin coupling g_0, spontaneous emission into the cavity becomes an additional relaxation mechanism for the spin. This is known as the Purcell effect [65] and is characterised by the Purcell rate [66, 67]

$$\Gamma_{\mathrm{P}} = \kappa\frac{g_0^2}{\kappa^2/4 + \Delta^2} \tag{2.8}$$

where $\Delta = \omega_s - \omega_c$ is the spin–cavity detuning.

At low temperatures, spin–lattice relaxation processes become suppressed which can lead to T_1 times measured in minutes to hours. This provides a limit on the rate at which experiments requiring an initially relaxed spin ensemble can be performed. The Purcell effect provides a way to accelerate this relaxation, if the Purcell rate becomes the dominant relaxation mechanism. This can be achieved with sufficiently low cavity loss rates κ (or equivalently high Q) and fast single-spin coupling g_0 [66, 68]. The single-spin coupling g_0 depends strongly on the B_1-field strength as $g_0 \propto B_1$, implying an inhomogeneous B_1 field creates an inhomogeneous Purcell enhancement over the spin ensemble, creating a spatially distributed relaxation time determined by individual spins' coupling to the cavity.

2.2.4 Resonator lineshape

Measuring the transmission of a cavity or resonator can be considered as probing a two-port network whose response as a function of frequency is characterised by the 2×2 scattering matrix

$$\begin{pmatrix} V_1^{\text{out}} \\ V_2^{\text{out}} \end{pmatrix} = \begin{pmatrix} S_{11} & S_{12} \\ S_{21} & S_{22} \end{pmatrix} \begin{pmatrix} V_1^{\text{in}} \\ V_2^{\text{in}} \end{pmatrix}$$

describing the voltage response of the resonator to inputs on ports 1 and 2. Microwave transmission measurements correspond to the parameters S_{21} or S_{12} while measuring reflection yields S_{11} or S_{22}. Resonator measurements in this thesis correspond to measurement of the S_{21} transmission, or measurement of voltage from port 2 for microwaves applied to port 1.

The response of the resonator $\mathrm{S}_{21}(f)$ depends strongly on the frequency f of the applied microwaves. For a continuous drive in steady-state with no background transmission, the transmission takes the form [48, 69, 70]

$$|\mathrm{S}_{21}(f)| = A \left| \frac{\kappa_c}{\mathrm{i}\Delta_r(f) - \kappa_c} \right| \tag{2.9}$$

where A characterises the amplitude of the resonance, κ_c is the cavity halfwidth (in $\mathrm{rad\,s^{-1}}$) and $\Delta_r(f) = 2\pi(f_0 - f)$ and gives the detuning between the cavity frequency f_0 and probe frequency f.

The experiment setup used in later chapters incorporates a 3D cavity enclosing the resonator, which has its own background transmission $\mathrm{S}_{21} = C(f)$. This background interferes with the response of the resonator to introduce an asymmetry to the

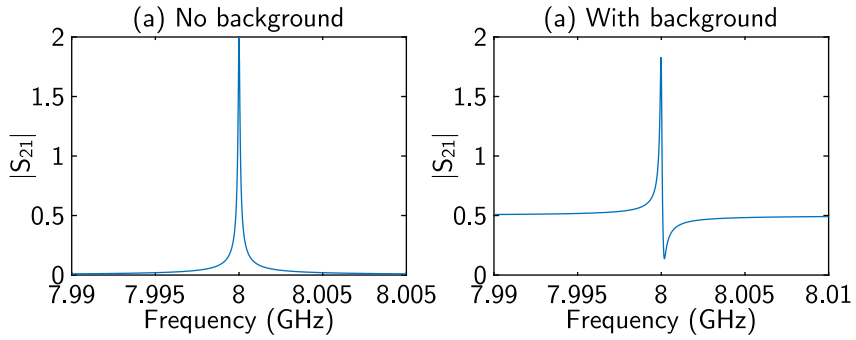

Figure 2.4: Simulated resonator response using (a) no background transmission with Eqn. 2.9 giving a Lorentzian resonance lineshape and (b) a background transmission interfering with the resonator response as per Eqn. 2.10 giving an asymmetric Fano lineshape. Parameters are $C = 0.5$, $A = 2$, $\phi = \frac{\pi}{3}$, $f_0 = 8\,\mathrm{GHz}$, and $\kappa_\mathrm{c} = 50\,\mathrm{kHz}$.

lineshape

$$|\mathrm{S}_{21}(f)| = \left| C(f) + A\mathrm{e}^{-\mathrm{i}\phi} \frac{\kappa_\mathrm{c}}{\mathrm{i}\Delta_\mathrm{r}(f) - \kappa_\mathrm{c}} \right| \tag{2.10}$$

where a phase parameter ϕ accounts for the phase difference between background and resonator response. A comparison between a resonance without and with a background is illustrated in Fig. 2.4.

This type of asymmetric lineshape from a resonant scattering process interfering with a background is equivalently expressed as Fano resonance [71, 72]

$$|\mathrm{S}_{21}(f)| \propto \frac{(q\Delta f/2 + f - f_0)^2}{(\Delta f/2)^2 + (f - f_0)^2} \tag{2.11}$$

where Δf is the resonance full-width at half-maximum and the Fano parameter q describes the ratio of the resonant scattering amplitude to the background.

Fitting experimental data to these models allows the centre frequency f_0 and quality factor $Q = \frac{f_0}{\Delta f} = \frac{\pi f_0}{\kappa_\mathrm{c}}$ (the factor of π arises from conversion of κ_c, the half-width in $\mathrm{rad\,s^{-1}}$, to Δf, the full-width in Hz) of a resonator to be extracted. A generalisation of Eqn. 2.10 to include the effect of spin coupling is given by Eqn. 2.12 in the following section.

2.2.5 Coupled resonator–spin lineshape

As seen in Section 2.7, the eigenstates of the resonator experience a shift in energy from interaction with a spin ensemble. This demonstrates that the centre frequency of the resonant mode measured in S_{21} shifts with interaction with spin, but does not fully describe the effect the spin interaction has on the resonance lineshape. A

theoretical model for this can be derived by solving the Heisenberg equations for the resonator and spin operators [70, 73–75]. This allows an equation describing the $|\mathrm{S}_{21}(B, f)|$ of the cavity to be produced; alternatively, a more complete description including the phase can be derived from the susceptibility of the circuit [76].

First we introduce losses into the Tavis–Cummings Hamiltonian by redefining the resonator and spin frequencies to include imaginary components

$$\omega_\mathrm{c} \mapsto \omega_\mathrm{c} - \mathrm{i}\kappa_\mathrm{c} \qquad \omega_\mathrm{s} \mapsto \omega_\mathrm{s} - \mathrm{i}\gamma_\mathrm{s}$$

where κ_c and γ_s are the loss rates of the resonator and spin ensemble respectively. The Heisenberg equations for the resonator and spin annihilation operators are then [69, 70]

$$\begin{aligned}\dot{\hat{a}} =& \frac{\mathrm{i}}{\hbar}[\hat{H}^\mathrm{TC}, \hat{a}] + [\hat{H}_\mathrm{drive}, \hat{a}] + \kappa_\mathrm{c}\hat{a} \\ \dot{\hat{\sigma}}^- =& \frac{\mathrm{i}}{\hbar}[\hat{H}^\mathrm{TC}, \hat{\sigma}^-] + \gamma_\mathrm{s}\hat{\sigma}^-\end{aligned}$$

where a weak drive of the resonator $\hat{H}_\mathrm{drive}$ with frequency ω and amplitude η is included. In the frame rotating at the drive frequency ω this results in two coupled differential equations [70]

$$\begin{aligned}\dot{\hat{a}} =& -(\mathrm{i}\Delta_\mathrm{r} + \kappa_\mathrm{c})\hat{a} - \mathrm{i}g_\mathrm{ens}\hat{\sigma}^- + \eta \\ \dot{\hat{\sigma}}^- =& -(\mathrm{i}\Delta_\mathrm{s} + \gamma_\mathrm{s})\hat{\sigma}^- - \mathrm{i}g_\mathrm{ens}\hat{a}\end{aligned}$$

where $\Delta_\mathrm{r} = \omega_\mathrm{c} - \omega$ and $\Delta_\mathrm{s} = \omega_\mathrm{s} - \omega$. In the steady-state $\dot{\hat{a}} = \dot{\hat{\sigma}}^- = 0$ and the resonator operator becomes

$$\hat{a} = \frac{\eta}{\mathrm{i}\Delta_\mathrm{r} - \kappa_\mathrm{c} + \frac{g_\mathrm{ens}^2}{\mathrm{i}\Delta_\mathrm{s} + \gamma_\mathrm{s}}}.$$

The mean photon number $\langle \hat{a}^\dagger \hat{a} \rangle$ determines the energy in the resonator, and is proportional to its power transmission $|\mathrm{S}_{21}|^2$. Hence the S_{21} of a resonator coupled to a spin ensemble can be written

$$|\mathrm{S}_{21}| = A \left| \frac{\kappa_\mathrm{c}}{\mathrm{i}\Delta_\mathrm{r} - \kappa_\mathrm{c} + \frac{g_\mathrm{ens}^2}{\mathrm{i}\Delta_\mathrm{s} + \gamma_\mathrm{s}}} \right|$$

where the prefactor $A = \frac{\eta}{\kappa_\mathrm{c}}$ is the peak transmission through the cavity.

The effect of interference with a background transmission, as is the case when driving the resonator via a 3D cavity which will be described in Section 4.1, can be accounted for by including a background transmission as in Section 2.2.4 to complete our parametrisation of S_{21}

$$|S_{21}(B,f)| = \left| C(f) + Ae^{-i\phi} \frac{\kappa_c}{i\Delta_r(f) - \kappa_c + \frac{g_{ens}^2}{i\Delta_s(B,f)+\gamma_s}} \right| \tag{2.12}$$

where $C(f)$ is the background S_{21} transmission of the 3D cavity, A a fit parameter for the amplitude of the resonance, and ϕ the relative phase between background and resonator modes, which introduces the asymmetry to the lineshape. The frequency and field dependences are parameterised by the detuning of the drive frequency f from the resonator frequency f_c and spin frequency f_s according to $\Delta_r(f) = 2\pi(f_0 - f)$ and $\Delta_s(B,f) = 2\pi(f_s(B) - f)$, where f_s can be calculated directly from the spin Hamiltonian or from the gyromagnetic ratio $\frac{df_s}{dB_z}$ with $f_s(B) = f_c + \frac{df_s}{dB_z}(B - B_0)$.

Models using this detailed formulation are necessary when the lineshape of a coupled resonator–spin system is in a regime where the vacuum Rabi splitting can be resolved [48, 77]. If the coupling is sufficiently weak, the coupling strength is less than the spin linewidth $g_{ens} < \gamma_s$ and the vacuum Rabi splitting is not resolvable. In this regime, the full treatment of S_{21} as above is not necessary and a model with two coupled oscillators can be used instead to parametrise the shift in frequency ω and broadening of linewidth κ of the resonator lineshape [73, 77, 78] according to

$$\begin{aligned} \omega &= \omega_c - g_{ens}^2 \frac{\Delta}{\Delta^2 + \gamma_s^2} \\ \kappa &= \kappa_c + g_{ens}^2 \frac{\gamma_s}{\Delta^2 + \gamma_s^2} \end{aligned} \tag{2.13}$$

where $\Delta = m_0(B - B_0)/\hbar$ is the field detuning calculated from the spin magnetic moment $m_0 = \hbar\frac{d\omega}{dB_0}$. This accounts for cases where $\frac{d\omega}{dB}$ varies with B, as is the case for mixed spin systems in the low-field limit or near zero first-order Zeeman (ZEFOZ) points.

2.2.6 Coupling regimes and coooperativity

The relative values of the coupling strength g_{ens} and linewidths of the resonator κ_c and spin κ_s determine how coherently information can be transferred between resonator and spin, and can be characterised into three rather broad regimes. A

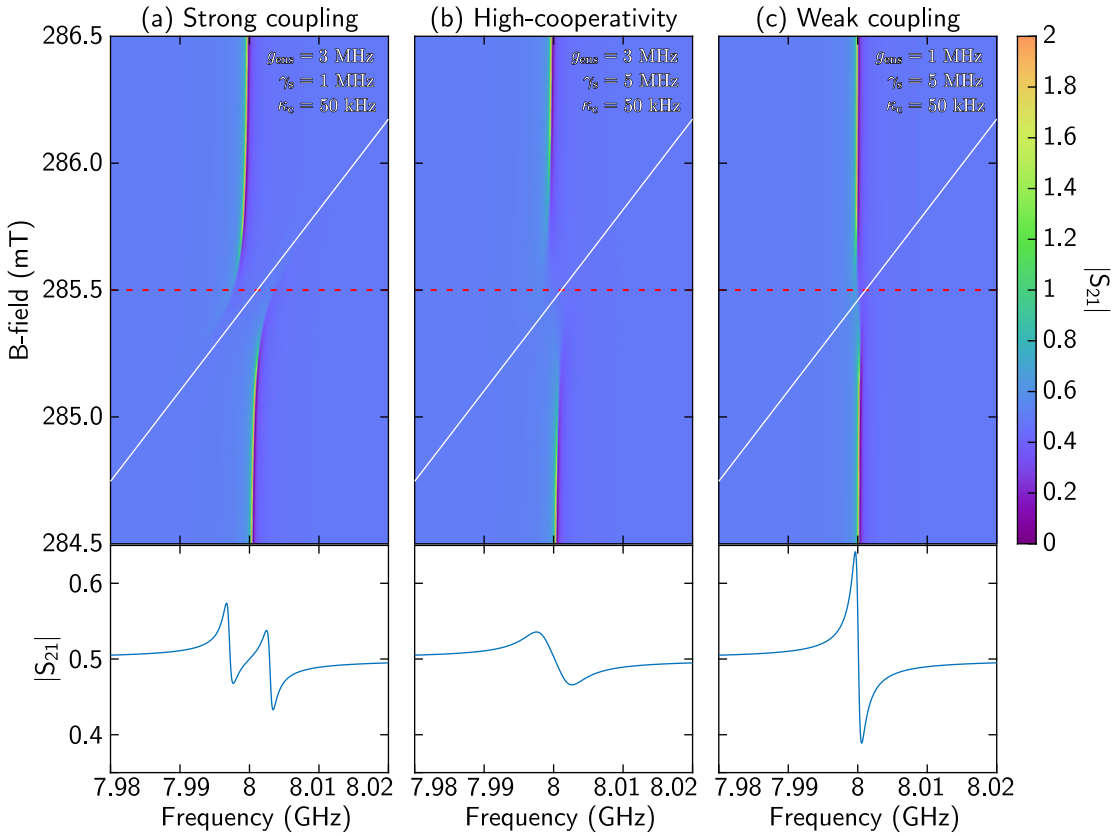

Figure 2.5: Three coupling regimes, illustrated by simulating S_{21} with Eqn. 2.12 for a $g = 2$ electron (with spin tuning shown by the white line). An asymmetric resonator lineshape is introduced with a background transmission of 0.5 interfering with a resonance of amplitude $A = 2$ and relative phase $\phi = \frac{\pi}{2}$, with a linewidth $\kappa_c = 50\,\text{kHz}$. The dotted red line indicates a cut along the 2D plot at the centre of the avoided crossing, with trace shown below. (a) In the strong coupling regime, an avoided crossing is clearly visible with distinct vacuum Rabi modes at its centre separated by $2g_{ens}$. (b) In the high-cooperativity regime the onset of an avoided crossing is visible, but vacuum Rabi splitting may not be resolvable due to broadening of the vacuum Rabi modes. (c) A weak coupling may result in a broadening of the lineshape but any frequency shift is small.

relevant measure is the cooperativity[7] $C = \frac{g_{\text{ens}}^2}{\kappa_c \gamma_s}$ which describes the entangling strength of the resonator–spin interface. These regimes are illustrated in Fig. 2.5 with simulated S_{21} calculated from Eqn. 2.12 for a $g = 2$ electron.

The *strong coupling* regime describes a situation where $g_{\text{ens}} \gg \kappa_c, \gamma_s$ and $C \gg 1$. With these parameters an avoided crossing is clearly visible between the resonator and spin modes, and two distinct vacuum Rabi modes with splitting $2g_{\text{ens}}$ are visible at the centre of the crossing. In this regime, a quantum state can be coherently exchanged from resonator to spin ensemble and back faster than the information decoheres.

If $C > 1$ but $g_{\text{ens}} \not\gg \kappa_c, \gamma_s$, we are in a *high-cooperativity* regime. The onset of an avoided crossing is visible but the broadening of the two resonant modes is typically less than the splitting between them $2g_{\text{ens}}$, meaning the two peaks often cannot be distinguished. With superconducting resonators generally $\kappa_c \ll \gamma_s$ if not at a ZEFOZ condition, so the cooperativity is typically limited by the interplay between g_{ens} and κ_c.

If $g_{\text{ens}} \ll \kappa_c, \gamma_s$ we are in a *weak coupling* regime. A broadening of the resonator lineshape may be observed on-resonance, but any shift in frequency is small and not suggestive of an avoided crossing. Coherent state transfer is not possible.

There are additional coupling regimes beyond strong coupling, which are not well described with the models presented here but have nonetheless proven experimentally realisable using circuit QED. If $g_{\text{ens}} \approx \omega$ we approach the ultrastrong coupling regime [79, 80] and beyond this the deep strong coupling regime $g_{\text{ens}} > \omega$ [81, 82], where the rotating wave approximation used in the derivation of the Jaynes-Cummings model breaks down.

2.3 ESR simulation

To assist with experimental design and enable a thorough analysis of experimental data, it is necessary to numerically simulate the rare-earth spin system to determine locations and properties of resonant transitions. This section describes the simulation and the parameters describing the spin system, presents simulated data relevant to experiments in later chapters, and highlights the presence of coherence-enhancing ZEFOZ transitions in ^{171}Yb.

[7] The cooperativity is sometimes seen with an additional factor of 4, $C = \frac{4g_{\text{ens}}^2}{\kappa_c \gamma_s}$. This arises when the values of κ_c and γ_s are the full-width, rather than the half-width as described here.

2.3.1 Hamiltonian parameters

Simulating the mixed spin system of an electron with spin $\boldsymbol{S}$ coupled to a nuclear spin $\boldsymbol{I}$ within a magnetic field $\boldsymbol{B}$ involves solving the ESR spin Hamiltonian Eqn. 2.2 derived in Section 2.1:

$$H = \mu_{\mathrm{B}} \boldsymbol{B}^{\mathrm{T}} \boldsymbol{g} \hat{\boldsymbol{S}} + \hat{\boldsymbol{S}}^{\mathrm{T}} \boldsymbol{A} \hat{\boldsymbol{I}}.$$

This includes two terms, the Zeeman tensor $\boldsymbol{g}$ describing the field dependence of the electron spin and the hyperfine tensor $\boldsymbol{A}$ which parametrises the interaction between electron and nuclear spin. These in general are 3×3 matrices, describing the field dependence of an anisotropic spin system such as rare-earths in Y_2SiO_5. A convenient orthogonal basis for these tensors is the [D_1, D_2, b] frame described in Section 1.1.1, a coordinate frame use throughout the rest of this thesis.

These values depend on the specific rare-earth under investigation, and must be derived empirically from ESR measurements of the crystal in a magnetic field. The two rare-earth systems used in this thesis are neodymium and ytterbium, whose Hamiltonian parameters $\boldsymbol{g}$ and $\boldsymbol{A}$ are given in the literature:

Neodymium

Neodymium $_{60}$Nd, when doped substitutionally replacing Y in Y_2SiO_5, forms the trivalent ion Nd^{3+} with a larger ionic radius than Y and most rare-earths [83]. As a result it preferentially substitutes into Y_2SiO_5 site 1, which has a larger coordination number and correspondingly greater distance to nearest-neighbour oxygens leaving more room for the Nd^{3+} ion.

As such, only for site 1 have both the Zeeman and hyperfine tensors been derived. Hannes Maier-Flaig [84] performed EPR spectroscopy on isotopically purified ^{145}Nd:Y_2SiO_5 to arrive at the values

$$\boldsymbol{g} = \begin{pmatrix} 1.30 & 0.62 & 0.22 \\ 0.62 & -2.07 & 1.62 \\ 0.22 & 1.62 & -2.86 \end{pmatrix}_{(\mathrm{D_1},\mathrm{D_2},\mathrm{b})}$$

$$\boldsymbol{A} = \begin{pmatrix} -37.1 & -99.9 & -83.4 \\ -99.9 & -589.2 & 169.4 \\ -83.4 & 169.4 & -678.4 \end{pmatrix}_{(\mathrm{D_1},\mathrm{D_2},\mathrm{b})} \quad \text{MHz}.$$

A small residual component of Nd in Y_2SiO_5 site 2 is also resolvable. The signal is too weak to derive the hyperfine tensor from but Robert Marino [85] gives the

Zeeman tensor for Nd site 2

$$\boldsymbol{g} = \begin{pmatrix} 2.42 & -0.30 & -0.94 \\ -0.30 & 0.27 & -0.69 \\ -0.94 & -0.69 & 3.14 \end{pmatrix}_{(\mathrm{D}_1,\mathrm{D}_2,\mathrm{b})}$$

These values are used for analysis of experimental data using isotopically purified ^{145}Nd, a $I = \frac{7}{2}$ isotope, in chapters 5 and 6.

Ytterbium

Ytterbium $_{70}$Yb has an ionic radius more similar to Y^{3+} than Nd^{3+}, and dopes equally into both sites 1 and 2. Alexey Tiranov combines EPR measurements with ODMR [29] to calculate the Hamiltonian parameters for ^{171}Yb. For site 1, the Zeeman and hyperfine tensors are

$$\boldsymbol{g} = \begin{pmatrix} 6.072 & -1.460 & -0.271 \\ -1.460 & 1.845 & -0.415 \\ -0.271 & -0.415 & 0.523 \end{pmatrix}_{(\mathrm{D}_1,\mathrm{D}_2,\mathrm{b})}$$

$$\boldsymbol{A} = \begin{pmatrix} 4.847 & -1.232 & -0.244 \\ -1.232 & 1.425 & -0.203 \\ -0.244 & -0.203 & 0.618 \end{pmatrix}_{(\mathrm{D}_1,\mathrm{D}_2,\mathrm{b})} \text{GHz},$$

and for site 2

$$\boldsymbol{g} = \begin{pmatrix} 0.999 & -0.766 & 0.825 \\ -0.766 & 0.825 & -0.424 \\ 0.825 & -0.424 & 5.867 \end{pmatrix}_{(\mathrm{D}_1,\mathrm{D}_2,\mathrm{b})}$$

$$\boldsymbol{A} = \begin{pmatrix} 0.686 & -0.718 & 0.492 \\ -0.718 & 0.509 & -0.496 \\ 0.492 & -0.496 & 4.729 \end{pmatrix}_{(\mathrm{D}_1,\mathrm{D}_2,\mathrm{b})} \text{GHz}.$$

These data parametrise the spin Hamiltonian for ^{171}Yb ($S = \frac{1}{2}$, $I = \frac{1}{2}$). By neglecting the hyperfine interaction $\boldsymbol{A} = 0$ the g-tensor alone simulates the $I = 0$ isotopes, and the $I = \frac{5}{2}$ isotope ^{173}Yb can be simulated by multiplying $\boldsymbol{A}$ by the nuclear gyromagnetic factor $g_\mathrm{n} = -0.27$ for ^{173}Yb [27].

These values are used to describe experimental data in Chapter 7 and for a study into ZEFOZ transitions in ^{171}Yb in Section 2.1.5.

2.3.2 Simulation

With the parameters for ^{145}Nd and Yb, the spin Hamiltonian can be numerically solved as a function of magnetic field $\boldsymbol{B}$. This is performed using EasySpin [86], a MATLAB toolbox for simulation of EPR spectra. An example of using EasySpin for ESR simulation of doped Y_2SiO_5 is presented in Appendix A.

Using various solvers provided by EasySpin, the anisotropic ESR properties of the doped Y_2SiO_5 crystal can be investigated. Three types of simulation that help illustrate the spin system and produce experimentally relevant diagrams and data are presented here.

Breit-Rabi diagram

A Breit-Rabi diagram describes the dependence of the energy levels of the electron–nucleus spin system on applied magnetic field strength. In the low-field limit the hyperfine interaction between the magnetic fields generated by the electron and the nucleus dominates, mixing the eigenstates of the electron and nuclear spins and causing a zero-field splitting of the energy levels. Increasing magnetic field strength breaks any degeneracy of electron spin states, and in the high-field limit this splitting dominates with $m_s = +\frac{1}{2}$ states increasing in energy and $m_s = -\frac{1}{2}$ decreasing.

A series of Breit-Rabi diagrams for ^{145}Nd and Yb are shown in Fig. 2.6 for fields applied along the three axes [D_1, D_2, b], calculated with the `levels` solver. The anisotropy of the g-tensor is evident from the varying gradients between field angles in the diagram, with shallow gradients corresponding to smaller g-factors along that axis.

Transition frequency vs. field

An experiment performing ESR with a resonator at a fixed frequency f is more appropriately illustrated by plotting the frequency of spin transitions against magnetic field B as in Fig. 2.7. In this simulation, calculating resonant frequencies at each field point using the `resfreqs_matrix` solver, as magnetic field is increased the Zeeman term typically causes the resonant frequency of ESR transitions to increase. In the high-field limit $\frac{\mathrm{d}f}{\mathrm{d}B}$ becomes constant, with smaller g-factors giving lower $\frac{\mathrm{d}f}{\mathrm{d}B}$.

In the high-field limit, allowed transitions are determined by the selection rule $\Delta m_s = \pm 1$. At lower fields the significant contribution of the hyperfine term mixes the electron and nuclear spin states, causing spin transitions to not be pure ESR

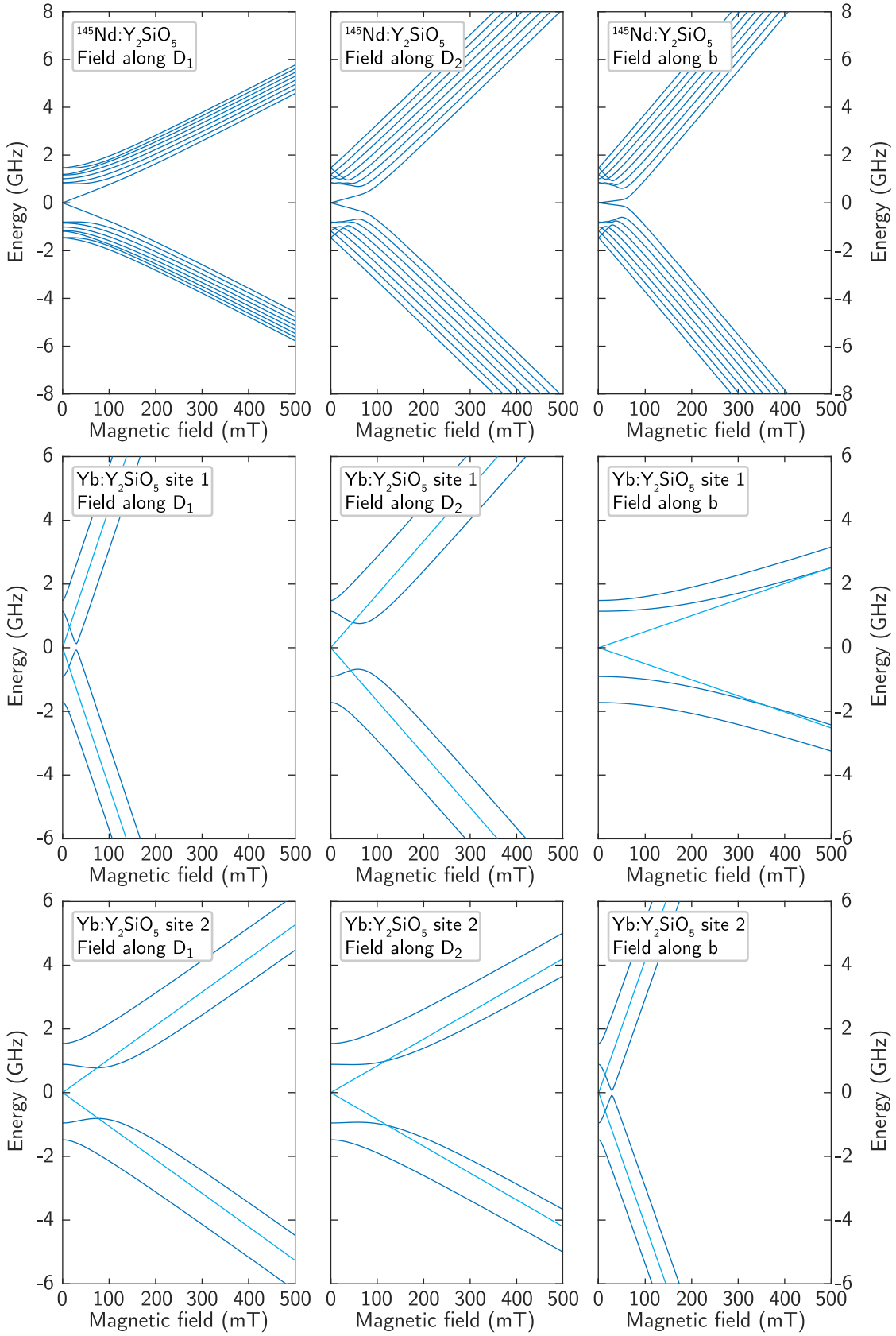

Figure 2.6: Breit-Rabi (energy levels vs. field) diagram for ^{145}Nd and Yb, highlighting the anisotropy of the field dependence in Y_2SiO_5. Top: ^{145}Nd with $I = \frac{7}{2}$, which almost exclusively dopes into Y_2SiO_5 site 1. Middle & Bottom: ^{171}Yb with $I = \frac{1}{2}$ (blue) and the $I = 0$ Yb isotopes (cyan) for both Y_2SiO_5 sites 1 and 2. The $I = \frac{5}{2}$ ^{173}Yb isotope is not shown for simplicity.

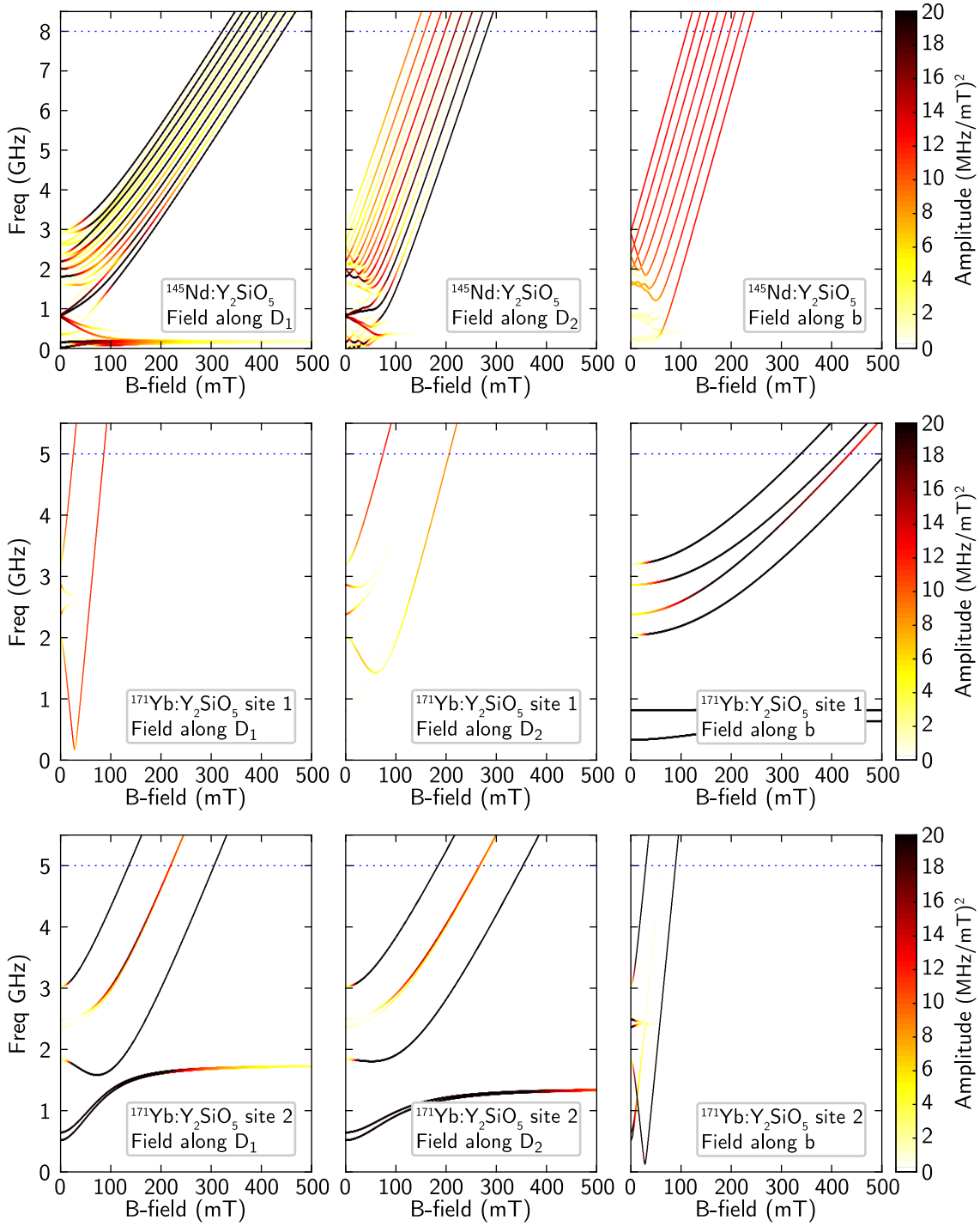

Figure 2.7: Diagrams of spin transition frequency versus field strength. Top: ^{145}Nd. Middle & Bottom: ^{171}Yb. Allowed transitions are identified by calculating their amplitude using Fermi's golden rule [87], such that forbidden transitions are plotted invisibly in white. As field is increased, spin transitions come in resonance with the resonator (indicated in blue at $f = 8\,\mathrm{GHz}$ for Nd, 5 GHz for Yb). This indicated fields at which a spin transition can be driven via the resonator.

$\Delta m_s = \pm 1$ or NMR $\Delta m_I = \pm 1$ transitions, and the selection rules break down. The amplitude of each transition is instead calculated from Fermi's golden rule [87] to give the colours presented in Fig. 2.7.

Allowed transitions are brought in resonance with the resonator frequency ($f =$ 8 GHz for Nd, 5 GHz for Yb) at certain fields, where the B_1 field of the resonator drives these spin transitions, causing a detectable shift in resonator prominence or frequency. This forms the motivation of field-swept spectra, whereby the magnetic field strength is swept along a constant axis while tracking the resonator frequency, a tool used in chapters 5–7.

Roadmap

For anisotropic spin systems, the angular dependence of the spin transitions can be illustrated by a figure displaying resonant fields against angle of magnetic field in a plot known as a "roadmap". Roadmaps for ^{145}Nd and ^{171}Yb are shown in Fig. 2.8 for B_0 field perpendicular to the b axis, rotating in the D_1–D_2 plane. These are calculated using the `resfields` solver for a fixed resonator frequency and field orientation. This orientation is chosen because the Y_2SiO_5 chips used for fabrication in this project are prepared with a polished face approximately perpendicular to the b crystal axis, such that the plane of the superconducting resonator lies close to the D_1–D_2 plane, and to perform high-field experiments we must constrain the magnetic field to lie parallel with this plane as described later in Chapter 3.

These roadmaps serve two purposes. Firstly, the anisotropy of a spin species is typically unique, and can be used to verify the identity of a particular spin transition as being due to a known spin species or some unknown impurity. Secondly, the roadmap depends heavily on the axis of rotation and initial starting vector. By constraining the magnetic field to lie within the plane of the superconductor and measuring a roadmap in this plane, the alignment of the crystal axes with respect to this plane can be determined. This enables experiments that require a field accurately aligned within [D_1, D_2, b] to be performed, such as experiments benefiting from near-ZEFOZ in ^{171}Yb as described in the next section.

2.3.3 ZEFOZ in ^{171}Yb

The large and highly anisotropic hyperfine tensor in ^{171}Yb (see Section 2.3.1) causes it to have non-zero eigenvalues $A_1 \neq A_2 \neq A_3$. This results in the zero-field degeneracy of the four spin states to be completely lifted, with energies $\frac{1}{4}[-A_3 \pm (A_1 + A_2)]$, $\frac{1}{4}[A_3 \pm (A_1 - A_2)]$ [29]. It also results in eigenstates consisting of maximally en-

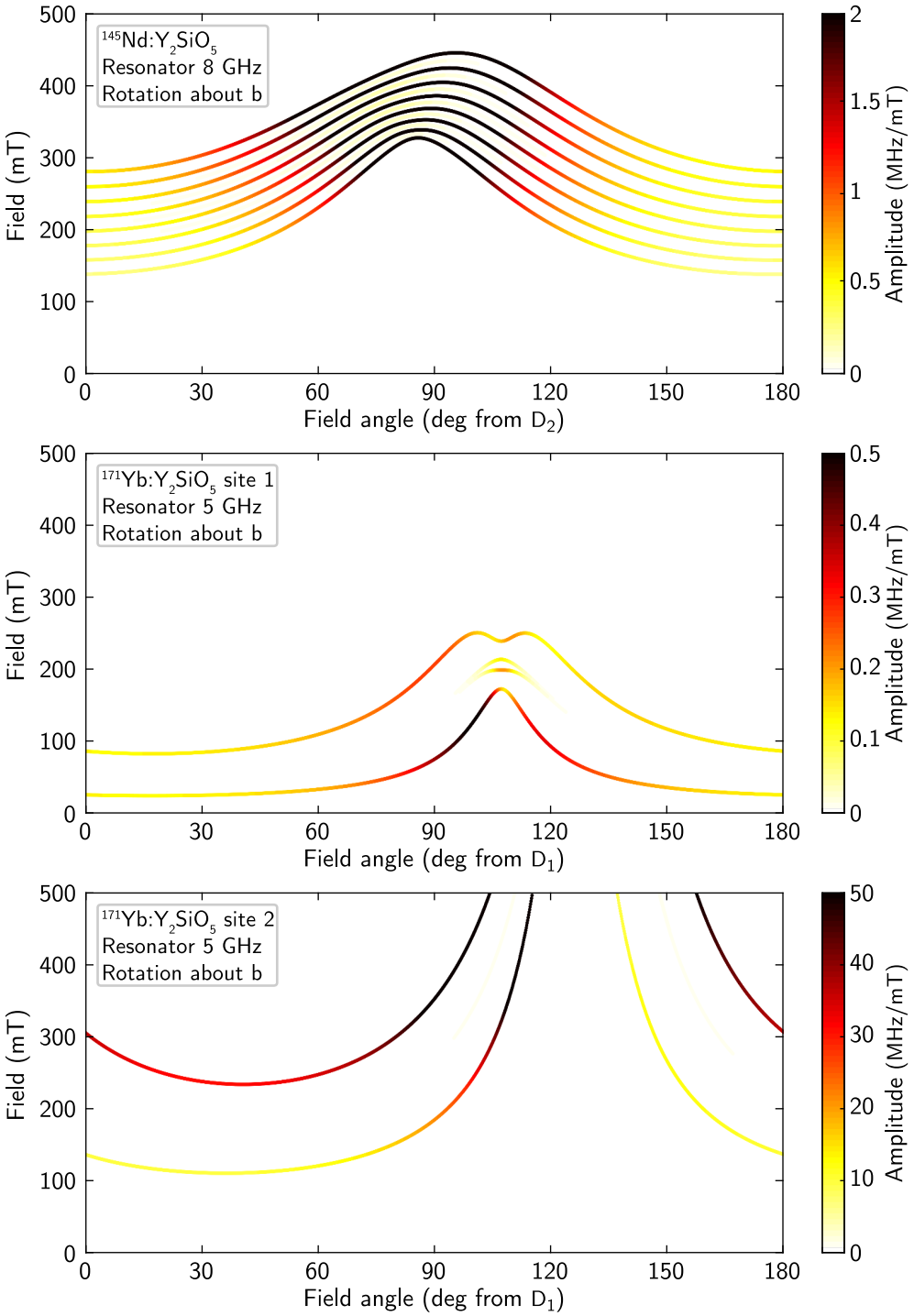

Figure 2.8: Roadmap showing angular dependence of ESR transition fields for angle of B_0 within the D_1–D_2 plane. Top: ^{145}Nd. Middle & Bottom: ^{171}Yb. The angular dependence can be used to positively identify the spin species causing an observed transition, as well as the crystal orientation with respect to the lab frame.

tangled Bell states between electron and nucleus $|\Psi^{\pm}\rangle = \frac{1}{\sqrt{2}}[|\uparrow\Downarrow\rangle \pm |\downarrow\Uparrow\rangle]$, $|\Phi^{\pm}\rangle = \frac{1}{\sqrt{2}}[|\uparrow\Uparrow\rangle \pm |\downarrow\Downarrow\rangle]$ [14] where $|\uparrow / \downarrow\rangle$ and $|\Uparrow / \Downarrow\rangle$ are the states of the electron and nuclear spin respectively.

For any of the eigenstates $|\xi\rangle = |\Psi^{\pm}\rangle, |\Phi^{\pm}\rangle$, taking the partial trace over the nuclear or electronic term $\mathrm{Tr}_{I,S}[|\xi\rangle]$ gives the maximally mixed state $\rho = \frac{\mathbb{1}}{2}$ which has a total spin of zero for both the nuclear $\langle \boldsymbol{I} \rangle = 0$ and electron spin $\langle \boldsymbol{S} \rangle = 1$. This implies that for both the electron and nuclear Zeeman terms in the spin Hamiltonian, $\langle \xi | \boldsymbol{B}^{\mathrm{T}} \boldsymbol{g} \hat{\boldsymbol{S}} | \xi \rangle = \langle \xi | \boldsymbol{B}^{\mathrm{T}} \boldsymbol{g}_{\mathrm{N}} \hat{\boldsymbol{I}} | \xi \rangle = 0$ and that any shift in the energy levels due to a perturbing B-field is zero to first order.

Therefore in ^{171}Yb, all spin transitions have a first-order Zeeman coefficient $\frac{\mathrm{d}f}{\mathrm{d}B}_{B=0} = 0$ making the transition frequency insensitive to perturbations in magnetic field in any direction. Hence this spin system exhibits a ZEFOZ condition at zero field, also known as zero field, zero first-order Zeeman (ZEFIZEFOZ).

Zero-field ZEFOZ (ZEFIZEFOZ)

The ZEFIZEFOZ condition in ^{171}Yb:Y_2SiO_5 provides a degree of protection against decoherence mechanisms by detuning the spin transition frequency from changes and fluctuations in magnetic field strength. Using the Hamiltonian parameters for ^{171}Yb reported in Section 2.3.1, ESR simulation of the spin system for magnetic field centred around $B = 0$ can be used to verify the existence of the ZEFIZEFOZ condition for all spin transitions. To do this, resonant frequencies are calculated using `resfreqs_matrix` over a cartesian grid of magnetic fields over all 3 [D_1, D_2, b] axes. The first and second-order Zeeman coefficients are calculated at each point $\nabla f = \frac{\mathrm{d}f}{\mathrm{d}B_x}\hat{x} + \frac{\mathrm{d}f}{\mathrm{d}B_y}\hat{y} + \frac{\mathrm{d}f}{\mathrm{d}B_z}\hat{z}$, $\nabla^2 f = \frac{\mathrm{d}^2 f}{\mathrm{d}B_x^2}\hat{x} + \frac{\mathrm{d}^2 f}{\mathrm{d}B_y^2}\hat{y} + \frac{\mathrm{d}^2 f}{\mathrm{d}B_z^2}\hat{z}$, and their norm gives the steepest gradient $\left|\frac{\mathrm{d}f}{\mathrm{d}B}\right|$ and greatest second derivative $\left|\frac{\mathrm{d}^2 f}{\mathrm{d}B^2}\right|$ respectively.

This has been calculated for ^{171}Yb site 1 (site 2) in Fig. 2.9 (Fig. 2.10). These plots take a slice perpendicular to the D_1 (b) axis to plot $\left|\frac{\mathrm{d}f}{\mathrm{d}B}\right|$ around $B = 0$. The motivation of the orientation of these slices is discussed in the next subsection. Finding local minima across each slice verifies that each transition minimises its first-order Zeeman term at $B = 0$, where $\left|\frac{\mathrm{d}f}{\mathrm{d}B}\right| = 0\,\mathrm{kHz\,mT^{-1}}$.

While all transitions exhibit identically zero first-order Zeeman terms, their second derivatives are not equivalent. A smaller second-order term provides additional insensitivity to fluctuations in magnetic field and hence would yield a further improvement to coherence time at zero field, or reduces the extent to which the magnetic field must be suppressed to observe a ZEFOZ enhancement. These

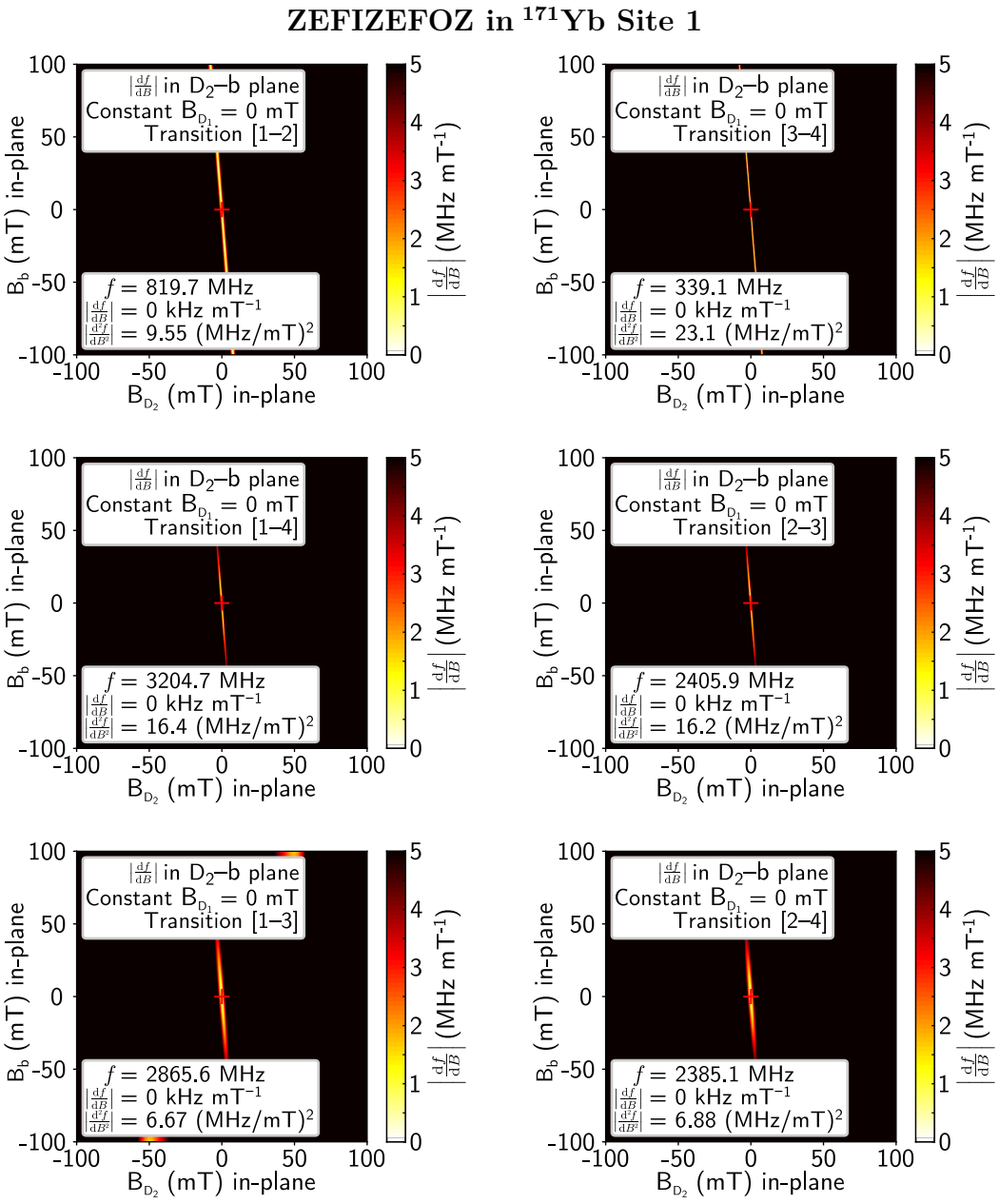

Figure 2.9: Zero-field ZEFOZ (ZEFIZEFOZ) condition in ^{171}Yb:Y_2SiO_5 site 1. For each of the 6 spin transitions, the spin frequency, first-order Zeeman term $\left|\frac{df}{dB}\right|$ and second-order Zeman term $\left|\frac{d^2f}{dB^2}\right|$ are calculated across a grid of magnetic field along [D_1, D_2, b]. Plotted is a slice of $\left|\frac{df}{dB}\right|$ across the D_2–b plane indicating the presence of a ZEFIZEFOZ point at $B = 0$ for all transitions with $\left|\frac{df}{dB}\right| = 0\,\mathrm{kHz\,mT^{-1}}$. $\left|\frac{d^2f}{dB^2}\right|$ is minimised for transitions [1–3] and [2–4], providing the greatest protection against magnetic field fluctuations.

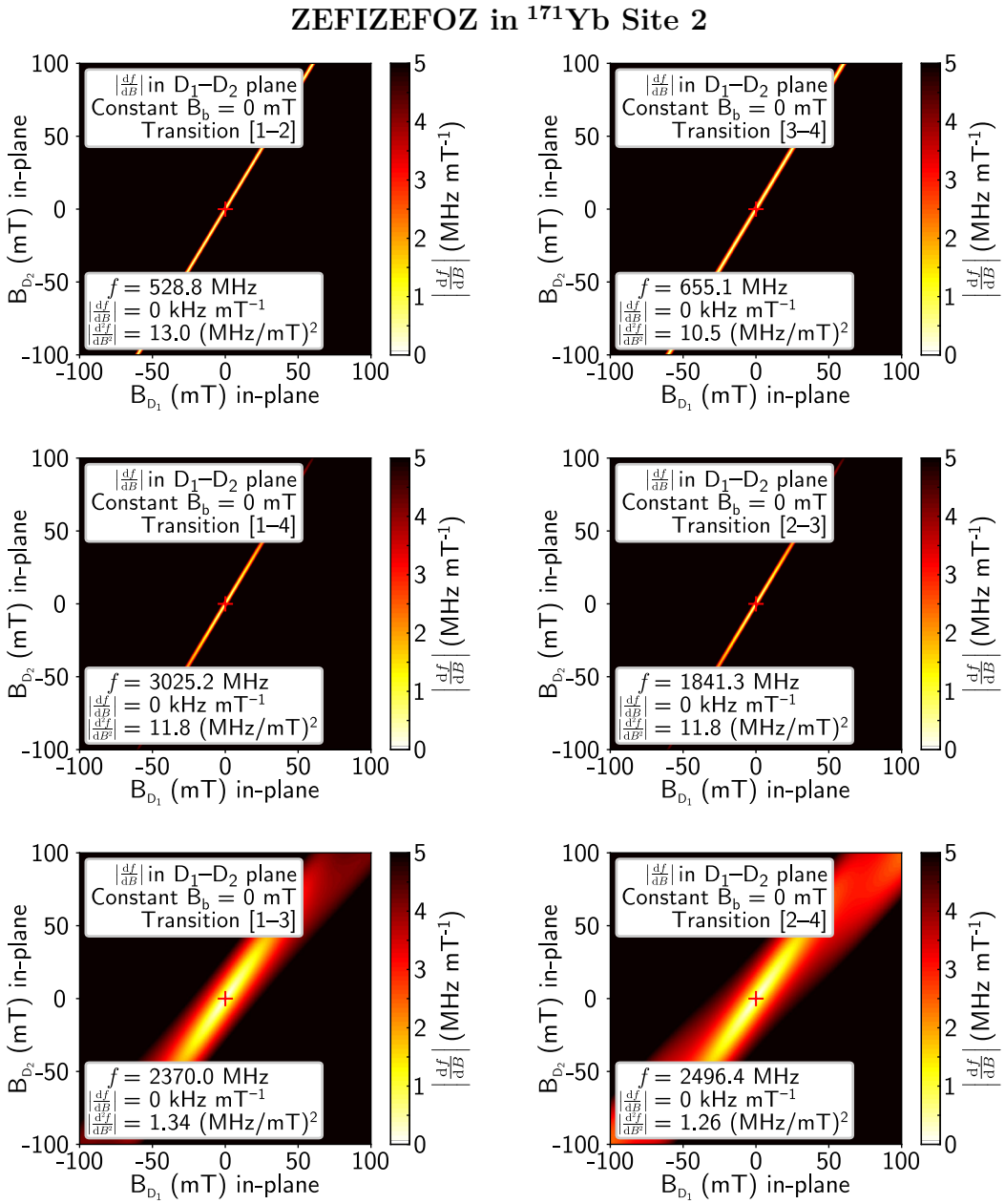

Figure 2.10: Zero-field ZEFOZ (ZEFIZEFOZ) condition in ^{171}Yb:Y_2SiO_5 site 2. For each of the 6 spin transitions, the spin frequency, first-order Zeeman term $\left|\frac{df}{dB}\right|$ and second-order Zeman term $\left|\frac{d^2f}{dB^2}\right|$ are calculated across a grid of magnetic field along [D_1, D_2, b]. Plotted is a slice of $\left|\frac{df}{dB}\right|$ across the D_1–D_2 plane indicating the presence of a ZEFIZEFOZ point at $B = 0$ for all transitions with $\left|\frac{df}{dB}\right| = 0\,\mathrm{kHz\,mT^{-1}}$. $\left|\frac{d^2f}{dB^2}\right|$ is minimised for transitions [1–3] and [2–4], providing the greatest protection against magnetic field fluctuations.

simulations indicate $\left|\frac{\mathrm{d}^2 f}{\mathrm{d}B^2}\right|$ is minimised for the [1–3] and [2–4] transitions, with $\left|\frac{\mathrm{d}^2 f}{\mathrm{d}B^2}\right| \approx 6.8\,(\mathrm{MHz/mT})^2$ for site 1 and $\approx 1.3\,(\mathrm{MHz/mT})^2$ for site 2.

Operating at a ZEFOZ point requires a resonator capable of being tuned to match the ESR transition frequency. Some methods of tuning superconducting resonators are discussed in Section 3.2, and one of the most reliable methods involves the application of a global magnetic field to change the device's kinetic inductance (see Section 3.1.2). While this method is, by definition, incompatible with $^{171}\mathrm{Yb}{:}\mathrm{Y_2SiO_5}$ the zero-field ZEFOZ transition, there are nonetheless "near-ZEFOZ" conditions where a coherence enhancement has been observed at finite magnetic fields.

near-ZEFOZ

The first-order Zeeman term is only uniquely zero (ZEFOZ) at $B = 0$, but around this ZEFIZEFOZ point there is a substantial region where a small field can be applied while keeping the first-order Zeeman term low (but nonzero), providing some protection against magnetic field fluctuations. This near-ZEFOZ condition arises due to the high anisotropy of the Zeeman tensor in both sites [14], with one strong component of the $\boldsymbol{g}$-tensor perpendicular to two weaker components.

This effect can be simulated using the same numerical approach as for the ZEFIZEFOZ simulations, this time taking slices centred around $B \neq 0$. The lowest $\left|\frac{\mathrm{d}^2 f}{\mathrm{d}B^2}\right|$ from the ZEFIZEFOZ simulation comes from [1–3] and [2–4] transitions in both sites, and these transitions occur at microwave frequencies 2.3 GHz–2.9 GHz compatible with superconducting resonators, so we focus on these four transitions for the following simulations.

Figs. 2.11–2.14 present simulations of the first-order Zeeman coefficient for slices of constant magnetic field applied parallel to the axis with the strongest component of the $\boldsymbol{g}$-tensor. For site 1 this is D_1, and for site 2 this is b. $\left|\frac{\mathrm{d}f}{\mathrm{d}B}\right|$ is plotted in the D_2–b (D_1–D_2 for site 2) for each of three slices at $B = 0$, 2, and 5 mT along the perturbing axis. Finding local minima locates the 3D magnetic field that minimises $\left|\frac{\mathrm{d}f}{\mathrm{d}B}\right|$, corresponding to the near-ZEFOZ point.

In each Fig. (a), the minimum $\left|\frac{\mathrm{d}f}{\mathrm{d}B}\right|$ is shown for each field slice. This increases as with the magnitude of the field, remaining below 1 % of a $g_\mathrm{e} = 2$ free electron[8] for site 1 and below 0.6 % for site 2 up to 5 mT along the strongest g-tensor axis. The plot has a significant scatter due to the simulated field points being restricted to the 0.1 mT grid resolution — for many points a lower first-order term could be found with greater field precision but for these simulations the memory requirements

[8] A $g_\mathrm{e} = 2$ free electron tunes at $28.0\,\mathrm{MHz\,mT^{-1}}$.

proved prohibitive. If a more accurate estimate for the near-ZEFOZ point around a particular field is required, a finer grid can be simulated over that specific region of $\boldsymbol{B}$-field.

Alongside this, each Fig. (b) indicates the volume of $\boldsymbol{B}$-field space which encloses a first-order Zeeman term of $\left|\frac{\mathrm{d}f}{\mathrm{d}B}\right| = [0.5, 1, 1.5]$ MHz mT^{-1}, helping visualise how the near-ZEFOZ point moves in 3D space. For site 1 there is some aliasing visible due to the grid precision.

Due to its greater second-order term $\left|\frac{\mathrm{d}^2 f}{\mathrm{d}B^2}\right| \approx 6.8\,(\mathrm{MHz/mT})^2$, site 1 in general yields larger first-order Zeeman coefficients than site 2. In addition, the orientation of site 2 yields a near-ZEFOZ point within the D_2–D_2 plane for any field along b < 5 mT. This orientation is much more convenient than that of site 1, where a near-ZEFOZ point can be found in the D_2–b plane for any field along $D_1 < 5$ mT, as the Y_2SiO_5 crystals used for this project have a face perpendicular to b polished for device fabrication, requiring that any small perturbing field be applied along this axis.

For these reasons the site 2 near-ZEFOZ transitions in ^{171}Yb are of particular interest for this application. To drive one of these transitions requires application of a specific 3D magnetic field with a small component along b, as well as a resonator capable of accurately hitting the frequency of the near-ZEFOZ transition. Fabricating a resonator to accurately reach a particular frequency is a highly challenging task, so some method of tuning the resonator to reach this frequency is needed. As will be discussed in Chapter 3, this can be performed by applying a small magnetic field perpendicular to the plane of the superconductor — which in this case is the b axis, the same as required for reaching near-ZEFOZ transitions in ^{171}Yb site 2. The details of an experiment aiming to use a field-tunable superconducting resonator to drive a near-ZEFOZ ^{171}Yb transition are discussed and attempted in Chapter 7.

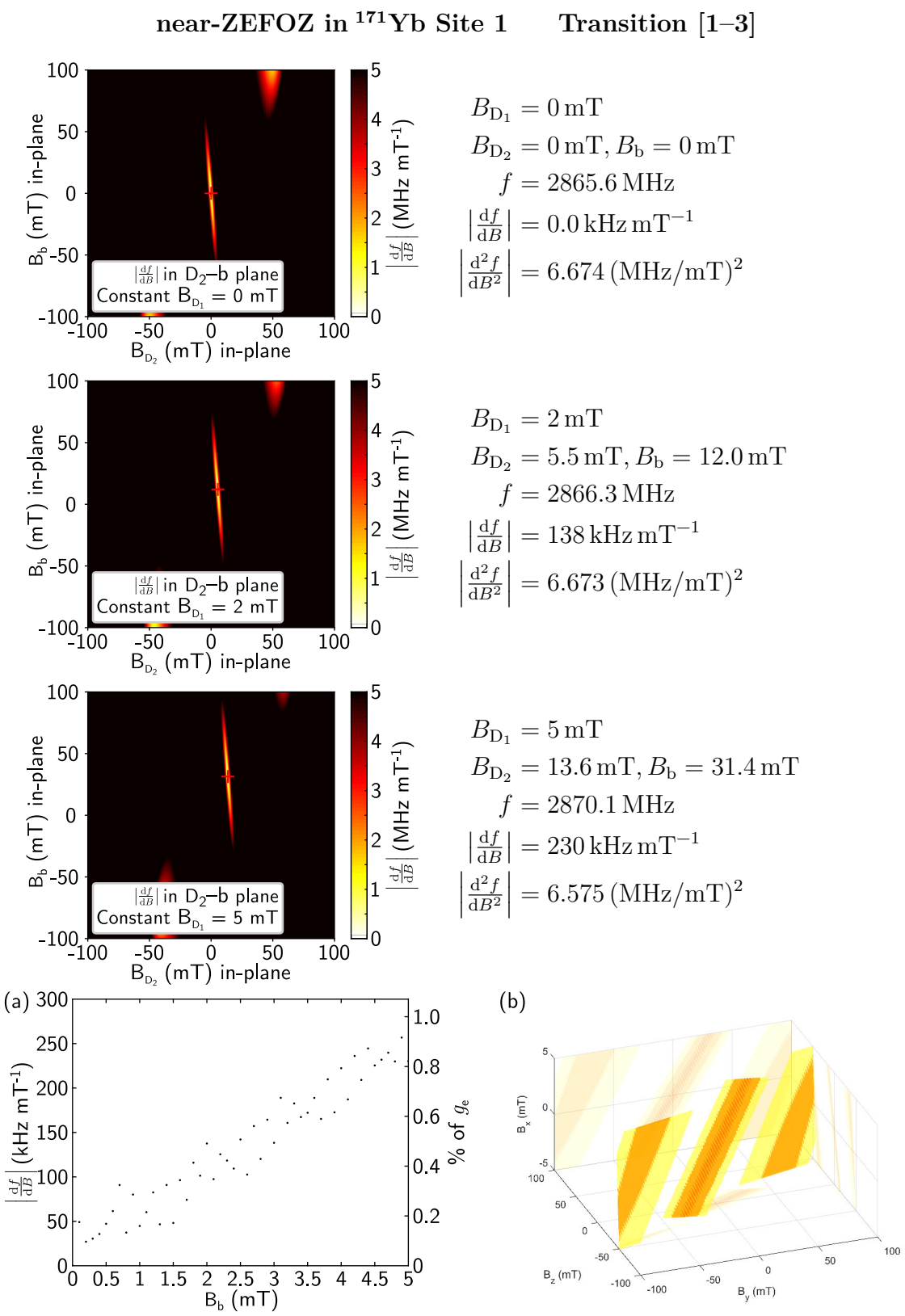

Figure 2.11: near-ZEFOZ transitions in ^{171}Yb in site 1 for the [1–3] transition. Top: Slices of constant B_{D_1} are simulated for [0, 2, 5] mT, with $\left|\frac{df}{dB}\right|$ for fields within the D_1–D_2 plane are shown. Near-ZEFOZ points which minimise $\left|\frac{df}{dB}\right|$ are identified. (a) Minimum $\left|\frac{df}{dB}\right|$ as a function of B_b, compared to $\frac{df}{dB} = 28\,\mathrm{MHz\,mT^{-1}}$ for a $g_e = 2$ electron. (b) Isosurfaces at $\left|\frac{df}{dB}\right| = [0.5, 1, 1.5]\,\mathrm{MHz\,mT^{-1}}$.

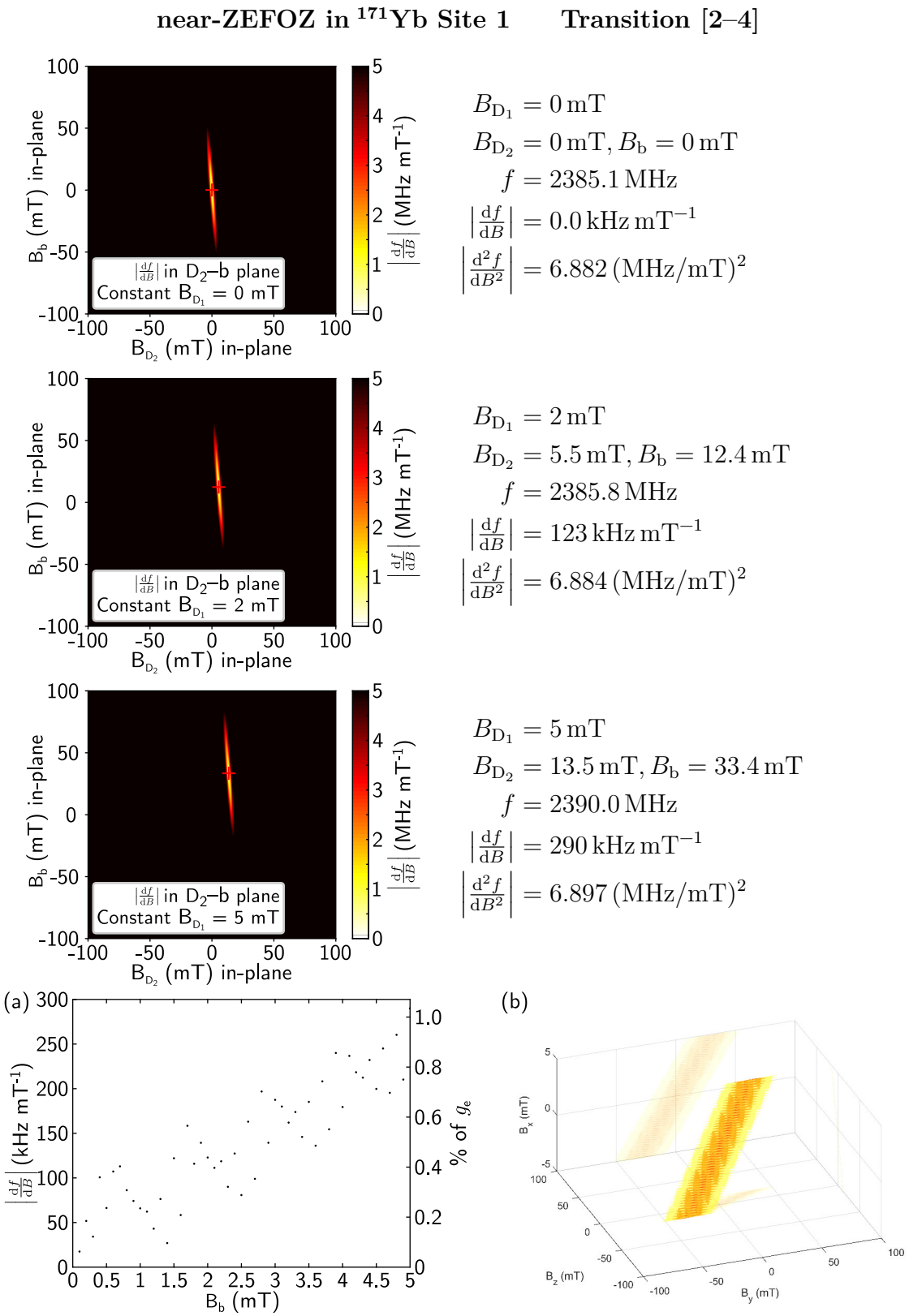

Figure 2.12: near-ZEFOZ transitions in ^{171}Yb in site 1 for the [2–4] transition. Top: Slices of constant B_{D_1} are simulated for [0, 2, 5] mT, with $\left|\frac{df}{dB}\right|$ for fields within the D_1–D_2 plane are shown. Near-ZEFOZ points which minimise $\left|\frac{df}{dB}\right|$ are identified. (a) Minimum $\left|\frac{df}{dB}\right|$ as a function of B_b, compared to $\frac{df}{dB} = 28\,\mathrm{MHz\,mT^{-1}}$ for a $g_e = 2$ electron. (b) Isosurfaces at $\left|\frac{df}{dB}\right| = [0.5, 1, 1.5]\,\mathrm{MHz\,mT^{-1}}$.

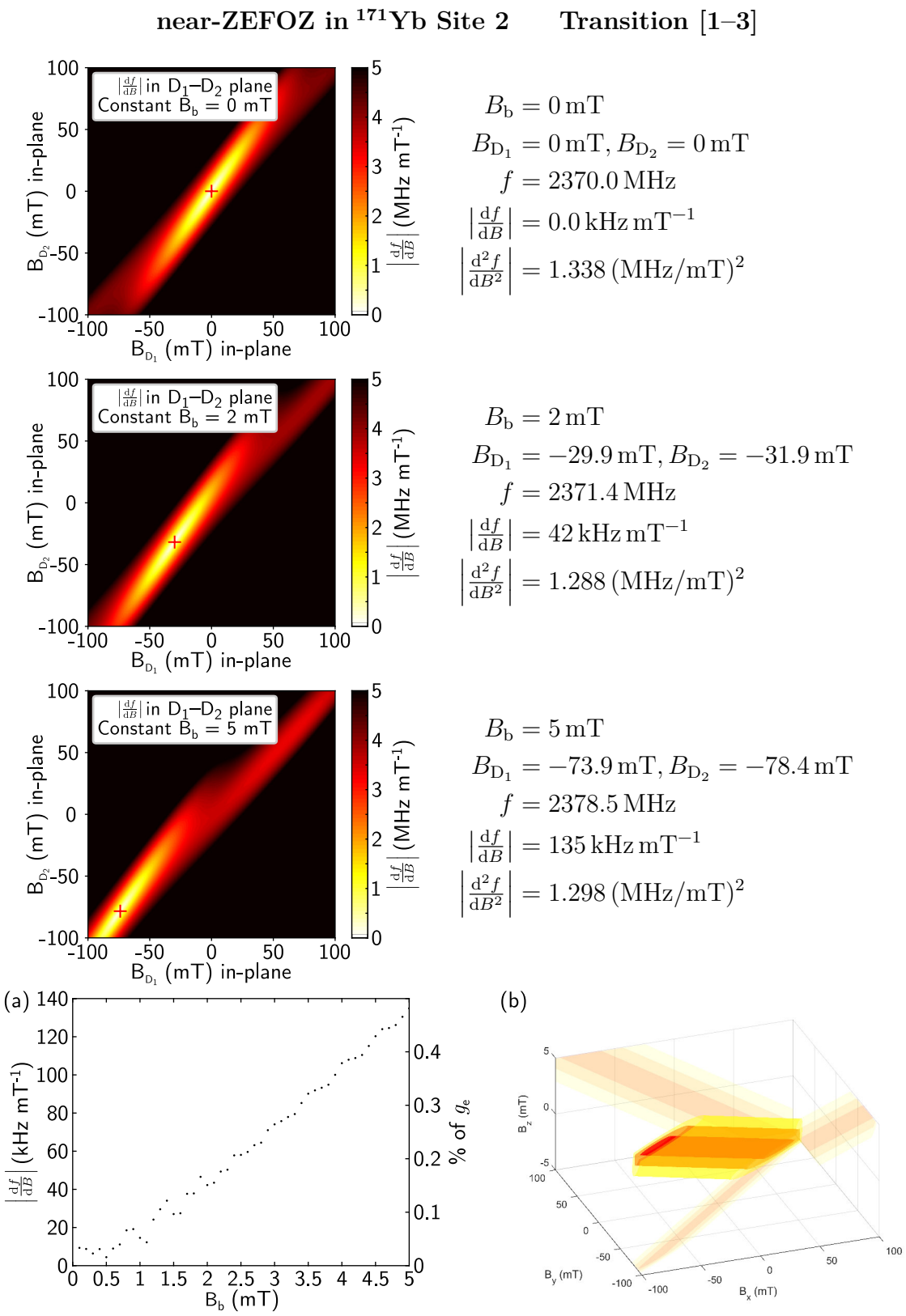

Figure 2.13: near-ZEFOZ transitions in ^{171}Yb in site 2 for the [1–3] transition. Top: Slices of constant B_b are simulated for [0, 2, 5] mT, with $\left|\frac{\mathrm{d}f}{\mathrm{d}B}\right|$ for fields within the D_1–D_2 plane are shown. Near-ZEFOZ points which minimise $\left|\frac{\mathrm{d}f}{\mathrm{d}B}\right|$ are identified. (a) Minimum $\left|\frac{\mathrm{d}f}{\mathrm{d}B}\right|$ as a function of B_b, compared to $\frac{\mathrm{d}f}{\mathrm{d}B} = 28\,\mathrm{MHz\,mT^{-1}}$ for a $g_\mathrm{e} = 2$ electron. (b) Isosurfaces at $\left|\frac{\mathrm{d}f}{\mathrm{d}B}\right| = [0.5, 1, 1.5]$ MHz mT^{-1}.

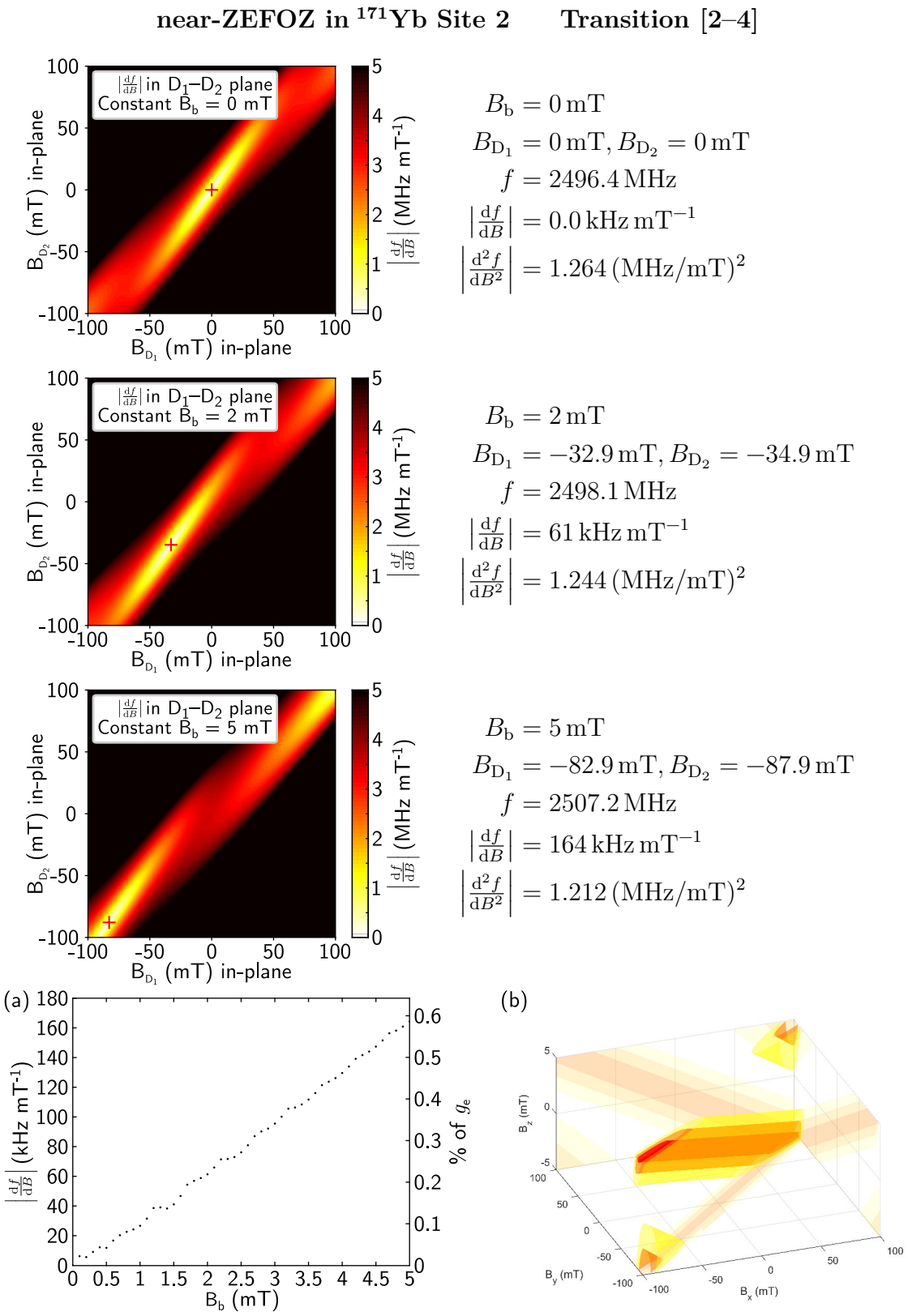

Figure 2.14: near-ZEFOZ transitions in ^{171}Yb in site 2 for the [2–4] transition. Top: Slices of constant B_b are simulated for [0, 2, 5] mT, with $\left|\frac{\mathrm{d}f}{\mathrm{d}B}\right|$ for fields within the D_1–D_2 plane are shown. Near-ZEFOZ points which minimise $\left|\frac{\mathrm{d}f}{\mathrm{d}B}\right|$ are identified. (a) Minimum $\left|\frac{\mathrm{d}f}{\mathrm{d}B}\right|$ as a function of B_b, compared to $\frac{\mathrm{d}f}{\mathrm{d}B} = 28\,\mathrm{MHz\,mT^{-1}}$ for a $g_\mathrm{e} = 2$ electron. (b) Isosurfaces at $\left|\frac{\mathrm{d}f}{\mathrm{d}B}\right| = [0.5, 1, 1.5]$ MHz mT^{-1}.

Chapter 3

Superconducting resonators

The experiments in this thesis use two distinct style of superconducting resonator — a 'thin-ring' and a 'spiral' resonator. This chapter covers some necessary background on superconducting resonators and presents models describing the coupling between resonator and spin ensemble, introduces the resonator schematics and the considerations that went into their design, presents some electromagnetic simulations of the resonator, details their fabrication in the LCN cleanroom, and characterises the frequency dependence of spiral resonators depending on their geometry, as well as their tunability with applied magnetic field.

3.1 Superconducting resonators

Superconductivity is a quantum mechanical phenomenon that occurs in some materials below a critical temperature T_c, where its resistivity vanishes and it exhibits perfect diamagnetism as magnetic flux is expelled from the material. BCS theory [88] describes the process behind this by the binding of pairs of electrons in a macroscopic quantum state, called Cooper pairs. This occurs due to the presence of an arbitrarily weak attractive potential, which in most conventional superconductors is attributed indirectly to an interaction between each electron and the lattice[1] [89]. Over large distances this attraction can overcome the mutual repulsion due to the electrons' negative charge, creating a state where pairs of electrons become correlated and exist in a bound state.

Cooling the material below T_c causes the vibrations of the lattice to be insufficient to break this attraction, and many pairs of electrons become bound forming a highly collective condensate of Cooper pairs with n_c and a band gap 2Δ centred at the

[1] Basically, the attraction between the negatively charged electron and positively charged lattice ions distorts the lattice in the wake of a passing electron, slightly increasing the positive charge density in the vicinity of the electron, weakly attracting distant electrons.

Fermi level [89]. In this highly correlated state, breaking one pair changes the energy of the whole condensate, increasing the energy required to perturb the condensate and effectively preventing the collective flow of Cooper pairs from being scattered by the lattice. This gives rise to superconductors' vanishing resistivity.

Superconductors also exhibit perfect diamagnetism, known as the Meissner effect, whereby magnetic field is expelled in the superconducting state [90]. Persistent electric currents circulating at the surface of the superconductor generate a magnetic field which cancels magnetic field applied to the bulk superconductor. This causes a decay in the magnetic field $\boldsymbol{B}$ below the surface of the superconductor $\nabla^2\boldsymbol{B} = \lambda^{-2}\boldsymbol{B}$ characterised by the London penetration depth $\lambda = \sqrt{\frac{m_e}{\mu_0 n_c e^2}}$ [89, 91].

Exploiting this superconducting state allows the creation of circuits with extremely low losses. Typical quality factors for lumped-element resonators using standard electrical components struggle to exceed 100–1000, while circuits created using a superconductor can routinely reach $Q = 10^5$–10^6. A high Q-factor is beneficial for spin sensing as the B_1 field strength generated by the resonator scales proportionally with $\sqrt{Q}$ resulting in a stronger coupling to spins, increasing the ESR sensitivity.

Having a high resonator Q comes with a few caveats, however. A narrow cavity bandwidth $\kappa_c = \frac{\omega}{Q}$ limits the population of the inhomogeneously broadened spin ensemble the resonator can excite when the spin linewidth γ_s exceeds the resonator bandwidth κ_c. The high-Q resonator also exhibits an extended damping time resulting in excessive ring-up and ring-down times that necessitate long microwave pulses ~µs and result in a distortion between the temporal profiles of the applied pulse and the generated B_1 field. This distortion can be accounted for by calculating the transfer function between applied pulse and resonator field, and producing shaped microwave pulses designed to stimulate a Gaussian time-domain resonator response [92].

Types of superconducting resonator

A film of superconductor acts as a near-perfect electrical conductor, and by patterning the film electronic and microwave circuits can be fabricated out of the superconductor. In this work, we use the superconductor to pattern resonators which support a resonant electromagnetic mode of frequency f which generates a B_1 oscillating magnetic field which can be used to drive ESR transitions.

The geometry of superconducting resonators in the literature can broadly be split into two distinct categories. A coplanar waveguide (CPW) resonator is simply a

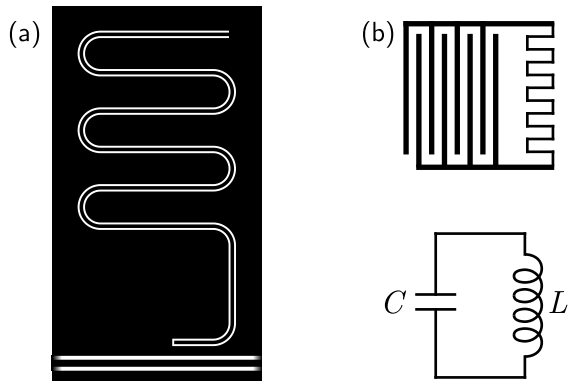

Figure 3.1: Two categories of superconducting resonator. (a) Coplanar waveguide resonator, consisting of a centre conductor and a ground plane. This quarter-wave resonator is open at one end such that its length determines its resonant wavelength $l = \frac{\lambda}{4}$. It is coupled to a transmission line for measurement. (b) A lumped-element resonator has distinct capacitive and inductive regions with inductance L and capacitance C, to give a resonant frequency $f = \frac{1}{2\pi}\frac{1}{\sqrt{LC}}$.

section of waveguide (consisting of a centre conductor with a gap between it and the ground plane) of length l which supports a standing electromagnetic wave [93]. A half-wave CPW resonator breaks the centre conductor with an open circuit at each end, creating two antinodes at the end with a node in the middle to create a standing wave of wavelength $\lambda = 2l$ [94]. A quarter-wave CPW resonator has one end short-circuited to ground creating a node at this point, supporting a wavelength $\lambda = 4l$ [48, 95, 96].

A lumped-element resonator instead consists of separate regions of capacitance C and inductance L with a resonant frequency $f = \frac{1}{2\pi}\frac{1}{\sqrt{LC}}$. Electromagnetic energy in the resonator oscillates between being stored in the capacitor as an electric field, generating a voltage that then drives a current through the inductor to create a magnetic field, which maintains a current until the field is fully in the capacitor once more. This style of resonator leaves much flexibility in the design [93, 97], with some devices incorporating interdigitated capacitors or meandering inductors [45, 66, 98, 99], nanoconstrictions [100], or fractal designs [101].

3.1.1 Loss mechanisms

A characteristic parameter describing losses in resonant systems is the quality factor Q which describes the amount of damping in the resonator. It is defined as $Q = 2\pi f \times \frac{\text{energy stored}}{\text{power loss}}$, or alternatively from the frequency f and bandwidth (full-width at half-maximum) Δf of the resonance $Q = \frac{f}{\Delta f}$. These two definitions become

equivalent at high values of Q corresponding to low losses. This second definition is used for all calculations in this thesis.

Superconducting resonators can exhibit extremely high quality factors Q due to their very low internal resistance. However, there are additional contributing mechanisms through which power is lost from a superconducting device which should be taken into account. These contributions add inversely to give a total measured quality factor

$$\frac{1}{Q_{\text{tot}}} = \frac{1}{Q_{\text{i}}} + \frac{1}{Q_{\text{c}}} + \frac{1}{Q_{\text{r}}} + \frac{1}{Q_{\text{spin}}}. \tag{3.1}$$

The first contribution describes loss mechanisms intrinsic to the device, with a limiting quality factor Q_{i}. This includes residual surface resistivity in the superconductor due to the confinement of microwave current to the surface of the superconductor [89, 102] and dielectric losses due to power absorbed by two-level systems interacting with the electric field of the cavity [98, 103, 104]. Properties of dielectric loss and its measurable effect on the resonator will be discussed shortly.

Coupling the resonator to a measurement setup is necessary for driving the resonator and reading out its response, but this also acts as a mechanism by which energy is emitted from the resonator along the measurement line. This results in another limiting quality factor Q_{c}. The coupling between measurement and resonator should generally be kept sufficiently weak as to avoid Q_{c} being the limiting factor in Eqn. 3.1, but high enough to permit measurement of the device. This typically requires some fine-tuning to optimise.

Many resonators, particularly lumped-element designs, exhibit an electric dipole. The oscillating electric field of this dipole causes it to emit EM radiation to the environment, another form of loss from the resonator. This contributes another loss mechanism Q_{r}. Radiative losses can be mitigated by enclosing the resonator in a box such that only a discrete set of EM box modes are allowed as opposed to the continuum of an open environment, suppressing emission at the wavelengths of the resonator.

Finally, absorption of energy from spins interacting with the magnetic field of the resonator contributes another mechanism which can cause an observable drop in resonator quality factor via Q_{spin}. This naturally has a dependence on magnetic field B_0 and proves a sensitive method of detecting resonant ESR transitions via the resonator [20].

Dielectric loss

The dielectric properties of a lossy material can be described by the material's complex permittivity which describes how an electric field is affected by a dielectric medium [105],

$$\varepsilon = \varepsilon' - \mathrm{i}\varepsilon''$$

where we assume the conductivity of the dielectric to be negligible. The inclusion of an imaginary component in the permittivity corresponds to a phase shift of the electric polarisation $\boldsymbol{P}$ with respect to the electric field $\boldsymbol{E}$ which results in attenuation of EM waves propagating through the medium. The relative contribution of the lossy reaction to the electric field versus the lossless reaction is typically quantified with the loss-tangent

$$\tan\delta = \frac{\varepsilon''}{\varepsilon'}$$

where δ is the loss angle.

In the context of superconducting thin-film devices, the primary source of dielectric loss is attributed to so-called "two-level systems" (TLS), a term used to describe the influence of dilute dielectric fluctuators interacting with the electric properties of a material. The nature of these TLSs remains an active area of research [98, 103, 104] with ongoing experiments aiming to better understand their origins [106, 107], though they are generally attributed to the interface between superconductor and dielectric [108, 109] or residue from certain types of lithographic resist [110].

The dissipation from TLS exhibits a significant saturation with increasing measurement power, as the contribution of TLS loss diminishes compared to the peak energy in the resonator at high powers. As a result, a signature of TLS-limited loss is a strong power dependence of the quality factor $Q_\mathrm{i} \propto P$ [103] which asymptotically approaches a constant minimum in the low-power limit, corresponding to the single-photon Q where TLS show no saturation. This low-power limit is the regime where many quantum experiments take place, so the single-photon Q is an important characteristic of a superconducting device.

TLS theory also predicts a temperature dependence of the real component of the dielectric constant due to thermal polarisation of the TLS bath [103]

$$\frac{\varepsilon(T) - \varepsilon(T_0)}{\varepsilon(T_0)} = \frac{\Delta\varepsilon}{\varepsilon} = -\tan\delta\left(\ln\frac{T}{T_0} - [g(T,\omega) - g(T_0,\omega)]\right) \tag{3.2}$$

where $g(T,\omega) = \mathrm{Re}\,\Psi(\frac{1}{2} + \hbar\omega/2\pi\mathrm{i}k_\mathrm{B}T)$, T_0 is a reference temperature, and Ψ is the complex digamma function. This is then linked to the frequency shift by

$$\frac{\Delta f}{f} = -\frac{F}{2}\frac{\Delta\varepsilon}{\varepsilon} \tag{3.3}$$

where the filling factor F depends on the device geometry and electric field distribution. This permits direct measurement of loss-tangent $\tan\delta$ [34, 106] from the temperature dependence of the resonator frequency.

Several studies of dielectric loss with differing dielectric have been published. Typical values of $F\tan\delta \approx 6\times10^{-5}$ are found for SiO_2/Si [103], while fabrication on sapphire or HF-treated Si can reduce this dramatically to $F\tan\delta \approx 2\times10^{-6}$ [103, 111]. Measurements of the loss-tangent from a resonator fabricated on Y_2SiO_5 are presented in Section 5.2.

3.1.2 Kinetic inductance and field tunability

In materials with a high carrier mobility such as superconductors, the inertial mass of the charge carriers cannot be neglected. The effect of this can be described starting from the Drude model of electrical conductivity [102, 112]

$$\begin{aligned}\sigma &= \sigma_0\frac{1}{1+\mathrm{i}\omega\tau}, \qquad \sigma_0 = \frac{nq^2\tau}{m}\\ &= \sigma_0\frac{1}{1+\omega^2\tau^2} - \mathrm{i}\sigma_0\frac{\omega\tau}{1+\omega^2\tau^2}\end{aligned}$$

where n is the charge carrier density (for a superconductor this is the Cooper pair density n_s), q its charge ($2e$ for a Cooper pair), m the effective mass of the charge carrier ($2m_\mathrm{e}$ for a Cooper pair), τ the mean collision time, and ω the frequency.

For a normal metal typically $\omega\tau \ll 1$ and the conductivity is wholly real. However, at very high frequencies or in superconductors where the mean collision time $\tau\to\infty$, the time to accelerate the charge carrier becomes significant, $\omega\tau \gg 1$ and the conductivity becomes predominantly imaginary giving a reactivity

$$\mathrm{Im}\left\{\frac{1}{\sigma}\right\} = \omega\frac{m}{nq^2}.$$

For a wire of length l and cross-sectional area A this gives an impedance

$$Z = \mathrm{i}\omega\frac{m}{nq^2}\frac{l}{A} \tag{3.4}$$

which as part of a circuit has the same effect as an inductor $Z = \mathrm{i}\omega L$ with inductance L. Hence this effect is commonly characterised by introducing the *kinetic inductance*

$L_\mathrm{k} = \frac{m}{nq^2}\frac{l}{A}$. While this inertial effect is unrelated to Faraday's law, it is typically included alongside the geometric inductance L_g due to the generation of magnetic field around the conductor to give an overall inductance $L = L_\mathrm{g} + L_\mathrm{k}$. It is worth noting this effect is not specific to superconductivity, and can be observed in normal conductors given sufficiently high conductivity or frequency [113].

For a superconductor with Cooper pairs of density n_s with mass $m = 2m_\mathrm{e}$ and charge $q = 2e$, the expression for kinetic inductance becomes $L_\mathrm{k} = \frac{m_\mathrm{e}}{2n_\mathrm{s}e^2}\frac{l}{A}$. Notably, the kinetic inductance depends inversely on the cross-sectional area A of the wire. This implies that thinner films give a greater kinetic inductance fraction for the same device geometry.

Tuning kinetic inductance with magnetic field

The dependence of kinetic inductance on Cooper pair density $L_\mathrm{k} \propto \frac{1}{n_\mathrm{s}}$ can be exploited to give some control over the frequency of a resonator. The application of a static magnetic field B to a superconductor increases the London penetration depth $\lambda = \lambda_0 + \kappa B^2$ [114, 115] where the linear term must vanish due to symmetry as the penetration depth can depend only on the field magnitude and not its sign [116]. The dependence of the penetration depth on Cooper pair density [117] $\lambda = \sqrt{\frac{m_\mathrm{e}}{2n_\mathrm{s}e^2\mu_0}} \propto \sqrt{\frac{1}{n_\mathrm{s}}}$ allows a series expansion to first-order of the kinetic inductance

$$\begin{aligned} L_\mathrm{k} &\propto \frac{1}{n_\mathrm{s}} \propto \sqrt{\lambda} \\ &\propto \sqrt{\lambda_0 + \kappa B^2} \\ &\propto \sqrt{\lambda_0} + \frac{1}{2\sqrt{\lambda_0}}\kappa B^2 + \cdots \\ &\propto L_0 + \alpha B^2 \end{aligned} \tag{3.5}$$

and a corresponding expansion for the resonant frequency of a device with inductance L and capacitance C

$$\begin{aligned} f &= \frac{1}{2\pi}\frac{1}{\sqrt{LC}} \propto \frac{1}{\sqrt{L}} \\ &\propto \frac{1}{\sqrt{L_0 + \alpha B^2}} \\ &\propto \frac{1}{\sqrt{L_0}} - \frac{1}{2L_0^{3/2}}B^2 + \cdots \\ &\propto f_0 - \beta B^2 \end{aligned} \tag{3.6}$$

so application of a magnetic field to a resonator reduces its frequency quadratically with the strength of the applied field [118–121].

This shift in frequency is observed for magnetic fields both in-plane and out-of-plane, with different coefficients β for field components in-plane and out-of-plane [119] due to the different cross-sectional areas the magnetic flux is threaded along, with a much stronger response to out-of-plane fields. This can be exploited to tune a resonator to a particular frequency by applying magnetic flux perpendicular to the film. This has been characterised in detail using a scheme where a magnetic field corresponding to a clock transition in Bi:Si is aligned predominantly in the plane of a thin-ring style resonator, similar to the designs discussed in Section 3.2, and subsequently rotated to provide a small out-of-plane component while keeping the absolute field strength constant [121]. The resonator maintains a high quality factor $>10^5$ for in-plane fields up to 2.6 T and exhibits a tunability of up to 30 MHz for a 5 mT out-of-plane component. This scheme is less easily applied to ZEFOZ transitions in rare-earth doped crystals due to the anisotropy of the spin system, but a similar method for tuning resonators to near-ZEFOZ transitions in ^{171}Yb:Y_2SiO_5 with a global field is discussed in later chapters.

3.2 Resonator design

There are several factors to consider in designing a superconducting resonator intended to drive ESR transitions in an applied magnetic field.

Resilience to high in-plane magnetic fields ~1 T is essential to establish the Zeeman splitting necessary for bringing electron spins in resonance with the resonator. Approaches toward this have included patterned antidots in the resonator and ground plane to trap flux [122, 123] and a 'fractal' resonator geometry [101] with heavily patterned ground planes to allow flux to escape.

It is also desirable to have some freedom to tune the resonator frequency to hit a particular field–frequency combination corresponding to a clock or ZEFOZ transition. Methods to do this include applying a bias current to the centre of a CPW resonator [124–126], exploiting the strong magnetic field dependence of a SQUID as a tunable inductor incorporated into a resonator [96, 127, 128], and applying a global magnetic field [118–121].

Many resonator geometries have been explored in the literature [97, 116] including quarter-wave [96] and half-wave [129] coplanar waveguides coupled via a transmission line, lumped-element resonators with distinct capacitive and inductive regions [66, 68, 121], photonic bandgap resonators incorporating Bragg mirrors on either

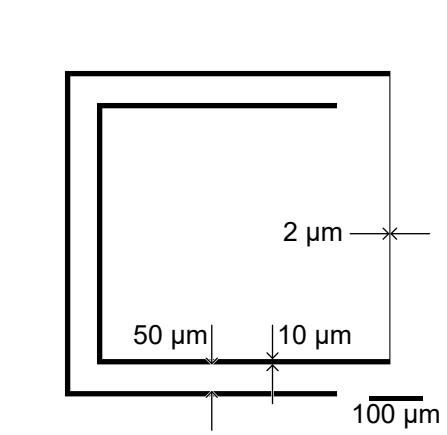

(a) Thin-ring resonator design.

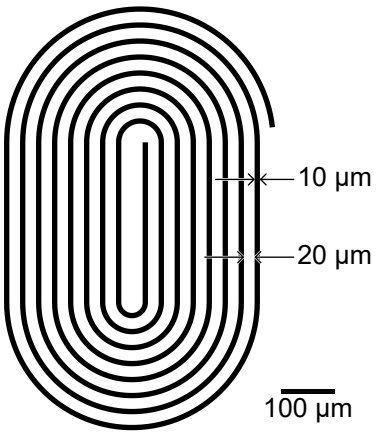

(b) Spiral resonator design.

(c) Thin-ring resonator cross-section illustrating magnetic field around inductor.

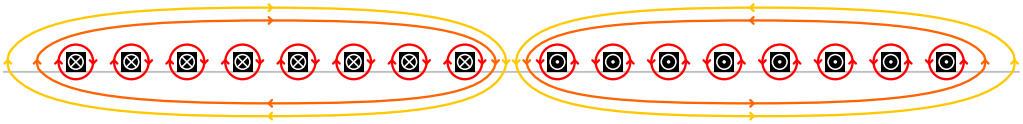

(d) Spiral resonator cross-section illustrating magnetic field around resonator.

Figure 3.2: Resonator designs and cross-sections.

side of a cavity [126], thin loops of nanowire [119], and spirals of superconducting wire [130]. These different geometries each have their own capabilities and advantages, and in this thesis we focus on lumped-element and wire geometries as these avoid the need for an extensive superconducting ground plane which distorts magnetic field and traps flux.

Several materials are commonly used for fabrication of superconducting resonators such as Al, Nb, NbN, NbTiN, and TiN [97]. These differ in their superconducting properties and possible patterning methods. We choose to fabricate resonators out of NbN for several reasons: It has a high T_c of 12.5–14.5 K [131] (depending on nitrogen content), is resilient to high magnetic fields [121, 132], resists oxidation [133], and exhibits a high kinetic inductance [134] beneficial for reaching low frequencies and tuning with magnetic field.

Thin-ring resonator

The first resonator design we consider is a 'thin-ring' resonator, shown in Fig. 3.2(a). This lumped-element resonator has two distinct regions — a 2 µm wide inductive wire with inductance L, shunted by a pair of capacitive arms each 10 µm wide

and separated by 50 µm with capacitance C. This then has a resonant frequency $f = \frac{1}{2\pi}\frac{1}{\sqrt{LC}}$. A thin-ring resonator is used for ESR measurements in chapters 5 and 6.

The goal of this design is to create a resonator which generates an oscillating magnetic field B_1 circulating around one axis defined by the inductor as illustrated in Fig.3.2(c), such that when a static magnetic field B_0 is applied along the inductor axis, $B_1 \perp B_0$ in line with conventional perpendicular-mode EPR for driving $\Delta m_s = \pm 1$ transitions in Kramers ions [59]. The design also eliminates as much of the superconductor as possible by avoiding the need for a ground plane as with coplanar geometries, which reduces magnetic field focusing due to the Meissner effect resulting in a more homogeneous B_0 field, and minimises the surface area through which magnetic flux can be trapped.

Thin-ring resonators fabricated from ~50 nm NbN on high-resistivity ($\rho > 5000\,\Omega\,\mathrm{cm}$) Si substrates [121] have achieved high quality factors $>10^5$ in the few-photon limit, and maintain a high quality factor at up to 2.6 T applied in-plane. With an out-of-plane field component they exhibit a tunability of 30 MHz at 5 mT.

With a single straight inductive wire, the B_1 field at distance r generated at the fundamental mode of a thin-ring resonator in the far-field limit drops as $B_1 \propto \frac{1}{r}$. This simple model is in agreement with finite-element simulation in Section 3.3 and results in a highly inhomogeneous B_1 field, preventing simple pulses from producing accurate θ rotations on the Bloch sphere for a spin ensemble. The thin-ring design also poses challenges for reaching low frequencies <4 GHz, as the wavelength scales roughly with the perimeter of the resonator. An alternative resonator design is investigated for measurements at lower frequencies.

Spiral resonator

A spiral resonator as shown in Fig. 3.2(b) helps mitigate the highly inhomogeneous B_1 field of the thin-ring resonator due to the geometry of having several adjacent wires carrying parallel current as illustrated in Fig. 3.2(d). Simulations of a spiral resonator in Section 3.3 demonstrate this increased field homogeneity, and a similar spiral resonator design is characterised in greater detail by simulation and experiment in [130].

As the spiral design makes more effective use of the resonator's footprint, its wavelength scales more closely with the area of the resonator (rather than its perimeter) making it easier to reach lower frequencies with small devices than the thin-ring

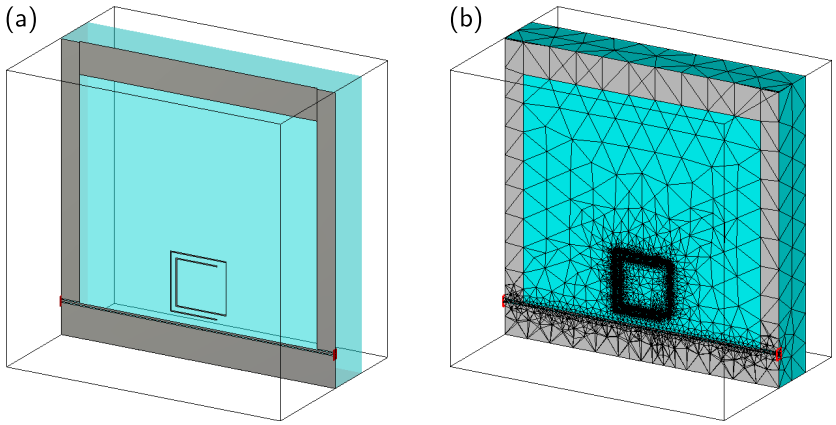

Figure 3.3: (a) CST model for simulating resonators via coupling to a coplanar waveguide. (b) Tetrahedral mesh of model, with increased mesh density across waveguide and resonator.

resonator. By using a thinner ~15 nm NbN film the kinetic inductance fraction of the material can be increased, additionally helping reach low frequencies.

Details of the fabrication and tunability of spiral resonators are discussed in Section 3.4.

3.3 Resonator simulation

To assist with resonator design, frequency optimisation, and determination of B_1 magnetic field distribution, finite-element simulation of the resonators is employed. We use the commercial software CST Microwave Studio 2015 [135], which allows the definition of the simulation model with a CAD-like interface, and includes an eigenmode solver to efficiently calculate resonant modes as well as a frequency solver to determine $S_{21}(f)$ response of the resonator.

An example model is shown in Fig. 3.3(a). A coplanar waveguide with associated ground plane is used to couple energy into the resonator, with two microwave ports at either end enabling transmission measurement of the resonator response. A Y_2SiO_5 substrate is defined with $\epsilon_r = 10.2$ (being the mean of the anisotropic permittivity of Y_2SiO_5 at low temperatures [38]), with 1 mm vacuum above the device surface and 500 µm below the substrate. Electrically grounded boundary conditions ensure the CPW behaves appropriately.

The superconductor is modelled by an infinitely thin metallic sheet with a tabulated surface impedance. By giving it zero resistance but a linearly increasing sheet reactance with frequency it emulates a lossless superconductor with a kinetic inductance as in Eqn. 3.4. The value of this reactance is determined empirically by

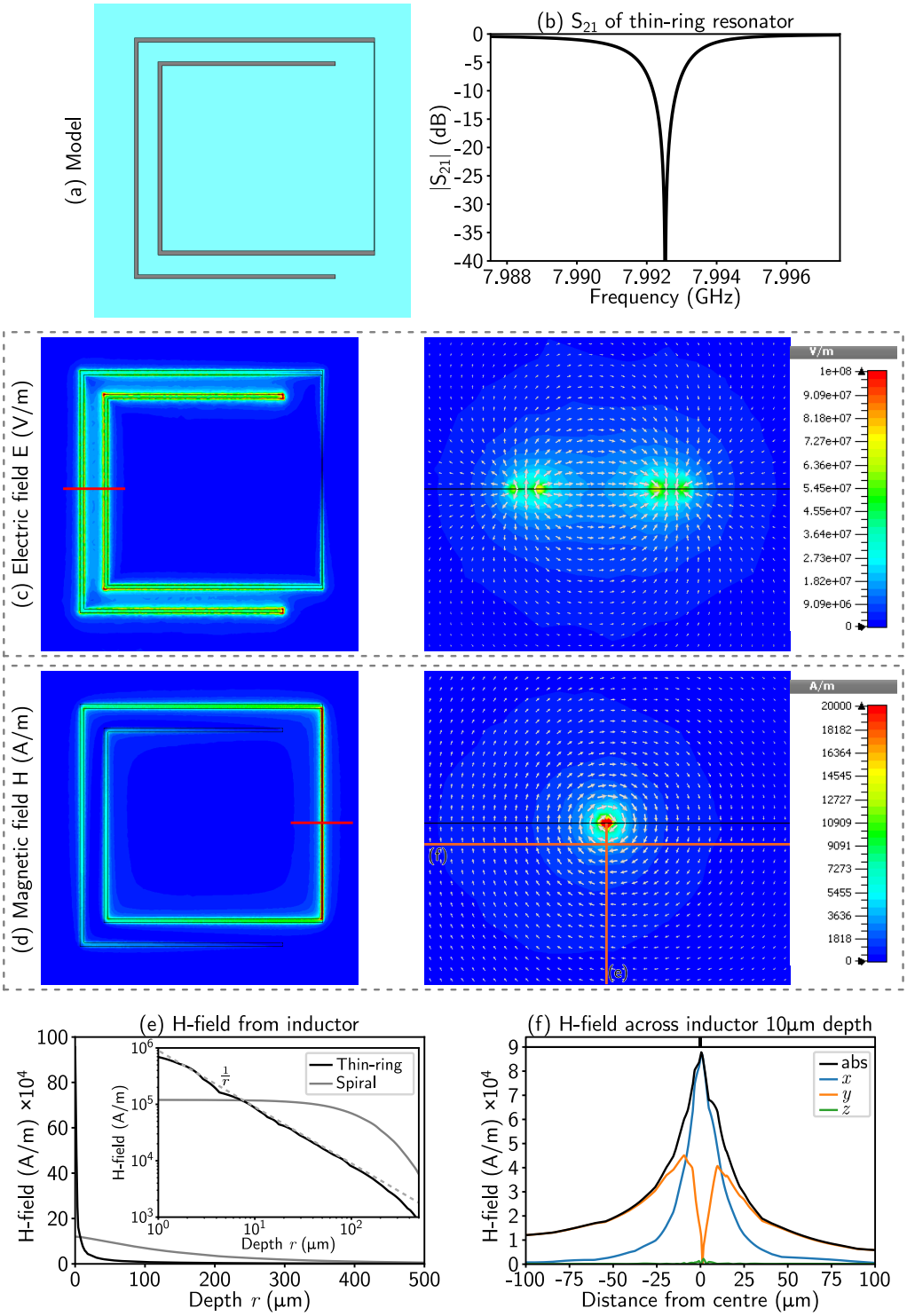

Figure 3.4: CST simulation of a thin-ring resonator. (a) Model of the resonator. (b) Calculated S_{21} of the resonator model measured via a nearby coplanar waveguide, accounting for kinetic inductance with an additional reactance of $0.1\,\Omega/\square$ per GHz showing a resonance at 7.992 GHz. (c, d) Electric and magnetic field distributions with cross-sections around the capacitor and inductor respectively. (e) Magnetic field measured along a line directly down from the inductor, showing the $\frac{1}{r}$ dependence, and a comparison to the spiral simulation in Fig. 3.5(e). (f) Magnetic field strength along a horizontal line perpendicular to the inductor, 10 µm below the surface.

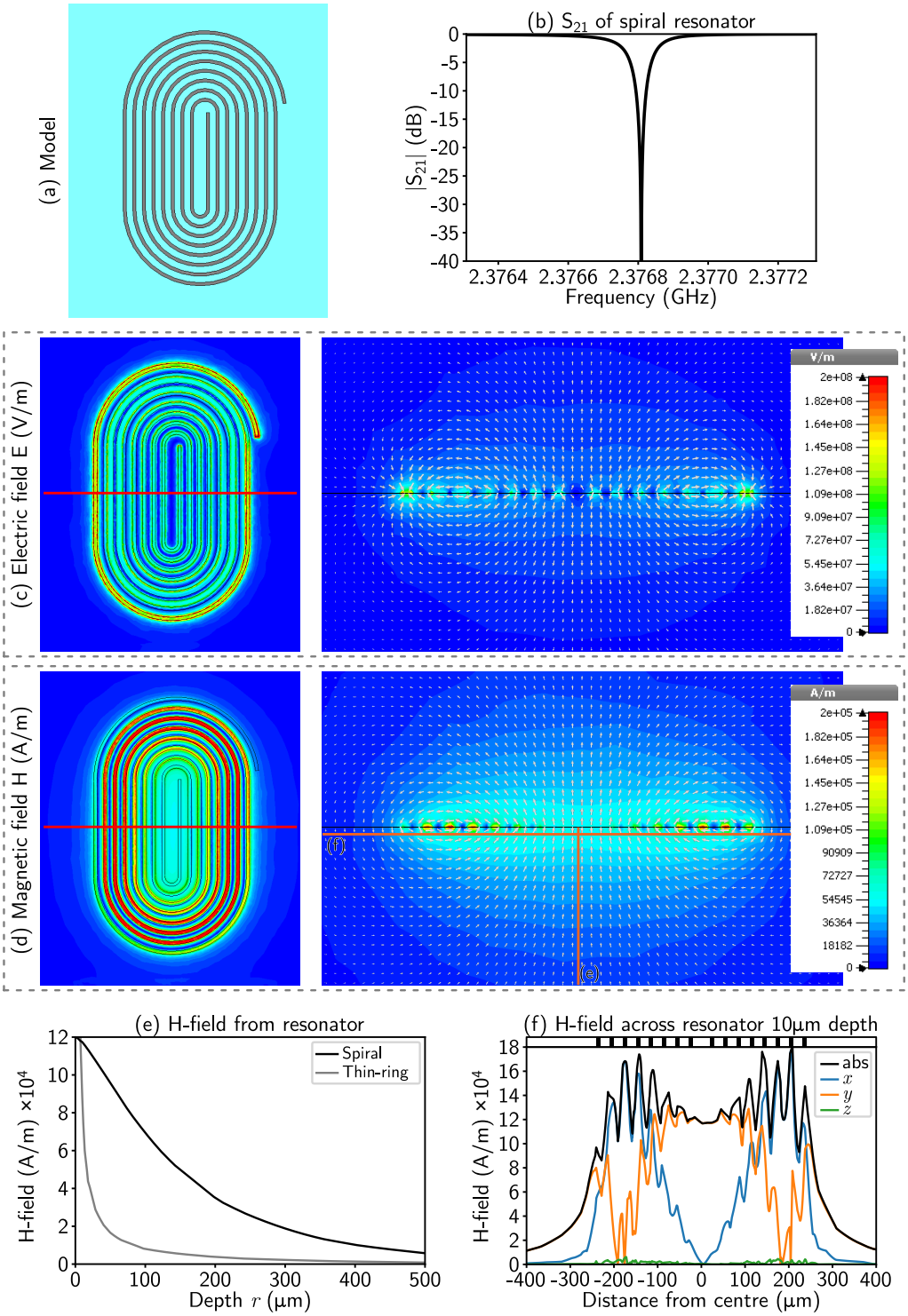

Figure 3.5: CST simulation of a spiral resonator. (a) Model of the resonator. (b) Calculated S_{21} of the resonator model measured via a nearby coplanar waveguide, accounting for kinetic inductance with an additional reactance of $0.6\,\Omega/\square$ per GHz showing a resonance at 2.377 GHz. (c, d) Electric and magnetic field distributions with cross-section across the resonator. (e) Magnetic field measured along a line directly down from the centre of the resonator, and a comparison to the thin-ring simulation in Fig. 3.4(e). (f) Magnetic field strength along a horizontal line across the resonator, 10 µm below the surface.

fabricating and measuring a resonator, then modifying the reactance in the simulation such that the frequency mode solver reproduces the measured frequency.

The model is fractured into a tetrahedral mesh seen in Fig. 3.3(b), with an increased mesh density of 5 µm for the resonator and 25 µm for the centre conductor of the CPW. The fundamental resonant mode is determined using the Eigenmode solver[2], which iteratively refines the mesh further where necessary. The refined mesh is then run through the Frequency mode solver to determine the frequency from the S_{21} response, and a field monitor at this frequency calculates the **E** electric field and **H** magnetic field[3] of the resonant mode.

Simulations of a thin-ring resonator and a spiral resonator are presented in Figures 3.4 and 3.5 respectively. Comparisons of the magnetic field in (e) highlight the $\frac{1}{r}$ decay of field strength from the thin-ring's inductor, and the much weaker decay with distance from the centre of the spiral resonator. Taking a horizontal cross-section 10 µm below the surface in (f) indicates a more homogeneous spatial distribution of magnetic field strength in the spiral resonator, in agreement with simulation from [130].

With simulation of resonators indicating they behave as designed and at appropriate frequencies, we proceed to detail the process of fabricating these devices in the cleanroom.

3.4 Cleanroom fabrication

The cleanroom at LCN contains the equipment necessary for complete in-house fabrication of superconducting devices. This section summarises the fabrication process, an overview of which is illustrated in Fig. 3.6. The steps as described assume a Y_2SiO_5 substrate, though the same process is applicable for fabrication on Si or sapphire substrates.

Preparation

The Y_2SiO_5 samples were cut into wafers from the boule perpendicular to the b crystal axis. To achieve a polished surface a Logitech PM5 lapper was used with two plates: A cast iron plate with an Al_2O_3 microparticle solution for lapping to produce a flat unpolished surface, followed by an expanded polyurethane plate

[2]The Eigenmode solver does not support a tabulated surface impedance and does not account for kinetic inductance, so the frequency and field distributions may be inaccurate. The Frequency solver should be used for accurate treatment of kinetic inductance.

[3]This is related to the magnetic flux density **B** and magnetisation **M** by $\mathbf{H} \equiv \frac{\mathbf{B}}{\mu_0} - \mathbf{M}$

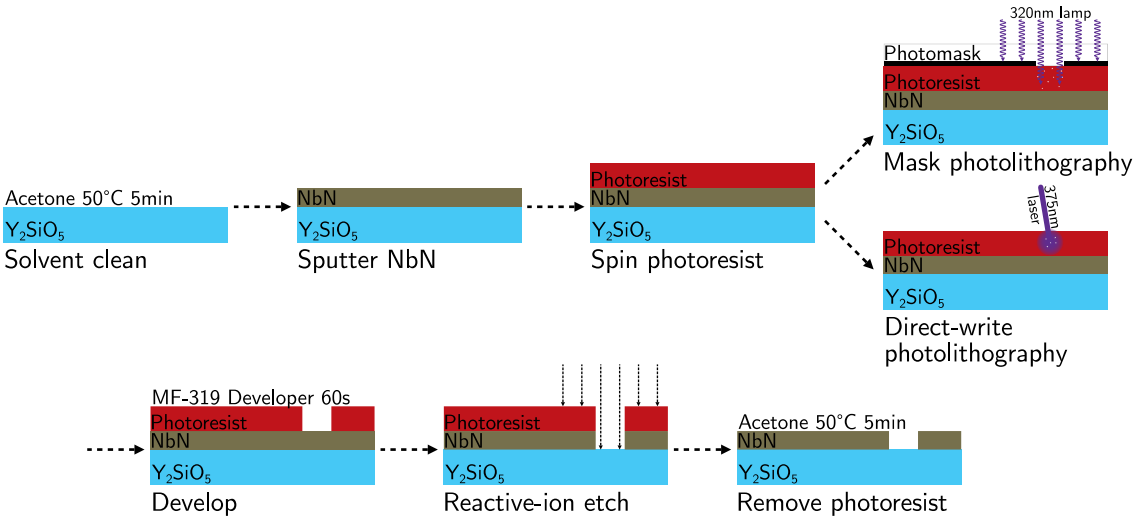

Figure 3.6: Overview of the fabrication process, with the lithography step performed by either mask or direct-write photolithography.

with a $CeCO_3$ solution and SiO_2 in distilled water to polish. The resulting surface roughness measured by a Bruker DektakXT stylus profilometer shows a typical peak-to-trough roughness of ~3 nm measured over 10 µm, with a flatness of ~10 nm over 100 µm.

The wafer is cut into 5×5 mm chips using a Disco DAD3220 dicing saw. A general-purspose resin blade is used, cutting in several passes of depth steps 250 µm and a conservative cutting speed of 2–4 mm s^{-1}.

Cleaning

Prior to and during fabrication, the sample must be cleaned of organic matter and particulates to ensure a good adhesion of the film to the substrate and ensure the lithography and subsequent etch are not affected by contaminants.

The standard cleaning process used for Y_2SiO_5 is a solvent clean with acetone, sonicated in a water bath at 50 °C for 5 min. Keep a lid on the beaker to limit evaporation. The acetone is then rinsed off with isopropanol (IPA) as soon as the sample is removed from the acetone beaker to prevent evaporating acetone from leaving a residue, followed by another 5 min sonication with IPA. The IPA is blown dry with N_2 gas.

It should be noted that cleaning with Piranha solution, a commonly used organic cleaning mixture consisting of 3:1 sulphuric acid to hydrogen peroxide, is not compatible with Y_2SiO_5 [136].

NbN deposition by DC magnetron sputtering

With a clean substrate, the superconducting thin-film must be deposited prior to lithography. A Scientific Vacuum Systems (SVS) model V6000 DC magnetron sputterer is employed, which uses a metallic target composed of the material to be deposited. The sputter chamber is pumped to a vacuum and backfilled with Argon process gas. A high voltage of several kV is applied between the target and a surrounding cathode which ignites an Ar plasma, which bombards the surface of the metal target, ejecting atoms which strike the substrate and adhere to the surface, growing a thin film of material on the substrate.

To grow NbN, a pure Nb target is used. The sputter chamber is pumped to an initial base pressure of $<9 \times 10^{-7}$ mbar. The chamber is then backfilled with both argon and nitrogen, at flow rates of 50 SCCM (standard $\mathrm{cm}^3\,\mathrm{min}^{-1}$) measured by a mass flow controller to run with a gas pressure of 5×10^{-3} mbar. A DC voltage is applied to the target to ignite a plasma, controlled by the power supply at 200 W, which sputters Nb atoms from the target surface. The ejected Nb reacts with N gas in the sputter chamber to form NbN.

Two pre-sputter stages are used to improve the reproducibility of the process. Two shutters are employed, one covering the sputter target and one covering the substrate. With both shutters are closed, a getter process is run for 5 min. This reduces the pressure in the sputter chamber as the Nb reacts with residual contaminant gases. The target shutter is then opened and the process run for a further 5 min to clean the Nb surface leaving a pure target.

The process then runs with both shutters open to deposit the thin NbN film. The substrate is rotated at 20 RPM to provide a more even coating. With these parameters the NbN grows at a typical rate of approximately $15\,\mathrm{nm\,min}^{-1}$, though this rate changes over time and should be recharacterised occasionally.

The NbN films used to fabricate thin-ring resonators were sputtered in LCN to a thickness of 45 nm. Due to contamination of Nb sputter processes when the spiral resonators were due to fabricated, a 15 nm NbN film was instead deposited in Cambridge in collaboration with Jason Robinson and Chang-Min Lee of the Device Materials group.

Photolithography

With a NbN film coating the substrate, the device is patterned using photolithography. Two types of photolithography are used in this thesis, with earlier thin-ring

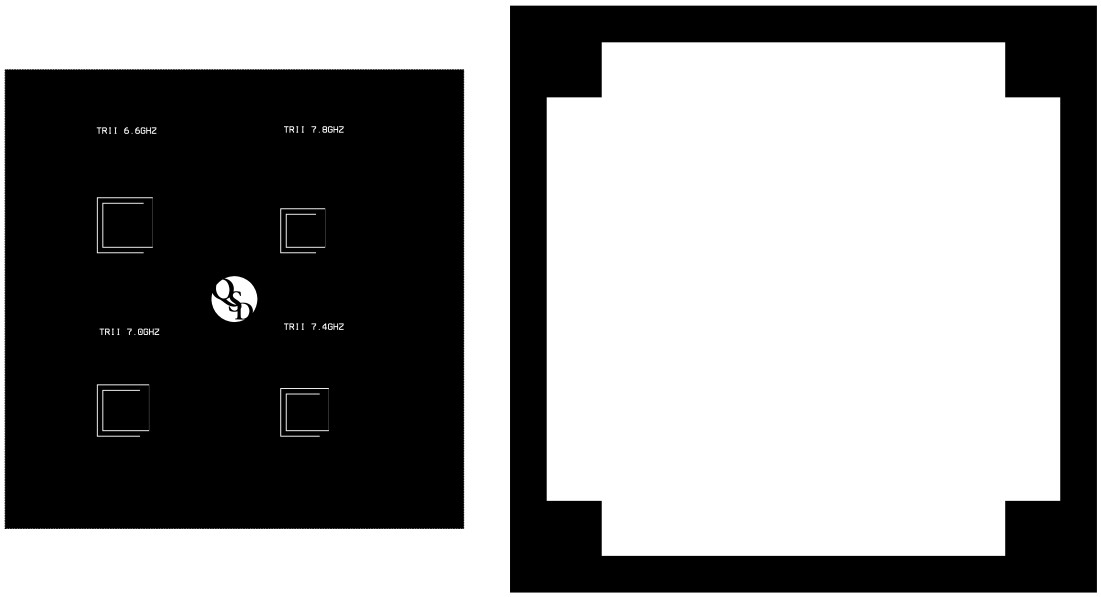

(a) Left: pattern for mask photolithography of thin-ring resonators, where dark regions are exposed and white is masked by chrome on the photomask. Right: Pattern for removal of edge beads from 5×5 mm samples.

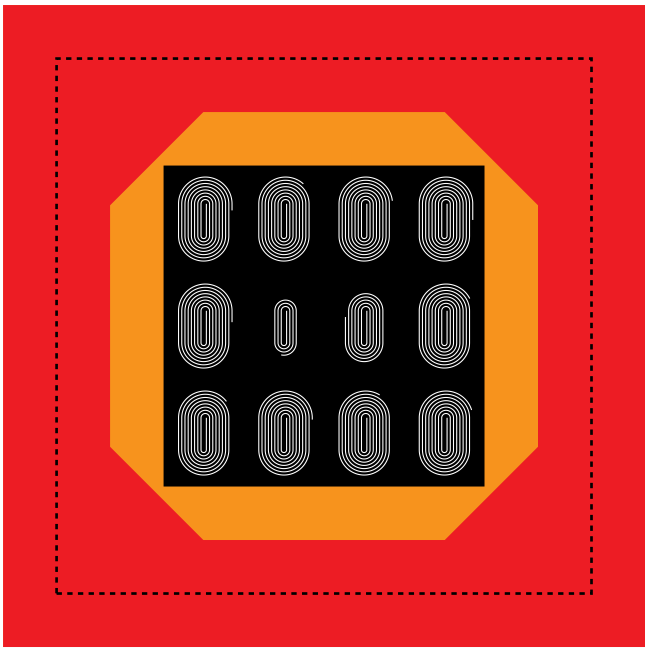

(b) A pattern for spiral resonator fabrication by direct-write photolithography. The black region is exposed with an optimised laser power, while the coloured regions are exposed with a higher laser power to fully remove any edge bead. The dashed line indicates the edges of a 5×5 mm chip.

Figure 3.7: Photolithography patterns.

devices in chapters 5 and 6 defined by mask photolithography and later spiral devices in Chapter 7 patterned by direct-write photolithography.

Both processes first involve spinning S1805 photoresist over the sample surface. This contains a photosensitive polymer which degrades into shorter chains when exposed to intense UV. Photoresist dissolved in a solvent is pipetted onto the sample surface and spun to achieve a 0.5 µm thick layer of resist, and the sample is placed on a hot plate to evaporate the solvent. For small 5×5 mm samples the resist tends to pool at the edges and corners leaving a thicker "edge bead" which can present challenges when fabricating.

For mask photolithography, the design must first be transferred to a photomask, consisting of a flat piece of soda-lime glass with the design patterned into a layer of chrome on one side, which the sample is pressed up against. The chrome prevents the transmission of UV light, exposing only regions where the photomask's chrome has been removed. The mask design for fabricating thin-ring resonators is shown in Fig. 3.7(a). The mask and sample are loaded into a Karl Suss MJB3 mask aligner. When using a photomask, a substantial edge bead would prevent the sample from making close contact with the chrome, leaving a gap over which light can diffract and prevent fine features from being resolved. An edge bead removal pattern shown alongside Fig. 3.7(a) enables these thicker regions to be exposed and developed while the centre region is shielded by chrome. This enables the edge bead to be removed, enabling photolithography at a resolution of 2 µm. An exposure time of ~2 s is optimal.

Later devices are patterned by direct-write photolithography. This removes the requirement of a photomask by exposing photoresist with a UV laser, enabling faster turnaround between design and fabrication. A Heidelberg DWL 66^+ is used with a write head capable of 1 µm resolution. A pattern for exposure of spiral resonators is shown in Fig. 3.7(b), where the black region is exposed with a laser power of 60 mW at 50 % intensity with a 50 % filter to achieve an optimal exposure. The other shaded regions are exposed at higher powers, which helps remove most of the edge bead to prevent remaining superconductor from shielding the devices. The dotted line indicates the edge of the 5×5 mm chip.

With the pattern exposed by photolithography, the photoresist is developed by mild agitation in MF-319 developer solution for 60 s. The exposed short-chain polymers are dissolved leaving the patterned photoresist covering only regions where NbN should remain in the final device.

(a) Photograph of a Yb:Y_2SiO_5 chip fabricated with spiral resonators.

(b) Micrograph of chip from (a) showing resonators and some remaining edge bead.

Figure 3.8: Spiral resonator photograph and micrograph.

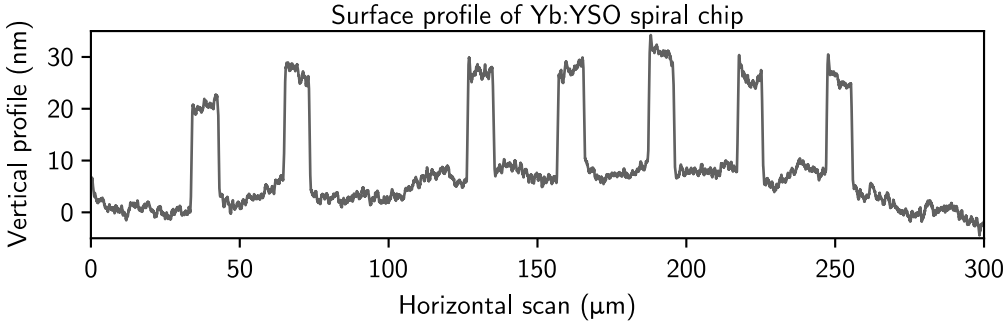

Figure 3.9: Surface profile of fabricated Yb:Y_2SiO_5 chip across a spiral resonator, measured with a Bruker DektakXT profilometer. This enables measurement of film thickness, etched depth, and surface roughness.

Etch

The device is cleaned by mild agitation in deionised water followed by a N_2 dry before being loaded into an Oxford Instruments Plasma Pro NGP80 RIE. This uses heavy and chemically reactive gases ignited into a plasma and directed toward the substrate to bombard and remove material in regions not covered by photoresist.

A standard Nb on Si recipe is used, where 14 SCCM SF_6 and 35 SCCM CHF_3 process gas is ignited into a 100 W plasma at a pressure of 100 mtorr (0.133 mbar). The etch is performed in 1 min stages, waiting 1 min between each stage to allow the sample to cool and prevent the photoresist from melting or baking. With these parameters NbN etches at ~50 nm min^{-1}, and a cumulative 2 min etch is typically performed. A completed etch can be easily identified by the significant contrast between reflective NbN and transparent Y_2SiO_5. The photoresist is then removed with a standard solvent clean.

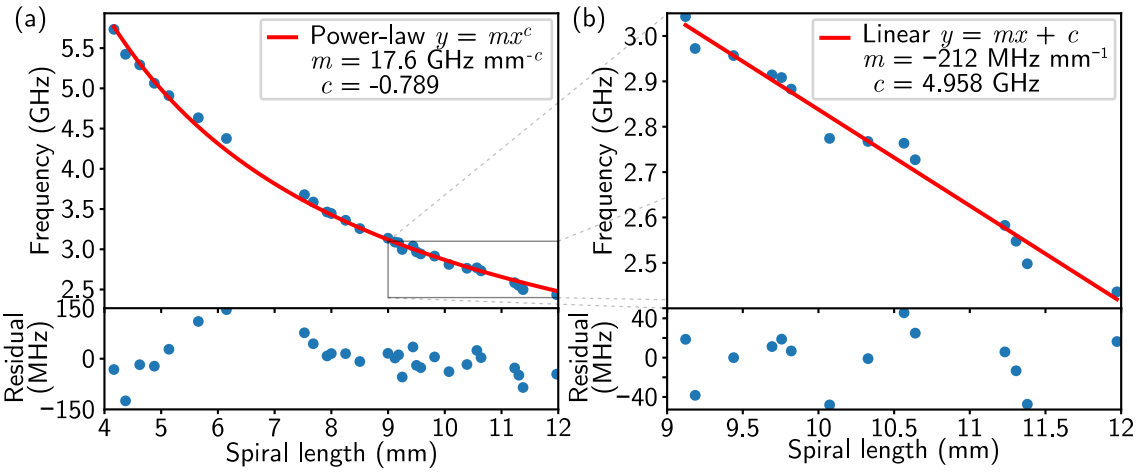

Figure 3.10: Fabrication of spiral resonators on 4 NbN-on-Y_2SiO_5 chips to determine a relationship between cumulative length of spiral and resonant frequency. (a) Fitting a power-law $y = mx^c$ to the measured resonators on all four Y_2SiO_5 chips broadly captures the frequency–length relationship but with some bias visible in the residual. (b) On a smaller scale the frequency–length dependence is close to linear, and fitting $y = mx+c$ to the two lowest frequency Y_2SiO_5 chips gives a less biased residual. This model is used to generate the spiral resonator designs fabricated on Yb:Y_2SiO_5.

A fabricated Yb:Y_2SiO_5 chip, measured in Chapter 7, is shown in Fig. 3.8(a) alongside a micrograph from the same chip in (b). A measurement of the surface profile across a spiral resonator from this chip is presented in Fig. 3.9, showing ~20 nm steps where superconductor remains.

3.5 Spiral resonator characterisation

The spiral resonator design, intended for coupling to near-ZEFOZ transitions at well-defined frequencies and fields, required an empirical study into the resonant frequency as a function of device geometry and applied magnetic field. This provides the information necessary for fabrication of a resonator near the intended frequency, and demonstrates the capability to tune it down to match the exact frequency to hit a near-ZEFOZ transition.

3.5.1 Frequency calibration

The film used to fabricate spiral resonators was sputtered to a thickness of 20 nm, significantly thinner than used to fabricate the thin-ring devices. This was deliberate, in order to increase the kinetic inductance of the superconductor and assist in

reaching low ~2.4 GHz frequencies and provide a strong tunability with magnetic field.

To vary the resonant frequency f the cumulative length l of the coil of wire forming the spiral was varied. Broadly speaking we expect the wavelength to increase with this length, giving $f \propto l^{-1}$, but the capacitance and mutual inductance between adjacent turns of the coil cause this to deviate from an exact inverse relationship. To determine a model to predict resonant frequencies, a set of 4 NbN-on-Y_2SiO_5 chips were fabricated with 9 devices per chip and measured with a VNA at 1.6 K using a closed-cycle cryostat as will be described in Section 4.2.

The resulting data is presented in Fig. 3.10. As the length of a coil with finite width is not well defined, the length of each spiral was estimated from its area A and perimeter P with $l = \frac{P}{4} + \sqrt{\frac{P^2}{16} - A}$.[4] The data exhibits an approximately inverse relationship as expected, and fitting a power law $f = ml^c$ gives the fit in Fig. 3.10(a) with $m = 17.6\,\mathrm{GHz\,mm}^{-c}$ and $c = -0.789$. This gives a simple model to generate resonators over a wide frequency range, but the residual indicates some bias suggesting this model may not be accurate enough for resonators targeting exact frequencies. For a more accurate model, a linear model $f = ml + c$ is used to fit to resonances from the lowest two chips with $m = -212\,\mathrm{MHz\,mm}^{-1}$ and $c = 4.958\,\mathrm{GHz}$, the residual showing no visible bias on this smaller scale and a standard deviation $\sigma = 28\,\mathrm{MHz}$.

This model was used to generate a design of 12 resonators, 10 distributed around ~2.4 GHz with 10 MHz spacing predicted with the linear fit, with another two predicted with the power-law fit at 3.5 GHz and 5 GHz. This design was used to fabricate on a Yb:Y_2SiO_5 chip, with two resonators at 4.939 GHz and 2.376 GHz measured in Chapter 7.

3.5.2 Field tunability

Due to the variance in the fabricated resonator frequency, reliably hitting a transition to within <1 MHz is not possible, so some degree of tunability of resonator frequency is required. This can be achieved by applying a magnetic field to the resonator to increase the kinetic inductance of the superconducting film (see Section 3.1.2).

A chip with spiral resonators around 2.7 GHz–3.1 GHz was fabricated from 20 nm NbN on Si and loaded into the closed-cycle cryostat at 1.6 K. The device is most

[4] This is derived by eliminating the width w from simultaneous equations for the perimeter and area of a rectangle $P = 2l + 2w$ and $A = l \times w$, which gives a quadratic whose two solutions return l and w.

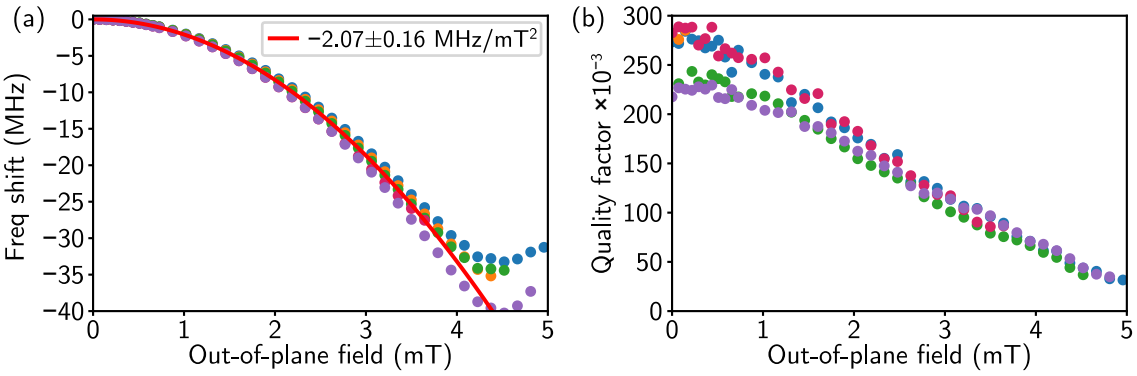

Figure 3.11: (a) Field tunability of spiral resonators fabricated on Si within the frequency range 2.7 GHz–3.1 GHz to applied out-of-plane magnetic field. Colour represents each of 5 tracked resonators. A quadratic fit ($\Delta f = \beta B^2$) in red highlights a tunability of ~20 MHz at 3 mT. (b) Simultaneous measurement of resonator quality factor shows a deterioration at fields above 1 mT.

sensitive to out-of-plane magnetic field, so the devices were aligned with the field axis perpendicular to the superconductor plane. The frequencies and quality factors of 6 resonators were measured as a function of magnetic field strength, giving the data in Fig. 3.11. Fitting a pure quadratic $\Delta f = \beta B^2$ to the frequency shift gives $\beta = (-2.07 \pm 0.16)\,\mathrm{MHz\,mT^{-2}}$ in agreement with Eqn. 3.5. The internal losses of the resonators also increase with magnetic field due to flux threading through the type-II superconductor, causing a drop in quality factor.

3.6 Discussion

We have described both the thin-ring and spiral resonator designs used for experiments in the following three chapters. Electromagnetic simulations used to assist with designing and characterising their magnetic fields have been summarised, showing $B_1 \propto \frac{1}{r}$ for the thin-ring resonator while the spiral generates a more homogeneous magnetic field with a slower drop-off with distance into the substrate. The fabrication process was detailed, consisting of DC magnetron sputtering of NbN, photolithography, and a reactive ion etch. To enable fabrication of spiral resonators targeting near-ZEFOZ transitions at ~2.4 GHz a series of NbN spiral resonators were measured to create a model to predict resonant frequency based on geometric parameters and to characterise its frequency tunability with magnetic field. This data informed the design of a chip of 12 spiral resonators, fabricated on Yb:Y_2SiO_5 and measured in Chapter 7.

Chapter 4

Experimental setup

This chapter describes the equipment used in this thesis, including the interface between the superconducting resonator and measurement setup, the cryostats and microwave circuits used to measure the device at mK temperatures, and the spectrometer and microwave bridges used to perform pulsed ESR measurements.

4.1 3D copper cavity

To couple the superconducting resonator to the measurement setup, the fabricated device is enclosed within a 3D copper cavity [50]. This serves two purposes: to provide a mechanism by which the resonator can be excited and read out via two antennae within the cavity; and to shield the resonator from the environment by providing a series of discrete box modes at higher frequencies and detuned from the resonator to suppress radiative losses.

For a rectangular cavity of dimensions a, b, d the wavenumber k and frequency f of its resonant modes are given by [137]

$$\begin{aligned} k_{mnl} &= \sqrt{\left(\frac{m\pi}{a}\right)^2\left(\frac{n\pi}{b}\right)^2\left(\frac{l\pi}{d}\right)^2} \\ f_{mnl} &= \frac{c}{2\pi}k_{mnl} \end{aligned} \tag{4.1}$$

where the indices m, n, $l \in \mathbb{Z}$ indicate the number of half-wavelengths of the standing wave along the respective axes of the cavity, and c is the speed of light in the cavity dielectric which is typically vacuum. Conventionally the dimensions are assigned $b < a < d$ such that the lowest frequency mode is the electric TE_{101} mode.

Motivated by the requirement that the cavity fit within the depth of the characterisation cryostat in Section 4.2 and the diameter of the vector magnet of the fridge described in Section 4.3.2, the dimensions $30\,\mathrm{mm} \times 6\,\mathrm{mm} \times 50\,\mathrm{mm}$ were chosen,

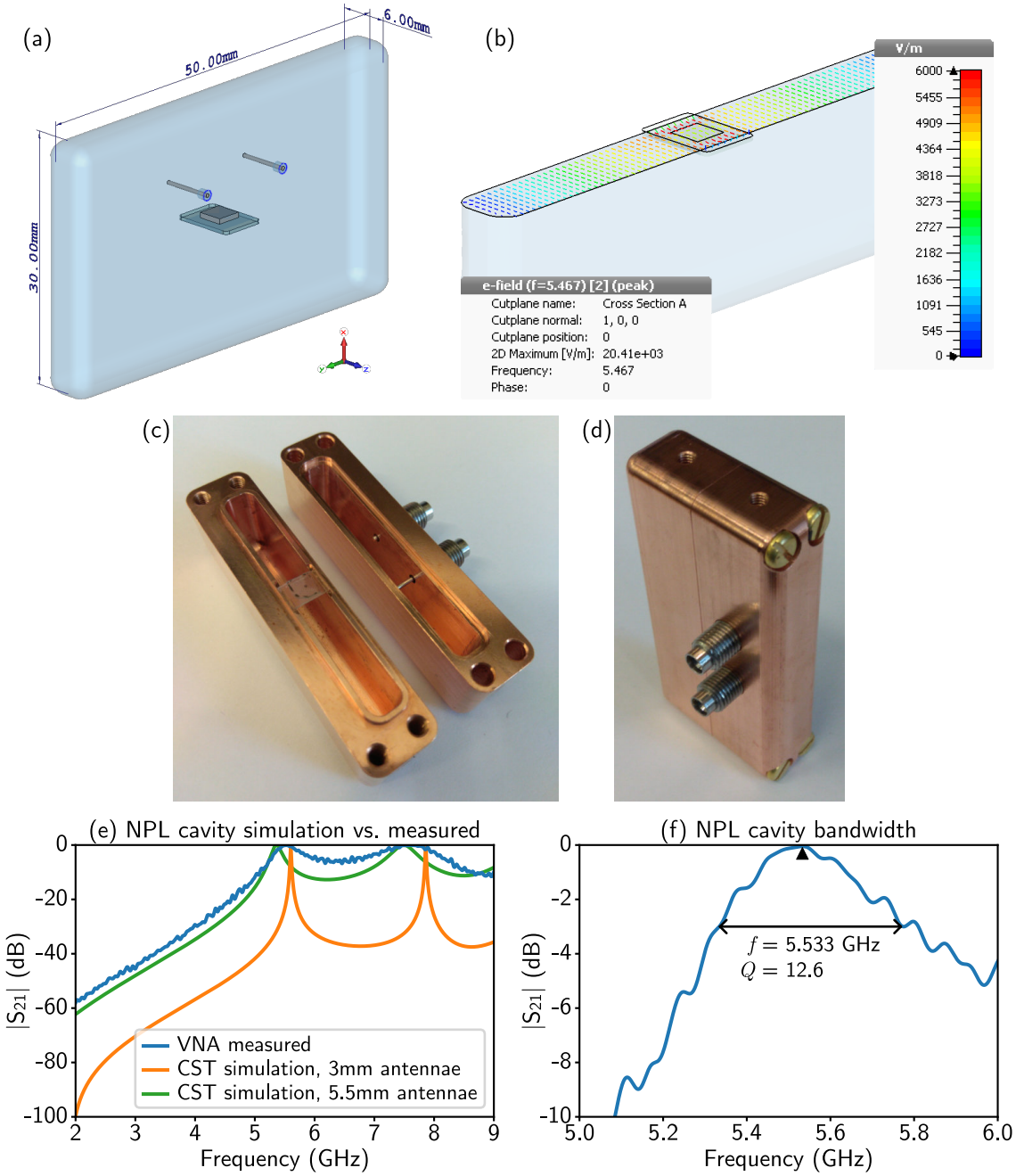

Figure 4.1: Measurement of the resonator via a 3D copper cavity provides both a route to drive and readout the resonator via two antennae, and shields the resonator from radiative emission to the environment. (a) A CST model of the 3D cavity, along with its dimensions. (b) A CST simulation of the TE_{101} mode of the cavity. (c, d) Photographs of the cavity, showing a fabricated Y_2SiO_5 chip mounted on a sapphire sample holder, and the antennae protruding into the cavity with SMP connectors outside the cavity. (e) CST frequency-domain simulations allow the S_{21} of the cavity to be simulated for different antenna geometries. (f) A 5.5 mm antenna length gives a broad measured cavity Q.

being the largest cavity meeting these requirements to produce the lowest possible frequency TE_{101} mode $f_{101} = 5.8\,\text{GHz}$. Simulating the cavity mode using CST Microwave Studio [135] with a model shown in Fig. 4.1(a) shows this electric field mode at $f_{101} = 5.5\,\text{GHz}$, reduced from the theoretical calculation by the presence of additional dielectric from the sapphire sample holder and Si chip included in the model. The electric field lies parallel to the shortest axis of the cavity in Fig. 4.1(b).

The cavity was milled from a block of OFHC copper, split along its longest axis to enable the chip to be placed on a sapphire sample holder, held in place with a small quantity of vacuum grease as seen in Fig. 4.1(c). The antennae are formed by inserting a length of copper, cut from the centre conductor of a semi-rigid coaxial cable, into an SMA female to SMP male adaptor. Screwing together the two halves forms the copper box in Fig. 4.1(d), an integral component in every measurement setup presented subsequently.

The coupling between antennae and cavity has two contributions: a capacitive coupling between each antenna and the resonator, and a coupling mediated by the electric field of the cavity. These can be tuned by varying the length of the antenna within the cavity, and is typically set up so the input antenna extends $<1\,\text{mm}$ into the cavity while the output antenna is significantly longer at $\sim 5\,\text{mm}$ to ensure the resonator preferentially emits along the output line, though for low frequency measurements both antennae extend most of the length of the cavity to facilitate driving the resonator. Frequency-domain simulations of the S_{21} of the cavity in CST for short 3 mm and long 5.5 mm antennae are compared to the measured S_{21} with a VNA in Fig. 4.1(e). For the longest antennae used the cavity mode has a $Q \approx 12$ as measured in Fig. 4.1(f).

4.2 Device characterisation with closed-cycle cryostat

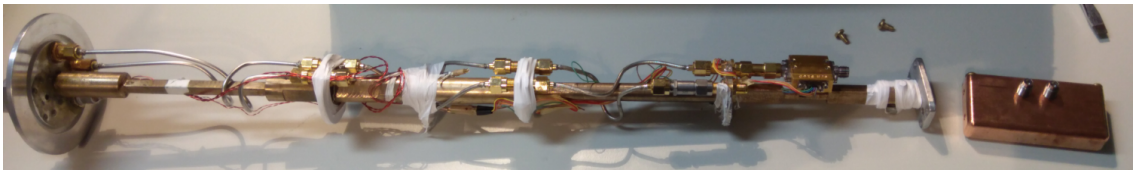

Figure 4.2: EPR cryostat insert for superconducting resonator measurements with 3D cavity, incorporating a 20 dB attenuator on the input line, low-noise cryogenic amplifier on the output, and a LakeShore Cernox temperature sensor. Inserting this probe into a closed-cycle ^{4}He cryostat enables resonator characterisation at 1.6 K.

To facilitate characterising superconducting resonators with a fast turnaround, a probe built to be compatible with standard EPR cryostats with a KF40 flange was used. Seen in Fig. 4.2, it incorporates a series of acrylic baffles with SMA feedthroughs, separated by bronze rods, to impede He gas flow. Two coaxial lines provide an input attenuated by 20 dB at the coldest baffle, and an output with a 1 GHz–12 GHz cryogenic low-noise amplifier (Low Noise Factory LNF-LNC1_12A). DC connections at the top provide power to the amplifier and enable thermometry via a LakeShore Cernox temperature sensor. The 3D copper cavity described in the previous section, containing the device under test, attaches at the bottom.

The probe is inserted within a closed-cycle cryostat built by Cryogenic Ltd. and powered by a Sumitomo two-stage pulse tube cryocooler to reach a base temperature of 1.6 K. The cryostat is mounted within an EPR magnet (Bruker ER073) enabling application of fields ~1 T, and the probe can be rotated within the field by use of a motorised goniometer (Huntington Mechanical Labs MVF-274-450) mounted on the cryostat.

Connecting a vector network analyser (VNA) to the input and output of the probe enables measurement of the S_{21} of the device, characterising the frequency and quality factor of fabricated resonators. Their resilience to in-plane magnetic field and tuneability with out-of-plane field can both be measured accurately by rotating the sample within the field using the goniometer. Measurements of devices at 1.6 K using this probe are presented in Chapter 3.

4.3 mK measurements with a dilution refrigerator

By pumping on ^{4}He the Cryogenic closed-cycle cryostat can achieve a base temperature of 1.6 K, and the most efficient commercially available cryostats based on ^{4}He typically reach 1.3 K. To extend this range below 1 K, the much rarer isotope ^{3}He can be used. Pumping on ^{3}He is significantly more effective than ^{4}He due to its larger vapour pressure and considerably greater specific heat <1 K [138], enabling cooling down to ~300 mK.

The cooling power from evaporating He is proportional to the vapour pressure of the liquid, which drops exponentially with temperature [139]. This limits the temperatures achievable by exploiting the latent heat of evaporation of He. An alternative is to use the heat of mixing ^{3}He with ^{4}He to reach lower temperatures, in a cryostat known as a dilution refrigerator.

4.3.1 Working principle of a dilution refrigerator

A dilution refrigerator is the only currently available method of continuous cooling below 300 mK. To understand its operating principle we begin by looking at the %–T phase diagram of isotopic proportions % of the ^{3}He–^{4}He mixture versus temperature T in Fig. 4.3(a) [138]. Pure ^{4}He has a superfluid transition at 2.177 K, while ^{3}He being a fermion requires much lower temperatures ~2.49 mK for superfluidity and is not shown on this chart. ^{3}He and ^{4}He remain fully miscible down to 867 mK, below which the two isotopes only mix in a range of concentrations which depend on temperature. This implies a mixture of ^{3}He–^{4}He, cooled below 867 mK, separates into two phases of different concentrations of ^{3}He, with the more concentrated ^{3}He floating on top of the denser dilute mixture. As the temperature approaches 0 K, the limiting concentrations approach 100 % ^{3}He for the concentrated phase and 6.6 % ^{3}He in the dilute phase. This remaining miscibility of ^{3}He and ^{4}He at 0 mK enables the dilution fridge to operate down to low mK temperatures as the cooling power scales with T^2 rather than exponentially as for evaporative cooling [139].

The cooling in a dilution refrigerator comes from the enthalpy of mixing $\Delta H = H_\mathrm{d}(T) - H_\mathrm{c}(T)$ between the two phases. As ^{3}He in the dilute phase has a greater specific heat than concentrated ^{3}He [138], the enthalpy of the dilute phase H_d is greater than the concentrated phase H_c, so the heat of mixing is [139]

$$\frac{\mathrm{d}Q}{\mathrm{d}t} = \frac{\mathrm{d}n}{\mathrm{d}t}\Delta H \tag{4.2}$$

where $\frac{\mathrm{d}n}{\mathrm{d}t}$ is the molar flow rate of ^{3}He atoms from the concentrated phase into the dilute phase. ΔH can be calculated from measurements of the specific heat of each isotope to be $\Delta H \approx 84T^2[\mathrm{J\,mol^{-1}}]$ [139].

Hence the cooling power of a dilution refrigerator is directly proportional to the ^{3}He flow rate across the phase boundary. This flow can be driven by pumping on the dilute phase. The greater vapour pressure of ^{3}He than ^{4}He [138] means this preferentially pumps ^{3}He from the dilute liquid, creating an osmotic pressure which pulls ^{3}He across the phase boundary between the two concentrations, driving the cooling process.

A physical implementation of a dilution unit is illustrated in Fig. 4.3. Circulating ^{3}He vapour is pre-cooled and condensed before coming into thermal contact with the still at 700 mK. It then flows through a series of heat exchangers, typically an initial concentric heat exchanger followed by several sintered silver heat exchangers,

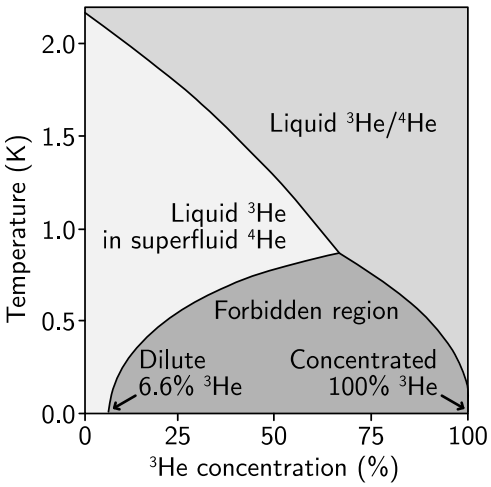

(a) Phase diagram of ^{3}He concentration $\% = \frac{n_3}{n_3+n_4}$ versus temperature, at saturated vapour pressure. At $T = 0$ two separate phases form, one entirely concentrated ^{3}He, the other a dilute mixture of 6.6 % ^{3}He, with a phase boundary between them. Data from [138].

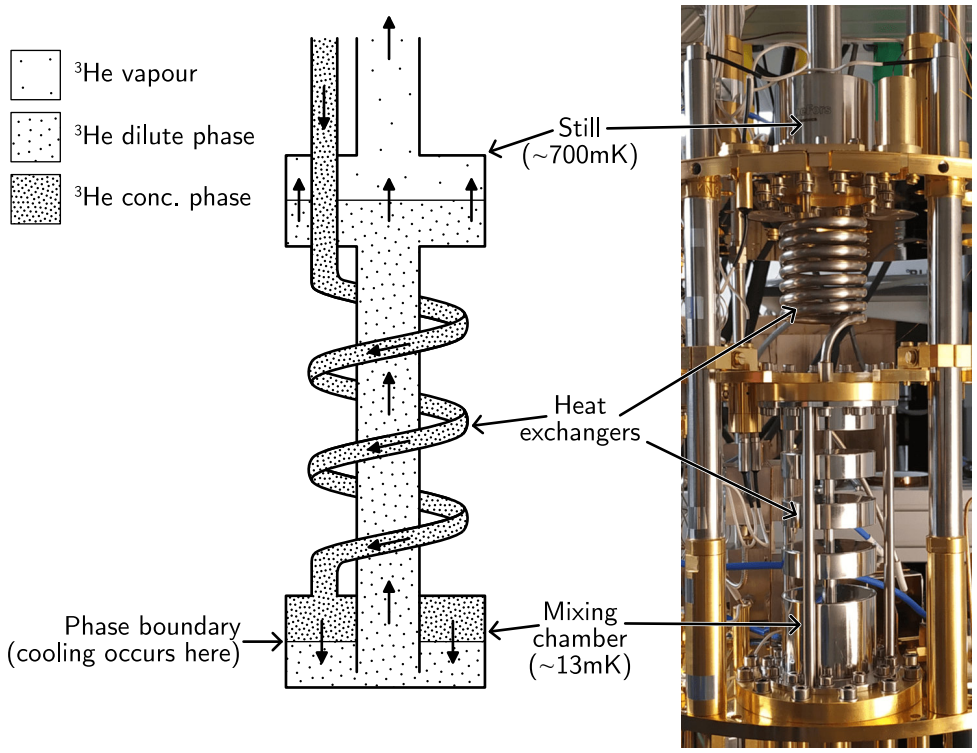

(b) Schematic of a dilution unit. Incoming concentrated ^{3}He is precooled by thermal contact with the still and a concentric heat exchanger followed by a series of sintered silver heat exchangers. It enters the mixing chamber where the phase boundary between the two concentrations lies. The dilute phase lies between the mixing chamber and the still, where the liquid boundary is pumped on while heat is applied, preferentially evaporating ^{3}He due to its greater vapour pressure. This creates an osmotic pressure within the dilute phase, pulling ^{3}He atoms across the phase boundary in the mixing chamber and absorbing heat in accordance with Eqn. 4.2. Photograph shows the dilution unit of the LCN BlueFors LD-400 fridge, detailed in Section 4.5.

Figure 4.3: Working principle of a dilution refrigerator.

which brings the temperature of the incoming concentrated ^{3}He close to that of the outgoing dilute ^{3}He before it enters the mixing chamber.

During steady-state operation of the dilution fridge, with the ^{3}He–^{4}He mixture condensed within the dilution unit, the phase boundary between the concentrated and dilute phase lies within the mixing chamber. ^{3}He atoms pulled across the boundary experience by osmotic pressure a change in enthalpy due to the mixing, absorbing energy in accordance with Eqn. 4.2 and cooling the mixing chamber.

A wide tube runs from the dilute phase in the mixing chamber up to the still, via the heat exchanger. In normal operation almost all the ^{4}He lies in this mixture, in a superfluid state, with the liquid–vapour boundary of the dilute mixture lying within the still. Inside, ^{3}He evaporates from the ^{4}He superfluid, driven by pumping on the vapour from the still and by a heater next to the still. This drives the circulation of ^{3}He through the circuit and creates the osmotic pressure necessary to pull ^{3}He atoms through the phase boundary at the mixing chamber.

For a flow rate of 0.5 mmol s^{-1} at a temperature of 10 mK, fairly typical parameters for operation of a commercial fridge at base temperature, the cooling power of a dilution unit calculated from Eqn. 4.2 is 5 µW, increasing to 100 µW at 50 mK.

The efficiency of the heat exchanger is a critical factor in determining the base temperature of a dilution refrigerator. The lowest temperature recorded in a dilution fridge is ~1.75 mK at the Lancaster Microkelvin Facility [140], achieved with a highly efficient concentric heat exchanger followed by a series of 15 discrete heat exchangers. The greatest mass cooled by a dilution refrigerator is found in the cryostat for the CUORE project [141], where a series of 988 TeO_2 crystals with associated measurement apparatus weighing 1500 kg is continuously maintained at 10 mK.

Until recently, dilution refrigerators relied on vessels of liquid He to pre-cool the experimental mass, heat shields, and the circulating ^{3}He. Modern dry fridges dispense with the liquid He bath in favour of a closed-cycle pulse-tube refrigerator to cool two stages of the dilution fridge to ~50 K and ~4 K while minimising vibrations. mK experiments presented later in this thesis use a pair of commercial dry dilution refrigerators from BlueFors, the specifics of which follow in the next two sections.

4.3.2 NPL fridge

The first mK experiments presented in this thesis, in Chapter 5, were performed at the National Physical Laboratory (NPL) in a BlueFors LD-400 dry dilution refrigerator, seen in Fig. 4.4. This fridge has a base temperature ~10 mK as measured

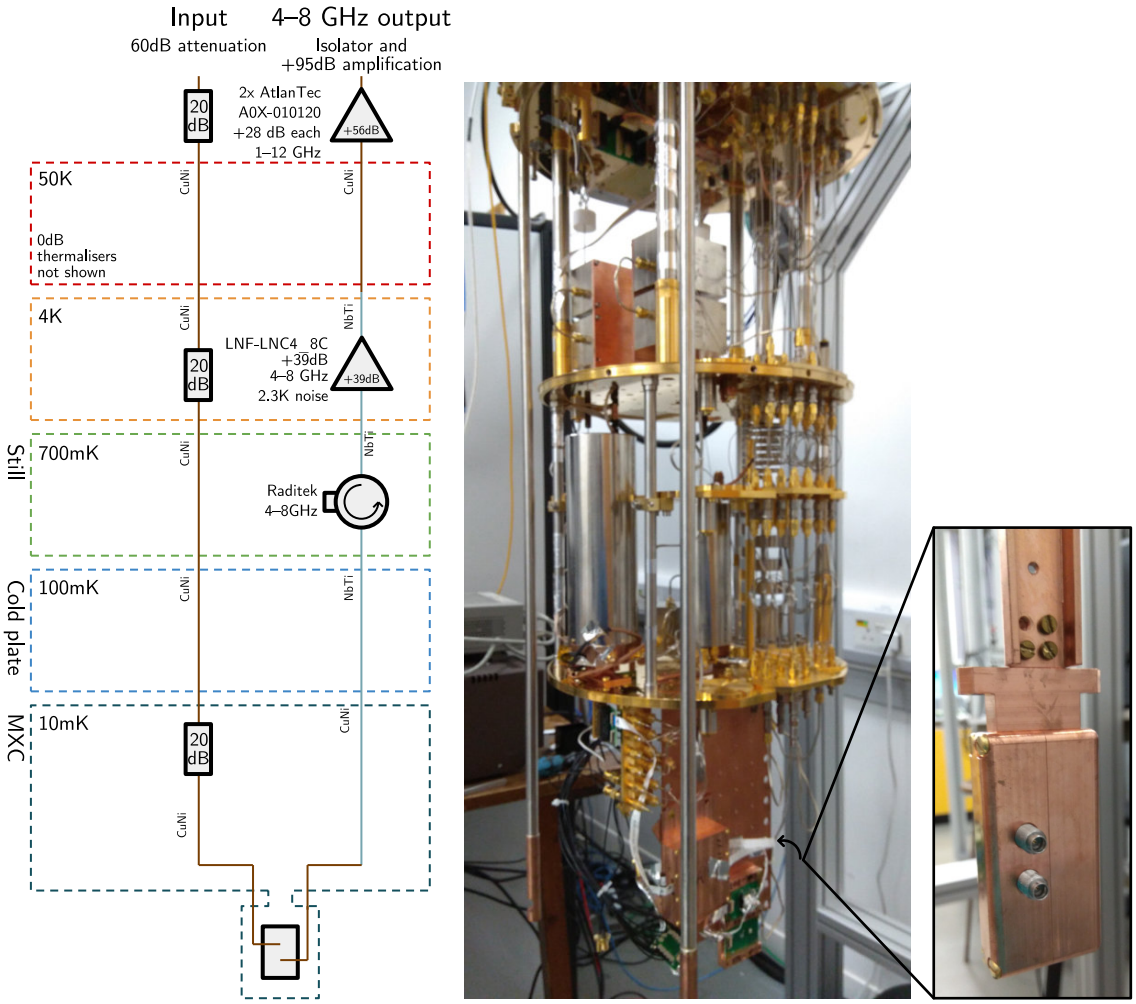

Figure 4.4: Microwave wiring schematic and photographs of the BlueFors LD-400 dilution refrigerator at NPL, used for continuous-wave measurements in Chapter 5.

at the mixing chamber stage, and is equipped with several coaxial microwave input and output lines as well as a 9–1–1 T 3-axis superconducting NbTi vector magnet built by American Magnetics Inc. (AMI) anchored to the 4 K stage and powered by a 4Q06125PS four-quadrant power supply with model 430 power supply programmer, capable of supplying a magnetic field up to 1 T in any direction or up to 9 T along the z-axis.

The sample is installed within the 3D copper cavity, anchored to the mixing chamber stage via a copper rod (inset) to hold the cavity at the centre of the bore of the vector magnet to supply an accurate and homogeneous field to the sample.

Two microwave lines enable transmission measurements across the 3D cavity, measuring the signal from the resonator inside. Blackbody radiation present in the cables thermalised at room temperature at the top of the fridge is transmitted down these measurement lines, and if left unchecked would cause a large background photon occupation number in the resonator, driving the electron spin population out of thermal equilibrium with the mixing chamber. This thermal noise is sometimes called Johnson–Nyquist noise. To account for this the input line must be attenuated in several stages to reduce the number of thermal photons to a level comparable to the blackbody radiation at the mixing chamber [142]. The noise level is typically quantified by the noise temperature $T_\mathrm{n} = \frac{P_\mathrm{n}}{k_\mathrm{B}}$ where P_n is the power spectral density of the noise. The noise temperature $T_{\mathrm{n},i}$ at stage i is then a function of the noise temperature radiating from the previous stage $T_{\mathrm{n},i-1}$, the real temperature of T_i of stage i, and the attenuation A_i at stage i defined such that a 20 dB attenuator corresponds to $A_i = 0.01$:

$$T_{\mathrm{n},i} = A_i T_{\mathrm{n},i-1} + T_i(1 - A_i) \tag{4.3}$$

where the first term comes from attenuation of noise from the previous stage, and the second term comes from blackbody radiation thermalised at stage i. The noise temperature can then be calculated for each attenuated stage in sequence to give the final blackbody noise temperature at the mixing chamber.

In this fridge, the CuNi input line is attenuated by 20 dB at the 4 K stage and 20 dB at the mixing chamber, giving a noise temperature $T_\mathrm{n} < 80$ mK at the mixing chamber stage. An additional 20 dB attenuator is installed at room temperature to assist in few-photon measurements, and there is another approximately 6 dB of attenuation from losses in the microwave cables, as well as an unknown insertion loss from the cavity to the superconducting resonator. The output line consists of a superconducting NbTi cable to reduce attenuation of the weak output signal, with

a cryogenic 4 K low-noise amplifier (LNA) from Low Noise Factory providing 39 dB gain, with an isolator (Raditek RADI-4-8-Cryo) with 17 dB return loss between the amplifier and the sample at the still stage to attenuate noise radiating down the output line from the amplifier. A further 56 dB amplification from two room-temperature amplifiers from AtlanTecRF brings the signal to a level measurable by a VNA.

Continuous-wave (CW) measurements in this fridge were performed by a Rohde & Schwarz ZNB20 vector network analyser connected between the input and output lines, as described in Chapter 5.

4.3.3 LCN fridge

Measurements in chapters 6 and 7 were performed at the London Centre for Nanotechnology, in a BlueFors LD-400 dilution refrigerator illustrated in Fig. 4.5. This fridge is equipped with a 3–1–1 T superconducting vector magnet by AMI, and has a cold-loading mechanism enabling a fast exchange of devices and measurements without the need to warm up the entire fridge to room temperature.

The 3D cavity is loaded within a cylindrical sample box seen in Fig. 4.5 with the cylindrical shield removed to expose the scaffold and 3D cavity mounted inside. DC ports at the bottom connect to a 4-lead RuO_2 temperature sensor mounted within the sample box, which typically reads ~13 mK at base temperature, and a resistor for heating the sample box to control the temperature with a PID temperature controller (LakeShore Cryotronics Inc. model 372).

Three microwave lines are used in the experiments presented in this thesis. One attenuated CuNi input line is installed, with attenuators totalling 50 dB which according to Eqn. 4.3 gives a noise temperature $T_\mathrm{n} = 18$ mK at the mixing chamber stage. This input line is used in both Chapters 6 and 7. Measurements in Chapter 6 at 8 GHz are performed with the 4 GHz–8 GHz NbTi output line, with a 39 dB amplifier at 4 K isolated from the sample box with three Quinstar QCY-G0451051AS isolators providing a total of 54 dB return loss. Two room temperature amplifiers provide an additional 44 dB gain before measurement. In Chapter 7 where measurements in the range 2 GHz–4 GHz are performed, a new output line was used with a 1.5 GHz–6 GHz amplifier. Due to a lack of availability of circulators below 4 GHz, the measurement was performed with no isolation between the LNA and the sample except the insertion loss between the cavity and superconducting resonator. The resulting thermal microwave radiation background from the amplifier at 4 K may excite the electron spin ensemble out of thermal equilibrium at 13 mK.

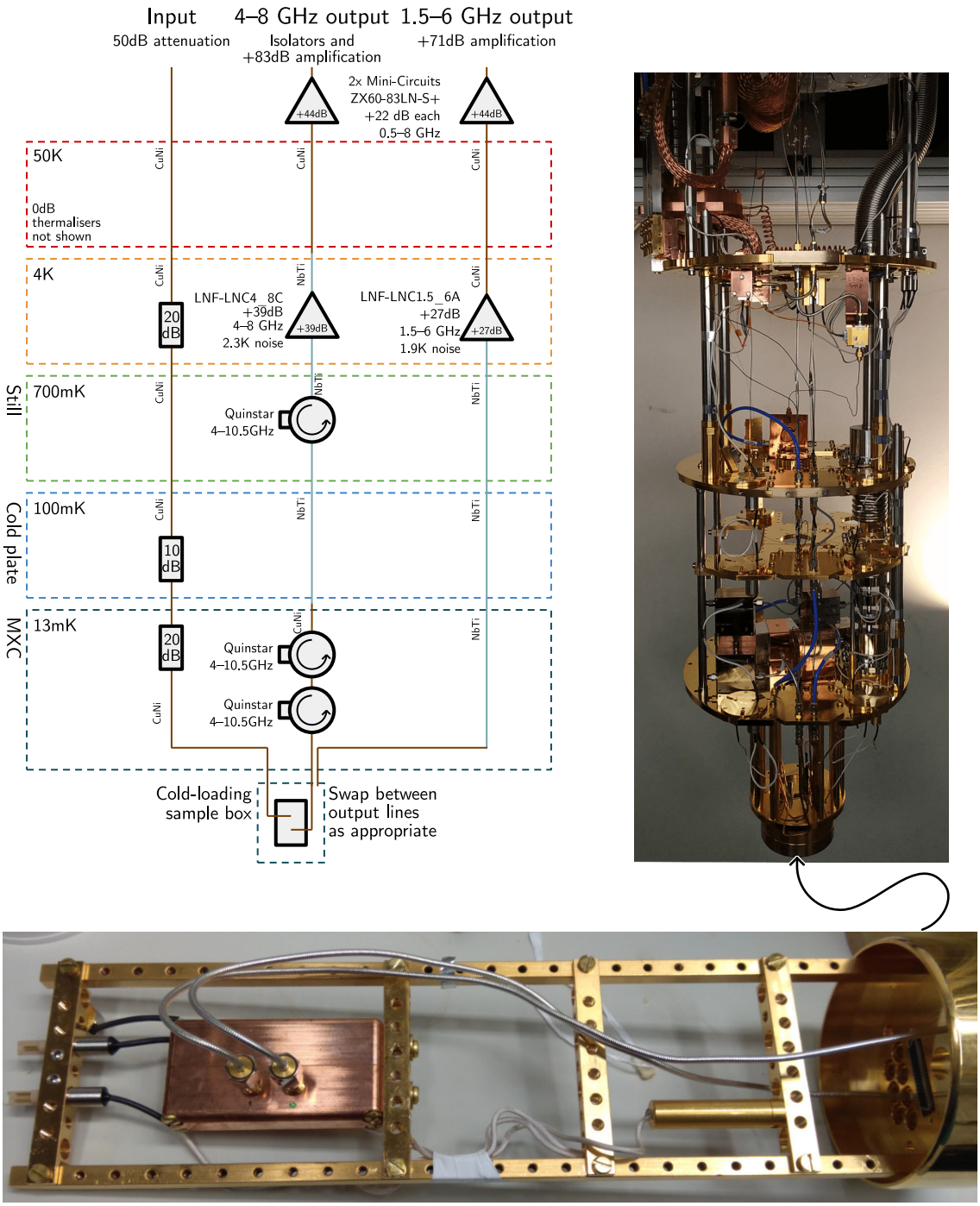

Figure 4.5: Wiring schematic and photographs of the BlueFors LD-400 dilution refrigerator at LCN, including the mounting of the 3D cavity within the cold-loading sample box, used for CW and pulsed measurements in chapters 6 and 7

Moving on from the CW measurements performed in the NPL fridge in Chapter 5 with a VNA, the LCN fridge was set up with a lab-built ESR spectrometer with two microwave bridges in frequency ranges compatible with each measurement line, enabling pulsed measurements measuring spin echoes and coherence properties of electron spins.

4.4 Pulsed ESR spectrometer

To perform pulsed ESR, a spectrometer is required whose purpose is to generate well-defined pulses of microwave radiation and capture the response from the device under test. Generating arbitrary sequences requires a microwave setup capable of creating fast frequency-swept amplitude-modulated pulses. At frequencies of several GHz it is typically not possible to generate these pulses directly, so a setup similar to that shown schematically in Fig. 4.6(a) is used.

To generate pulses, an arbitrary waveform generator (AWG) produces low-frequency fast modulated output in two analogue channels, one in-phase (I) and one out-of-phase (Q) and three digital markers. The I/Q signal encodes both amplitude and frequency offset, and is fed into a vector signal generator (VSG) which mixes it with a high-frequency carrier to produce an arbitrarily modulated high frequency pulse, as illustrated in Fig. 4.6(b). This upmixed pulse enters the microwave bridge and is sent to the cavity. The retrieved signal is demodulated inside the microwave bridge with an I/Q mixer that is referenced to the VSG's local oscillator (LO) carrier frequency output. This downmixes the signal down to a frequency at which it can be accurately sampled by the digitiser. The three marker pulses from the AWG control the gate and acquisition switches detailed in the following section, and trigger the digitiser to gather data.

The microwave bridge controls the amplification of control pulses and retrieved signals, contains fast switches to protect amplifiers from high power pulses and prevent leakage of microwaves from high-power amplifiers, and downmixes the retrieved signal for digitisation. The components required for this have a limited bandwidth, so a separate microwave bridge is typically required for different frequency ranges. A custom-built spectrometer was already available for pulsed experiments, but with its bridge (detailed in Section 4.4.2) operating at X-band 7–12 GHz, it was not suitable for eventual low-frequency measurements for which a new bridge had to be designed and built while maintaining compatibility with the existing AWG, VSG, and digitiser.

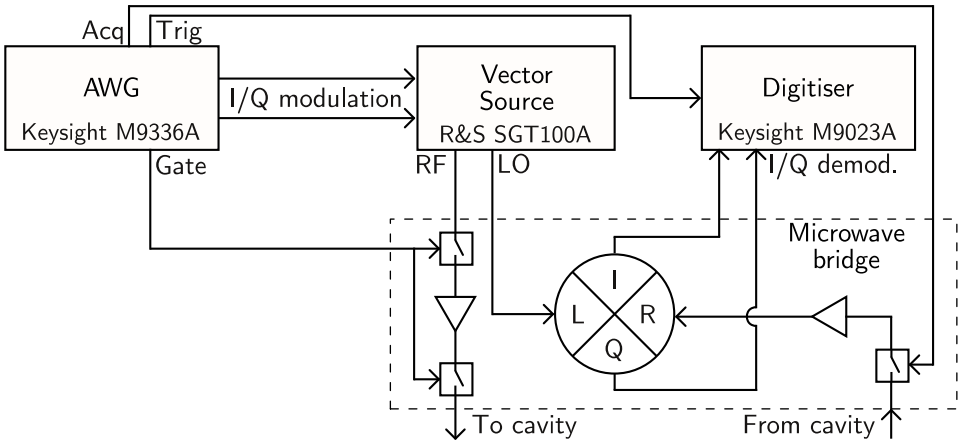

(a) Schematic of the components of a spectrometer outside the microwave bridge. The arbitrary waveform generator (AWG) generates two analogue channels I and Q which a vector signal generator (VSG) upmixes with a carrier frequency to create high-frequency pulses. The retrieved signal is downmixed in the bridge by an I/Q mixer referenced to the VSG's local oscillator, producing a signal that can de digitised. Three marker pulses from the AWG control switches in the bridge and trigger the digitiser.

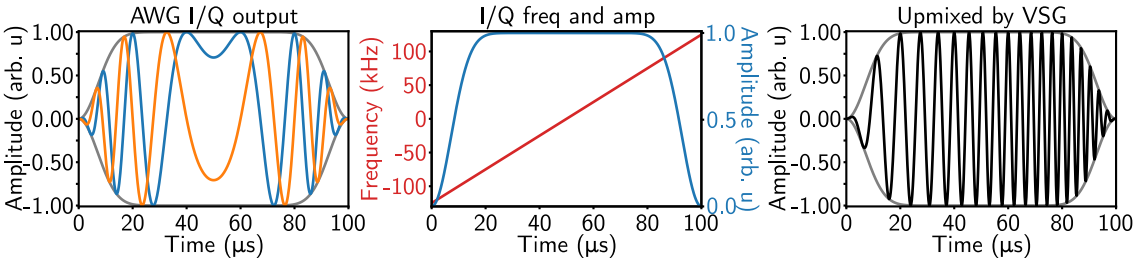

(b) Steps toward producing frequency and amplitude modulated microwave pulses in a pulsed spectrometer using an AWG and VSG. The AWG produces two analogue channels I and Q encoding the frequency offset and amplitude, which is fed to a VSG which mixes it with a carrier frequency to produce the upmixed microwave pulse. This figure illustrates the process with a ±125 kHz swept WURST pulse [143, 144], details of which are given in Section 6.6.1, mixed with a 200 kHz carrier. Later experiments typically sweep over ~1 MHz with a carrier in the GHz.

Figure 4.6: Overview of pulse generation and retrieval in a pulsed ESR spectrometer.

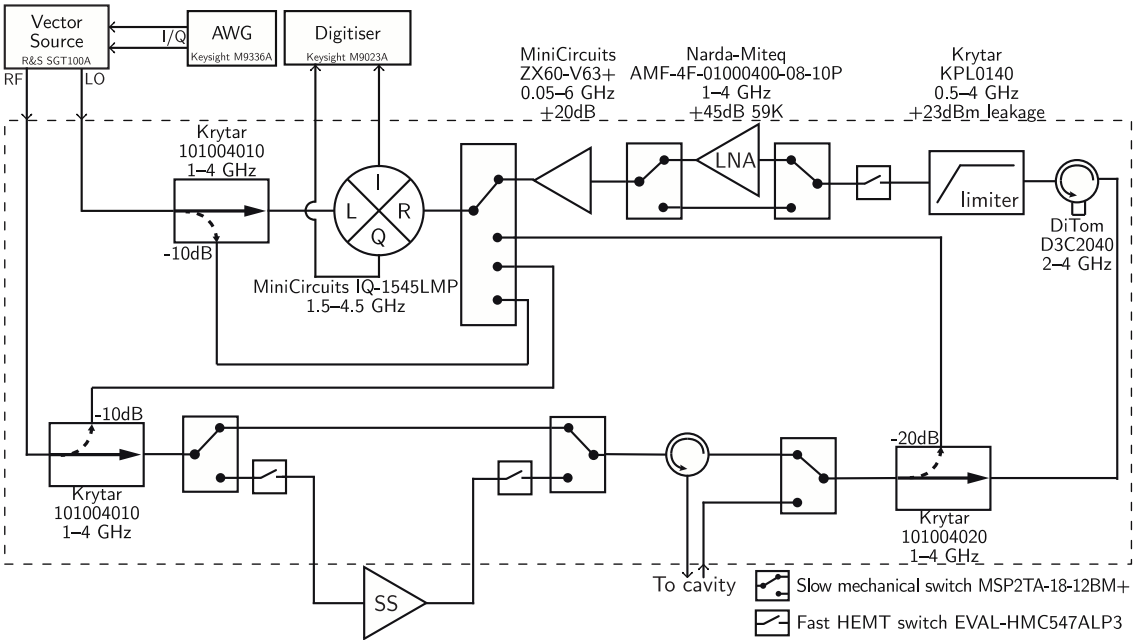

Figure 4.7: Schematic of the 2–4 GHz microwave bridge, details of which are given in the main text. The layout of this bridge is inspired by a previous generation ESR bridge operating around X-band 7–12 GHz detailed in Section 4.4.2 and Figure 4.10.

4.4.1 2–4 GHz microwave bridge

For pulsed ESR experiments in Chapter 7, where compatibility with 2–4 GHz was required, a new ESR spectrometer bridge had to be built. This piece of equipment[1] works in tandem with the external VSG, AWG, and digitiser, to form a spectrometer which generates arbitrary pulse sequences, retrieves the returned signal and acquires any spin echo.

This section summarises the workings of the 2–4 GHz bridge, the schematic of which is shown in Fig. 4.7. For detailed characterisation of its internal losses and amplification in various operational modes see the tables in Appendix B.

Pulse generation

Pulses are generated by modulating the VSG's carrier frequency via the I/Q output from the AWG. The modulated output from the VSG is then fed into the RF port of the bridge. Here a pair of slow electromechanical switches, controlled by the *Pulse amp* switch on the front panel, allows the choice of passing the RF signal straight through, or gating the signal (see markers and gates) and passing it

[1]Nicknamed "Zoidberg", as the coaxial cables coming from its front panel loosely resemble the mouth tentacles from its eponymous *Futurama* character.

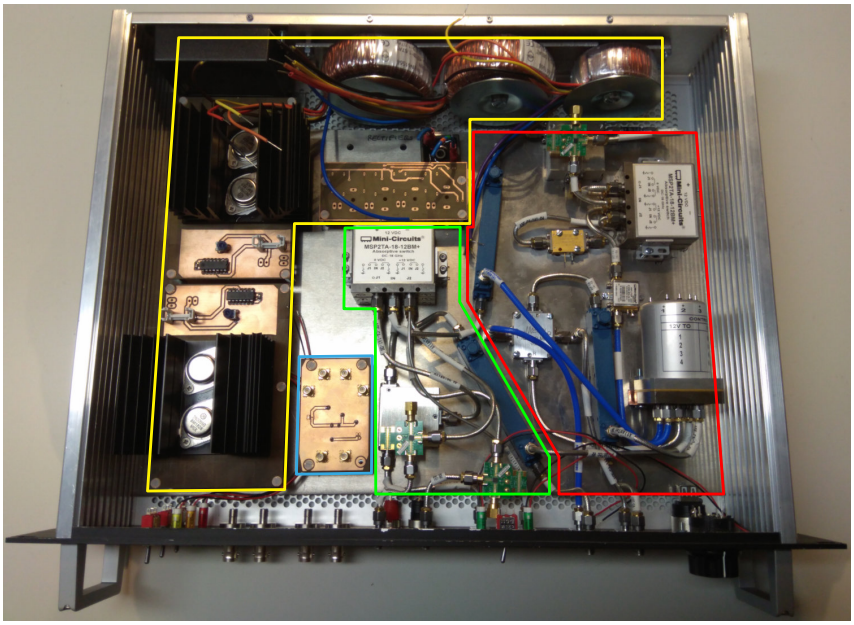

(a) Inside the ESR bridge. Yellow: power supply. Blue: fast switch logic. Green: pulse amplification and gating. Red: acquisition chain.

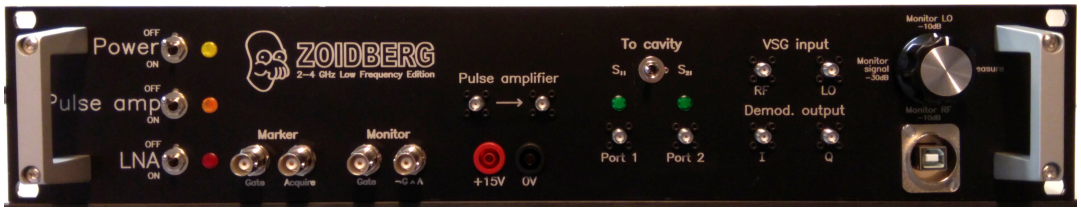

(b) Front panel of ESR bridge.

Figure 4.8: Photographs of the internals of the bridge, taken before the wiring was added for clarity of the RF components.

through the *Pulse amplifier* SMA ports where an external pulse amplifier (typically a Mini-Circuits ZVE-3W-83 solid state amplifier) can be connected and powered by the bridge's +15V supply. The RF pulse then passes through a circulator and out of *Port 1* of the front panel where it can be sent to the sample.

Acquisition

The bridge can operate in either reflection or transmission modes, depending on the electrical path to the sample. A switch on the front panel enables the reflected signal from *Port 1* to be extracted via a circulator, or for the transmitted signal to be routed through *Port 2*. The signal passes through an isolator, power limiter with +23 dBm leakage, and a fast switch. The limiter protects the switch and subsequent amplifiers from being damaged by high power MW pulses. The fast

switch protects the amplifiers by passing the signal through only when pulses are not being sent, more details are given in the markers and gates section shortly. The isolator prevents any reflected signal from the switch or limiter from returning to the cavity.

A pair of slow switches allows the sensitive low noise amplifier (LNA) to be included in the chain or not, controlled by the *LNA* front panel switch. The signal is then further amplified before being demodulated by the I/Q mixer. This takes the LO from the VSG, routed through the *LO* front panel port, and outputs the components of the RF signal that are in-phase (I) and out-of-phase (Q) with the LO. These demodulated signals can then be routed from the front panel to a digitiser or oscilloscope for acquisition. It is recommended a ~500 MHz low pass filter is added prior to digitisation to remove any remaining LO component from the I/Q signal.

Diagnostic monitors

This bridge incorporates a series of directional couplers and a rotary switch on the front panel to monitor the RF signal at various parts of the measurement chain, for diagnostic purposes. The switch should be set to *Measure* for normal operation. With *Monitor RF*, the RF output from the VSG can be sent straight to the I/Q mixer to check the pulse sequence matches what the user is expecting. Selecting *Monitor signal* bypasses the amplification chain, enabling measurement of transmitted pulses or to diagnose any faults in the bridge. *Monitor LO* routes the LO signal into the I/Q mixer's RF port, to verify the LO output from the VSG is being correctly generated and the I/Q mixer is operating normally.

Markers and gates

The bridge incorporates fast switches, controlled by a pair of markers from the AWG, to perform two functions.

Firstly, a pair of "gate" switches are placed at the input and output of the external pulse amplifier. The first switch ensures that any leakage of RF from the VSG when the output is meant to be off is heavily attenuated before reaching the amplifier. The second switch ensures that noise from the pulse amplifier is attenuated before being sent to the sample. Without these precautions, a constant low power signal would reach the sample, continuously driving any resonant spins causing the transition to saturate. These gate switches are controlled by a "gate marker" output from the AWG.

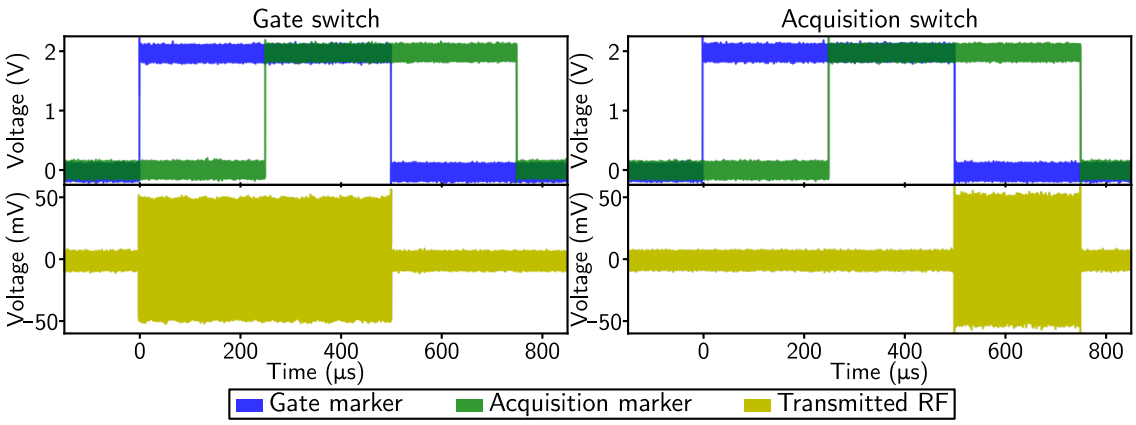

Figure 4.9: The function of the markers and fast switches in the bridge, measured using a fast oscilloscope. The top of each graph shows the status of the gate marker (blue) and the acquisition marker (green). Below in yellow is shown the transmitted signal from a 3 GHz source from the front panel RF port to Port 1 (left), and from Port 2 to the input of the IQ mixer (right) with the bridge in transmission mode. RF signal is only transmitted through the pulse amplifier with the gate switch opened by the gate marker. The acquisition marker opens the acquisition switch only once the gate switch has closed. This acts as a fail-safe to prevent damage to the acquisition circuit from high-power pulses.

Secondly, an "acquisition" switch is placed before the amplifiers in the acquisition chain. This switch serves to protect the amplifiers (and particularly the sensitive and expensive LNA) from high power pulses that may be returned from the cavity. This switch is controlled by an "acquisition marker" from the AWG. For those familiar with commercial Bruker EPR spectrometers, this switch performs a similar role to the defence diode.

Without further precautions, it is possible for the user to turn on the acquisition marker before the gate marker has been turned off, putting the amplifiers in danger of being damaged from pulses passing through the open gate switch. To mitigate this, a small logic board inside the bridge ensures that the acquisition switch will not open until the gate switch has closed, and prevents the gate from opening while the acquisition is open. The action of this logic can be seen in Fig. 4.9.

4.4.2 7–12 GHz microwave bridge

The spectrometer used alongside the 2–4 GHz bridge is also compatible with X-band 7–12 GHz measurements using an existing bridge shown schematically in Fig. 4.10. It is functionally similar to the 2–4 GHz bridge, with the addition of two switches to select between a solid-state amplifier and a travelling wave tube (TWT) amplifier

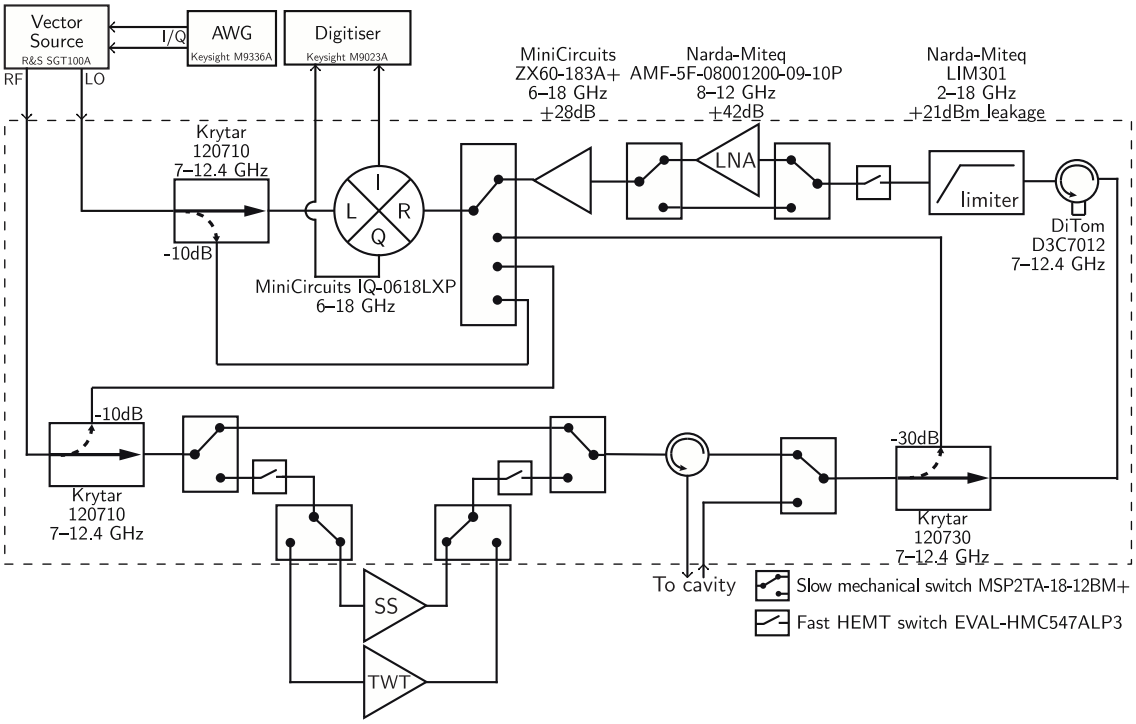

Figure 4.10: Schematic of the X-band 7–12 GHz microwave bridge which the 2–4 GHz bridge was designed to emulate to maintain compatibility with the rest of the spectrometer.

for use with conventional ESR cavities. This was omitted due to the bandwidth of the available TWTs being incompatible with low-frequency measurements.

This high frequency bridge is used for pulsed measurements using a superconducting resonator at 8 GHz in Chapter 6.

4.4.3 Two-pulse echo

Recalling the description of a two-pulse "Hahn" echo sequence from Section 2.1.2, a typical implementation of this using the ESR spectrometer is presented in Figure 4.11(a). The spectrometer uses the AWG to modulate the VSG to produce $\frac{\pi}{2}$ and π pulses with a gaussian time profile of FWHM 5 µs, to facilitate loading into a high-Q cavity, and are differentiated by their amplitude — a π pulse has $\times 2$ the voltage amplitude of the $\frac{\pi}{2}$, to produce double the B_1 field strength within the cavity.

In a two-pulse or "Hahn" spin echo sequence, an initial $\frac{\pi}{2}$-pulse rotates the Bloch vector of the spin ensemble onto the x–y plane. Due to inhomogeneity in each spin's local magnetic environment, they precess around the z axis at different rates, causing dephasing over a characteristic time T_2^*. After a time τ, a π inversion pulse

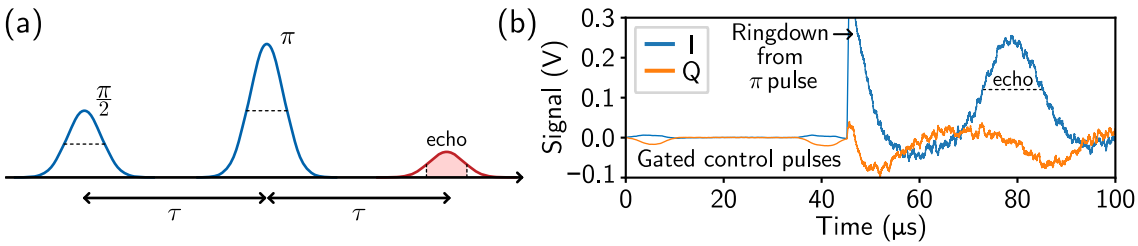

Figure 4.11: (a) A typical two-pulse Hahn sequence produced and retrieved with the ESR spectrometer for spin echo experiments. (b) Experimental realisation of a two-pulse echo sequence with a superconducting resonator, pulsing on a ^{145}Nd:Y_2SiO_5 spin ensemble at $B_0 = 326.0\,\mathrm{mT}$.

is applied which inverts the magnetisation in the x–y plane, causing the spins to refocus and reverse the time evolution. After a time 2τ the spins' magnetisations rephase and emit an echo as a detectable voltage.

To illustrate the acquisition of an echo, an example of a two-pulse echo sequence retrieved from a ^{145}Nd:Y_2SiO_5 sample and resonator (the device detailed in Chapter 6) is shown in Fig. 4.11(b), using the 7–12 GHz microwave bridge with a wait time $\tau = 35\,\mu\mathrm{s}$ and pulse width $\tau = 10\,\mu\mathrm{s}$. A 3 W amplifier connected to the bridge output provides a peak π-pulse power of approximately 3 µW into the 3D cavity. The retrieved signal is routed through the I/Q mixer, referenced to the LO of the VSG, to return the in-phase (I) and out-of-phase (Q) components. The phase of the applied pulses was adjusted to yield a spin echo predominantly in one channel (I). The high power control pulses appear weak in the retrieved signal due to the acquisition switch being open while the gate switch is closed. Shortly after 45 µs ($\tau = 35\,\mu\mathrm{s}$ plus an additional 10 µs due to the ringup and ringdown of the Gaussian pulses), the gate switch opens and acquisition switch closes, showing the high-Q resonator relaxing or "ringing down" following the pulse. As the spin ensemble refocuses, a spin echo is seen to reform around 75 µs (where the delay from being exactly 2τ is due to the ringup time of the initial $\frac{\pi}{2}$ pulse).

This basic two-pulse sequence forms an essential tool for the experiments in Chapters 6 and 7. These typically involve measuring the voltage amplitude of each spin echo, quantified by integrating over the FWHM of the echo (indicated in Fig. 4.11(b)) for either I and Q separately, or the amplitude of the signal $\sqrt{\mathrm{I}^2 + \mathrm{Q}^2}$.

Chapter 5

Continuous-wave measurements

Coupling between planar superconducting resonators and spin ensembles has previously been demonstrated for several varieties of spin system, including group V donors in silicon [50, 51], NV centres in diamond [17], ruby (Al_2O_3:Cr^{3+}) [48], molecular spins [145], and rare-earth doped crystals [45, 46, 52].

While doped silicon is frequently used as a substrate on which devices are fabricated, other spin systems are typically measured by fabricating the device on a separate silicon or sapphire substrate, and gluing or mechanically pressing the spin-doped sample onto the resonator in a *flip–chip* approach. The use of Y_2SiO_5 directly as a substrate for superconducting device fabrication has not been previously demonstrated.

This chapter investigates the suitability of Y_2SiO_5 as a substrate for fabrication of superconducting devices capable of driving ESR transitions. The dielectric loss of the Y_2SiO_5 is characterised and compared to commonly used substrates, and the coupling strength between resonator and doped ^{145}Nd electron spins is analysed, demonstrating the viability of fabricating on Y_2SiO_5 for performing ESR with rare-earth doped crystals.

5.1 Device

The device is a lumped-element superconducting resonator, fabricated on a Czochralski-grown single crystal of Y_2SiO_5 [32] doped with 10 ppm ($2 \times 10^{23}\,\mathrm{m}^{-3}$) isotopically purified ^{145}Nd. Neodymium was used for these initial experiments as its anisotropic ESR properties have been well studied, its preferential doping into Y_2SiO_5 site 1 simplifies analysis of its ESR spectra, and because samples suitable for fabrication were readily available. The crystal was cut into a 5 mm×5 mm×460 µm chip along the principal dielectric axes (D_1, D_2, b) and a face perpendicular to b was polished for thin-film growth.

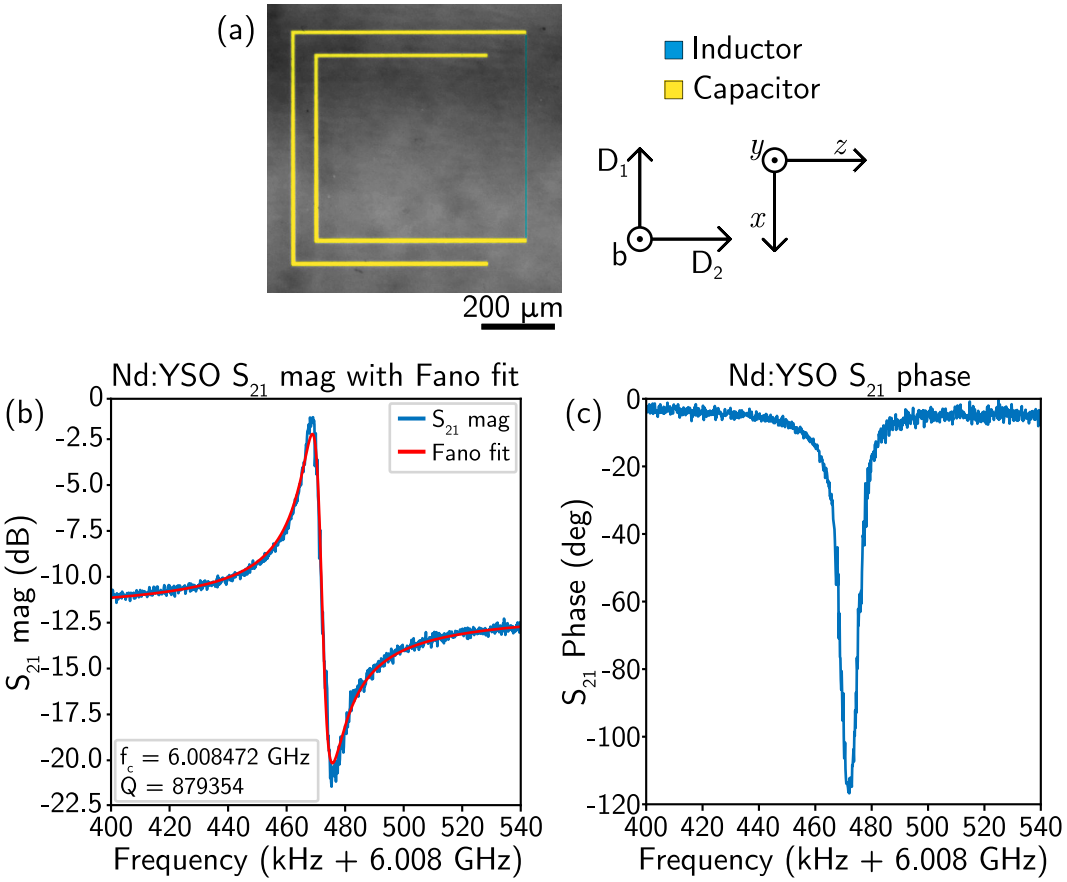

Figure 5.1: (a) False-colour micrograph of the superconducting thin-ring resonator on ^{145}Nd:Y_2SiO_5 substrate. The 2 µm inductive wire is highlighted in blue, the capacitor arms in yellow. The approximate alignment of the (D_1, D_2, b) crystal frame and (x, y, z) magnet frame are indicated. The S_{21} transmission through the measurement setup for an applied MW power of −75 dBm into the 3D cavity, showing the resonance of the NbN resonator in (b) magnitude and (c) phase, measured at zero applied magnetic field. The lineshape of the resonance deviates from a Lorentzian due interference between the resonant modes of the NbN resonator and 3D cavity, resulting in an asymmetry described by a Fano resonance [71, 72]. A fit to the S_{21} magnitude yields the centre frequency $f_c = 6.008\,472$ GHz and quality factor $Q = 880$k for −75 dBm into the cavity. This device was measured at a mixing chamber temperature of 10 mK.

The resonator is a "thin-ring" design [34, 121] described in Section 3.2, consisting of a 2 µm wire which functions as an inductor due to the constriction increasing the contribution of kinetic inductance, and a pair of 10 µm thick capacitive arms separated by a 50 µm gap. The use of narrow features increases the resilience of the resonator to applied magnetic field, and the large gap between the capacitive arms reduces the peak electric field of the resonator decreasing its susceptibility to dielectric losses from two-level systems. This forms a lumped-element resonator seen in the micrograph in Fig. 5.1(a) which generates an oscillating B_1 magnetic field around the inductor which can drive ESR transitions.

Fabrication consisted of 40 nm of sputtered NbN being patterned by photolithography using a photomask and a SF_6/Ar reactive ion etch process. The patterned chip was enclosed within a 3D copper cavity as described in Section 4.1 to suppress spontaneous emission from the resonator to the environment [50]. This was installed in the bore of a vector magnet in the NPL dilution refrigerator (see Section 4.3.2) at 10 mK (measured at the mixing chamber plate).

5.1.1 Resonator properties

Continuous wave (CW) measurements of the device were performed using a Rhode & Schwarz ZNB vector network analyser (VNA). This provides a microwave excitation at a calibrated frequency f and power P into the input line of the fridge, and measures the amplitude and relative phase of the returned signal along the detection path expressed as the complex transmission scattering parameter $S_{21}(f)$.

A typical zero-field S_{21} measurement of this device is shown in Fig. 5.1(b, c). The resonant mode of the NbN resonator appears on top of the background transmission of the 3D cavity. Naïvely one would expect a peak in transmission at the resonant frequency as the resonator forms an additional path between the antennae of the 3D cavity, however due to interference between the resonant modes of the resonator and cavity an asymmetry is introduced and the $|S_{21}|$ takes the form of a Fano resonance as described in Section 2.2.4.

Fitting Eqn. 2.11 to the measured $|S_{21}|$, shown in Fig. 5.1(b), yields a centre frequency of $f_c = 6.008$ GHz a quality factor $Q = \frac{f_c}{\Delta f}$ of the order 10^6 at high powers. However, the regime of interest for quantum applications is at low temperature and low power. In the next section we investigate the effect of dielectric losses in this regime, and its limit on the quality factor of the device.

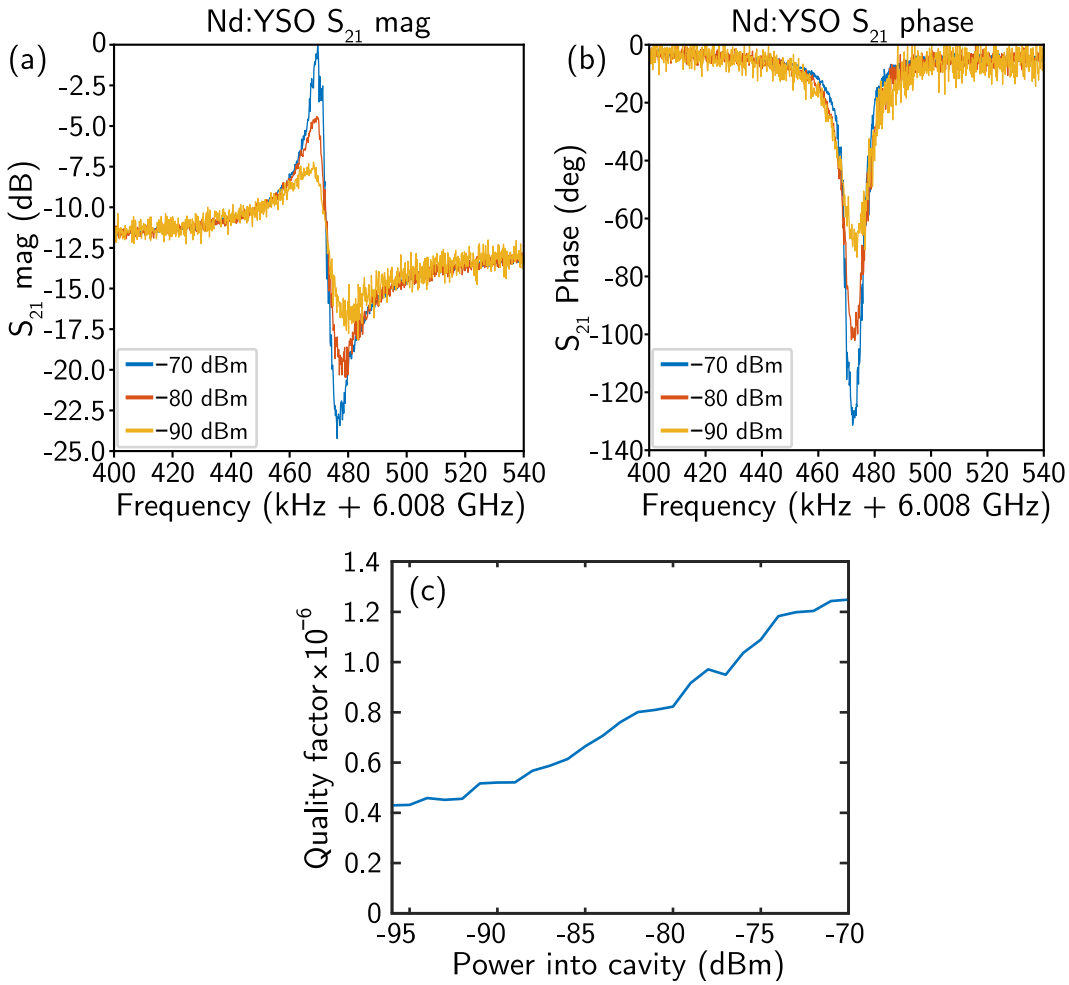

Figure 5.2: Power dependence of the resonant mode of the NbN resonator at 10 mK in (a) S_{21} magnitude and (b) S_{21} phase at zero applied magnetic field. The prominence and quality factor of the resonance decreases with decreasing applied MW power, due to the saturation of two-level systems (TLS) at higher powers [116]. The dependence of quality factor on applied power is shown in (c). As the power in the resonator approaches the low power single-photon limit, the dielectric loss from TLS becomes maximal and the TLS-limited quality factor reaches $Q = 400$k.

5.2 Dielectric loss

In the low temperature, low power regime, the primary source of dissipation in superconducting resonators typically comes from dielectric loss — two-level systems (TLS) near the device which absorb energy from the resonator. At high temperatures and at high powers, these TLS become saturated and contribute relatively less to the energy dissipation of the device. This increases the intrinsic quality factor Q_i, increasing the measured Q_tot if the quality factor is not limited by radiative or coupling losses in Eqn. 3.1.

The effect of saturating TLS at high power can be seen in Fig. 5.2(a, b). At high powers the resonance has a large prominence and narrow linewidth, but as the power is reduced the contribution of TLS to the dissipation becomes more significant, reducing the resonator's quality factor. In the regime where the mean photon number in the resonator is low $\langle n \rangle \approx 1$ the quality factor becomes constant as it is maximally limited by TLS. A sweep of fitted quality factor vs. applied power is shown in Fig. 5.2(c), where at the lowest applied powers the quality factor reaches a constant limit at $Q \approx 400\mathrm{k}$.

The temperature dependence of TLS loss, discussed in Sec. 3.1.1, is due to the difference in population between the two states of the TLS. Hence at elevated temperatures the TLS absorb less power and contribute less to the dielectric permittivity, giving rise to a decrease in resonator frequency with decreasing temperature. This was measured with a VNA set to track the peak resonance frequency as the temperature of the dilution refrigerator's mixing chamber was raised by applying a current to a resistive coil anchored to the stage, giving the data presented in Fig. 5.3.

This frequency shift can be used to extract information about the dielectric loss in the substrate, by fitting Eqn. 3.2 to the data in Fig. 5.3. Only the linear section of the data, shown in green, is used for the fit, as the parameter $\tan\delta$ is most sensitive to the gradient of this section. This fit parametrises the dielectric loss with the loss-tangent $\tan\delta = 4 \times 10^{-6}$.

This loss-tangent is comparable to resonators fabricated on sapphire [103], a substrate routinely used to minimise dielectic loss and reach high quality factors. This indicates Y_2SiO_5 is well-suited for fabrication of superconducting devices incorporating resonators and qubits which are typically susceptible to dielectric losses from TLSs [146], while also incorporating doped spins for cavity QED.

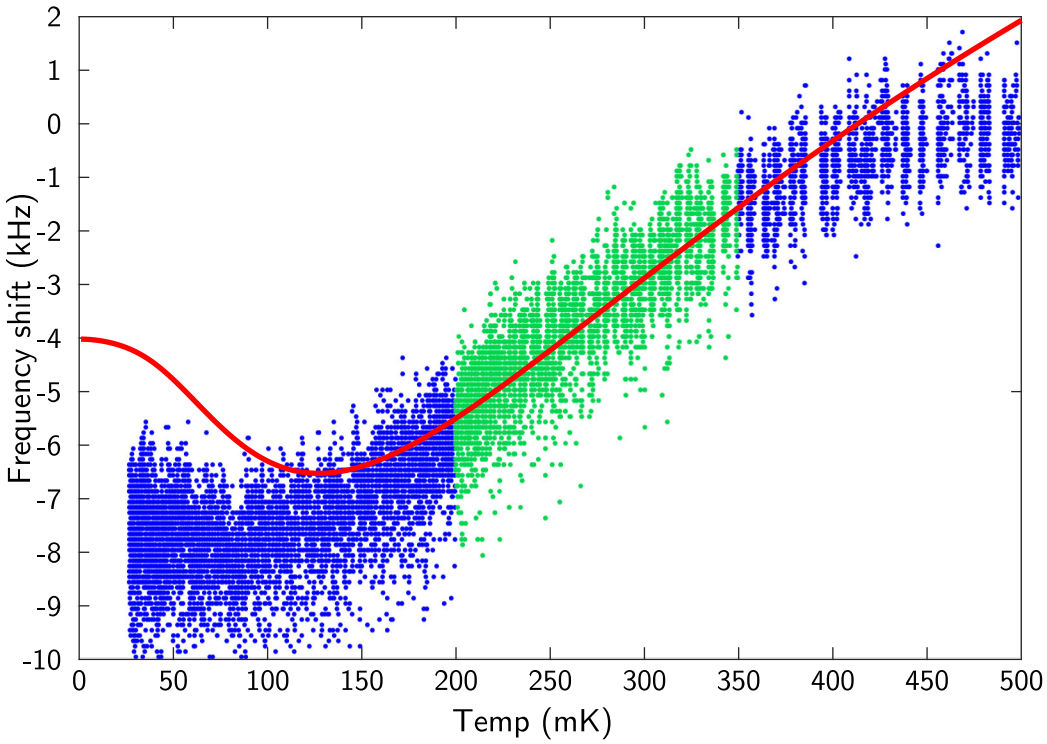

Figure 5.3: Frequency shift of resonator as function of temperature at the mixing chamber, from which a fit to theory [103] (red) of the gradient of the linear section (green) yields the loss-tangent $\tan\delta = 4 \times 10^{-6}$.

5.3 ESR measurements

5.3.1 Magnetic field alignment

Having studied the resonator, we now use it to perform ESR to characterise the Nd spins in the Y_2SiO_5 that are coupled to the resonator. This resonator design is resilient to out-of-plane magnetic fields up to 5 mT [121], which is not sufficient to drive ^{145}Nd ESR transitions at 6 GHz, so the magnetic field was restricted to be applied within the plane of the superconducting thin film (which is close to the D_1–D_2 plane of the crystal) which this resonator design has proven resilient to up to 2.6 T [121].

To determine the orientation of the magnetic field, a 5 mT field was applied along the x magnet axis, near the D_1 crystal axis. This shifts the frequency of the resonator downward due to an increase in the kinetic inductance of the NbN film. The misalignment between the x magnet axis and the superconducting plane was then found by applying small fields along y to maximise the resonator frequency, corresponding minimising the out-of-plane field due to the relationship between

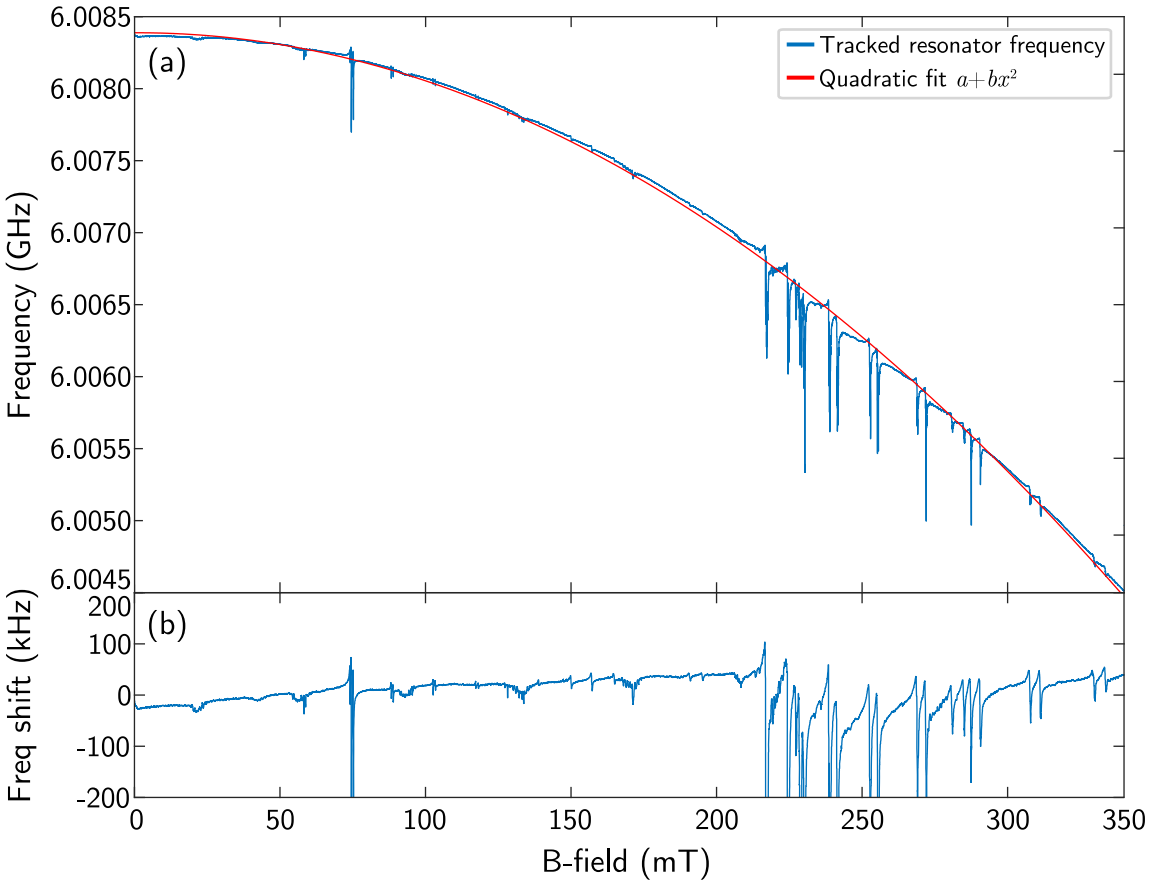

Figure 5.4: Trace of the resonator frequency, tracked by a VNA monitoring the position of the resonance peak, as an applied B-field is swept in the superconductor plane close to the D_1 crystal axis. (a) shows a quadratic background shift in resonator frequency, which can be fitted to and subtracted. The result (b) is an ESR trace where a strong interaction with resonant spins causes a dispersive shift in the frequency of the resonator.

kinetic inductance and magnetic field (see Section 3.1.2). Repeating this procedure by applying a perturbing field along y for a main field component along z identifies two vectors along the superconducting plane, sufficient to fully identify the (x, y, z) components needed to restrict the applied field to be in-plane and minimise magnetic flux threaded through the superconductor.

5.3.2 Measuring an ESR spectrum

To measure the interaction of electron spins with the resonator, the magnetic field B_0 was continuously swept at a rate of $3\,\mathrm{mT\,min^{-1}}$ from 0 mT–360 mT in the plane of the NbN film at an angle close to the D_1 crystal axis.

The resonator was tracked with a VNA set to a fast measurement bandwidth of 1 MHz with 10 000 points per trace over a frequency span of 2 MHz. By setting a marker on the VNA to track the max $|S_{21}|$, the shift in resonant frequency could be monitored with a precision of 200 Hz at a rate of 2 measurements per second. To account for the short acquisition time due to the fast bandwidth, a high power of −45 dBm into the cavity was used to increase signal-to-noise.

Applying a magnetic field the resonator increases its kinetic inductance due to the reduction in Cooper pair density, as discussed in Section 3.1.2. As a result its resonant frequency shifts downward quadratically with applied field. To account for this in the measurement, after every 1 mT step the centre of the VNA measurement span would be set to the median of the previous 10 measured frequencies, allowing the VNA to track the resonator beyond its original measurement window. Then by simultaneously measuring the magnetic field and VNA marker frequency, a trace of resonator frequency vs. applied field can be built up. Occasional spurious data where noise caused a stray point to have a higher prominence than the resonator and be picked out as the maximum of the S_{21} trace can be filtered out with a moving 3-point median filter.

An example of such a trace is shown in Fig. 5.4(a). The quadratic shift is an effect of the magnetic field directly on the superconductor itself, so by fitting to a quadratic (shown in red), this can be subtracted leaving only the shift in frequency due to other effects, shown in Fig. 5.4(b), predominantly due to a dispersive interaction between the ^{145}Nd electron spin and the resonator.

Simulating the site 1 ^{145}Nd spin system with Easyspin as described in Sec. 2.3, a Breit-Rabi diagram showing energy levels vs. applied B_0 field along D_1, shown in Fig. 5.5(a), shows how the ESR transitions coming into resonance with the 6.008 GHz resonator match up with fields at which an avoided crossing is observed in Fig. 5.5(b). A breaking of the Y_2SiO_5 subsite degeneracy is observed in the experimental ESR spectrum, indicating the B_0 field is not quite being applied within the D_1–D_2 plane, hence that there is a misalginment between the crystal axes and the superconductor plane — the Y_2SiO_5 wafer has not been polished perfectly perpendicular to the b crystal axis.

An additional set of weaker transitions are observed at lower B_0-fields. These can be attributed to site 2 of ^{145}Nd:Y_2SiO_5, and the weaker prominence on the ESR spectrum is due to the preferential doping of ^{145}Nd into site 1.

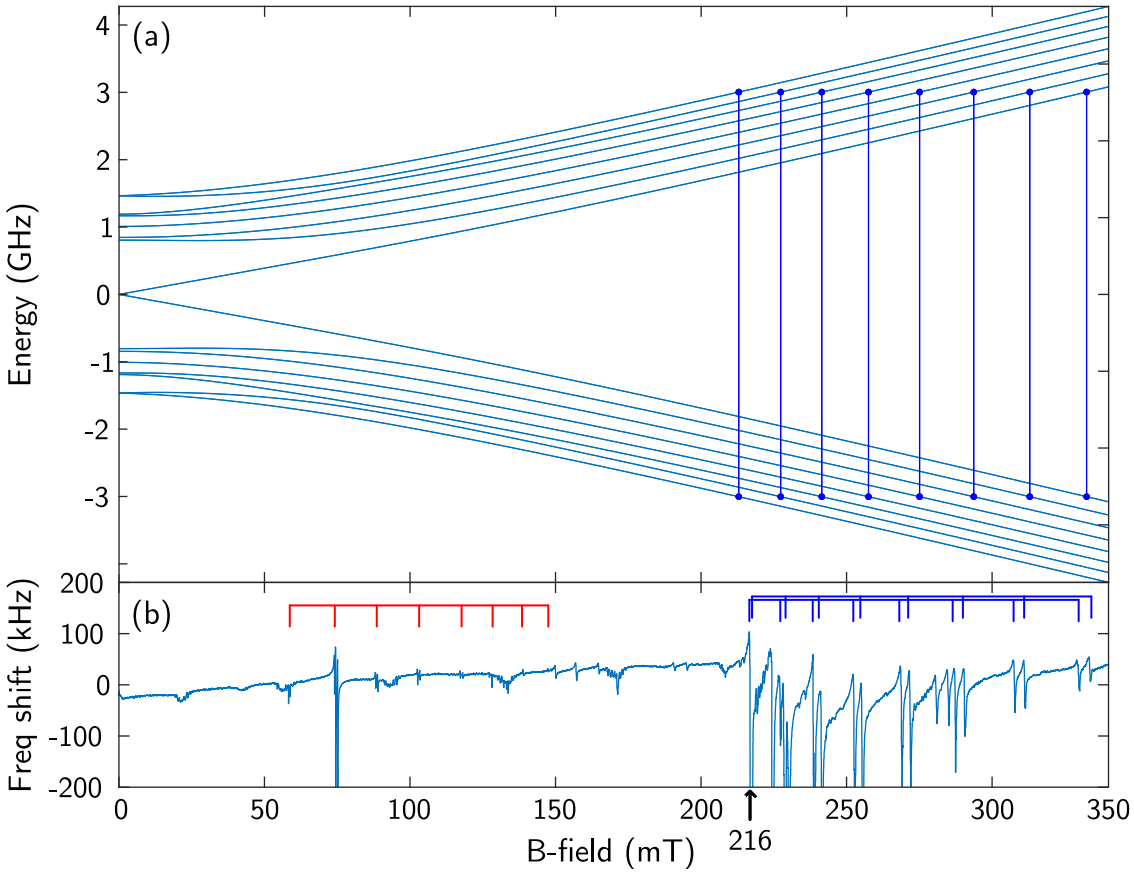

Figure 5.5: (a) Breit-Rabi diagram of ^{145}Nd in Y_2SiO_5 for magnetic field B_0 oriented along D_1, with ESR transitions at 6.008 GHz indicated. (b) ESR spectrum with the magnetic field B_0 oriented along D_1, as measured with a VNA tracking the resonator centre frequency. The quadratic dependence of resonator frequency with applied magnetic field has been subtracted. Transitions from Site 1 are indicated in blue, Site 2 in red. Two sets of site 1 transitions are seen due to a broken sub-site degeneracy. An additional set of unidentified transitions whose angular dependence do not match ^{145}Nd are observed in the ESR spectrum, as indicated in Fig. 5.6. The avoided crossing studied in Section 5.4 is indicated at $B_0 = 216$ mT, corresponding to the $m_I = \frac{7}{2}$ ESR transition of ^{145}Nd.

5.3.3 Anisotropic ESR roadmap

By measuring several ESR traces as described in the previous section for a range of B_0 field angles over 0°–180° in 10° steps in the superconducting plane, the ESR spectrum is seen to shift due to the anisotropy of the Y_2SiO_5 crystal. Plotting these transitions as a function of field angle forms a *roadmap*, shown in Fig. 5.6. To create this, positions of avoided crossings on each ESR trace were marked on both an upsweep and downsweep of magnetic field, and the mean of the field strengths for features which were marked on both sweeps was added to the plot.

With this roadmap and the individual ESR spectra for each field angle, it is possible to identify what observed transition corresponds to which spin species. The first clue to identify spin species is whether the number of transitions matches the number of hyperfine levels — eight in the case of ^{145}Nd. At mK temperatures, the polarisation of the population toward the ground state (shown in Fig. 5.8) should also encode itself in the transition strength, seen in the progressive weakening of transitions with increasing field in Fig. 5.5(b) where the $m_I = +\frac{7}{2}$ transition from the ground state at 216 mT is strongest.

Next we can factor in the roadmap, by comparing the fields at which transitions are observed to simulation from the ESR tensors. This identifies the crystal orientation, by looking for angles at which the g-factor changes significantly, and for a splitting of the sub-site degeneracy, indicating the extent to which the field is misaligned from D_1–D_2 or b, as we observe in Fig. 5.5(b) where the eight hyperfine levels split into sixteen. Finally, if a transition does not follow the angular dependence expected from simulation this is a good indication that this transition is not due to the spin species being simulated.

Applying these methods identify both ^{145}Nd site 1 (in blue, for which both the Zeeman $\boldsymbol{g}$ and hyperfine $\boldsymbol{A}$ tensors are available) and ^{145}Nd site 2 (red, with only the Zeeman $\boldsymbol{g}$ tensor available) in the roadmap and spectrum.

There were two additional transitions marked in green and black, whose strength and angular dependence set them aside from the ^{145}Nd transitions. These could not be positively identified from simulation of other rare-earth species for which ESR data was readily accessible including erbium and ytterbium, but could potentially arise from iron group impurities in the Y_2SiO_5 [44].

The data also appear to include a series of regularly-spaced magnetic fields where the resonator prominence and frequency decreased due to an increased loss, seen in Fig. 5.7(a) for the trace at 0°. These had a much wider linewidth ~5 mT than the other observed transitions, were repeatable for sweeping up and down in field,

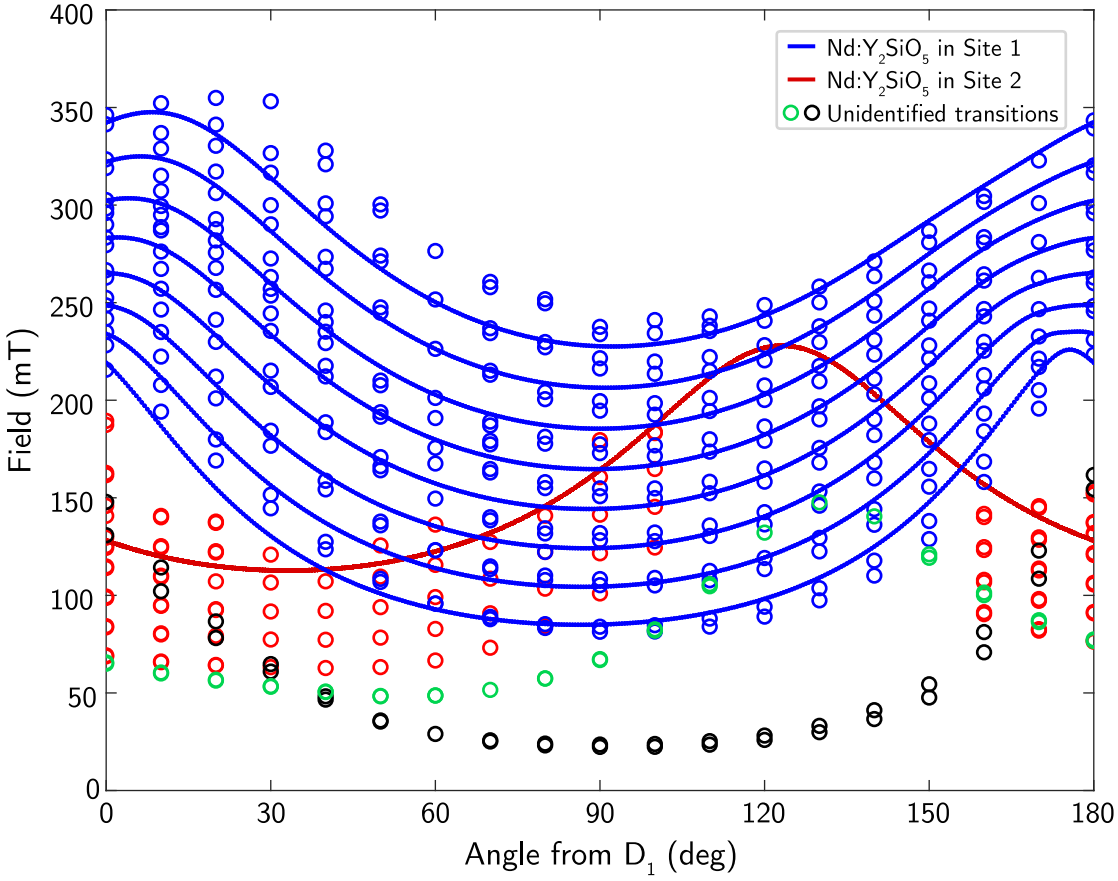

Figure 5.6: Roadmap of ESR transition fields with respect to the B_0 angle from the D_1 axis, in the D_1–D_2 plane. Circles mark the positions of transitions from traces such as in Fig. 5.5, with Site 1 in blue and Site 2 in red. Signals from site 2 between 110°–150° could not be resolved due to weak transition amplitudes at these angles. Lines represent simulated data assuming an ideal rotation about the crystal b axis. For Site 2 we only show one line as only the g-tensor is known for this site. Green and black represent as yet unidentified impurities.

and did not appear hysteretic. This, alongside its apparent angular dependence in Fig. 5.7(b), could be consistent with additional resonant transitions from impurities in the substrate.

The purpose of this roadmap is to ensure ESR transitions can be positively identified by comparing their angular dependence to simulations and bulk ESR data, ensuring further analysis of spin–resonator coupling properties can be clearly linked to a particular spin species. We now focus on one strong ^{145}Nd site 1 transition to quantify the strength of the resonator–spin coupling.

5.4 Resonator–spin coupling

The highest intensity transition in ^{145}Nd site 1 was seen at $B_0 = 216\,\mathrm{mT}$ along D_1, corresponding to an ESR transition from the ground state with $m_I = +\frac{7}{2}$. With 50 % of the electron and nuclear population in the ground state at 10 mK, calculated from the Boltzmann distribution over ^{145}Nd's sixteen energy levels and shown in Fig. 5.8, this transition was a promising candidate for maximising the coupling strength between resonator and electron spin.

5.4.1 Avoided crossing

To characterise the coupling, a detailed scan of the avoided crossing around $B_0 = 216\,\mathrm{mT}$ was taken. A VNA was set up to measure the S_{21} of the resonance around 6.007 GHz with a 5 MHz span, measuring 20 001 points at a bandwidth of 10 kHz. The power used corresponded to −50 dBm into the cavity, with 8 averages to improve signal-to-noise. The B_0 field was swept from 210 mT–224 mT in 20 µT steps, with a VNA trace taken at each field.

By plotting the $|\mathrm{S}_{21}|$ of the resonance in Fig. 5.9, we confirm the onset of an avoided crossing due to spin–resonator interaction as tracked by the faster measurements presented in Sec. 5.3.2. As the field increases, the resonator tunes down in frequency due to the shift in kinetic inductance, and the ESR transition tunes up (indicated by the almost flat white line around 216.4 mT). As the two approach in frequency, a non-resonant dispersive interaction between resonator and spin causes the resonance to shift in frequency away from the spin transition, as can be seen in cuts (b) and (d). The resonance linewidth is also seen to broaden and the prominence drops compared to a cut (a) taken further from the resonance, indicating the spins are contributing significantly to the losses of the combined resonator–spin

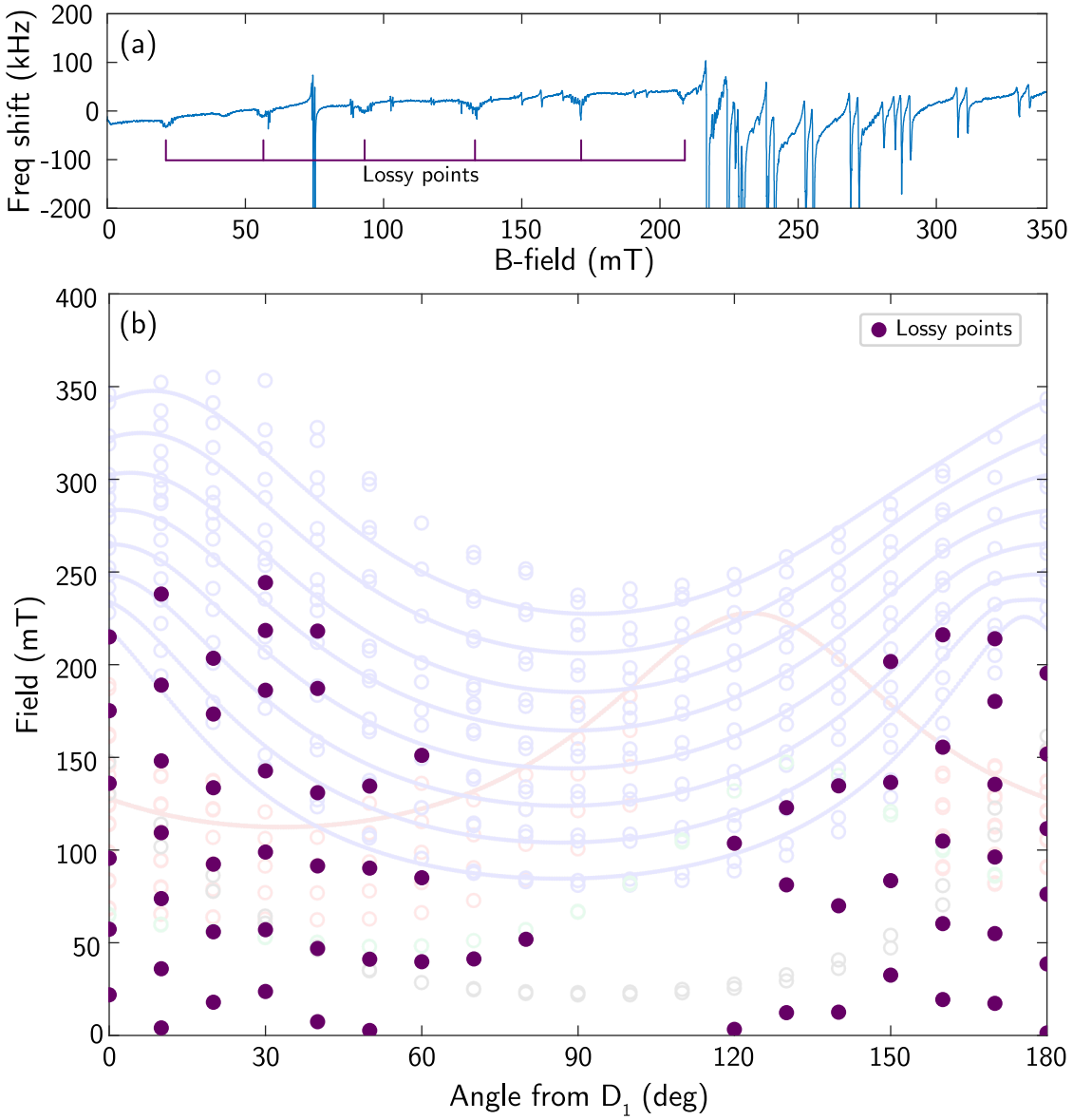

Figure 5.7: (a) Regularly spaced lossy points in seen in the ESR spectrum. These were seen at different fields for many angles of the sweep; the trace shown here is at 0°. (b) Identifying the lossy points on all the traces produces a roadmap of these features, shown over the ESR roadmap from Fig. 5.6. While some angular dependence is apparent, the exact relationship of these features with field angle is not obvious.

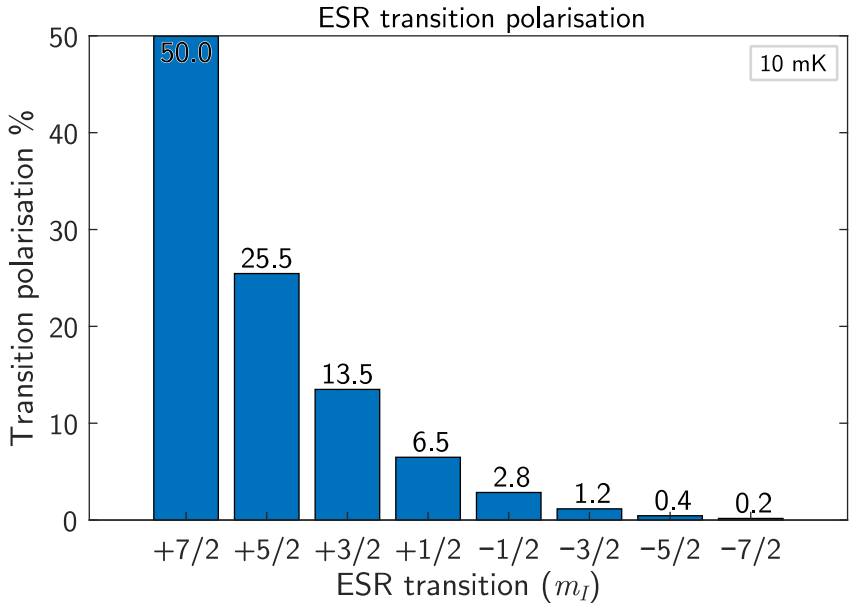

Figure 5.8: Spin polarisation of the eight ESR transitions, calculated from the Boltzmann distribution for the sixteen energy levels of ^{145}Nd at 216 mT along D_1 at 10 mK. The $m_I = +\frac{7}{2}$ transition from the ground state contains 50 % of the spin population, giving this transition a high intensity compared to transitions from excited nuclear states.

system, and hence the decoherence rate of the spins γ_s is greater than that of the resonator κ_c.

A characteristic of the strong coupling regime is the vacuum Rabi splitting, where the modes of the resonator and spin hybridise when on-resonance, and two modes are seen simultaneously separated by the vacuum Rabi frequency $\Omega = 2g_{ens}$ determined by the the coupling strength g_{ens} between resonator and spin ensemble. A cut (c) at 216.4 mT of Fig. 5.9 shows that the peak disappears on-resonance due to losses from the spin ensemble broadening the resonance and reducing its prominence. This suggests the strong coupling regime is not reached as this would require the resolution of two peaks separated by $2g_{ens}$, however the clear onset of an avoided crossing indicates a high cooperativity between resonator and spin nonetheless.

5.4.2 High-cooperativity coupling

Without a visible vacuum Rabi splitting, which would allow the coupling strength to be read off directly from the vacuum Rabi frequency, the coupling parameters, namely the ensemble coupling strength g_{ens} and inhomogeneous spin ensemble half-

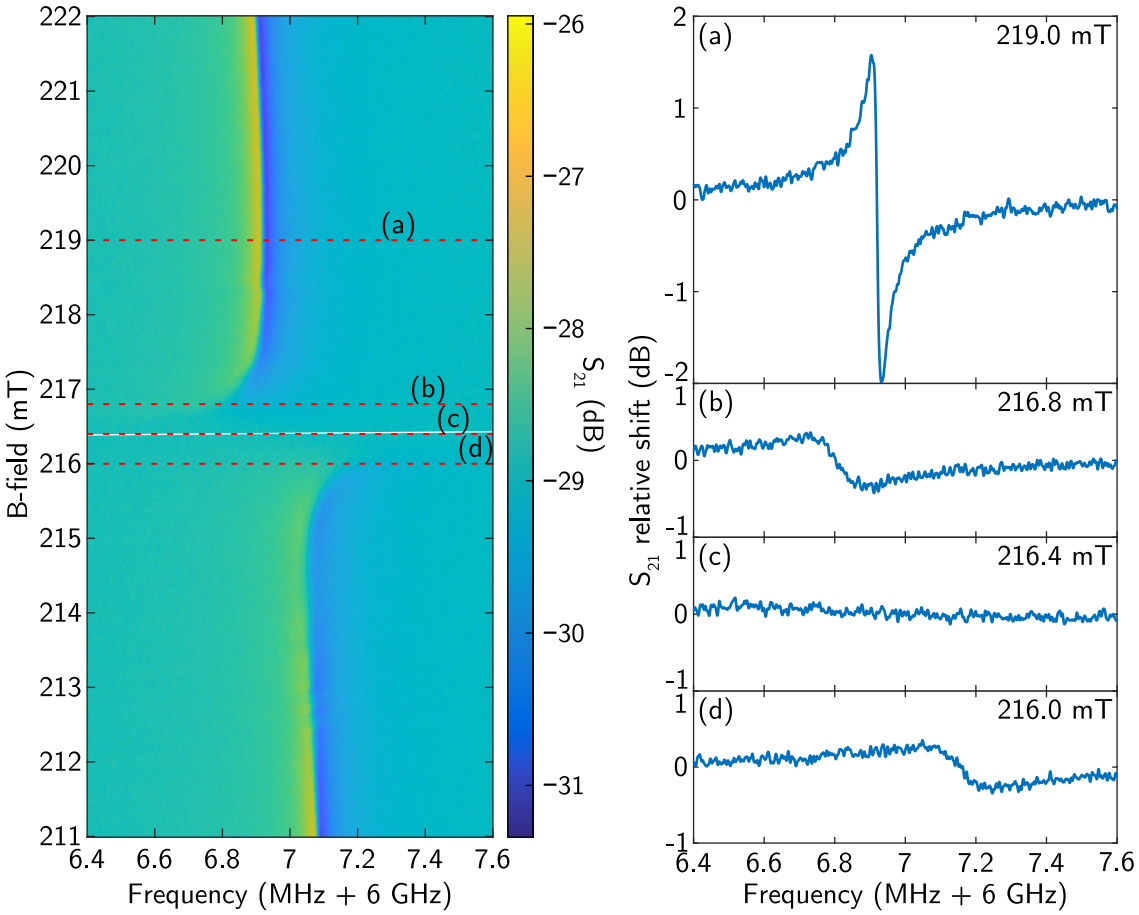

Figure 5.9: Left: the onset of an avoided crossing measured in the S_{21} magnitude by a VNA, at $B_0 = 216\,\mathrm{mT}$ along D_1 corresponding to the $m_I = \frac{7}{2}$ ESR transition of ^{145}Nd. Increasing strength of the B-field shifts the resonator frequency downward, while the frequency of the ESR transition increases (white line). A dispersive shift in the resonator frequency is seen as the two are brought in resonance. (a, b, c, d) show cuts across the 2D plot at fixed B-fields, with the background transmission subtracted. Cuts (b) and (d) show the dispersive frequency shift. Cut (c) shows the centre of the avoided crossing where resonator and electron spin frequencies are in resonance, where prominence of the resonance is reduced enough to no longer be resolvable.

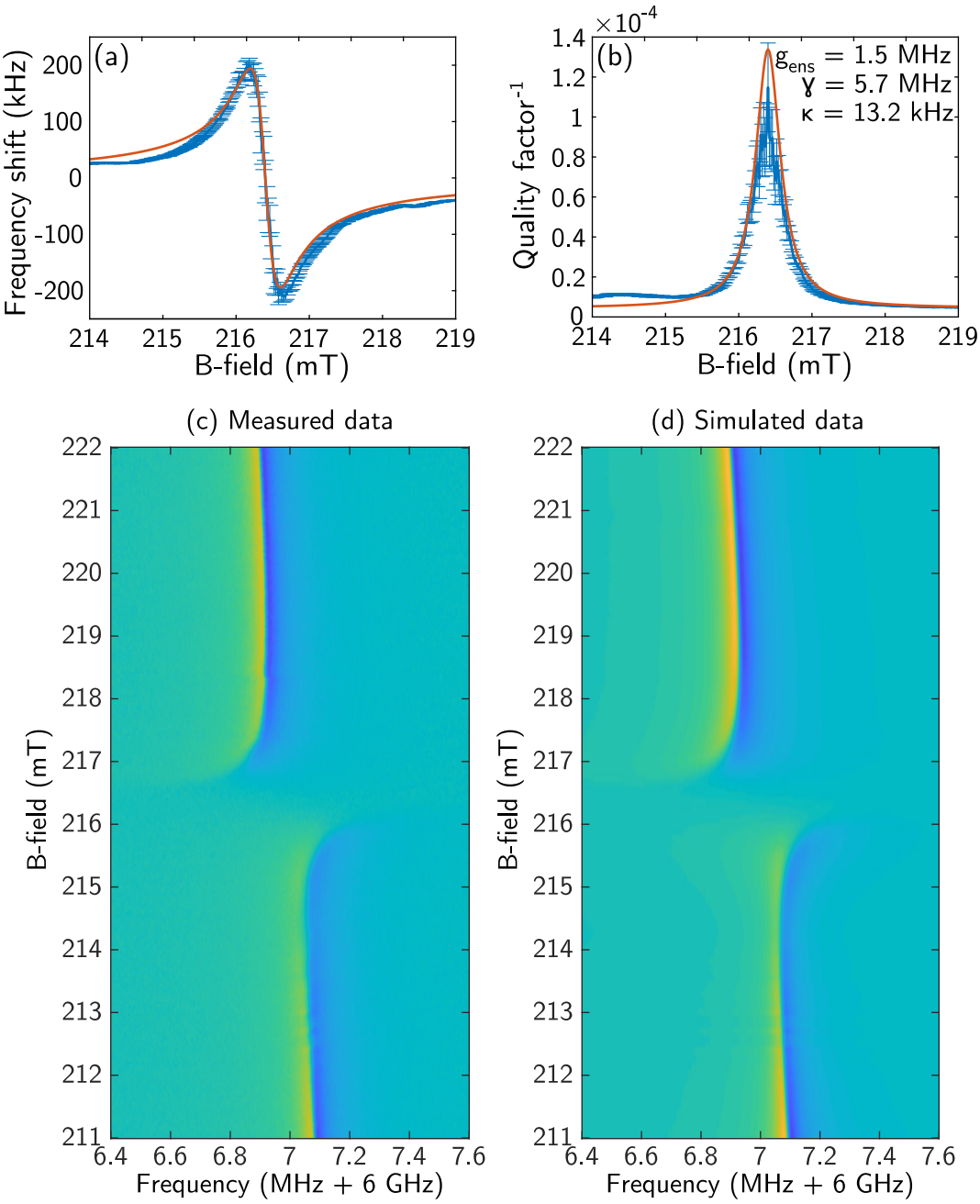

Figure 5.10: Fitting to (a) the resonator frequency ω and (b) inverse quality factor at each field point allows us to extract the coupling strength $g_{\mathrm{ens}}/2\pi = 1.5\,\mathrm{MHz}$ and spin linewidth $\gamma_{\mathrm{s}}/2\pi = 5.7\,\mathrm{MHz}$ for this ESR transition. Combined with the resonator linewidth far detuned from spins of $\kappa_{\mathrm{c}}/2\pi = 13.3\,\mathrm{kHz}$ this yields a high cooperativity $C = \frac{g_{\mathrm{ens}}^2}{\kappa\gamma} = 30$. Beneath is a comparison between (c) the measured data and (d) simulated data of the avoided crossing given the extracted coupling parameters.

width γ_s can be extracted from a fit to the resonance frequency and linewidth of the avoided crossing.

To perform this fit, first the resonator half-width in the absence of spins κ_c can be extracted directly from fitting a Fano resonance to the resonator far from the avoided crossing at 224 mT. This yields a resonator half-width of $\kappa_c/2\pi = 13.2\,\text{kHz}$.

The same Fano fit is then performed for each magnetic field point from 210 mT–224 mT. The quadratic shift due to the change in kinetic inductance of the NbN film is subtracted, leaving only the dispersive shift in resonator frequency due to spin interaction in Fig. 5.10(a) and the decrease in quality factor of the resonator in Fig. 5.10(b).

With the frequency and linewidth of the resonator as a function of B_0-field, we can now fit to Eqns. 2.13 parametrising these in terms of g_{ens} and γ_s:

$$\omega = \omega_c - g_{\text{ens}}^2 \frac{\Delta}{\Delta^2 + \gamma_s^2}$$
$$\kappa = \kappa_c + g_{\text{ens}}^2 \frac{\gamma_s}{\Delta^2 + \gamma_s^2}$$

where $\Delta = m_0(B - B_0)/\hbar$ is the field detuning calculated from the spin magnetic moment $m_0 = \hbar \frac{d\omega}{dB_0}$.

A fit to the resonance frequency ω and linewidth κ as a function of B yields the red curve in Fig. 5.10(a, b) with the coupling parameters $g_{\text{ens}}/2\pi = 1.5\,\text{MHz}$, $\gamma_s/2\pi = 5.7\,\text{MHz}$, and $\kappa_c/2\pi = 13.2\,\text{kHz}$.

Using these values to simulate the $|S_{21}|$ data for the resonance across the avoided crossing shows a close agreement between measured and simulated data in Fig. 5.10(c, d). These parameters match up with the qualitative conclusion from the previous section, that $\gamma_s > \kappa_c$, and that the conditions for strong coupling are not met in this device as $g_{\text{ens}} < \gamma_s$. However g_{ens} is sufficiently close to γ_s and greater than κ_c that the cooperativity $C = \frac{g_{\text{ens}}^2}{\kappa_c \gamma_s} = 30 > 1$ meets the conditions for high-cooperativity.

5.5 Discussion

This chapter has demonstrated the suitability of Y_2SiO_5 as a substrate for fabrication of high-quality superconducting devices. We fabricated a viable high-Q NbN resonator with low-power $Q = 400\,000$ and measured its loss tangent $\tan\delta = 4 \times 10^{-6}$ to be comparable to sapphire. In Section 5.3.2 we develop methods for measuring the anisotropic ESR spectra exhibited by rare-earth doped

Y_2SiO_5, and focusing on one ESR transition in ^{145}Nd we demonstrate the coupling between resonator and spin ensemble meets the conditions for high cooperativity $C = \frac{g_{\mathrm{ens}}^2}{\kappa_{\mathrm{c}}\gamma_{\mathrm{s}}} = 30$.

The coupling parameters $g_{\mathrm{ens}} = 1.5\,\mathrm{MHz}$, $\gamma_{\mathrm{s}} = 5.7\,\mathrm{MHz}$, and $\kappa_{\mathrm{c}} = 13.2\,\mathrm{kHz}$ indicate the coupling regime is limited by the spin linewidth $\gamma_{\mathrm{s}} > g_{\mathrm{ens}}$. Equivalently, the Nd spin ensemble is decohering at a faster rate than excitations are being exchanged between it and the resonator, such that photons can be coherently written from the resonator to the spin ensemble but tend to decohere before they are re-emitted from the spin ensemble to the resonator.

Some options are available for improving the cooperativity of the device. A more strongly doped rare-earth sample would increase the ensemble coupling strength $g_{\mathrm{ens}} \sim \sqrt{\rho}$ for spin density ρ, an option which we pursue in the next chapter where we move on from CW measurements to apply pulsed ESR methods to measure properties of the resonator–spin system. Alternatively we can exploit coherence-enhancing ZEFOZ transitions in REIs [14] to decrease γ_{s}, the possibility of which is discussed further in chapter 7.

Chapter 6

Pulsed ESR spectroscopy

Having demonstrated the viability of fabricating superconducting devices on Y_2SiO_5, and the high-cooperativity coupling to spins doped within the substrate, we progress from CW frequency-domain measurements to perform pulsed ESR spectroscopy of electron spins at mK temperatures via superconducting resonators.

Frequency-domain measurements of high-cooperativity coupling between spins and a superconducting resonator have previously been demonstrated for a number of spin systems, such as NV and P1 centres in diamond [17, 48, 147], phosphorus donors in silicon [51], molecular spins [145], and rare-earth doped crystals [34, 46, 52].

Performing time domain or pulsed measurements in this regime is much less studied. Prior work includes time-resolved measurements of NV centres by Johannes Majer's group [148] and two-pulse spectroscopy of phosphorus-doped silicon [149] in Hans Huebl's group. These publications focus on specific results in the high-cooperativity regime, but give less detail on the challenges and methods of performing pulsed ESR in such a system.

Operating in the high-cooperativity regime presents additional challenges over standard ESR measurements, due to the strong interaction between resonator and spin, and the resulting dispersive frequency shift of the resonator. The purpose of this chapter is to develop methods and tools for performing pulsed spectroscopy in this regime with a superconducting resonator, and to use these methods to facilitate measuring coherence properties of ^{145}Nd:Y_2SiO_5 spins in the substrate and their dependence on experimental parameters.

6.1 Device

For these experiments, a similar "thin-ring" resonator to that used in Chapter 5 was fabricated on a single crystal of Y_2SiO_5 doped with 200 ppm ($4 \times 10^{24}\,\mathrm{m}^{-3}$)

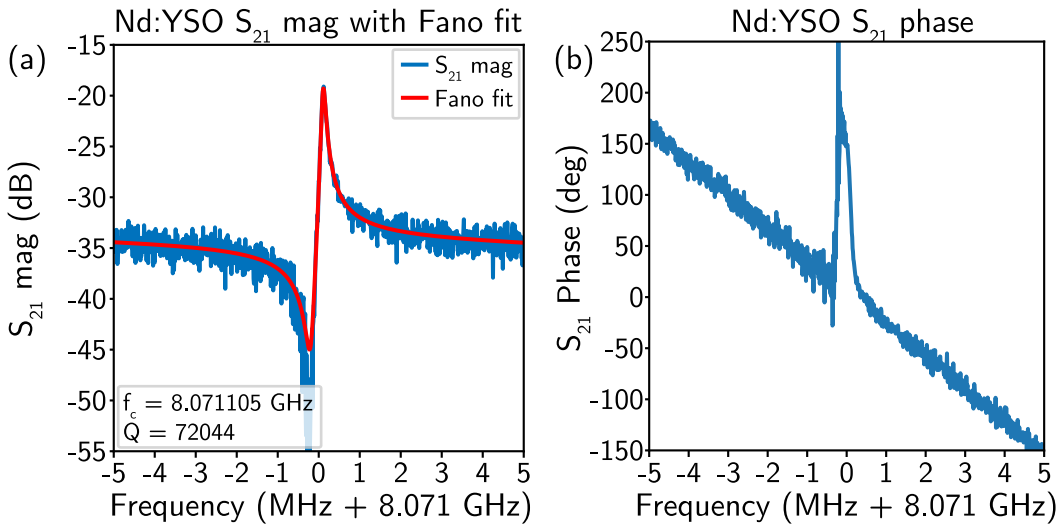

Figure 6.1: S_{21} transmission through the cavity for a MW power of $-105\,\mathrm{dBm}$ into the 3D cavity is shown in (a) magnitude and (b) phase for zero applied magnetic field. A Fano fit to the resonance magnitude $|S_{21}|$ using Eqn. 2.11 yields the centre frequency $f_c = 8.071\,\mathrm{GHz}$ and quality factor $Q_{\mathrm{tot}} = 72\,000$.

isotopically purified ^{145}Nd, a 20× increase in spin concentration from the previous chapter in order to increase the ensemble coupling strength g_{ens} to assist performing pulsed ESR in a high-cooperativity regime. The crystal was cut into a $5.0\,\mathrm{mm}\times5.0\,\mathrm{mm}\times2.7\,\mathrm{mm}$ chip, with the NbN resonator patterned by mask photolithography. The device was installed in the LCN dilution refrigerator described in Section 4.3.3 at a base temperature of 13 mK measured at a sample holder thermally anchored to the 3D copper cavity. Measurements in this chapter use the 4–8 GHz output line of the fridge.

6.2 CW characterisation

The resonator was probed with a Copper Mountain C2209 VNA to measure its transmission at zero applied magnetic field. Its S_{21} response is plotted in Fig. 6.1. The resonance profile again takes a Fano lineshape, and fitting to $|S_{21}|$ using Eqn. 2.11 gives its centre frequency $f_c = 8.071\,\mathrm{GHz}$ and quality factor $Q = 72\,000$ for power $P_{\mathrm{VNA}} = -45\,\mathrm{dBm}$ output from the VNA, corresponding to approximately $P_{\mathrm{cav}} = -105\,\mathrm{dBm}$ into the 3D cavity due to input line attenuation and cable losses. The quality factor of this resonator is approximately an order of magnitude lower than the device from Chapter 5, likely due to contamination of the Nb sputter processes in the LCN cleanroom at the time of fabrication.

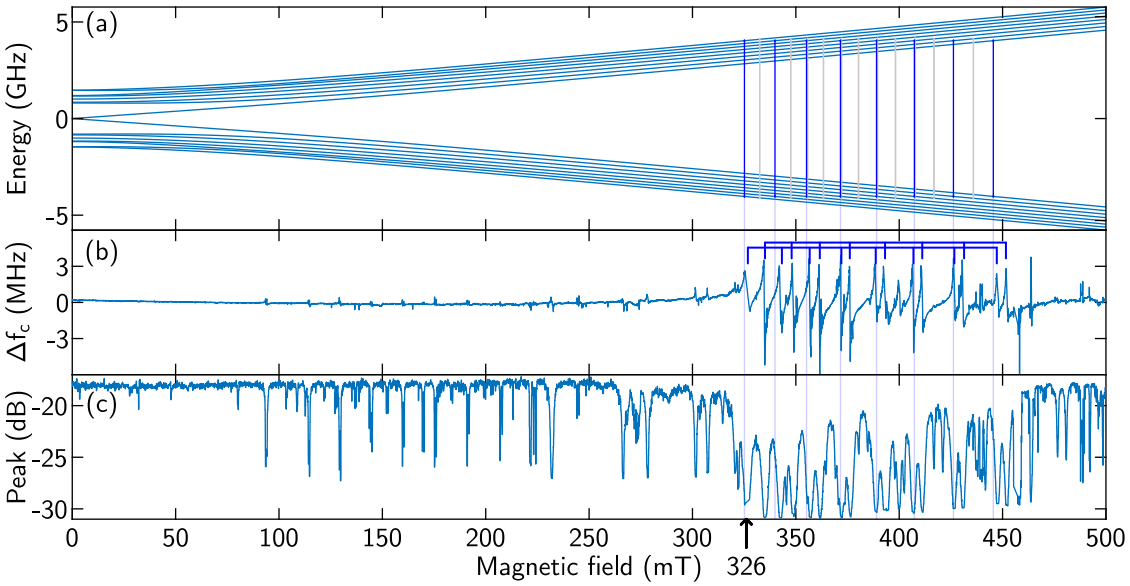

Figure 6.2: (a) Breit-Rabi diagram of ^{145}Nd:Y_2SiO_5 in site 1 for a magnetic field B_0 along the D_1 crystal axis. The fields at which a 8.071 GHz resonance occurs are indicated. (b) The VNA-tracked frequency shift of the resonator as magnetic field is swept up to 500 mT. The quadratic dependence of resonator frequency with field strength has been subtracted, leaving the dispersive shift of interaction with resonant spins. The 8 ESR transitions are split into 16 due to a misalignment of field direction from the D_1 axis breaking the subsite degeneracy, with the two sites indicated by the two combs. (c) The prominence of the resonance measured by the VNA. Dips in resonance magnitude occur alongside dispersive shifts, indicating absorption by the resonant spins.

6.2.1 ESR spectrum

Using methods described in Section 5.3.2, we use the resonator to measure an ESR spectrum from electron spins within the substrate by aligning the magnetic field of the vector magnet in the plane of the superconductor close to the D_1 crystal axis and ramping the field strength from 0 mT–500 mT, producing the data presented in Figure 6.2.

A Breit-Rabi diagram of dependence the ^{145}Nd:Y_2SiO_5 energy levels with B_0 strength along the D_1 crystal axis is shown in Fig. 6.2(a), with allowed transitions at 8.071 GHz indicated. ESR transitions are plotted in dark blue, and a series of weaker forbidden transitions with $\Delta m_I = 1$ are shown in grey. Fig. 6.2(b) shows the frequency shift of the resonator with the quadratic background shift subtracted leaving only the dispersive shift from interaction with resonant spins. The positions of avoided crossings are clearly visible, and closely match the predicted ESR transitions. As before, a breaking of the subsite degeneracy splits the ESR spectrum

into two, indicated by the dark blue comb. Unlike in Sec. 5.3.2, this measurement also tracks the peak $|S_{21}|$ transmission measured by the VNA tracking the resonance. Fig. 6.2(c) shows this data, illustrating how the resonator prominence dips strongly, indicating that absorption by resonant spins occurs alongside dispersion. This absorption proves a sensitive method for detecting weak spin transitions, such as low-field site 2 transitions or weak forbidden transitions with $\Delta m_I = 1$, but the strongly allowed site 1 ESR transitions can be identified by their larger dispersive shift indicating high-cooperativity.

Based on this ESR spectrum, the lowest-field site 1 ^{145}Nd:Y_2SiO_5 transition can be identified at $B_0 = 326\,\mathrm{mT}$, corresponding to the $m_I = +\frac{7}{2}$ ESR transition, which we now proceed to study in further detail.

6.2.2 Avoided crossing and cooperativity

A 2D field–frequency scan around $B_0 = 326\,\mathrm{mT}$ was taken with the VNA, scanning $\pm 25\,\mathrm{MHz}$ while the field was stepped from 310 mT–342 mT in 0.1 mT increments. A section of this scan is shown in Figure 6.3(a), with the avoided crossing visible. Taking cuts at constant B_0 for fields around the centre of the resonance, we see in blue the beginning of a dispersive shift in Fig. 6.3(c, e), and a vacuum Rabi splitting at the centre of the avoided crossing at 325.6 mT in Fig. 6.3(d). The ~12 MHz splitting of the peaks implies a coupling strength $g_{\mathrm{ens}} \approx 6\,\mathrm{MHz}$. These cuts have had the background transmission of the 3D cavity $C(f)$ subtracted.

With the presence of a vacuum Rabi splitting, the equations used to fit to the avoided crossing in Section 5.4.2 are no longer valid, and a more robust treatment is needed. In this regime we instead use Eqn. 2.12 to parametrise the full 2D sweep in terms of the ensemble coupling strength, enabling us to perform a least-squares fit directly on the 2D data. First the background transmission of the cavity $C(f)$ is measured by applying a large out-of-plane magnetic field to destroy the superconductivity. To extract A, ϕ, and κ_{c}, the $\frac{g_{\mathrm{ens}}^2}{\mathrm{i}\Delta_{\mathrm{s}}(B,f)+\gamma_{\mathrm{s}}}$ term is omitted to neglect the effect of spin resonance, and a fit to the resonator is performed when far detuned from spins at $B = 310\,\mathrm{mT}$. This yields the cavity half-width $\kappa_{\mathrm{c}}/2\pi = 76.9\,\mathrm{kHz}$, which along with A and ϕ become fixed parameters for the 2D fit.

Including the field dependence, a fit to the 2D data of Fig. 6.3(a) using the full $|S_{21}(B, f)|$ functional form is performed. This yields the final three parameters: the resonant field $B_0 = 325.59\,\mathrm{mT}$, spin half-width $\gamma_{\mathrm{s}}/2\pi = 2.99\,\mathrm{MHz}$, and ensemble coupling strength $g_{\mathrm{ens}}/2\pi = 5.933\,\mathrm{MHz}$. A simulation of the avoided crossing using

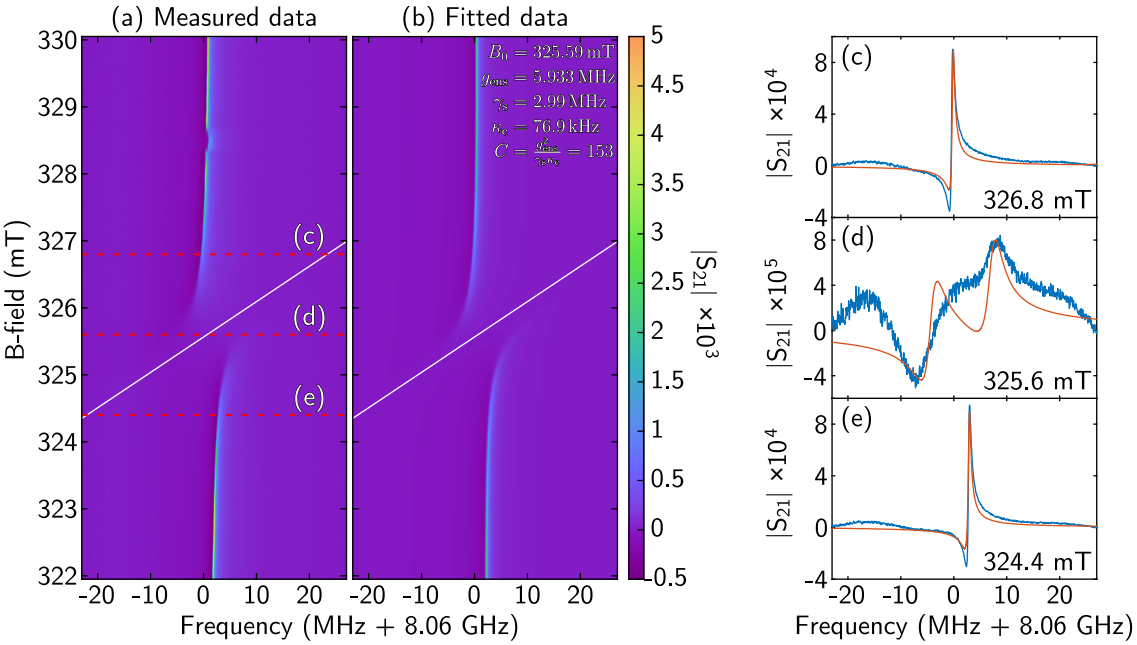

Figure 6.3: (a) An avoided crossing with the $m_I = +\frac{7}{2}$ ESR transition of ^{145}Nd measured in S_{21} magnitude by a VNA at $B_0 = 326\,\mathrm{mT}$. The white line indicates the ESR transition as it tunes with magnetic field across the resonator. (b) A 2D fit to the measured data, as described in Section 6.2.2. The fit parameters describing the spin coupling $g_{\mathrm{ens}}/2\pi = 5.933\,\mathrm{MHz}$, $\gamma_{\mathrm{s}}/2\pi = 2.99\,\mathrm{MHz}$, $\kappa_{\mathrm{c}}/2\pi = 76.9\,\mathrm{kHz}$ yield a high cooperativity $C = \frac{g_{\mathrm{ens}}^2}{\gamma_{\mathrm{s}}\kappa_{\mathrm{c}}} = 153$. Cuts (c, d, e) show the effect of the spins on the resonance profile, with a dispersive shift leading to a vacuum Rabi splitting visible at the centre of the avoided crossing in (d) of $\Omega = 2\frac{g_{\mathrm{ens}}}{2\pi} \approx 12\,\mathrm{MHz}$. The background transmission of the cavity has been subtracted in (c, d, e).

these values is shown in Fig. 6.3 alongside the measured data, and the cuts (c, d, e) include the fitted resonance in red.

These values yield a cooperativity $C = \frac{g_{\mathrm{ens}}^2}{\gamma_{\mathrm{s}}\kappa_{\mathrm{c}}} = 153$, putting this device well into the high-cooperativity regime, and on the border of strong coupling ($g_{\mathrm{ens}} > \gamma_{\mathrm{s}}, \kappa_{\mathrm{c}}$).

With the device and spin transition sufficiently characterised, we can now proceed to attempt pulsed ESR spectroscopy on this transition via the superconducting resonator.

6.3 Pulsed spectroscopy

To perform spin echo experiments, we apply a two-pulse sequence to the ^{145}Nd spin ensemble via the superconducting resonator. This sequence was detailed in Section 2.1.2, and a real example of a two-pulse sequence retrieving an echo from

this ^{145}Nd:Y_2SiO_5 sample and resonator has already been presented in Section 4.4.3 and Fig. 4.11. We now proceed to use this and related pulse sequences to measure properties of the ^{145}Nd:Y_2SiO_5 ensemble and its coupling to the superconducting resonator.

In this chapter, to operate at frequencies compatible with the ~8 GHz resonator, we use the 7–12 GHz microwave bridge described in Section 4.4.2. A 3 W amplifier provides a peak π-pulse power of approximately 3 µW into the 3D cavity.

6.3.1 Echo-detected avoided crossing

In the high-cooperativity regime, the resonator frequency becomes a strong function of the magnetic field due to the dispersive shift between resonator and spin ensemble. The strength of an echo then becomes a function of both magnetic field B and frequency f. To establish the optimal operating point, a two-pulse sequence was applied to create a 2D map of echo intensity, sweeping over $B = 321.5\,\mathrm{mT}$–$329.5\,\mathrm{mT}$ and $f = 8.052\,\mathrm{GHz}$–$8.070\,\mathrm{GHz}$. The retrieved waveforms in channels I and Q were integrated over a window 20 µs wide across the centre of the echo to determine the integrated I and Q, from which the echo magnitude and phase were calculated with magnitude $= \sqrt{\mathrm{I}^2 + \mathrm{Q}^2}$ and phase $= \arg(\mathrm{I} + \mathrm{iQ})$. The resulting map forms an echo-detected field and frequency sweep, in analogy to the echo-detected field sweep which forms an important tool in conventional ESR.

Performing this measurement produces the plots shown in Figure 6.4, showing an echo-detected measurement of the avoided crossing measured in CW in Fig. 6.3. The magnitude indicates the strongest echo is measured on the upper branch around 326 mT, and the separately integrated I and Q plots indicate the phase of the echo shifts across the avoided crossing.

More structure can be revealed by plotting magnitude on a log scale, where the weak echoes near the avoided crossing become more evident. A broadening of the linewidth is seen at the centre of the avoided crossing, as is a resolvable vacuum Rabi splitting. The phase can also be revealed in a 2D plot by assigning a hue to the measured phase increasing the lightness for weak echo magnitudes to highlight points where an echo was retrieved.

Taking cuts at constant B-field across the echo-detected avoided crossing in Fig. 6.4(a,b,c), we find that echoes are stronger when spin and cavity are detuned by ~0.9 mT from the centre of the avoided crossing, due to the reduction in resonator prominence when on-resonance causing retrieval efficiency to decrease. At the centre of the avoided crossing (b), the vacuum Rabi splitting is again observable

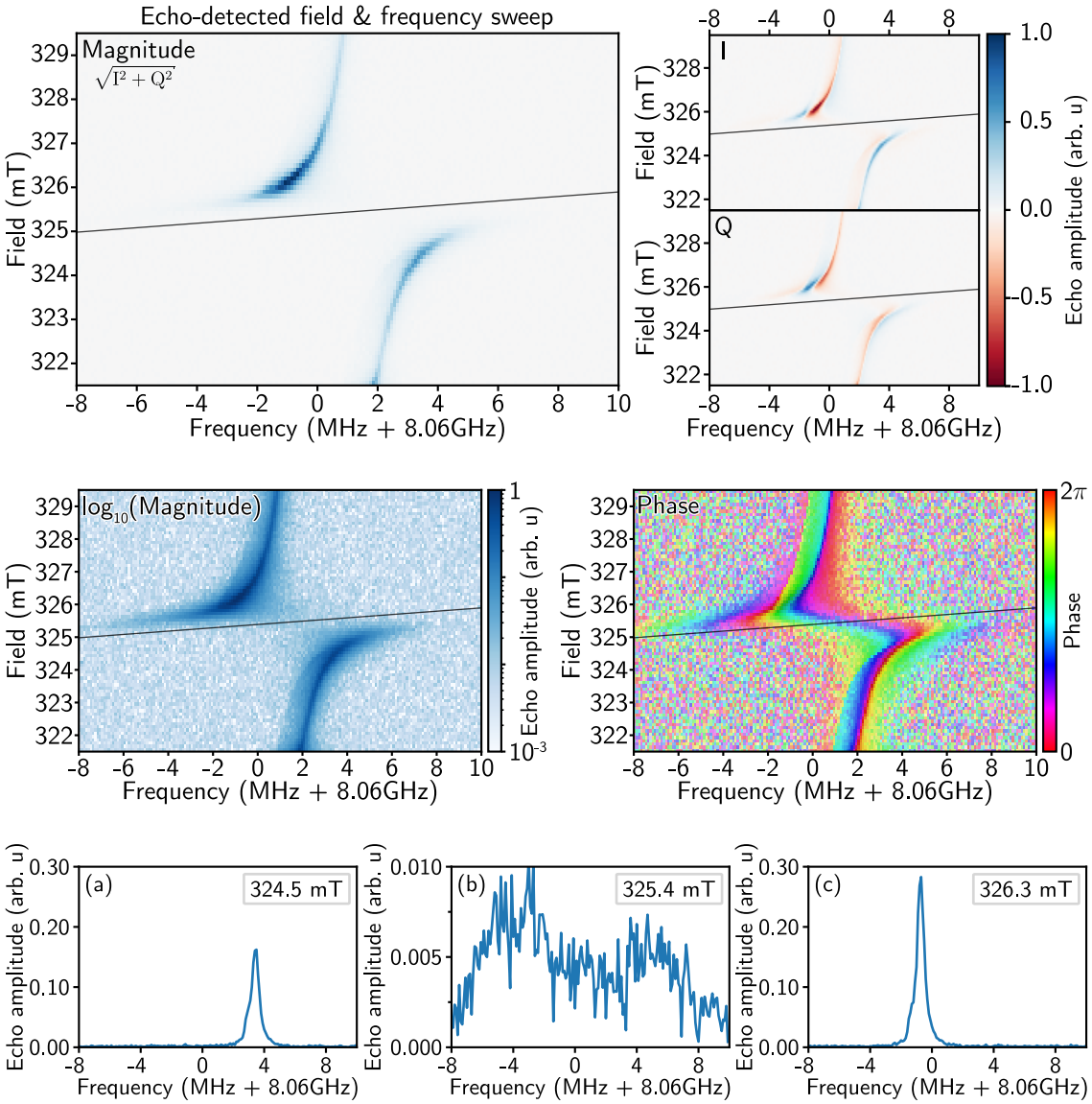

Figure 6.4: Echo-detected field–frequency sweep, measuring echo amplitude with a two-pulse sequence. The tuning of the spin frequency is indicated by the straight line on each 2D plot. Magnitude: Plotting echo magnitude $\sqrt{I^2+Q^2}$ reveals the avoided crossing, with the strongest echo appearing on the upper branch at $B = 326\,\mathrm{mT}$. Plotting I and Q separately reveals a change in phase of the echo over the avoided crossing. More structure can be revealed by plotting magnitude on a log scale, where the weak echoes near the avoided crossing become more evident, and by plotting the phase of the echo as the hue in a 2D image, weighting the luminosity by the echo amplitude. (a, b, c): Cuts at constant B-field show the echo amplitude over the avoided crossing, with a visible vacuum Rabi splitting at the centre (b).

with $\Omega \approx 10\,\mathrm{MHz}$, close to the splitting expected from the fitted ensemble coupling strength $2g_{\mathrm{ens}} = 12\,\mathrm{MHz}$.

This echo-detected scan of the avoided crossing illustrates one of the challenges in performing pulsed ESR in strong coupling and high-cooperativity regimes. In conventional (weakly coupled) ESR it is sufficient to tune the spins in resonance with the cavity by ramping magnetic field in an echo-detected field sweep while assuming the cavity frequency is static, however due to the dispersive frequency shift of the resonator in the high-cooperativity regime, changing the B-field necessitates performing an echo-detected frequency sweep to optimise the echo, forming plots as seen in similar to those plotted in Fig. 6.4(a,b,c). This process of ramping to a magnetic field and performing an echo-detected frequency sweep became a standard procedure, performed prior to every experimental run that follows. The strongest echo is retrieved on the upper branch of the avoided crossing, at around $B = 326\,\mathrm{mT}$. Next we will investigate coherence and relaxation properties at this point, as well as coherence properties at several other points on the avoided crossing.

6.4 Spin coherence time T_2

A two-pulse echo sequence enables measurement of coherence properties of the spin. By varying the pulse separation time τ, the echo amplitude decays as the spin ensemble decoheres for longer in the x–y plane, giving an exponential decay with the decoherence time T_2 as a function of the elapsed time 2τ

$$A(\tau) = A_0 \mathrm{e}^{-\frac{2\tau}{T_2}}. \tag{6.1}$$

where A_0 is a fit parameter effectively describing the extrapolated echo amplitude at $\tau = 0$.

A T_2 measurement at the most prominent point of the avoided crossing $B_0 = 326\,\mathrm{mT}$ at $13\,\mathrm{mK}$, with $\tau = 30\,\mu\mathrm{s}$–$2\,\mathrm{ms}$, is presented in Fig. 6.5. As expected, the echo decays exponentially toward zero. With the echo phased to appear predominantly in the I-channel, fitting an exponential decay with Eqn. 6.1 yields an artificially shortened T_2 time. This is due to phase noise, evident from a reduction in I amplitude correlated with an increase in Q amplitude in Fig. 6.5(a) as the phase of the echo drifts over the increasing wait time 2τ. This may be due to magnetic field noise from the superconducting magnet, causing the spin precession rate to fluctuate and accrue a deviation in phase over time 2τ. The effect becomes more

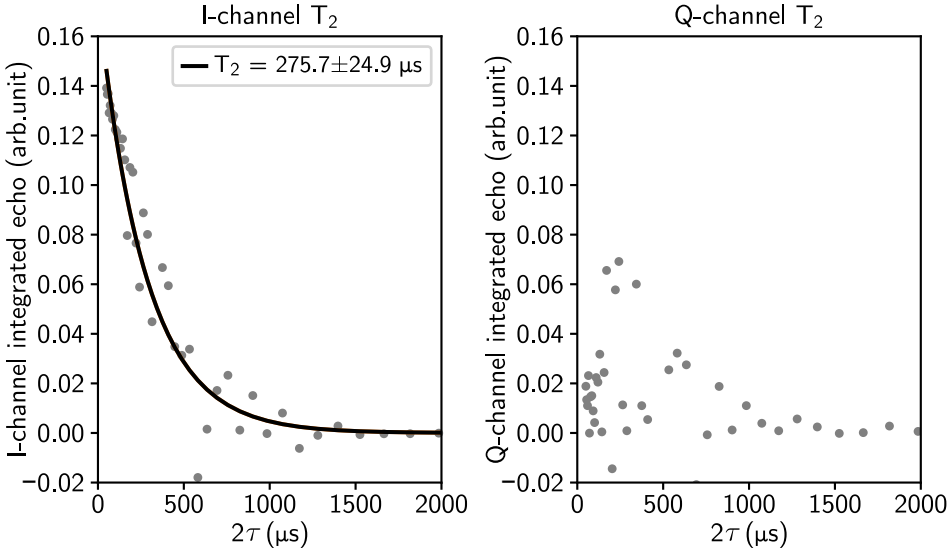

(a) With the echo phased to the I-channel, fitting an exponential decay to only the I-channel (left) yields an artificially shortened $T_2 = 276\,\mu s$ due to phase noise. This can be corrected by fitting to the echo amplitude $\sqrt{I^2 + Q^2}$, as in (b).

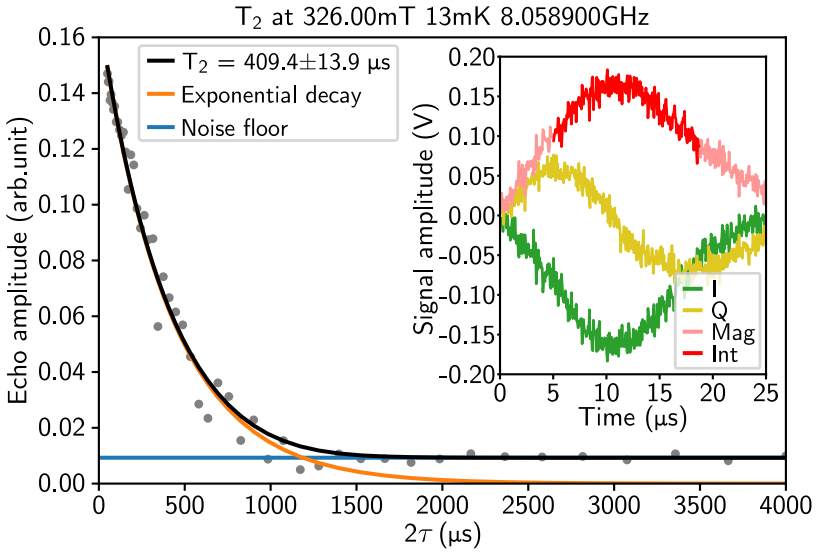

(b) The amplitude of the echo decay is fitted to Eqn. 6.2, with the decay signal and noise floor also separately indicated, yielding $T_2 = (409 \pm 14)\,\mu s$. Inset: the first echo at $\tau = 30\,\mu s$, shown in I/Q as well as amplitude $\sqrt{I^2 + Q^2}$. The overall amplitude of the echo, used for the decay measurement, is determined by integrating over the FWHM of the echo signal, indicated by the darker red data.

Figure 6.5: Two-pulse echo decay measurement, measuring the decoherence time T_2 at $B = 326.0\,mT$ and $T = 13\,mK$ measured at the sample box.

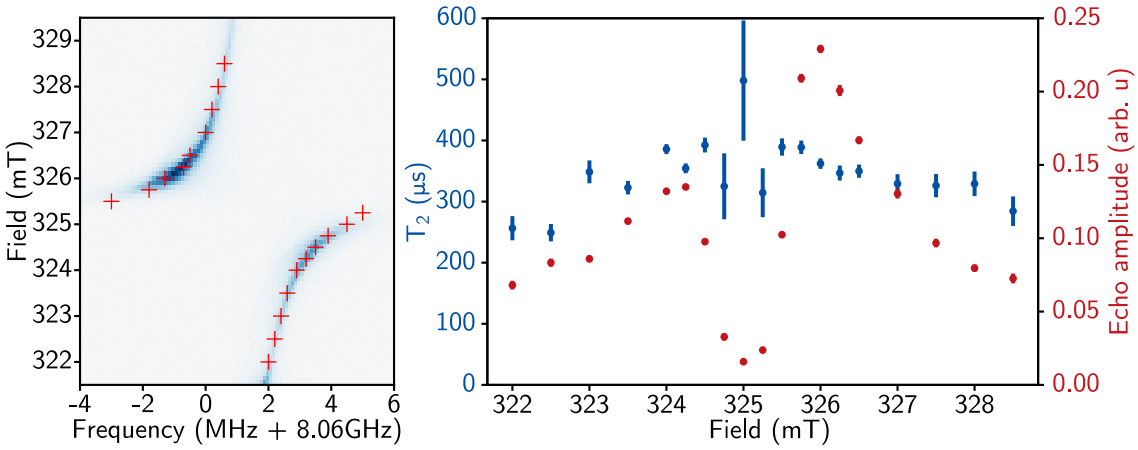

Figure 6.6: $T_2(B)$, measured for 19 points on the avoided crossing.

significant at longer τ. Phase noise can be accounted for by fitting instead to the echo amplitude $\sqrt{\mathrm{I}^2 + \mathrm{Q}^2}$.

When fitting to an echo amplitude, the voltage noise does not time-average to zero as it does for I or Q, but instead the noise power ($\propto V^2$) adds to the signal power. Hence the appropriate way to fit to such an amplitude decay measured in voltage is

$$A(\tau) = \sqrt{\left(A_0 \mathrm{e}^{-\frac{2\tau}{T_2}}\right)^2 + C^2} \tag{6.2}$$

where C is the noise floor, in this case measured by averaging the last 3 data points of the sweep.

Fitting the same decay with this function as in Fig. 6.5(b) yields the coherence time $T_2 = (409 \pm 14)\,\mu\mathrm{s}$. This was measured with the fridge at its base temperature, in a regime where spectral diffusion is significantly suppressed and instantaneous diffusion should limit the measured T_2. The effect of temperature on coherence time is studied in Section 6.4.2, and attempts to measure the contribution of spectral and instantaneous diffusion are discussed in sections 6.8 and 6.9.

6.4.1 T_2 across avoided crossing

To investigate whether the T_2 for the $m_I = +\frac{7}{2}$ transition measured at $B_0 = 326\,\mathrm{mT}$ generalised for other points on the avoided crossing, further measurements were performed for B-fields between 322.0 mT–328.5 mT. At each field point, an echo-detected frequency sweep determined the position of the strongest echo, which the T_2 measurement was then performed at.

Figure 6.6 presents this $T_2(B)$ measurement, marking the 19 points on the avoided crossing for which T_2 measurements were taken. A strong dependence of the echo

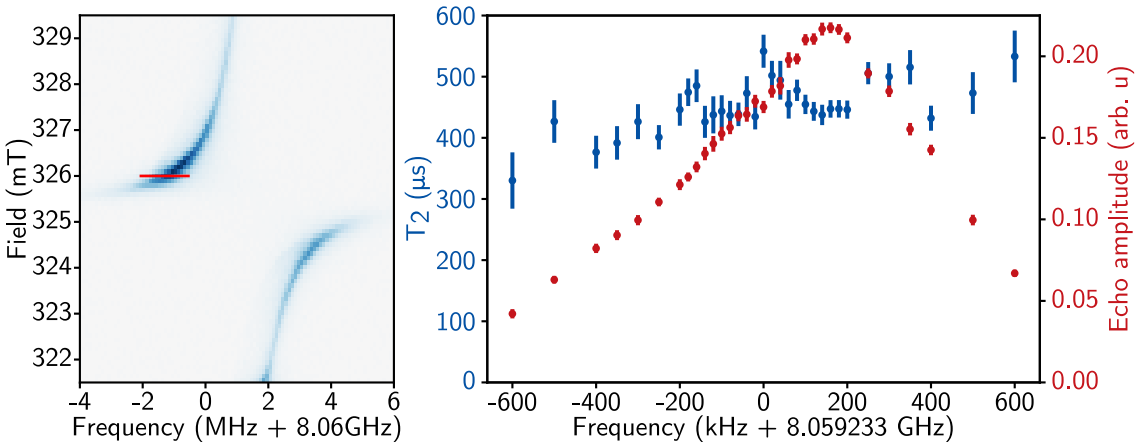

Figure 6.7: $T_2(f)$ measured at $B = 326.0\,\mathrm{mT}$ over $\pm 600\,\mathrm{kHz}$ from the frequency an initial echo-detected frequency sweep determined as giving the peak echo amplitude.

amplitude on B-field correlates with the strength of the echoes on the avoided crossing, but no T_2 convincingly exceeds $T_2 = (409 \pm 14)\,\mu\mathrm{s}$, with the longest measurement at 325.0 mT having a high uncertainty $T_2 = (498 \pm 98)\,\mu\mathrm{s}$ due to the weak echo amplitude.

A measurement of $T_2(f)$ was also performed, to verify whether a potential correlation between probe frequency f and T_2 could bias the conclusions of two-pulse echo experiments. This measurement is presented in Figure 6.7, at a constant $B = 326.0\,\mathrm{mT}$, for frequencies $\pm 600\,\mathrm{kHz}$ across the centre of the resonance. The amplitude agrees with echo-detected frequency sweeps in Section 6.3.1, but there is no convincing trend.

Some $T_2(f)$ data in Fig. 6.7 appears to exceed the $T_2 = (409 \pm 14)\,\mu\mathrm{s}$ measured in Fig. 6.5, notably the centre point of the sweep at 8.059 233 GHz with $T_2 = (542 \pm 27)\,\mu\mathrm{s}$, and the next 2 points of the sweep. However, this proved not to be repeatable. It is also evident that the centre frequency of the resonance shifted during the course of this measurement, which was initially set up with the centre frequency of the sweep determined by an echo-detected frequency sweep. This may be due to repeated pulsing on the spin transition causing bulk spins to gradually saturate, reducing the coupling strength and making the resonator shift up in frequency as the dispersive shift becomes less pronounced, an effect discussed further in Section 6.8.

6.4.2 Temperature dependence of T_2

A major contribution to decoherence comes from fluctuations in the magnetic environment, shifting the Larmor precession frequency of individual spins and causing dephasing of the spin ensemble. One cause of these magnetic fluctuations comes from energy-conserving flip-flop processes within the spin bath. To undergo a spin flip-flop, a relaxed spin must exchange with an excited spin, so the rate of spin-flips is dependent on the number of pairs of opposite spin. Hence this rate is proportional to the polarisation of the species making up the spin bath. The polarisation is given by the product of the occupation of the relaxed and excited states of the spin bath transition, given by the Boltzmann statistics which depends heavily on temperature [150–152]. Hence we expect a strong dependence of the coherence time as a function of temperature $T_2(T)$.

The thermal occupation of ^{145}Nd:Y_2SiO_5 energy levels at 326 mT is shown in Fig. 6.8(a). The population of the ESR states $n_\uparrow$, $n_\downarrow$ becomes significantly polarised below the Zeeman temperature $T_{\mathrm{Ze}} = \frac{hf}{k_{\mathrm{B}}} = 387\,\mathrm{mK}$. The polarisation P of a transition is then given by the product of the relative population of the ground $P_\downarrow$ and excited $P_\uparrow$ states

$$\begin{aligned}
n_\uparrow &= \mathrm{e}^{-\frac{T_{\mathrm{Ze}}/2}{T}}, \quad n_\downarrow = \mathrm{e}^{+\frac{T_{\mathrm{Ze}}/2}{T}}, \\
P_\downarrow &= \frac{n_\downarrow}{n_\uparrow + n_\downarrow} = \frac{1}{n_\uparrow n_\downarrow + n_\uparrow n_\uparrow} = \frac{1}{1+\mathrm{e}^{-\frac{T_{\mathrm{Ze}}}{T}}}, \\
P_\uparrow &= \frac{n_\uparrow}{n_\uparrow + n_\downarrow} = \frac{1}{n_\downarrow n_\uparrow + n_\downarrow n_\downarrow} = \frac{1}{1+\mathrm{e}^{+\frac{T_{\mathrm{Ze}}}{T}}}, \\
P &= P_\uparrow P_\downarrow = \frac{1}{\left(1+\mathrm{e}^{+\frac{T_{\mathrm{Ze}}}{T}}\right)\left(1+\mathrm{e}^{-\frac{T_{\mathrm{Ze}}}{T}}\right)}.
\end{aligned} \tag{6.3}$$

Plotting $P_\downarrow$ and $P_\uparrow$ as a function of temperature in Fig. 6.8(b), we find the ^{145}Nd ESR transition becomes heavily polarised below 100 mK, suppressing flip-flop processes. In this isotopically purified sample, ^{145}Nd in site 1 is the dominant source of magnetic fluctuations in the spin bath, due to the low occupation of site 2. Close to the D_1 axis the difference in T_{Ze} between sub-sites is negligible, so the spin bath can be well described by just this one species, ^{145}Nd in site 1.

By introducing a temperature-independent free parameter ξ related to the dipole–dipole interaction strength [40], and a residual decoherence rate Γ_{res} from temperature-independent interactions such as instantaneous diffusion, we can de-

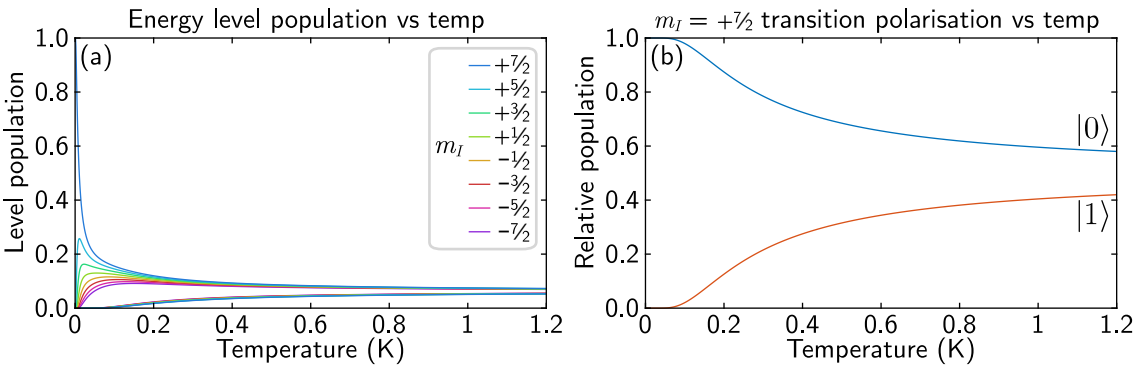

Figure 6.8: (a) Spin population of all 16 energy levels of ^{145}Nd:Y_2SiO_5 at 326 mT along D_1, calculated by Boltzmann statistics. The lines are coloured by the nuclear spin state m_I. The excited ESR states have a low occupation that becomes insignificant below 100 mK, creating a strong polarisation of the ^{145}Nd ensemble. (b) Polarisation of $m_I = +\frac{7}{2}$ ESR transition.

scribe the decoherence rate with [151, 152]

$$\frac{1}{T_2(T)} = \Gamma(T) = \Gamma_{\text{res}} + \frac{\xi}{\left(1 + \mathrm{e}^{+\frac{T_{\text{Ze}}}{T}}\right)\left(1 + \mathrm{e}^{-\frac{T_{\text{Ze}}}{T}}\right)}. \tag{6.4}$$

Taking two-pulse echo measurements for sample box temperatures between 14 mK–1.2 K, we measure the $T_2(T)$ presented in Fig. 6.9(a). A fit of Eqn. 6.4 to the experimental data shows a very close agreement with theory. The residual decoherence rate was set according to the coherence time measured at 14 mK, $\Gamma_{\text{res}} = \frac{1}{T_2} = \frac{1}{(409 \pm 14)\,\mu\text{s}}$, and the fitted $T_{\text{Ze}} = (360 \pm 4)$ mK is close to the calculated $T_{\text{Ze}} = 387$ mK, indicating that the spin temperature is close to that measured at the sample box at these temperatures. Below ~80 mK the measured coherence time appears shorter than predicted by the saturation of decoherence rate in the theoretical plot. This may indicate that the sample is slow to thermalise below these temperatures, due to material interfaces between the Y_2SiO_5 crystal and sample box.

The magnitude of the dipole–dipole coupling strength can be estimated using insights from DEER (double electron–electron resonance) spectroscopy, where the coupling rate between two electron spins A and B separated by distance r_{AB} is given by $\nu_{\text{dd}} = \frac{1}{2\pi}\frac{\mu_0\mu_{\text{B}}^2 g_{\text{A}} g_{\text{B}}}{4\pi\hbar}\frac{1}{r_{\text{AB}}^3}(3\cos^2(\theta_{\text{AB}}) - 1)$ where θ_{AB} is the angle between $\boldsymbol{B}_0$ and the axis between the spin A and B [59]. To provide an order-of-magnitude estimate in the case of a homogeneous distribution of spins with concentration $n = \frac{1}{r_{\text{AB}}^3}$, we neglect the angular dependence [153] and rewrite using the local gyromagnetic ratio

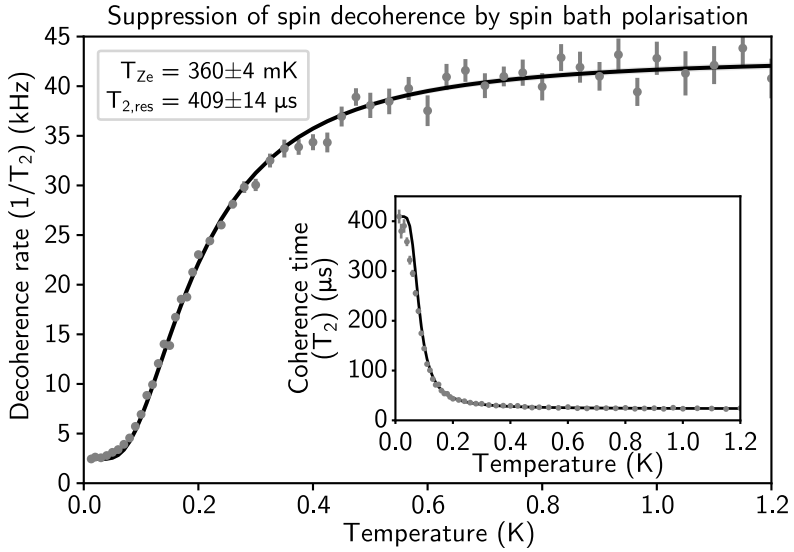

(a) Fit $T_{\mathrm{Ze}} = (360 \pm 4)\,\mathrm{mK}$. Expected from $f_c = 8.059\,\mathrm{GHz}$ $T_{\mathrm{Ze}} = 387\,\mathrm{mK}$. Residual $T_{2,\mathrm{res}} = (409 \pm 14)\,\mu\mathrm{s}$. $\xi = (162.0 \pm 0.9)\,\mathrm{kHz}$ is a temperature-independent free parameter determined by the dipole–dipole interaction strength. Inset: same data but time as opposed to rate.

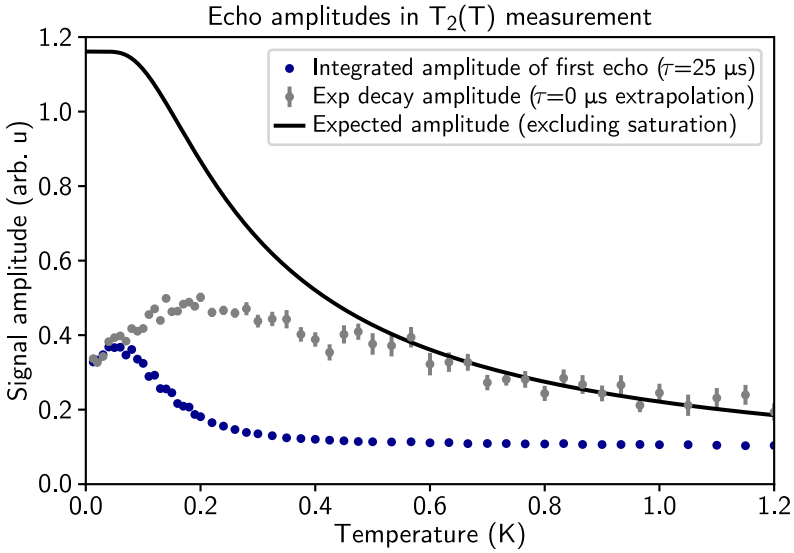

(b) Echo amplitude as a function of temperature, from the same data as in (a). Blue: amplitude of the first echo at $\tau = 25\,\mu\mathrm{s}$, these data are a function of both temperature and coherence time. Grey: fitted amplitude of the exponential decay for each T_2 measurement (A_0 in Eqn. 6.2), equivalent to the echo amplitude extrapolated to $\tau = 0$, which in the absence of saturation should be proportional to the difference in population between the ground and excited states $P_\downarrow - P_\uparrow$. The reduction of echo amplitude below ~500 mK from this expected curve may be due to the spin relaxation T_1 of a sub-ensemble exceeding the experimental shot repetition time.

Figure 6.9: Suppression of spin decoherence by spin bath polarisation at ~mK temperatures.

$\gamma = \frac{g\mu_B}{h} = \frac{df}{dB}$ [28]. This gives the expression

$$\nu_{dd} = \frac{h\mu_0}{4\pi}\gamma^2 n$$

which is consistent with the generally accepted $\nu_{dd} = \frac{52.2\ [\mathrm{MHz}]}{r^3_{AB}\ [\mathrm{nm}^3]}$ for a pair of $g = 2$ spins [153]. For this ensemble of $n = 4 \times 10^{24}\,\mathrm{m}^{-3}$ ^{145}Nd spins with $\gamma = 19.7\,\mathrm{MHz\,mT^{-1}}$ we estimate a coupling rate $\nu_{dd} = 102.9\,\mathrm{kHz}$, similar in magnitude to the fitted value of $\xi = (162.0 \pm 0.9)\,\mathrm{kHz}$. However, since the derivation of Eqn. 6.4 does not give an explicit expression for the fit parameter ξ including any pre-factors [151, 152], we cannot reliably draw further conclusions other than noting the similarity between these values.

Alongside the $T_2(T)$ measurements, in Fig. 6.9(b) we plot the amplitude of the fitted exponential decay (A_0 in Eqn. 6.2), equivalent to the echo amplitude extrapolated to $\tau = 0$. If the spins are permitted to fully relax between pulses, the echo amplitude should be proportional to the difference in population between the ground and excited states ($P_\downarrow - P_\uparrow$). Fitting this for a Zeeman temperature of $T_{Ze} = 387\,\mathrm{mK}$ we find the measured amplitude levels off below ~500 mK, suggesting that at these temperatures the T_1 of a sub-ensemble of weakly coupled bulk-like spins is exceeding the 5 s shot repetition time of the experiment, preventing them from fully relaxing between subsequent pulse sequences. The amplitude is then seen to decrease below ~200 mK as the T_1 time of more sub-ensembles exceeds the shot repetition time.

By polarising the spin bath, the effect of spontaneous diffusion is suppressed. This can be verified by measuring the spectral diffusion linewidth with a three-pulse measurement, discussed in Section 6.8. The residual decoherence rate at 14 mK should be due to interaction of spins within the bandwidth of the resonator during the measurement process, giving rise to instantaneous diffusion. The influence of instantaneous diffusion can be measured using a two-pulse sequence with progressively weaker refocusing pulses, to excite fewer spins during measurement; attempts to measure this are presented in Section 6.9.

6.5 Self-stimulated echo train

The two-pulse echo data presented so far has focused only on the first 2τ of the sequence, enough to acquire the primary echo. However for this sample, measuring beyond 2τ reveals the appearance of further echoes at 3τ, 4τ, 5τ, and beyond,

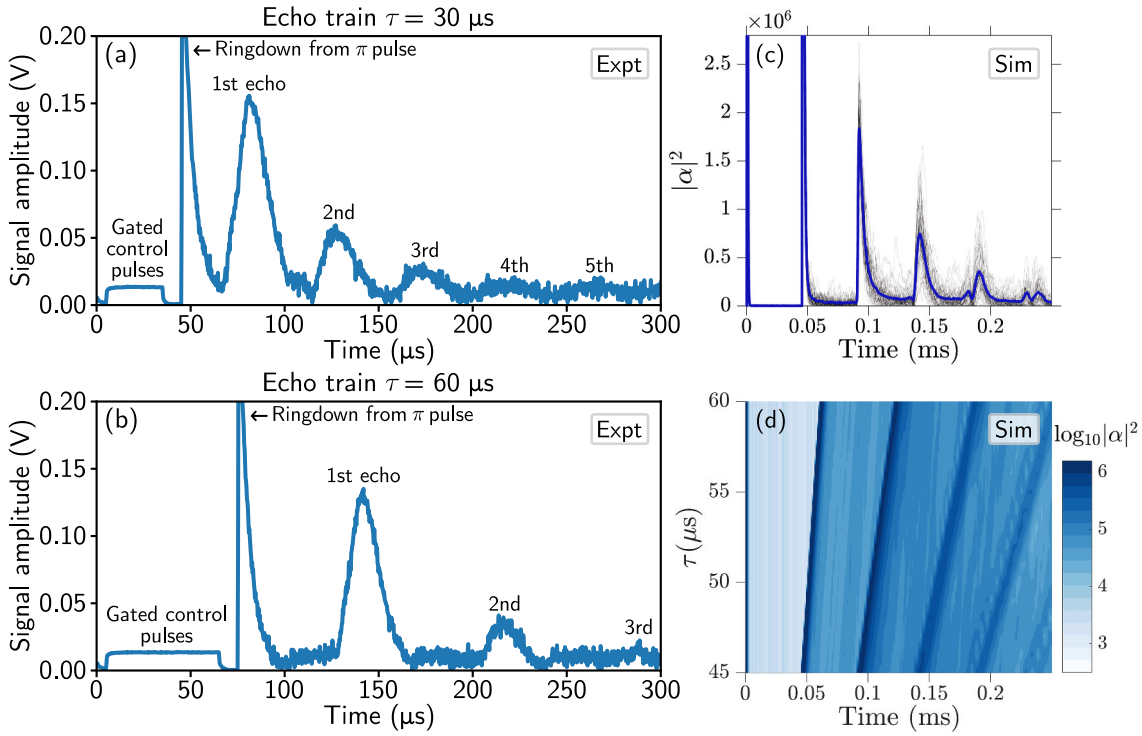

Figure 6.10: Two-pulse sequence with rectangular $\frac{\pi}{2}$ and π pulses at 326.00 mT, 14 mK. Each single-shot measurement produces a train of self-stimulated echoes due to the emitted echo being reabsorbed by the spin ensemble and displacing the spin vector. Echo trains react to changing τ for (a) $\tau = 30$ µs and (b) $\tau = 60$ µs. (c) Simulation developed by Kamanasish Debnath and Klaus Mølmer of the ^{145}Nd spin dynamics, producing an echo train for $\tau = 45$ µs. (d) Simulated echo train reacts appropriately to changing τ. Subfigures (c, d) have been reproduced from [154], with kind permission of Kamanasish Debnath.

as shown in Figure 6.10(a, b). These occur repeatably and reliably as part of a two-pulse echo, with no further application of pulses required.

The appearance of multiple echoes is not new. The very first article reporting a microwave spin echo in 1958 [155] noted the appearance of a secondary echo, and Hans Huebl's group reported the observation of echo trains on the arXiv in 2018 [149] shortly before the echo trains presented here were first observed.

The results shown here prompted a discussion with Kamanasish Debnath and Klaus Mølmer, who have been working on describing theoretically the dynamics of a strongly coupled spin–cavity system, to attempt to reproduce these measurements via simulation. A secondary echo occurs after a primary echo emitted into the cavity is partially reabsorbed by the spin ensemble, displacing the spin vector and initiating a second refocusing. It appears this effect arises due to the combination of imperfect refocusing pulses alongside the high-cooperativity spin–resonator

coupling, which causes spin echoes emitted into the cavity to initiate a further refocusing of the spin ensemble. Debnath and Mølmer model this with $N = 10^{10}$ spins in an inhomogeneously broadened ensemble coupled to an optical cavity with parameters similar to this sample, and drive with an external coherent pump to apply a two-pulse echo sequence. A detailed description is given in [154]. The simulated dynamics of the spin ensemble reproduce an echo train as shown in Fig. 6.10(c, d).

6.6 Adiabatic fast passage

The geometry of the thin-ring resonator used in these experiments, with the magnetic field generated by the inductive wire dropping off as $B_1 \propto \frac{1}{r}$, results in a highly inhomogeneous B_1 field driving the spins. For a given pulse length or power, spins far from the inductor will be driven weakly with only a small change in magnetisation, while spins close to the inductor will experience a significantly stronger field and may undergo multiple rotations around the Bloch sphere during the pulse. This makes the application of an accurate rotation angle impossible with rectangular or Gaussian pulses.

A solution to this comes from the arbitrary phase control available from using I/Q vector modulation, enabling the generation of frequency-swept pulses. To illustrate the additional control this provides, consider the application of a RF B_1 field with time-varying frequency $\omega(t)$ perpendicular to the B_0 field in the lab frame, $B_{\text{lab}} = [B_1 \cos(\omega t), B_1 \sin(\omega t), B_0]$. In the rotating frame in the presence of spins with Larmor frequency $\omega_{\text{s}} = \gamma B_0$ this becomes an effective magnetic field $B_{\text{eff}} = [B_1, 0, B_0 - \frac{\omega(t)}{\gamma}]$. When an RF pulse is on-resonance, $B_0 = \frac{\omega}{\gamma}$ and B_{eff} points purely along x, causing the spins to precess around the x-axis. However, for a detuned RF pulse a component along the z-axis remains.

This control over the angle of B_{eff} can be exploited to perform an adiabatic fast passage (AFP) [144, 156, 157], illustrated in Fig. 6.11. Consider starting with a spin ensemble whose magnetisation M predominantly points along $+z$. A frequency-swept pulse with $\omega(t = 0) \ll \gamma B_1$ causes B_{eff} to lie close to z, causing the magnetisation to precess around the z-axis. By slowly sweeping the frequency $\frac{\mathrm{d}\omega}{\mathrm{d}t} > 0$, B_{eff} smoothly rotates away from $+z$ toward $+x$. Provided the adiabaticity condition is met, that the rate of rotation of B_{eff} is slower than the precession of M around B_{eff}, $\left|\frac{\mathrm{d}\theta}{\mathrm{d}t}\right| < |\gamma B_{\text{eff}}|$, the precession of M around B_{eff} causes M to smoothly track B_{eff}. By ending the sweep with $\omega(t) \gg \gamma B_1$, B_{eff} and M both point along $-z$. The advantage of this adiabatic passage is that, unlike on-resonance pulses, it works regardless of the B_1 field strength provided the adiabaticity condition is met. This

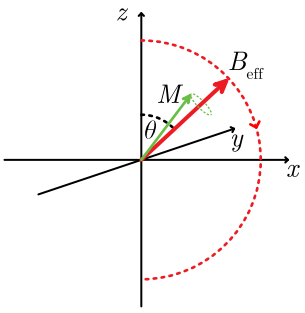

Figure 6.11: Adiabatic fast passage. By sweeping the frequency of a pulse $\frac{\mathrm{d}\omega}{\mathrm{d}t} > 0$, the effective magnetic field in the rotating frame B_{eff} rotates from $+z$ to $+x$ and through to $-z$. Provided the sweep is sufficiently slow $\left|\frac{\mathrm{d}\theta}{\mathrm{d}t}\right| < |\gamma B_{\text{eff}}|$ the magnetisation vector M of the spin ensemble follows this rotation as it precesses around B_{eff}. This can be exploited to invert magnetisation and produce arbitrary θ rotation despite an inhomogeneous B_1 field.

enables magnetisation inversion and arbitrary θ rotation even in the presence of a highly inhomogeneous B_1 field.

6.6.1 Echo inversion with WURST pulses

A purely rectangular amplitude profile to a swept pulse causes a finite offset at the start and end of the sweep, causing B_{eff} to lie slightly tipped from the z-axis. Introducing an amplitude modulation to the pulse ensures B_{eff} rotates smoothly from $+z$ to $-z$. This is what the WURST pulse[1] (Wideband, uniform rate, smooth truncation) achieves [143, 144].

The WURST pulse starts from a linear frequency sweep of length T with a chirp range Δf centred around f_0

$$f(t) = f_0 - \frac{\Delta f}{2} + \frac{\Delta f}{T} t$$

and modulates the amplitude with a profile

$$A(t) = 1 - \left|\sin\left(\pi\left[\tfrac{t}{T} - \tfrac{1}{2}\right]\right)\right|^n$$

where the index n changes the severity of the cutoff. A typical value is $n = 20$ [143].

An illustrative example of a WURST pulse is shown in Fig. 6.12(a). Shown in I/Q, the centre frequency $f_0 = 0$ because the upconversion to the carrier frequency is performed by a VSG. To measure the inversion caused by a WURST pulse, it

[1] This acronym was chosen because of the WURST's sausage-shaped envelope.

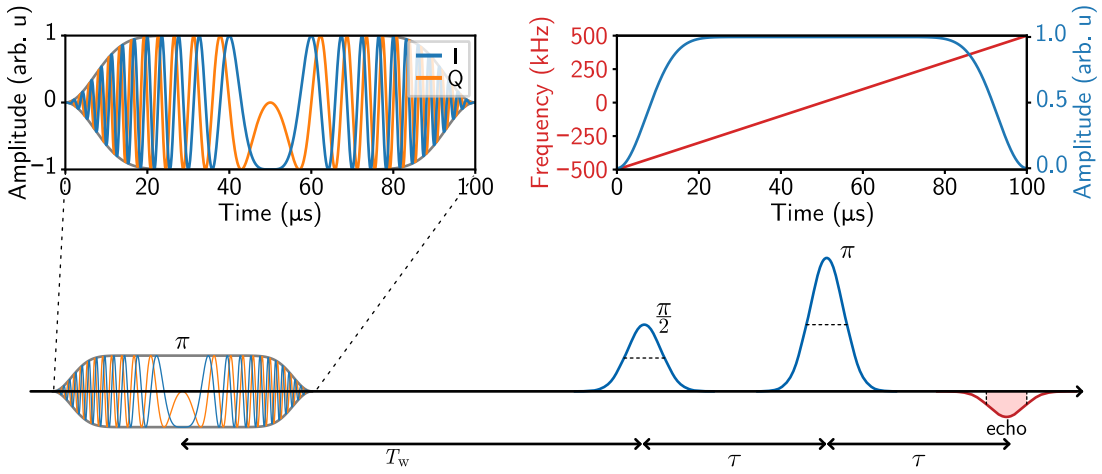

(a) WURST inversion sequence. In this illustrative example, the WURST pulse has a $\Delta f = 2\,\text{MHz}$ chirp and $T = 100\,\mu\text{s}$ duration.

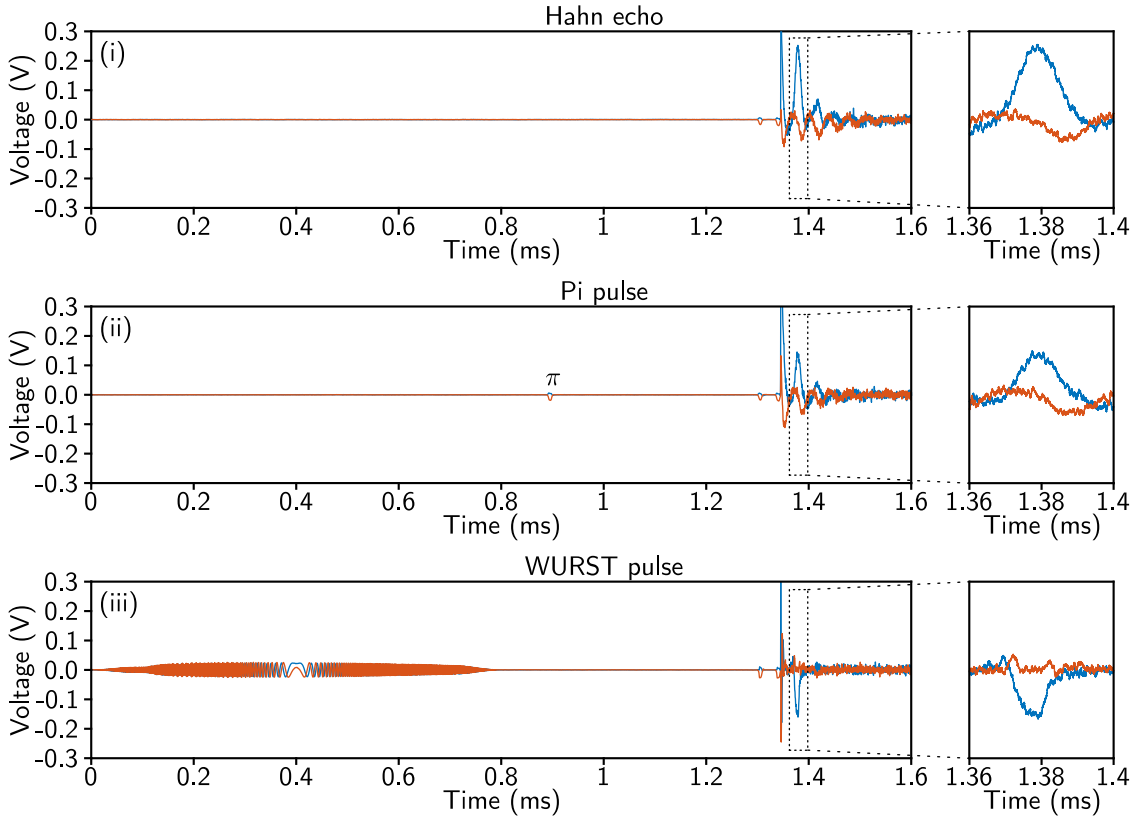

(b) Echo inversion with adiabatic fast passage. (i) A $\frac{\pi}{2}$–π Hahn echo sequence. (ii) shows that a simple π-pulse does not efficiently invert the Bloch vector to $-z$, as the echo remains positive. This is due to an inhomogeneous B_1 field from the resonator. (iii) Adiabatic fast passage with a $T = 800\,\mu\text{s}$, $\Delta f = 2\,\text{MHz}$ WURST pulse, creating an inverted echo. The right hand plot of each figure shows an expanded view of the primary echo for each sequence.

Figure 6.12: Adiabatic inversion with a WURST pulse.

can be followed by a two-pulse sequence, which shows a negative echo compared to a sequence without inversion as the magnetisation points along $-z$.

The experimental data in Fig. 6.12(b) demonstrates the effectiveness of a WURST pulse with this device. The two-pulse sequence is phased to produce a positive echo in the I channel in (i). Applying a gaussian π pulse 400 µs before the two-pulse sequence in (ii) does not invert the echo, but reduces its amplitude as the magnetisation over the inhomogeneously coupled spin ensemble is driven incoherently around the Bloch sphere. Applying a $T = 800\,\mu s$, $\Delta f = 2\,\text{MHz}$ WURST pulse in (iii) inverts the echo.

Using an inverted magnetisation we can measure T_1 relaxation of the spin ensemble by varying the wait time T_w, presented in Section 6.7.

6.6.2 Rabi oscillation with BIR-4 pulses

Adiabatic inversion can be implemented with a WURST pulse, but achieving a specific flip angle requires more complex chirped pulses. One possibility to achieve a $\frac{\pi}{2}$ rotation would be to truncate a WURST pulse to end at $\omega = \gamma B_1$, with B_1 aligned along $+x$, called an adiabatic half-passage (AHP), however in the presence of an inhomogeneously broadened spin ensemble this does not generalise well to arbitrary θ rotations. A pulse designed to implement such a rotation is the BIR-4 [158, 159] (B_1-insensitive rotation) pulse.

The BIR-4 consists of four AHP segments as illustrated in Fig. 6.13(a). The composite sequence is quite complex and covered in detail in [159], but the rotation angle θ is determined by a phase discontinuity between the first–second segments of

$$\Delta\phi = \pi + \frac{\theta}{2}$$

and $-\Delta\phi$ between the third–fourth segments.

By applying a $T = 100\,\mu s$, $\Delta f = 1\,\text{MHz}$ BIR-4 pulse, followed 2 ms later with a two-pulse echo sequence, the projection of the magnetisation along the z-axis can be measured analagously to the WURST inversion in the previous section. By varying the rotation angle $\theta = 0$ to $\theta = 4\pi$, a Rabi cycle is observable in Fig. 6.13(b). This demonstrates the capability to prepare a state by exploiting adiabatic passage, though the 100 µs pulse length required made pulse sequences incorporating arbitrary θ rotation within the pulse (as opposed to preparing a projection onto the z-axis) unreliable.

The standard BIR pulse [159] begins and ends with an abrupt change in amplitude, unlike the WURST pulse whose smooth truncation prevents misalignment of

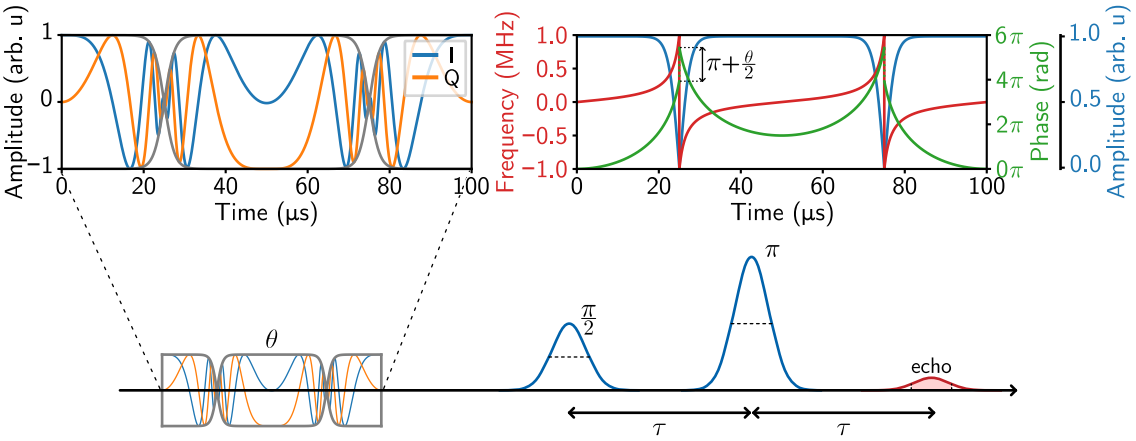

(a) BIR-4 rotation sequence. In this illustrative example, the BIR-4 pulse has a $\Delta f = 2\,\text{MHz}$ chirp and $T = 100\,\mu\text{s}$ duration.

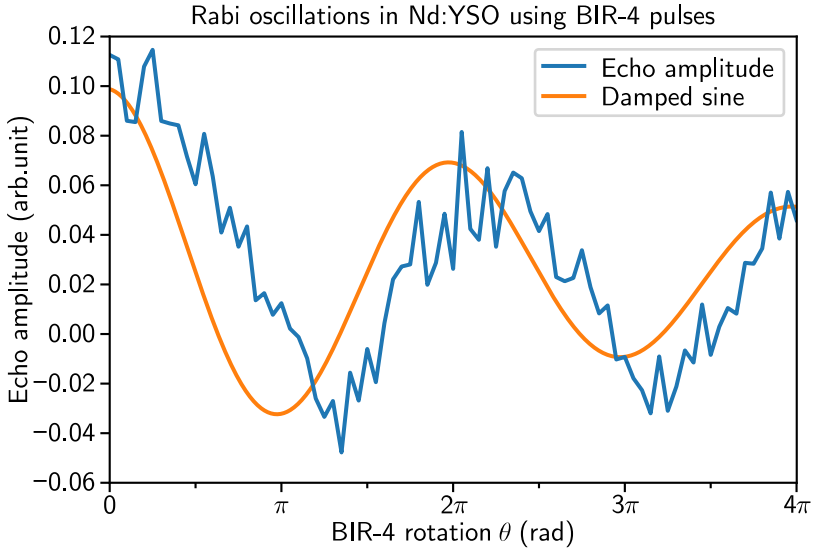

(b) Rabi oscillations using a BIR-4 pulse with $\Delta f = 1\,\text{MHz}$, $T = 100\,\mu\text{s}$. The initial θ rotation of the BIR-4 pulse prepares a projection of the magnetisation vector onto the z-axis, which is measured with a two-pulse echo sequence. The decay of echo amplitude from $\theta = 0$ to $\theta = \pi, 2\pi$ is due to a fast shot repetition time in this run causing weakly coupled spins to saturate over the course of the experiment. A damped sine has been fitted to the data as a guide to the eye.

Figure 6.13: Preparing a projection on the z-axis with a BIR-4 pulse.

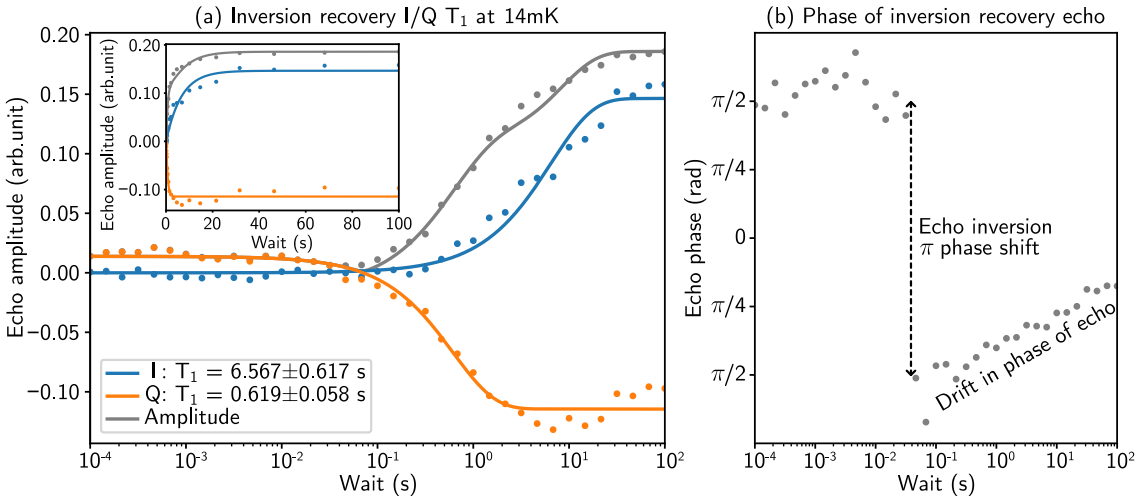

Figure 6.14: T_1 by inversion recovery at 14mK. The pulse sequence (shown in Fig. 6.12(a)) was phased to give an inverted echo in the Q channel. (a) Plotting both channels I (blue) and Q (orange) and fitting each with an exponential decay yields two decay timescales, differing by an order of magnitude. The amplitude of the fitted curve does not accurately describe the measured echo amplitude Amp $= \sqrt{\mathrm{I}^2 + \mathrm{Q}^2}$ (grey) at long timescales. (b) Plotting the phase shows the inversion of the echo at $T_\mathrm{w} \approx 40\,\mathrm{ms}$, but also a drift in the phase of the echo at long timescales. This motivates fitting to echo amplitude instead, as in Fig. 6.15.

initial and final B_eff. Examples in the literature of combining BIR-4 phase modulation with a WURST pulse envelope [95] have had success[2], but for this device showed no visible improvement in fidelity.

6.7 Spin relaxation time T_1

With the ability to prepare an inverted magnetisation using WURST pulses (see Sec. 6.6.1), we can measure T_1 relaxation of the spin ensemble by monitoring the recovery of the inversion from $-z$ to $+z$. We use the sequence presented in Fig. 6.12(a), varying the wait time T_w between the WURST inversion and a two-pulse echo sequence, measuring the echo amplitude as a function of T_w.

Measuring T_1 at 14 mK, we acquire the data in Fig. 6.14(a) for $T_\mathrm{w} = 100\,\mu\mathrm{s}$–$100\,\mathrm{s}$. Fitting a simple exponential decay directly to both I and Q yields two different decay rates $T_{1,\mathrm{I}} = (6.6 \pm 0.6)\,\mathrm{s}$ and $T_{1,\mathrm{Q}} = (620 \pm 60)\,\mathrm{ms}$, differing by an order of magnitude. The reason for this difference is evident in Fig. 6.14(b), where a drift in the phase of the echo is apparent for wait times beyond $T_\mathrm{w} \approx 100\,\mathrm{ms}$. This

[2]It should come as no surprise that BIR and WURST pair well together.

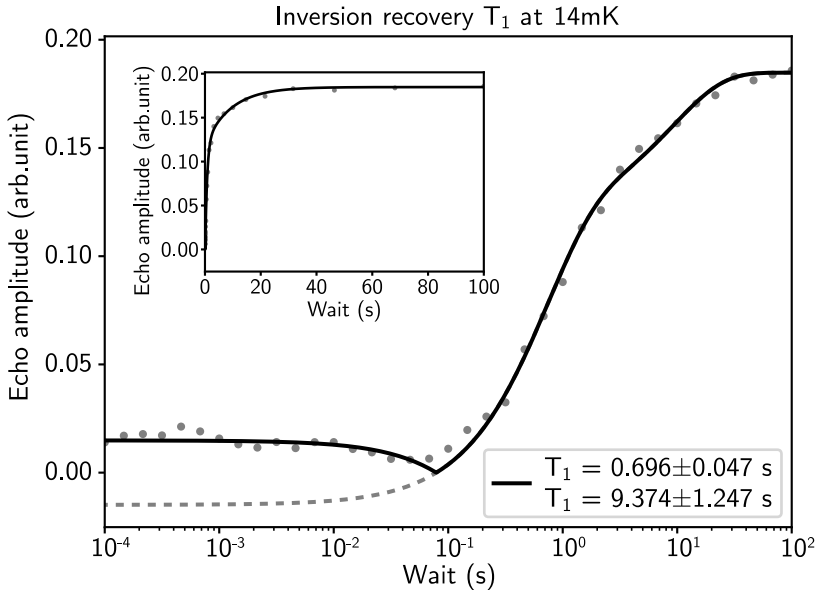

(a) T_1 by inversion recovery at 14mK yielding two characteristic decay times $T_{1,\mathrm{fast}} = (696 \pm 47)\,\mathrm{ms}$ and $T_{1,\mathrm{slow}} = (9.4 \pm 1.2)\,\mathrm{s}$ from a biexponential fit (Eqn. 6.5) to the echo amplitude (black line). The dotted grey line indicates the inversion of the echo for short T_w.

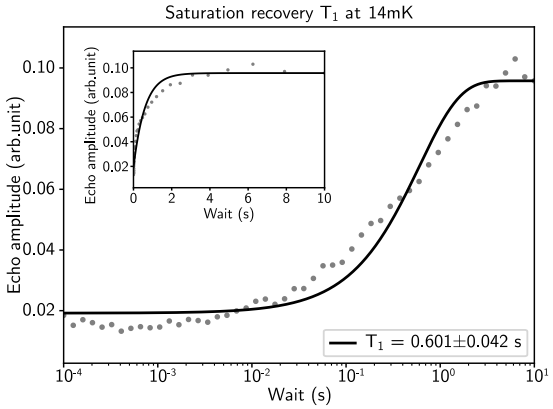

(b) T_1 measured by saturation recovery at 14mK, with $T_1 = (601 \pm 42)\,\mathrm{ms}$, consistent with $T_{1,\mathrm{fast}}$ from inversion recovery.

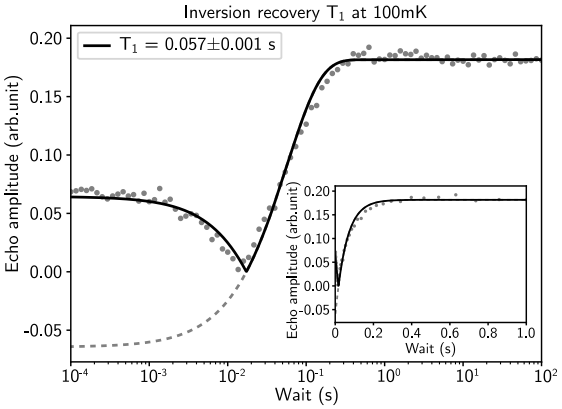

(c) T_1 by inversion recovery at 100mK, with a single exponential fit yielding $T_1 = (57 \pm 1)\,\mathrm{ms}$, consistent with cross-relaxation dominating over Purcell at 100 mK.

Figure 6.15: T_1 relaxation measurements by inversion and saturation recovery

drift in phase prevents accurate measurement of T_1 by considering each channel individually. Hence to accurately describe the recovery of the echo we analyse the echo amplitude instead in Fig. 6.15. It should be noted this has the effect of making the measured data always positive, even for an inverted echo.

For a resonator with an inductive wire generating an inhomogeneous $B_1 \propto \frac{1}{r}$, the single-spin coupling strength between the spin and resonator scales with $g_{\text{spin}} \propto B_1$ [66]. For strongly coupled ions, the cavity becomes an additional channel for spontaneous emission of microwave photons, with the Purcell rate $\Gamma_{\text{P}} = \frac{4g_{\text{spin}}^2}{\kappa}$ [66]. This implies an inhomogeneous B_1 field corresponds with an inhomogeneous Purcell-enhanced spin relaxation rate. As a result, we expect the measured T_1 to include contributions from a continuous range of relaxation rates from short-lived strongly Purcell-enhanced spins, to long-lived bulk-like spins.

The relaxation dynamics of an inhomogeneously Purcell-enhanced spin ensemble is complex to describe analytically. As an approximation to the wide range of T_1, we fit to the experimental data using a biexponential of the form

$$A(T_{\text{w}}) = \left| -C_{\text{fast}} \exp\left(-\frac{T_{\text{w}}}{T_{1,\text{fast}}}\right) - C_{\text{slow}} \exp\left(-\frac{T_{\text{w}}}{T_{1,\text{slow}}}\right) + D \right| \tag{6.5}$$

where $T_{1,\text{fast}}$ and $T_{1,\text{slow}}$ are fast and slow decay rates, C_{fast} and C_{slow} are the respective amplitudes of the decay, and D is the echo amplitude measured without a WURST inversion. The modulus accounts for the measurement of the echo amplitude. This biexponential model is a simplification, as the Purcell-enhanced emission rate varies continuously with B_1 field strength, but it broadly captures the dynamics involved. Fitting to relaxation decay from an inhomogeneous B_1 field with a multiexponential function is consistent with previous measurements in the literature [19].

Fitting Eqn. 6.5 to the echo amplitude in Fig. 6.15(a) returns two characteristic relaxation times $T_{1,\text{fast}} = (696 \pm 47)\,\text{ms}$ and $T_{1,\text{slow}} = (9.4 \pm 1.2)\,\text{s}$ where, within the approximation described above, $T_{1,\text{fast}}$ describes a rate at which strongly coupled spins are relaxing via their coupling to the resonator, and $T_{1,\text{slow}}$ is a contribution from a sub-ensemble more weakly coupled spins. The respective amplitudes $C_{\text{fast}} = 0.134 \pm 0.005$ and $C_{\text{slow}} = 0.065 \pm 0.005$ indicates the fast process is, broadly speaking, twice as significant as the slow.

We compare the relaxation times measured by inversion recovery to an experiment using saturation recovery, where the WURST pulse is replaced by a long MW pulse ~500 µs long. This scatters the magnetisation of the spin ensemble all over the Bloch sphere, resulting in no net magnetisation and hence no spin echo. The recovery of

the magnetisation with T_1 relaxation processes can be monitored by varying T_w. A saturation recovery experiment at 14 mK is presented in Fig. 6.15(b). As this experiment only used the range $T_\mathrm{w} = 100\,\mu\mathrm{s}$–10 s, a reliable fit to $T_{1,\mathrm{slow}}$ ~10 s is not possible. A single exponential fit yields $T_{1,\mathrm{fast}} = (601 \pm 42)\,\mathrm{ms}$, showing agreement between inversion recovery and saturation recovery.

Raising the temperature to 100 mK has a marked effect on the relaxation time, decaying with a single exponential with characteristic time $T_1 = (57 \pm 1)\,\mathrm{ms}$. This is consistent with another relaxation mechanism, faster than the Purcell-enhanced rate $T_{1,\mathrm{fast}} = 696\,\mathrm{ms}$, coming into play. With spin–lattice relaxation processes heavily suppressed at sub-Kelvin temperatures [160], this may be consistent with cross-relaxation between ^{145}Nd spins, which we can estimate using parameters from studies into spectral hole lifetimes in ^{145}Nd:Y_2SiO_5 [26],

$$R_\mathrm{FF} = \frac{\gamma_\mathrm{FF}}{B}\,\mathrm{sech}^2\left(\frac{hf}{2k_\mathrm{B}T}\right) \tag{6.6}$$

where the value from [26] $\gamma_\mathrm{FF} \approx 6.5\,\mathrm{Hz\,T}$ along D_1 scales with n^2 to give $\gamma_\mathrm{FF} \approx 280\,\mathrm{Hz\,T}$ for a 200 ppm as opposed to 30 ppm crystal. With $B = 326\,\mathrm{mT}$ and $f = 8\,\mathrm{GHz}$, this yields a cross-relaxation time $\frac{1}{R_\mathrm{FF}} \approx \frac{1}{70\,\mathrm{Hz}} \approx 15\,\mathrm{ms}$, within an order of magnitude of the measured T_1, supporting the conclusion that cross-relaxation dominates T_1 at 100 mK.

Interestingly, the WURST inversion in the 100 mK data appears to be more efficient than the inversion at 14 mK. Further experimentation with WURST pulses would be needed to provide insights into the cause.

6.8 Stimulated three-pulse echo spectroscopy

A stimulated or three-pulse echo sequence consists of two $\frac{\pi}{2}$ pulses, separated by time τ, followed by a third $\frac{\pi}{2}$ pulse at time T_w after the second pulse, illustrated in Figure 6.16(a). The first pulse excites spins from the z axis onto the x axis, where they dephase within the x–y plane for time τ. The second $\frac{\pi}{2}$ rotates these dephased spins onto the x–z plane, effectively parking the projection of the dephased spins from the x axis onto the z axis. This effectively encodes a frequency comb of spins whose accumulated phase is a multiple of π onto the $\pm z$ states. For a time T_w these spins undergo relaxation and spectral diffusion, before being projected back onto the $-x$ axis by the third $\frac{\pi}{2}$ pulse. The spins refocus and emit an echo after time τ.

The amplitude of the echo from a three-pulse sequence depends on τ due to T_2 effects while the spins are in the x–y plane, and on T_w due to T_1 relaxation, as well

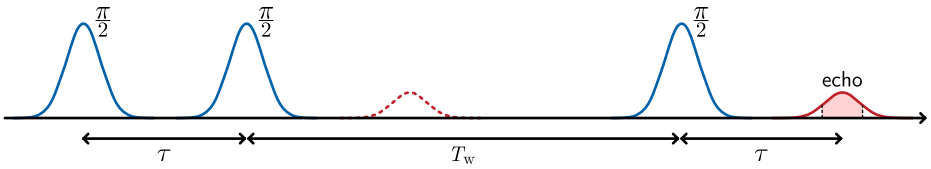

(a) A stimulated or three-pulse echo sequence. Two $\frac{\pi}{2}$ pulses store magnetisation on the z axis, which the third $\frac{\pi}{2}$ can project onto the x–y plane, stimulating an echo whose amplitude depends on both τ and T_w due to spectral diffusion and longitudinal and transverse relaxation. Typically an echo also appears at 2τ, which is the conventional two-pulse echo.

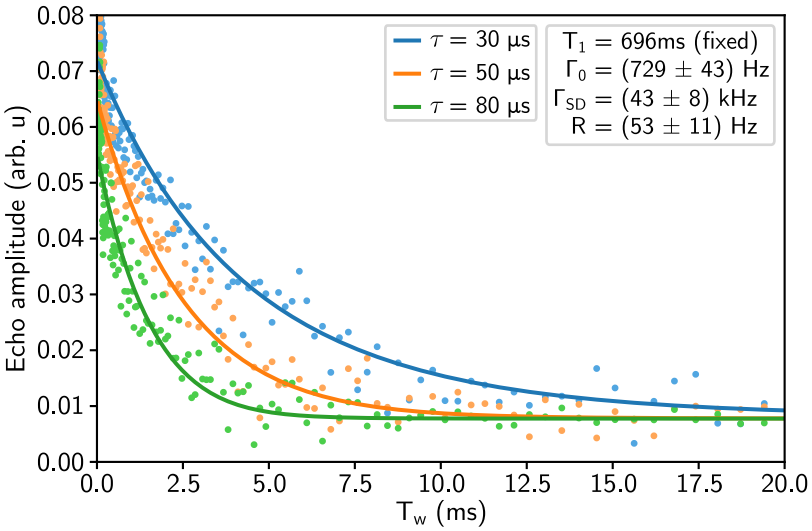

(b) Decay of a three-pulse echo experiment with T_w for $\tau = [30, 50, 80]\,\mu\mathrm{s}$, along with a fit to theory with Eqn. 6.7.

Figure 6.16: A three-pulse stimulated echo experiment,

as spectral diffusion which causes spin magnetisation to transfer into parts of the spectrum outside the measurement bandwidth, as described in Section 2.1.4. Thus by varying both τ and T_w in a three-pulse sequence, we can gain information about spectral diffusion, and longitudinal and transverse relaxation, of the spins being measured.

A three-pulse echo experiment was performed at $B_0 = 326\,\mathrm{mT}$ and 14 mK measured at the sample box, for $\tau = [30, 50, 80]\,\mu\mathrm{s}$ and $T_\mathrm{w} = 30\,\mu\mathrm{s}$–40 ms, with the echo decay shown in Fig. 6.16(b). The amplitude of the stimulated echo decays with T_w over a timescale ~ms before disappearing into the noise floor, and can be described as a function of τ and T_w [28]

$$A(\tau, T_\mathrm{w}) = A_0 \exp\left[-\left(\frac{T_\mathrm{w}}{T_1} + 2\pi\tau\Gamma_\mathrm{eff}\right)\right] \tag{6.7}$$

$$\text{where } \Gamma_\mathrm{eff} = \Gamma_0 + \tfrac{1}{2}\Gamma_\mathrm{SD}(R\tau + 1 - \mathrm{e}^{-RT_\mathrm{w}}), \tag{6.8}$$

and to account for the noise floor C we fit to the voltage amplitude using

$$V = \sqrt{A(\tau, T_\mathrm{w})^2 + C^2}\,. \tag{6.9}$$

Here, Γ_SD is the spectral diffusion linewidth, R the total spin-flip rate, and Γ_0 describes residual decoherence effects such as instantaneous diffusion and homogeneous broadening.

Due to a strong mathematical covariance between T_1 and Γ_SD, we fix $T_1 = 696\,\mathrm{ms}$ as the fast relaxation rate measured in Section 6.7. With the decay occurring over ~10 ms, the T_1 decay plays a negligible role in the dynamics measured here. A fit to the parameters Γ_0, Γ_SD, and R yields the values $\Gamma_0 = (729 \pm 43)\,\mathrm{Hz}$, $\Gamma_\mathrm{SD} = (43 \pm 8)\,\mathrm{kHz}$, and $R = (53 \pm 11)\,\mathrm{Hz}$.

First looking at the fitted Γ_0, this value should correspond to the decoherence rate with τ as in a two-pulse sequence, neglecting the effect of spectral diffusion. A three-pulse sequence is equivalent to a two-pulse sequence for $T_\mathrm{w} = 0$, so neglecting terms involving T_w and Γ_SD, the exponential decay of Eqn. 6.7 is equivalent to Eqn. 6.1 when $T_2 = \frac{1}{\pi\Gamma_0} = (440 \pm 30)\,\mu\mathrm{s}$. Hence the residual decoherence rate from three-pulse measurement agrees with the two-pulse $T_2 = (410 \pm 14)\,\mu\mathrm{s}$ measured in Sec. 6.4.

The spectral diffusion linewidth Γ_SD can be calculated from dipolar interactions between spins [28, 40]

$$\Gamma = \frac{\pi\mu_0 h}{9\sqrt{3}} n\gamma_1\gamma_2 \operatorname{sech}^2 \frac{hf}{2k_\mathrm{B}T} \tag{6.10}$$

where the spin concentration $n = 2 \times 10^{24}\,\mathrm{m}^{-3}$ is half the total ^{145}Nd concentration due to the splitting of the sub-site degeneracy, and γ_1 and γ_2 are the gyromagnetic ratios $\gamma = \frac{\mathrm{d}f}{\mathrm{d}B_z}$ in $\mathrm{Hz\,T^{-1}}$ for the resonant spin and an interacting spin. For this sample we assume the dominant contribution comes from the abundant ^{145}Nd in site 1, with $\gamma_1 = \gamma_2 = 19.7\,\mathrm{MHz\,mT^{-1}}$. To achieve the spectral diffusion linewidth (determined by fitting the data to Eqn. 6.7) $\Gamma_\mathrm{SD} = (43 \pm 8)\,\mathrm{kHz}$, Eqn. 6.10 implies a spin bath temperature of $T = (163 \pm 16)\,\mathrm{mK}$. The slow flip-flop rate $R = 53\,\mathrm{Hz}$ is consistent with a spin bath temperature of $T = (93 \pm 5)\,\mathrm{mK}$ according to Eqn. 6.6.

This temperature is an order of magnitude higher than that measured at the sample box $T = 14\,\mathrm{mK}$. The convincing fit of $T_2(T)$ down to 80 mK in Sec. 6.4.2 suggests the Y_2SiO_5 crystal is thermalising to at least this temperature, and the agreement between Γ_0 and the T_2 from two-pulse measurements suggests earlier experiments have measured spin decoherence with spectral diffusion mostly suppressed. From this we deduce that for this experiment the spin bath appeared to be out of thermal equilibrium with the crystal.

To explain this result, we return to the context of this particular experiment compared to others: the $T_2(T)$ experiment presented in Section 6.4.2 was performed after a fresh thermal cycle, ensuring the electron spins have thermalised with the crystal during an adiabatic cooldown. The three-pulse measurement presented here was not performed after a thermal cycle, but after a series of other experiments at 14 mK, where T_1 takes a biexponential form with a slow rate around $T_1 \approx 10\,\mathrm{s}$. This experiment, as well as some previous tests, had been set up to take advantage of the fast rate $T_1 \approx 700\,\mathrm{ms}$ by operating at a shot repetition time of 5 s to ensure the experiment could run overnight, however in doing so the spin bath was not being permitted to sufficiently relax to maintain thermal equilibrium. This appears to have resulted in an artificially elevated spin bath temperature, causing wider spectral diffusion linewidth than predicted by Eqn. 6.10. Future experiments requiring a spin bath in thermal equilibrium should take care to operate with a shot repetition time longer than the slowest T_1.

An elevated spin bath temperature can also be caused by leakage of microwave power down the signal lines leading to the device. With 50 dB attenuation on the input line of this experiment shown in Fig. 4.5, room temperature noise from the top of the fridge is attenuated to 18 mK by the time it reaches the mixing chamber stage. The low noise amplifier radiates noise of no more than 4 K down to colder

stages, but three circulators isolate this to 10 mK at the mixing chamber stage. Hence for this experimental setup, the noise temperature reaching the sample is not sufficient to disturb the thermal equilibrium at 14 mK.

6.9 Two-pulse T_2 with low refocusing amplitude

With spectral diffusion mostly suppressed at 14 mK, instantaneous diffusion between spins within the measurement bandwidth of the resonator (see Section 2.1.4) is likely to contribute to the residual decoherence rate Γ_{res} found from $T_2(T)$ measurements in Section 6.4.2. Instantaneous diffusion is proportional to the number of spins refocused during the second pulse of a two-pulse sequence. By reducing the amplitude of this pulse, fewer spins are refocused, effectively probing a more dilute spin ensemble where the excitation of a spin from application of a MW pulse has less of an influence on the magnetic environment of another measured spin. [19, 28]

A two-pulse sequence with variable second pulse angle θ, shown in Fig. 6.17(a), was used to perform measurements of T_2 as a function of spin flip probability $\langle \sin^2(\theta/2) \rangle$, down to the lowest pulse amplitude a reliable single-shot T_2 measurement could be performed. In conventional ESR this typically has a linear relationship [28, 161] if instantaneous diffusion is prevalent, but in Fig. 6.17(b) no credible conclusion can be drawn, with a constant decoherence rate $\frac{1}{T_2} \approx 2300\,\text{s}^{-1}$ being consistent with almost all the data gathered.

With a high spin concentration of 200 ppm, the density of resonant ^{145}Nd spins is significantly higher than other experiments with rare-earths [28] that have measured the contribution of instantaneous diffusion, so it is unlikely ID is not present. The similarity between $\pi\Gamma_0 = (2290 \pm 135)\,\text{Hz}$ from Section 6.8 and $\frac{1}{T_2} \approx 2300\,\text{s}^{-1}$ measured here suggests this measurement has largely suppressed spectral diffusion.

An explanation for this null result comes from the significantly inhomogeneous B_1 field generated by the resonator. For the geometry of this resonator, the inductor generating B_1 can be modelled as a wire, with field strength $\propto \frac{1}{r}$. The Rabi frequency of an individual spin then also scales as $\frac{1}{r}$, giving a strong spatial dependence of the rotation induced on an individual spin from a single MW pulse. Reducing the strength of the refocusing pulse then effectively probes spins closer to the resonator which experience a stronger B_1 field than those further away. If most of the signal comes from a volume of spins close to the resonator, then even small pulse amplitudes θ will drive these spins strongly, and the reduction of instantaneous diffusion in spins at further r not be resolved over the signal from the strongly driven spins.

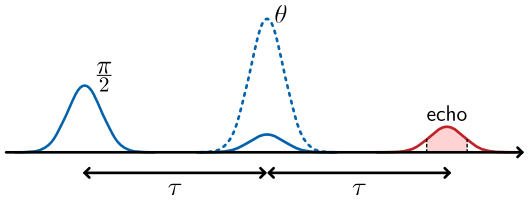

(a) Two-pulse sequence with variable refocusing pulse angle θ

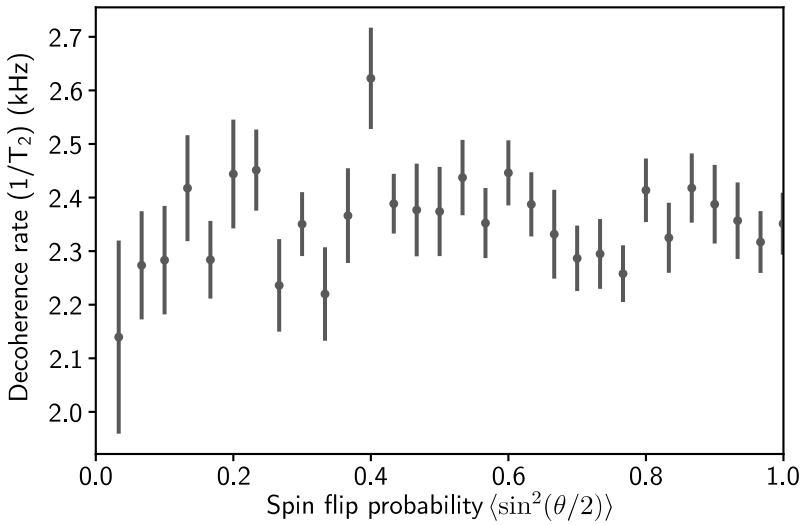

(b) Two-pulse T_2 measurement at 14 mK as a function of spin flip probability $\langle \sin^2(\theta/2) \rangle$ from refocusing pulse angle θ. In conventional ESR the signature of instantaneous diffusion would be a decrease in decoherence rate with lower spin flip probability. This effect is not visible with this device, likely due to the strongly inhomogeneous B_1 field preventing the application of an effective θ pulse.

Figure 6.17: Two-pulse echo measurements with variable refocusing pulse amplitude

6.10 Discussion

In this chapter we have demonstrated that a high-cooperativity $C = \frac{g_{\mathrm{ens}}^2}{\gamma_{\mathrm{s}}\kappa_{\mathrm{c}}} = 153$ coupling between a superconducting resonator and a ^{145}Nd:Y_2SiO_5 ensemble can be used to perform pulsed ESR spectroscopy. By performing an echo-detected field and frequency sweep in Section 6.3.1, the avoided crossing can be mapped and T_2 measurements at various points across the avoided crossing, varying both magnetic field B_0 and probe frequency f, do not show a strong effect on coherence time, which is measured at $T_2 = (409 \pm 14)\,\mu\mathrm{s}$ at 13 mK.

By varying the sample box temperature from 14 mK–1.2 K we show in Section 6.4.2 that polarising the spin bath suppresses spin decoherence substantially, in excellent agreement with theoretical models. The high-cooperativity coupling between spin and resonator results in several spin echoes in a self-stimulated echo train, as reported in Section 6.5. While the highly inhomogeneous B_1 field generated by the resonator prevents coherent driving of the spin magnetisation around the Bloch sphere using on-resonance pulses, in Section 6.6 adiabatic fast passage can be exploited to rotate the net magnetisation by π and invert the echo, and to implement an arbitrary θ pulse enabling Rabi oscillations to be observed. With an inverted echo, T_1 can be measured by inversion recovery as in Section 6.7, where the inhomogeneous B_1 causes a range of Purcell-enhanced relaxation times, approximated by a biexponential fit with $T_{1,\mathrm{fast}} = 696\,\mathrm{ms}$ and $T_{1,\mathrm{slow}} = 9.4\,\mathrm{s}$.

Challenges in performing pulsed ESR in these regimes include the dispersive frequency shift of the resonator, requiring both field and frequency to be calibrated. In practice this means performing an echo-detected frequency sweep at the start of each experimental run. The high $Q = 72\,000$ of the superconducting resonator causes a long ringup and ringdown time for each pulse, such that pulse lengths less than ~5 µs substantially reduce the echo amplitude. The long bulk T_1 times at 14 mK make measurements requiring a spin ensemble at thermal equilibrium challenging, as found in Section 6.8 where operating with a shot repetition time long enough to let bulk spins relax would make each experimental run infeasibly long. The highly inhomogeneous $B_1 \propto \frac{1}{r}$ field generated by this resonator design causes a spatial variation in Rabi frequency. This suggests a redesign of the resonator to achieve a more homogeneous B_1 field may provide more coherent control and enable additional measurements such as attempted in Section 6.9.

Chapter 7

Ytterbium doped Y_2SiO_5

So far in this thesis the experiments have focused on on ^{145}Nd:Y_2SiO_5. ^{145}Nd proved a convenient testbed for measurement techniques, due both to the ready availability of strongly doped isotopically purified samples, and the preference of Nd to dope into Y_2SiO_5 site 2 due to its large ionic radius compared to Y, simplifying the interpretation of anisotropic ESR spectra and decoherence mechanisms.

We now move on to fabricate superconducting resonators on Yb:Y_2SiO_5, measuring coherence properties in the high-field limit. Yb is a strong candidate for research in cavity QED using rare-earth spins as its ^{171}Yb isotope is unique in the rare-earths with its nuclear $I = \frac{1}{2}$ [27, 28], providing a simple 4-level atomic system that nonetheless exhibits exploitable ZEFOZ properties. This is motivated by demonstrating steps toward coupling resonators to near-ZEFOZ transitions at low magnetic fields [14, 29], and by Yb's strong optical transitions [28] being a potential route toward microwave–optical upconversion.

7.1 High-frequency measurements

We begin by performing measurements at high (~5 GHz) frequencies, corresponding to ESR transitions at similar magnetic fields to the previous chapters. This allows a comparison to the measurements of ^{145}Nd, and provides a reference coherence time in the high-field limit for later comparison to near-ZEFOZ measurements.

7.1.1 Device

The resonators used in this chapter are a spiral design, chosen to facilitate reaching low ~2 GHz frequencies compared to the thin-ring designs previously fabricated. A spiral geometry also generates a more homogeneous B_1 magnetic field [130] which may benefit future measurements requiring accurate Rabi frequencies.

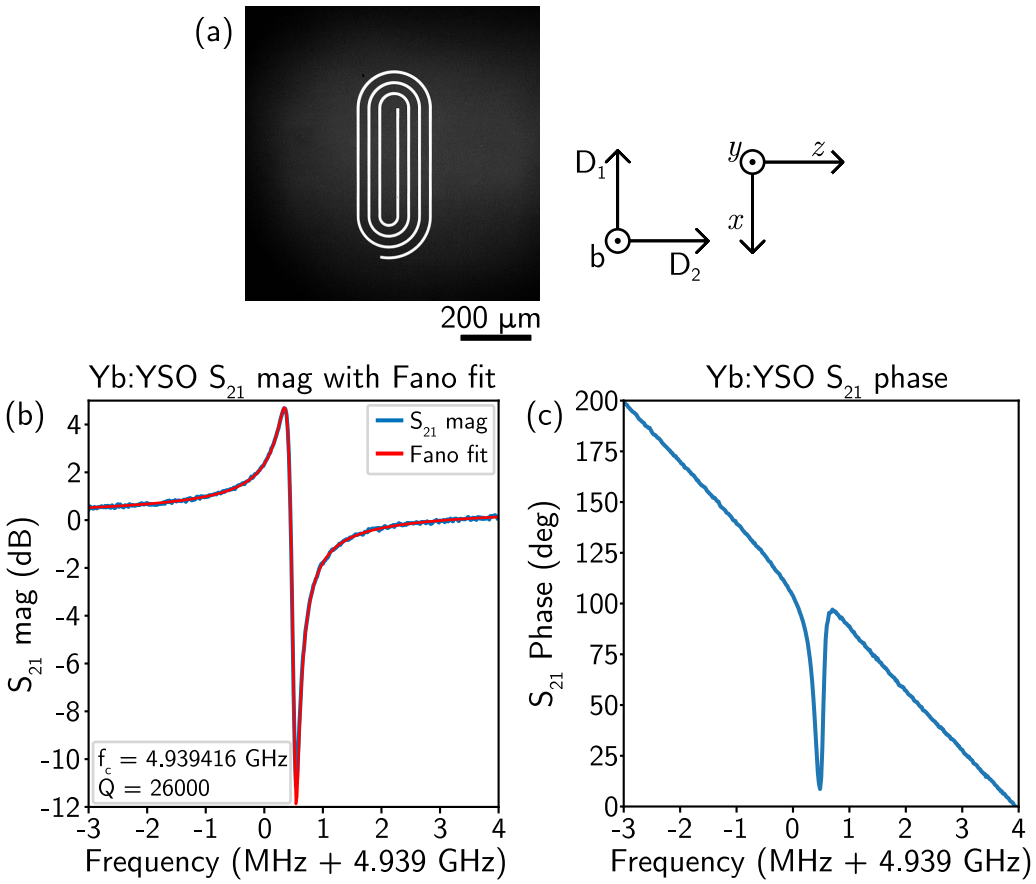

Figure 7.1: (a) Micrograph of the NbN resonator on 50 ppm ^{nat}Yb:Y_2SiO_5 substrate. The S_{21} transmission through the cavity for a MW power of −90 dBm into the 3D cavity is shown in (b) magnitude and (c) phase for zero applied magnetic field. A Fano fit to the resonance magnitude $|S_{21}|$ using Eqn. 2.11 yields the centre frequency $f_c = 4.939$ GHz and quality factor $Q = 26\,000$. These devices were measured at a sample box temperature of 20 mK.

A series of spiral resonators, 10 targeting 2 GHz–3 GHz and 2 at higher frequencies, were fabricated in 15 nm NbN sputtered on Y_2SiO_5 doped with 50 ppm (10^{24} m^{-3}) ^{nat}Yb. The crystal was cut into a 5.0 mm×5.0 mm×1.6 mm chip, with the NbN resonator patterned by direct write photolithography. The chip was installed in the LCN dilution refrigerator described in Section 4.3.3 at a temperature of 20 mK measured at a sample holder thermally anchored to the 3D copper cavity. This chapter uses the fridge's 1.5–6 GHz output line.

The resonator used for high frequency measurements is shown in Fig. 7.1(a). Using an identical CW measurement setup with a VNA to that in Section 6.2, the resonator's frequency response was measured and the $|S_{21}|$ was fitted with a Fano lineshape Eqn. 2.11 in Fig. 7.1(b). This gives its zero-field centre frequency $f_c = 4.939$ GHz and quality factor $Q = 26\,000$ for power $P_{cav} = -90$ dBm into the

cavity. The reduced quality factor of the resonator may be due to a less stringent solvent clean in a non-cleanroom environment prior to film deposition.

7.1.2 CW characterisation

To identify the origin of observed transitions, determine the precise misalignment between the lab frame (x, y, z) and crystal frame (D_1, D_2, b), and extract coupling parameters, we begin as before with CW measurements with a VNA.

ESR spectrum

The magnetic field was aligned to the plane of the superconductor, and an ESR spectrum taken by tracking the resonator frequency with increasing magnetic field strength 0 mT–450 mT, using methods developed in Section 5.3.2. Data for a scan close to the D_2 axis is shown in Fig. 7.2.

Yb, unlike Nd, dopes into both crystal sites to a similar extent so a signal is seen from both site 1 (red) and site 2 (blue). The natural isotopic mixture of Yb in the crystal results in a strong signal from $I = 0$ isotopes ^{168}Yb, ^{170}Yb, ^{172}Yb, ^{174}Yb, and ^{176}Yb at 370 mT, and a identifiable signal from the $I = \frac{1}{2}$ isotope ^{171}Yb at 236 mT and 433 mT. Breit-Rabi diagrams for both nuclear spins are presented in Fig. 7.2(a,b).

Roadmap

A roadmap of ESR transition fields against magnetic field angle is shown in Fig. 7.3. Simulating the angular dependence in sites 1 and 2 for both $I = 0$ and $I = \frac{1}{2}$ isotopes differentiates the site 2 transitions. Site 1 follows the correct general trend. The alignment of the magnetic field in the crystal axis frame is determined based on these measurements, with the deviation of B_0 from the D_1–D_2 plane determining the degree of sub-site splitting, and the rotation within D_1–D_2 shifting the roadmap plot along the x-axis. From these, the best fit is found for $0° \sim [0.986, -0.167, 0.015]_{(D_1,D_2,b)}$ and $90° \sim [0.167, 0.986, 0.001]_{(D_1,D_2,b)}$. This corresponds to a misalignment of 0.85° between the b crystal axis and the normal to the superconducting plane, and a 9.6° misalignment between D_1 and the magnet x axis.

This identification of the orientation of the crystal frame with respect to the superconductor and lab frames is vital for eventual alignment to a near-ZEFOZ transition.

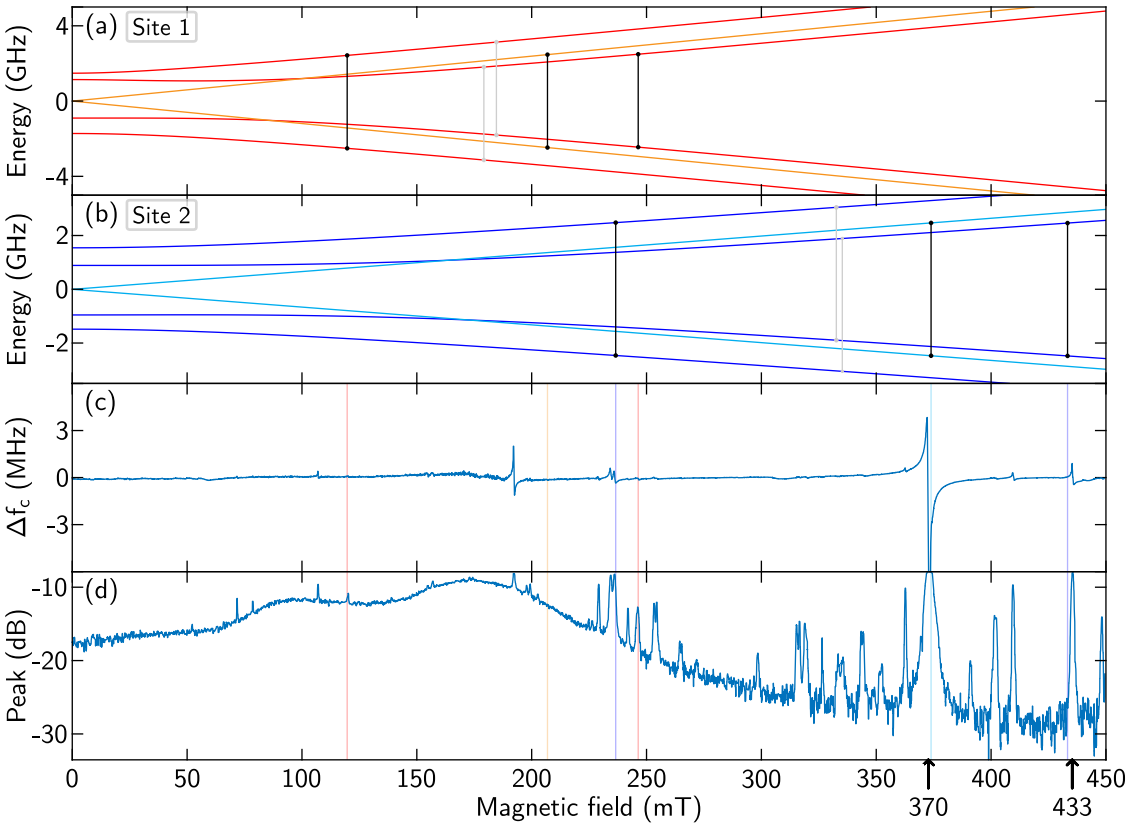

Figure 7.2: ESR spectrum for Yb:Y_2SiO_5 for magnetic field close to D_2, along the axis $B_0 \sim [0.167, 0.986, 0.001]_{(D_1,D_2,b)}$. (a,b) Breit-Rabi diagrams for (a) site 1 and (b) site 2 Yb:Y_2SiO_5, showing transitions for $I = 0$ and $I = \frac{1}{2}$ isotopes at 4.9395 GHz. (c) Frequency shift induced in resonator due to dispersive interaction with spins. Two strong signals from $I = 0$ isotopes ^{168}Yb, ^{170}Yb, ^{172}Yb, ^{174}Yb, ^{176}Yb in site 1 and site 2, along with weaker shifts from $I = \frac{1}{2}$ isotope ^{171}Yb and $I = \frac{5}{2}$ isotope ^{173}Yb. (d) Resonator prominence, measured from the minimum of the resonance profile. Reduction in resonator prominence manifests as a positive peak. Comparison between ESR spectrum and simulation of the spin Hamiltonian identifies the transitions at 370 mT and 433 mT as from $I = 0$ and $I = \frac{1}{2}$ isotopes respectively.

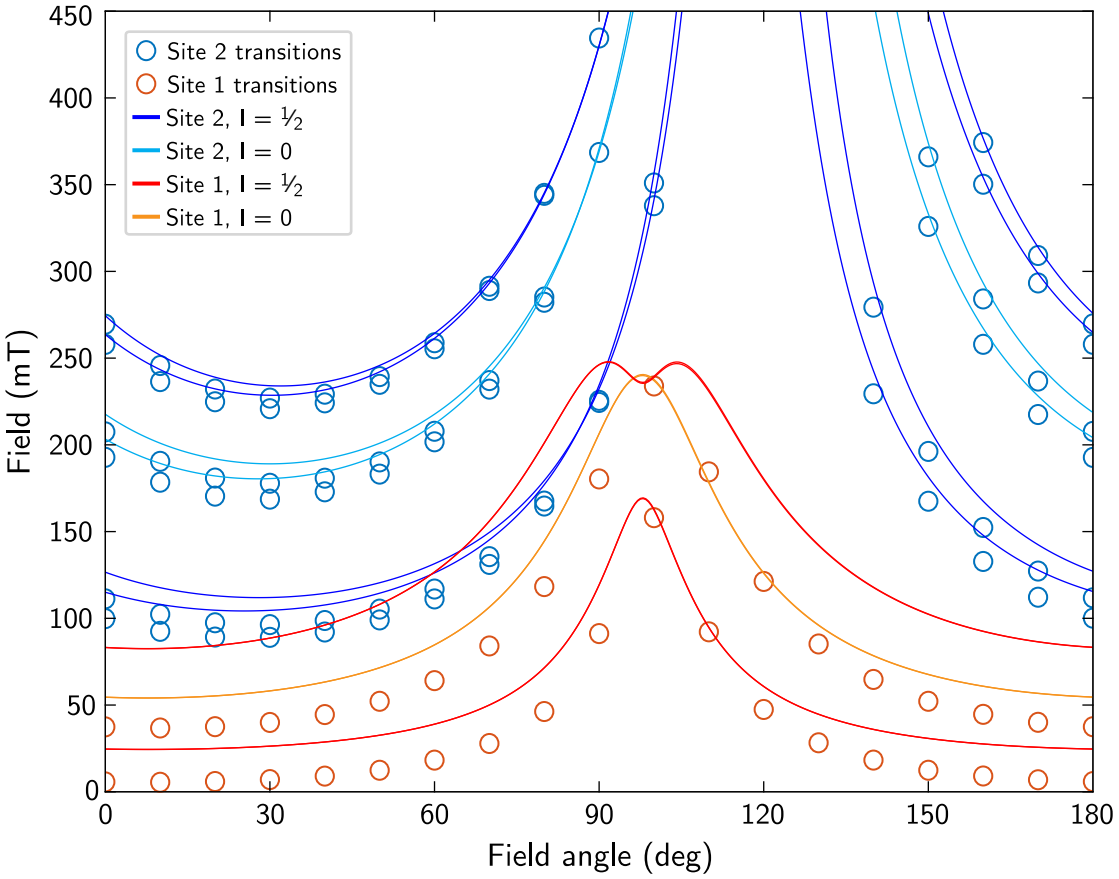

Figure 7.3: Roadmap of Yb:Y_2SiO_5 for field angles close to the D_1–D_2 plane. 0° corresponds to the axis $B_0 \sim [0.986, -0.167, 0.015]_{(D_1,D_2,b)}$ and 90° to $B_0 \sim [0.167, 0.986, 0.001]_{(D_1,D_2,b)}$. Transition fields are identified by tracking the resonance with a VNA as in Fig. 7.2. Transitions attributable to site 1 and site 2 for $I = 0$ and $I = \frac{1}{2}$ isotopes are shown, along with simulation from the spin Hamiltonian. A close agreement for the angular dependence of site 2 transitions is achieved, confirming the identification of the 370 mT $I = 0$ transition and the 433 mT $I = \frac{1}{2}$ transition in Fig. 7.2.

Coupling strengths

With two particular transitions along D_2 identified in Fig. 7.2 as being due to different isotopes of Yb, we investigate the $I = 0$ transition at 370 mT and $I = \frac{1}{2}$ transition of ^{171}Yb at 433 mT, where the gyromagnetic ratio $\left|\frac{df}{dB}\right| = 12.3\,\mathrm{MHz\,mT^{-1}}$.

A 2D field–frequency map of the 370 mT transition is shown in Fig. 7.4. An avoided crossing is visible, and fitting to the 2D data with Eqn. 2.12 as described in Section 6.2.2 yields the coupling parameters $g_{\mathrm{ens}}/2\pi = 7.12\,\mathrm{MHz}$, $\gamma_{\mathrm{s}}/2\pi = 4.01\,\mathrm{MHz}$, $\kappa_{\mathrm{c}}/2\pi = 49.5\,\mathrm{kHz}$, corresponding to a high cooperativity $C = \frac{g_{\mathrm{ens}}^2}{\gamma_{\mathrm{s}}\kappa_{\mathrm{c}}} = 255$.

For the 433 mT transition in Fig. 7.5. A broadening and small frequency shift is observed. The fit yields coupling parameters $g_{\mathrm{ens}}/2\pi = 1.20\,\mathrm{MHz}$, $\gamma_{\mathrm{s}}/2\pi = 3.73\,\mathrm{MHz}$, $\kappa_{\mathrm{c}}/2\pi = 45.3\,\mathrm{kHz}$, giving a weak coupling $C = \frac{g_{\mathrm{ens}}^2}{\gamma_{\mathrm{s}}\kappa_{\mathrm{c}}} = 8.5$.

The difference in coupling strengths g_{ens} is due to the different nuclear spins of the two transitions. Recall the coupling strength $g_{\mathrm{ens}} \propto g_0\sqrt{N}$. The difference in the single-spin coupling g_0 can be accounted for by calculating the amplitudes with Easyspin in Fig. 7.6(a), predicting a ratio $\frac{g_{0,433}}{g_{0,370}} = \frac{68.9}{107} = 0.644$. The relative number N of spins is affected by the spin density and the population of each ESR transition. The natural abundance of $I = 0$ Yb isotopes as illustrated in Fig. 7.6(b) is 69.59 % versus $I = \frac{1}{2}$ ^{171}Yb's 14.28 % [162], a ratio of $\frac{n_{I=0.5}}{n_{I=0}} = 0.205$. To account for the population of the ESR transition, consider that the 370 mT $I = 0$ transition is necessarily from the ground state, while the one at 433 mT is the $m_I = -\frac{1}{2}$ ESR transition from the excited nuclear state, 1.187 GHz above the ground state. The density of ^{171}Yb spins in the excited nuclear state is then determined by the nuclear spin polarisation $P_\uparrow = \frac{n_\uparrow}{n_\uparrow + n_\downarrow} = \frac{1}{1+\exp(T_{\mathrm{Ze}}/T)}$, plotted in Fig. 7.6(c), where the nuclear Zeeman temperature $T_{\mathrm{Ze}} = \frac{hf}{k_{\mathrm{B}}} = 57\,\mathrm{mK}$. The relative g_{ens} of the two transitions then depends on the temperature as

$$\frac{g_{\mathrm{ens},433}}{g_{\mathrm{ens},370}} = \frac{g_{0,433}}{g_{0,370}}\sqrt{\frac{n_{I=0}}{n_{I=0.5}} \times P_\uparrow}$$

giving the measured ratio $\frac{g_{\mathrm{ens},433}}{g_{\mathrm{ens},370}} = \frac{1.20\,\mathrm{MHz}}{7.12\,\mathrm{MHz}}$ at $T = 83\,\mathrm{mK}$. This elevated nuclear spin temperature (compared to the sample box temperature 20 mK) may be due to continuous-wave measurements prior to this scan throwing the nuclear spin polarisation out of thermal equilibrium.

7.1.3 Pulsed ESR

As the planned low-frequency measurements necessitated building a new microwave bridge compatible with 2 GHz–4 GHz, detailed in Section 4.4.1, pulsed measure-

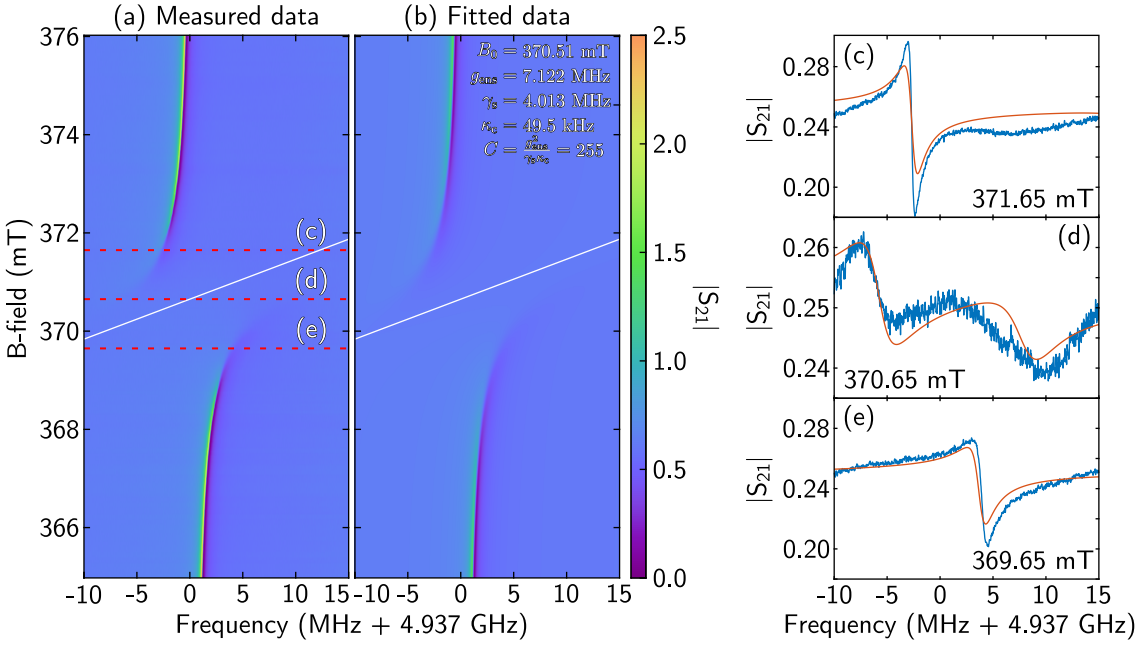

Figure 7.4: An avoided crossing with the ESR transition from $I = 0$ isotopes of Yb:Y_2SiO_5 in site 2. Extracted coupling parameters are $g_{ens}/2\pi = 7.12\,\text{MHz}$, $\gamma_s/2\pi = 4.01\,\text{MHz}$, $\kappa_c/2\pi = 49.5\,\text{kHz}$, yielding a high cooperativity $C = \frac{g_{ens}^2}{\gamma_s \kappa_c} = 255$.

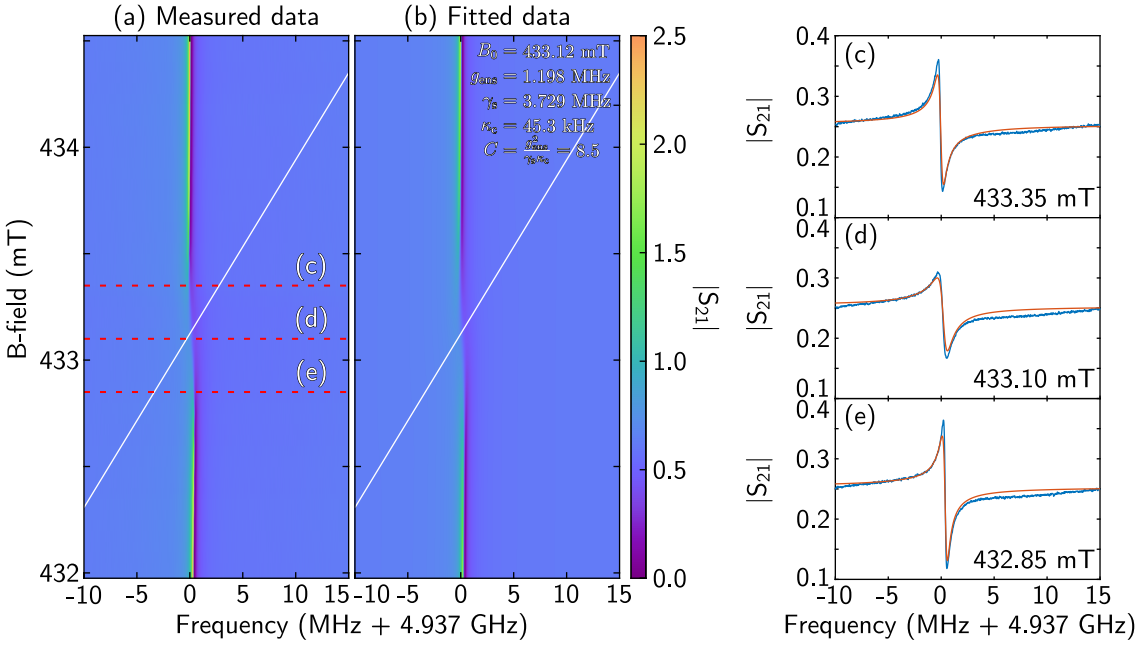

Figure 7.5: An avoided crossing with the $m_I = -\frac{1}{2}$ ESR transition from the $I = \frac{1}{2}$ isotope ^{171}Yb:Y_2SiO_5 in site 2. Extracted coupling parameters are $g_{ens}/2\pi = 1.20\,\text{MHz}$, $\gamma_s/2\pi = 3.73\,\text{MHz}$, $\kappa_c/2\pi = 45.3\,\text{kHz}$, yielding a weaker coupling $C = \frac{g_{ens}^2}{\gamma_s \kappa_c} = 8.5$.

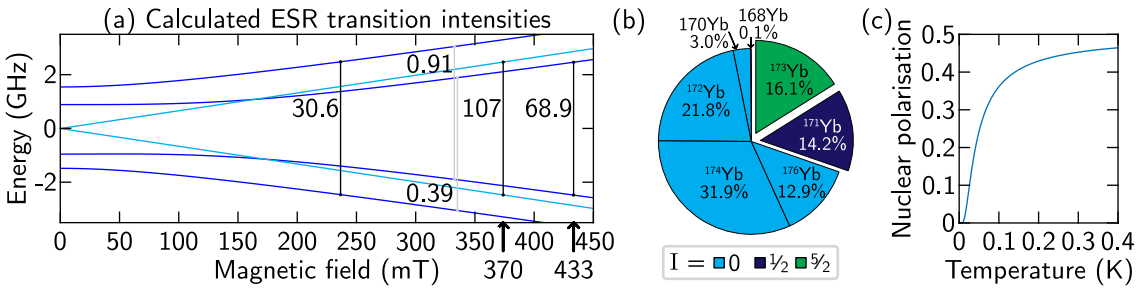

Figure 7.6: Factors contributing to the lower coupling strength for $I = \frac{1}{2}$ transition at 433 mT. (a) Lower transition intensity predicted by simulation. (b) Lower abundance of ^{171}Yb isotope. (c) Low thermal population of excited nuclear state at mK temperatures.

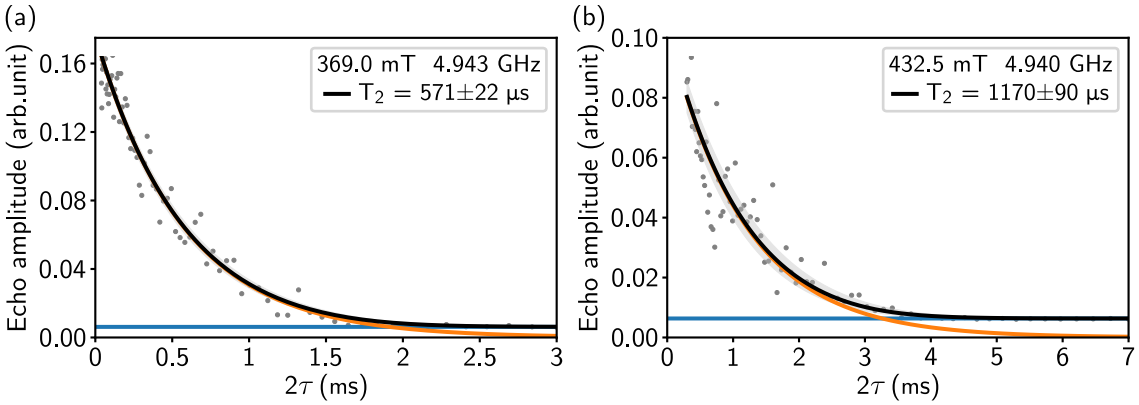

Figure 7.7: T2 measurements of (a) the $I = 0$ Yb transition at 370 mT and (b) the $I = \frac{1}{2}$ ^{171}Yb transition at 433 mT.

ments with the high frequency resonator were also performed with this bridge to establish that the bridge functions correctly. Despite the 4.939 GHz resonator being 1 GHz above the bridge's nominal frequency range (based on its constituent components' data sheets), the bridge functioned correctly and pulsed measurements of the 370 mT and 433 mT transitions were performed. The use of a 3 W amplifier proved unnecessary as the 13 dBm output of the VSG was sufficient to observe a strong echo, and was also potentially unsafe outside the specified window of the bridge's circulators due to the risk of large reflected pulses damaging the high-power amplifier.

Two-pulse T_2 measurement

Using the methods discussed in Section 6.4, two-pulse echo measurements of the two transitions were taken. Averaging the echo amplitudes of 8 consecutive runs and fitting to the amplitude decay shown in Fig. 7.7 using Eqn. 6.2 yields the coherence times $T_{2,370} = (571 \pm 22)$ µs and $T_{2,433} = (1170 \pm 90)$ µs.

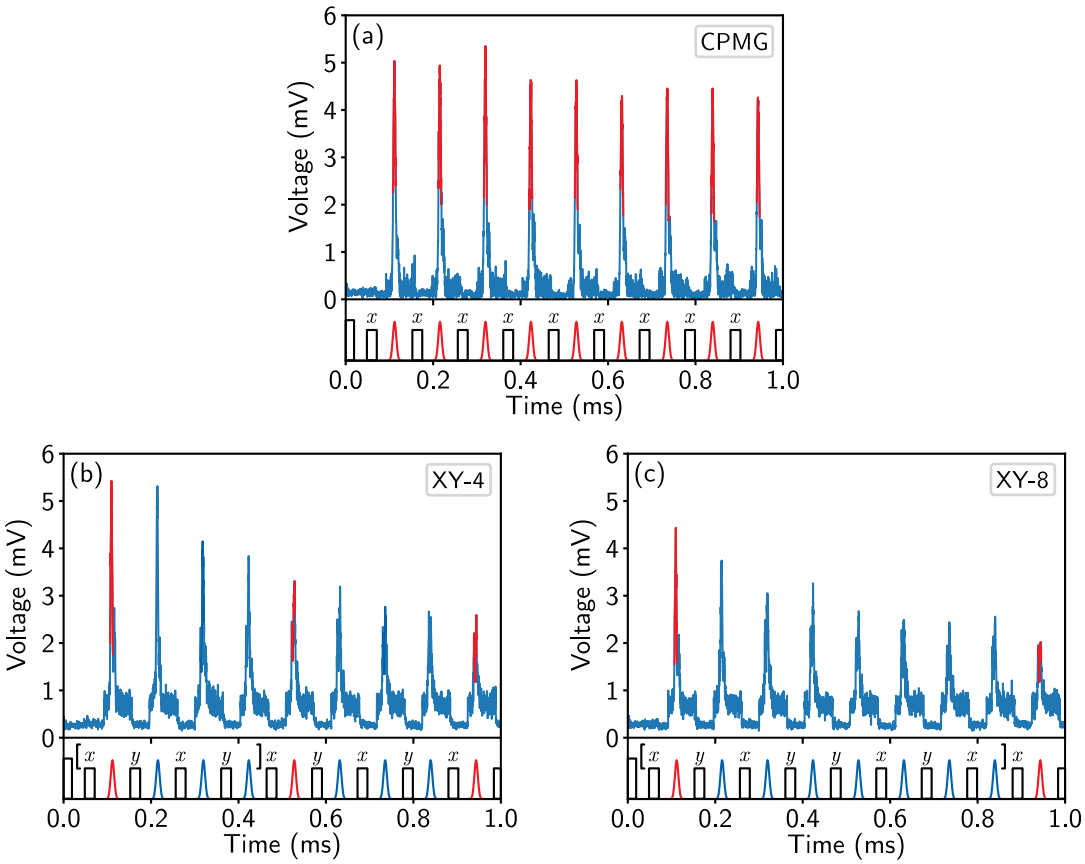

Figure 7.8: Dynamical decoupling sequences used to reduce the sensitivity of T_2 measurements to low-frequency magnetic field noise, showing both the control pulse sequence and an experimental echo chain. Red echoes indicate the echoes in the repeating unit that are used to generate the decay profiles in Fig. 7.9.

The difference in coherence time between these transitions may be attributed to the 5× greater spin density of $I = 0$ isotopes combined with the greater thermal population of the 370 mT ground state transition versus the 433 mT $I = \frac{1}{2}$ ^{171}Yb transition from the excited nuclear state. This results in a greater spectral diffusion rate Γ_{SD} for the $I = 0$ isotopes.

The coherence time $T_{2,433} = (1170 \pm 90)\,\mu s$ measured for ^{171}Yb is similar to published measurements of a ^{171}Yb:Y_2SiO_5 cut from the same boule as the sample measured here, with $T_2 = 1.3$ ms when not at a near-ZEFOZ transition [14].

Dynamical decoupling

Two-pulse echo sequences are sensitive to slow fluctuations in magnetic environment over the timescale of the experiment due to the long time over which magnetic noise can accumulate to give a different dephasing rate between the first τ and the second.

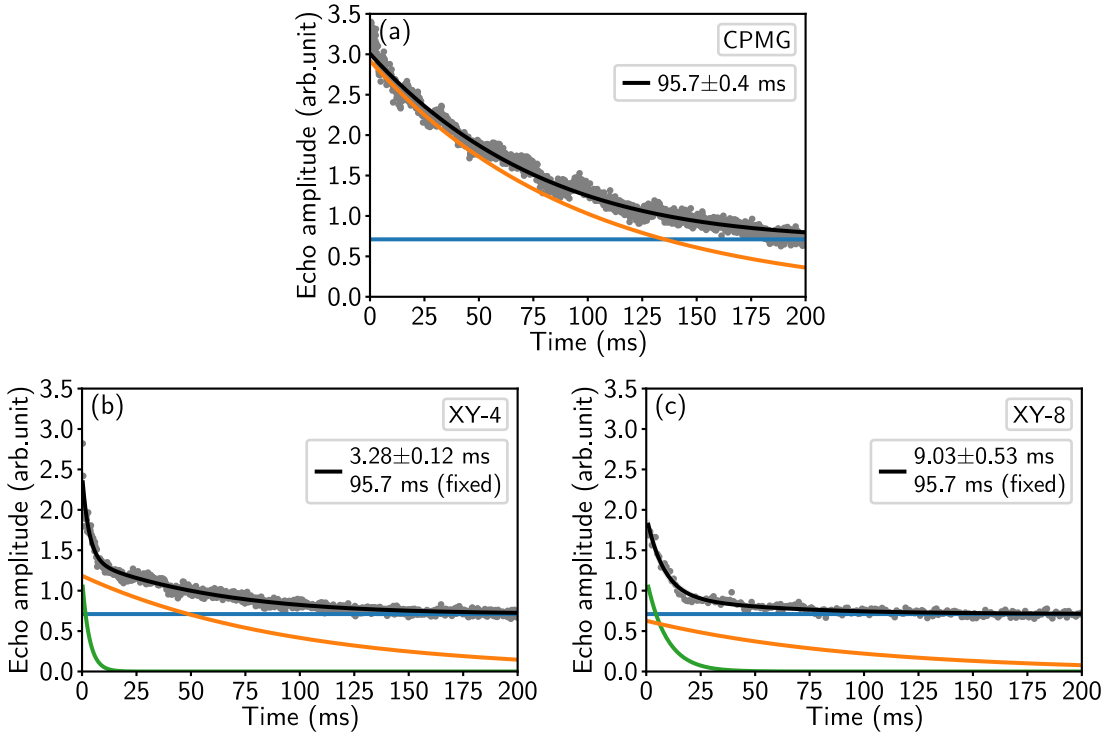

Figure 7.9: Echo decay profiles for each of the dynamical decoupling sequences in Fig. 7.8. The CPMG sequence (a) exhibits a slow exponential decay rate (95.7 ± 0.4) ms dominated by longitudinal relaxation processes. The slow exponential decay is indicated in orange, with the noise floor in blue. The XY sequences (a, b) are fitted with a biexponential using the same slow decay rate as measured by CPMG and fast decay rates $T_{2,\text{XY-4}} = (3.28 \pm 0.12)$ ms and $T_{2,\text{XY-8}} = (9.0 \pm 0.5)$ ms plotted in green, indicating the sequences are successful at extending the coherence time $T_2 = (1.17 \pm 0.09)$ ms measured by a two-pulse sequence.

This can be accounted for using dynamical decoupling, whereby a chain of closely-spaced π pulses repeatedly refocus the echo with a much shorter τ between each pulse. This greatly reduces the sensitivity of the measurement to low-frequency noise.

A simple dynamical decoupling method is the Carr-Purcell-Meiboom-Gill (CPMG) sequence [163] consisting of a $\frac{\pi}{2}$ pulse followed by repeated application of π pulses along an axis 90° rotated from the initial pulse. The sequence, and a measurement of the echo chain magnitude averaged over 10 shots when pulsing on the 433 mT ^{171}Yb transition, is shown in Fig. 7.8(a) where the control pulses are not visible in the measured trace due to the acquisition switch being closed during the high-power pulses. In the CPMG sequence the amplitude of every echo is measured by integrating over the FWHM, displayed in red.

Plotting the CPMG amplitudes versus time since the initial $\frac{\pi}{2}$ pulse in Fig. 7.9(a) results in a single exponential decay with a characteristic time (95.7 ± 0.4) ms. The CPMG sequence, consisting only of refocusing pulses along one axis, is highly effective for initial magnetisations along the refocusing axis where the decay rate is determined by longitudinal (T_1) processes [164] as the repeated application of pulses creates stimulated echoes from the projection on the z-axis. However for magnetisations perpendicular to the pulse axis, errors in the pulses from being perfect π rotations accumulate and cause a rapid decay. Hence the characteristic (95.7 ± 0.4) ms decay rate measured by a CPMG predominantly consists of incoherent relaxation processes.

Modifying the CPMG sequence to consist of alternating x and y rotations produces the XY-4 sequence $[\pi_x\pi_y\pi_x\pi_y]^n$, which provides a robustness to noise and pulse error for initial states for any input state [161, 165]. The sequence, and an acquired echo chain using this sequence, is shown in Fig. 7.8(b). Measuring the echo amplitude after every repeated unit, indicated by the red echoes, gives a decay profile in Fig. 7.9(a) consisting of a biexponential decay with a slow incoherent process corresponding to longitudinal relaxation and stimulated echoes, and a faster decay due to coherent processes. Fitting to this, fixing the slow rate to the rate measured by CPMG as the relaxation processes are assumed to be the same for both sequences, gives a fast decay rate $T_{2,\text{XY-4}} = (3.28 \pm 0.12)$ ms, a near three-fold improvement to the $T_2 = 1.2$ ms from the two-pulse measurement. A significant improvement to coherence times by using dynamical decoupling is consistent with previous measurements of ^{171}Yb:Y_2SiO_5 using conventional ESR spectrometers [28].

The XY-4 sequence can be extended to higher orders with the XY-8 sequence [161, 165] $[\pi_x\pi_y\pi_x\pi_y\pi_y\pi_x\pi_y\pi_x]^n$ shown in Fig. 7.8(c). This sequence typically performs better than lower order sequences [166], and fitting to the decay with a biexponential demonstrates an extension to the fast decay rate of the coherent process $T_{2,\text{XY-8}} = (9.0 \pm 0.5)$ ms, a further improvement over XY-4. The incoherent slow process remains the same for all three DD sequences.

Inversion recovery T_1 measurement

Spin relaxation measurements on both transitions were performed using WURST adiabatic fast passage pulses to invert the echo and monitor its recovery using methods developed in Section 6.7. The 370 mK transition gave a consistently inverted echo, and fitting to the data in Fig. 7.10(a) with 6.5 yields two char-

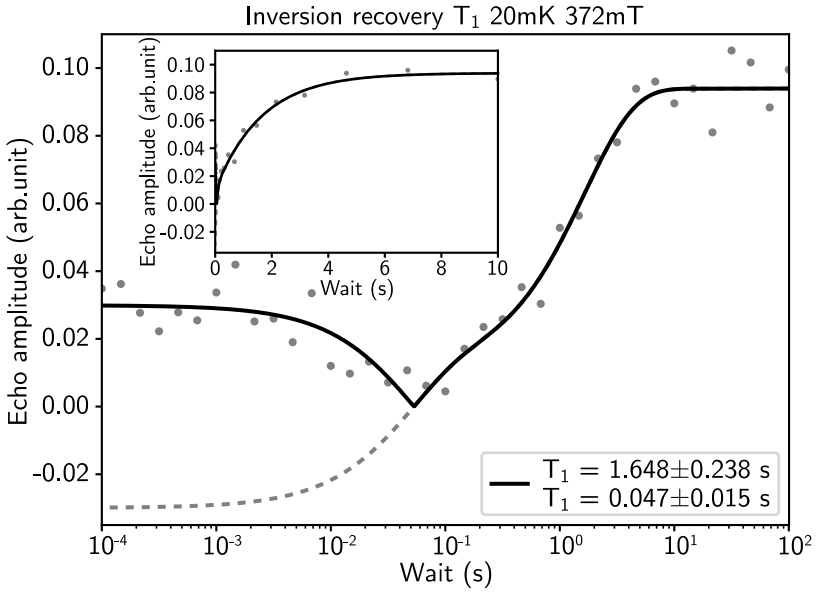

(a) T_1 measured at the 370 mT $I = 0$ Yb transition, fitted with a biexponential to give two characteristic decay rates $T_{1,\text{fast}} = 47\,\text{ms}$ and $T_{1,\text{slow}} = (1.6 \pm 0.2)\,\text{s}$.

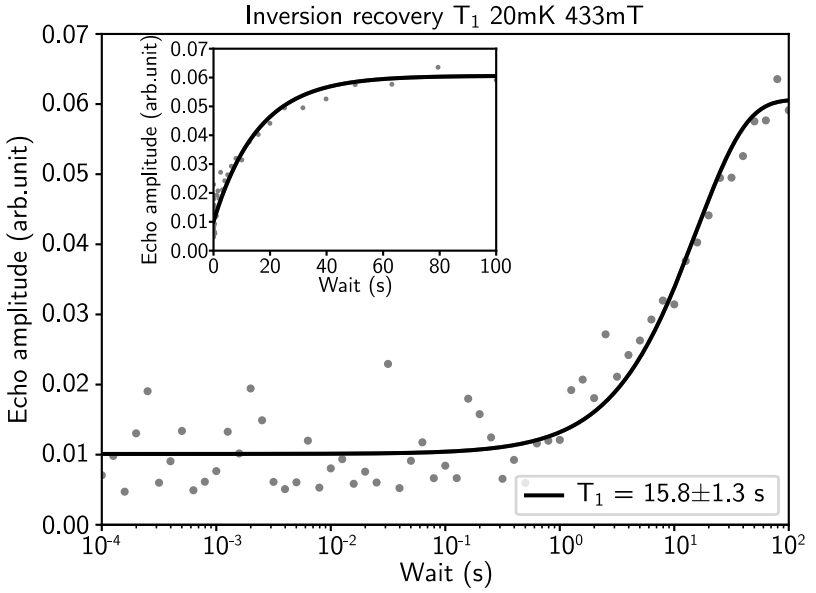

(b) T_1 measured at the 433 mT $I = \frac{1}{2}$ ^{171}Yb transition. Due to a highly inconsistent inverted echo magnitude below ~1 s a simple exponential fit was used to estimate the decay rate of $T_{1,\text{slow}} = (15.8 \pm 1.3)\,\text{s}$, significantly slower than the more populated 370 mT due to suppression of cross-relaxation.

Figure 7.10: T_1 of Yb:Y_2SiO_5 measured by inversion recovery.

acteristic decay rates $T_{1,\text{fast}} = 47\,\text{ms}$ and $T_{1,\text{slow}} = (1.6 \pm 0.2)\,\text{s}$ (with amplitudes $C_{\text{fast}} = 0.0040 \pm 0.0005$ and $C_{\text{slow}} = 0.0080 \pm 0.0005$).

Achieving a consistently inverted echo on the 433 mT transition proved challenging, as seen in Fig. 7.10(b) where the echo amplitude below ~1 s is extremely noisy. A rough fit to the data using a simple exponential decay yields a characteristic decay time $T_{1,\text{slow}} = (15.8 \pm 1.3)\,\text{s}$, significantly slower than the rate $T_{1,\text{slow}} = (1.6 \pm 0.2)\,\text{s}$ at 370 mT. This aligns well with the conclusion in Section 6.7 that the slow rate is dominated by cross-relaxation between resonant spins, as the rate depends heavily on spin concentration $R_{\text{FF}} \propto n^2$ [26] resulting in a significantly longer T_1 for the less populated 433 mT transition.

7.2 Low-frequency measurements

With the high-field coherence of Yb:Y_2SiO_5 characterised, we move on to couple one of the low-frequency spiral resonators to a low-field spin transition. This is part of an experimental plan to drive a coherence-enhancing near-ZEFOZ transition.

7.2.1 Near-ZEFOZ experimental plan

A ZEFOZ transition, as described in Section 2.1.5, enhances spin coherence by operating at a magnetic field at a specific point in 3D space at which $\frac{\mathrm{d}f}{\mathrm{d}B} = 0$, effectively detuning the spin precession from magnetic field noise and inhomogeneity in the environment and measurement setup. This results in an increase in coherence time. Similarly a near-ZEFOZ transition operates at a point which minimises $\left|\frac{\mathrm{d}f}{\mathrm{d}B}\right|$. ^{171}Yb:$Y_2SiO_5$ exhibits these near-ZEFOZ transitions, as previously demonstrated for low fields ~5 mT using an RF coil and optical detection [14]. Based on simulations in Section 2.3.3, we devise an experiment to drive these transitions with a tunable superconducting resonator.

Tuning a resonator with an out-of-plane magnetic field component, detailed for these spiral resonators in Section 3.5.2, complicates accessing a near-ZEFOZ transition as one B-field component is then determined by field required to tune the resonator. For ^{171}Yb ions in Y_2SiO_5 site 2, simulations indicate that, for small fields along the crystal b axis, a near-ZEFOZ transition can be reached by applying a moderate field in the D_1–D_2 plane. This proves to be a convenient orientation for the resonators on Y_2SiO_5 considered here, fabricated closely aligned to the D_1–D_2 plane such that a small field along b strongly tunes the resonator frequency. The

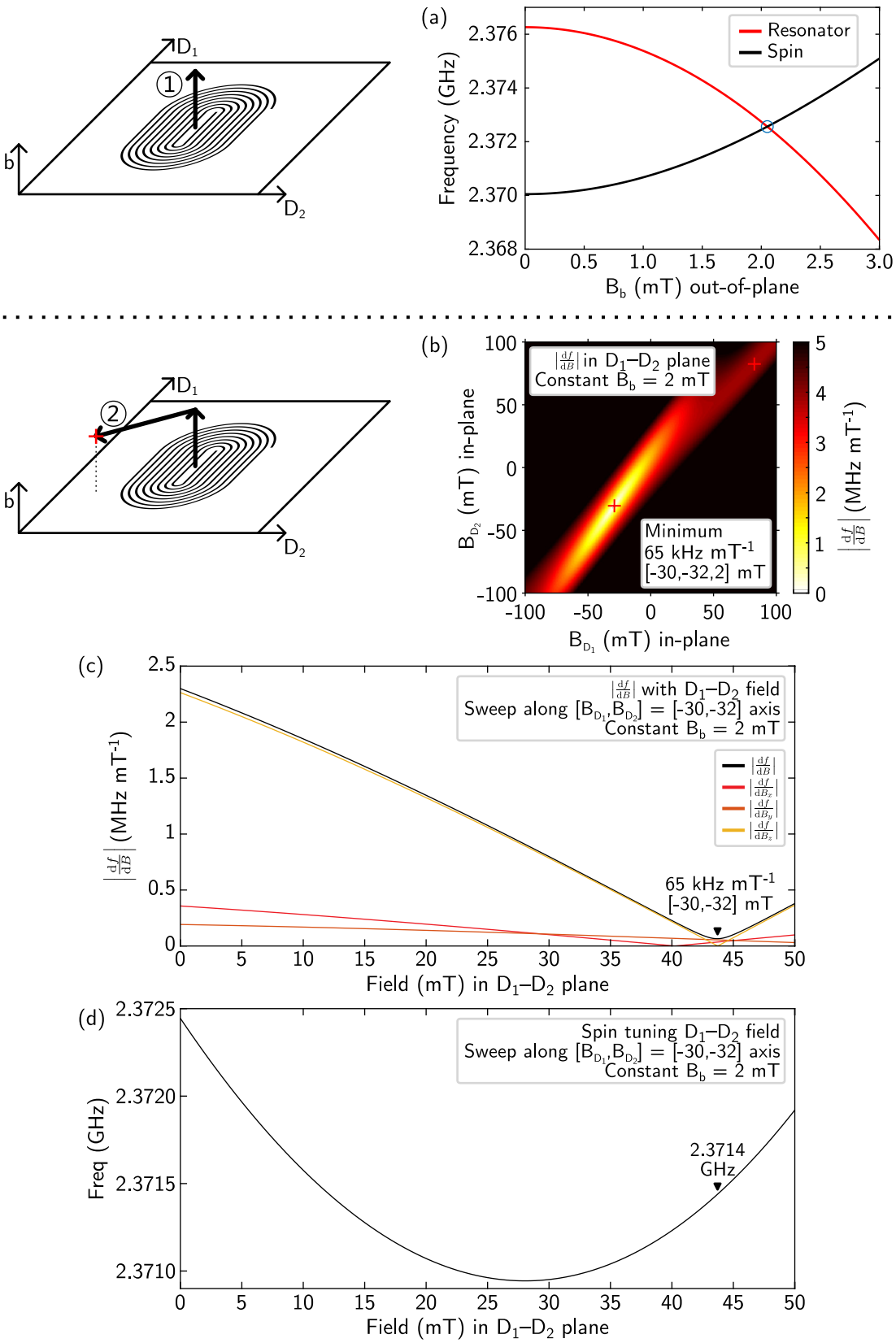

Figure 7.11: Near-ZEFOZ experimental plan. Transition considered here is the [1–3] transition of ^{171}Yb in Y_2SiO_5 site 2. 1: Apply out-of-plane field to tune resonator to match spin frequency as in (a). 2: For this out-of-plane field, identify in-plane field minimising $\left|\frac{df}{dB}\right|$ in (b, c). As spin frequency shifts (d), out-of-plane field may need adjustment.

data presented here corresponds to the [1–3] transition of ^{171}Yb in Y_2SiO_5 site 2, motivated by the experimentally accessible transition in Section 7.2.2.

The experiment is illustrated in Fig. 7.11. The first step is to determine the out-of-plane field required to tune the resonator to match the spin frequency, as indicated in (a). Applying a field along +b strongly tunes the resonator down and the spin up in frequency, bringing them in resonance around 2 mT. A simulated map of $\left|\frac{\mathrm{d}f}{\mathrm{d}B}\right|$ in (b) then locates a near-ZEFOZ transition at $[B_{\mathrm{D}_1}, B_{\mathrm{D}_2}, B_{\mathrm{b}}] = [-30, -32, 2]$ mT. Its $\left|\frac{\mathrm{d}f}{\mathrm{d}B}\right| = 64\,\mathrm{kHz\,mT^{-1}}$ corresponds to 0.52 % of the gyromagnetic ratio in the high-field limit along D_2 measured in Section 7.1.3, and 0.23 % that of a $g = 2$ spin[1].

Simulating ramping the field along the $[B_{\mathrm{D}_1}, B_{\mathrm{D}_2}] = [-30, -32]$ mT axis for fixed $B_{\mathrm{b}} = 2\,\mathrm{mT}$ as shown in (c) provides some indication of the accuracy needed to minimise the first-order Zeeman term. Within $\pm 1\,\mathrm{mT}$ the $\left|\frac{\mathrm{d}f}{\mathrm{d}B}\right|$ increases by 44 %, still a substantial improvement over the high-field gyromagnetic ratio, but to measure the longest coherence time the crystal orientation must be known accurately. This can be done by measuring the angular dependence of the ESR transitions and comparing the roadmap to simulations, as performed earlier in Section 7.1.2.

The spin frequency also tunes with field in the D_1–D_2 plane as shown in (d), and the resonator frequency exhibits a small shift with application of an in-plane field, so it may prove necessary to make small adjustments to the out-of-plane field required to tune the resonator to the near-ZEFOZ transition, which must then be accounted for in the calculation of the near-ZEFOZ in-plane field.

7.2.2 Device

A series of low-frequency resonators targeting 2 GHz–3 GHz were fabricated alongside the high-frequency device used for high-field characterisation. A trace of these resonances taken with a VNA is shown in Fig. 7.12, with the frequencies of zero-field transitions in ^{171}Yb:Y_2SiO_5 indicated. By applying an out-of-plane magnetic field, measurements in Section 3.5.2 indicate the resonators can be tuned down in frequency by up to 20 MHz by applying up to 3 mT. There are three resonators within this range of a zero-field transition, and only one at 2.376 GHz can be tuned in resonance with a site 2 transition at 2.370 GHz as per the scheme presented in Section 7.2.1. This resonator and the transition between states [1–3] of ^{171}Yb in site 2 were used for further spin resonance experiments due to the potential to reach a near-ZEFOZ point.

[1] Recall a $g = 2$ free electron tunes at $28.0\,\mathrm{MHz\,mT^{-1}}$.

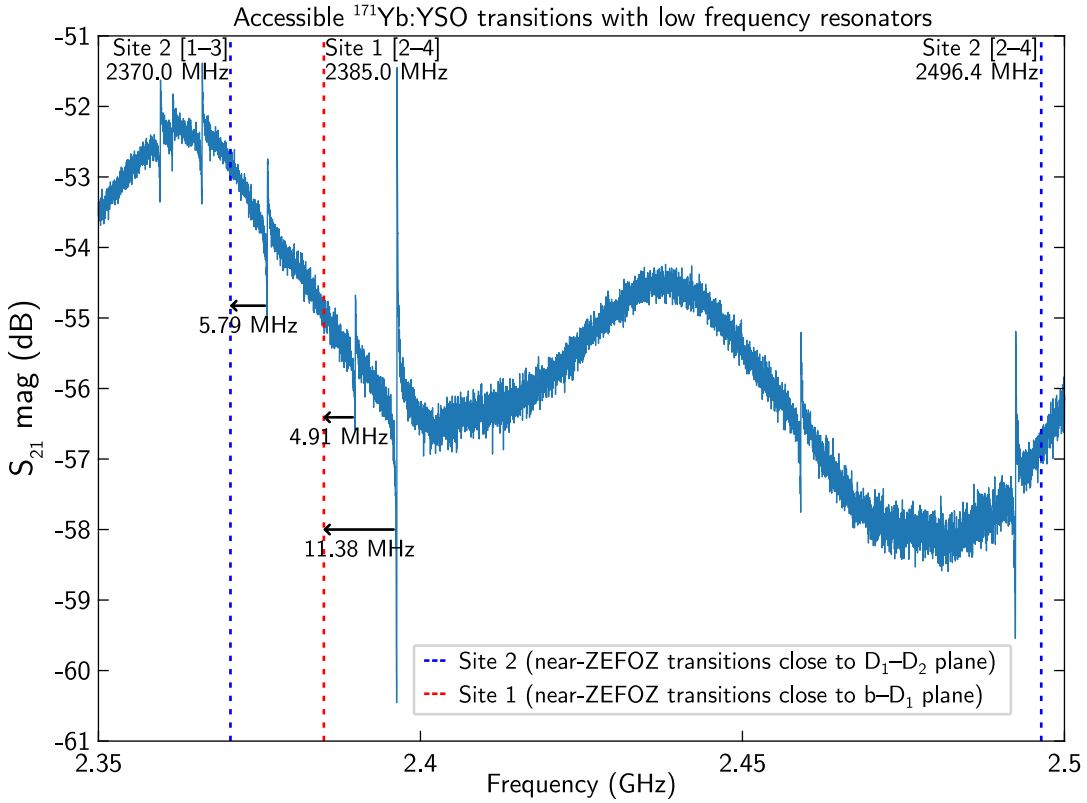

Figure 7.12: Accessible transitions with the resonators available on this chip.

CW scans of the resonator at zero applied field and low microwave power shown in Fig. 7.13 give its frequency 2.376 GHz and quality factor $Q = 26\,600$, comparable to the high frequency device in Fig. 7.1. Notably the level of background transmission through the measurement setup is approximately −53 dB lower than at 5 GHz, and the prominence of the resonance approximately 12 % that of the high frequency resonator, something we will return to in Section 7.2.4.

7.2.3 Resonator tuning

Following the experimental plan of Section 7.2.1, we apply an out-of-plane field to tune the resonator frequency down and the ESR frequency up, to bring them in resonance. This can be seen in Fig. 7.14(a), with a field applied close to the b crystal axis. A broadening of the resonance is observed at $B_0 = 2\,\mathrm{mT}$, in excellent agreement with simulation of the spin Hamiltonian.

Fitting to the 2D field-frequency map in Fig. 7.14(a) with Eqn. 2.12, accounting for the strong quadratic shift in resonator frequency for an out-of-plane field, yields the coupling parameters $g_{\mathrm{ens}}/2\pi = 450\,\mathrm{kHz}$, $\gamma_{\mathrm{s}}/2\pi = 875\,\mathrm{kHz}$, $\kappa_{\mathrm{c}}/2\pi = 27\,\mathrm{kHz}$,

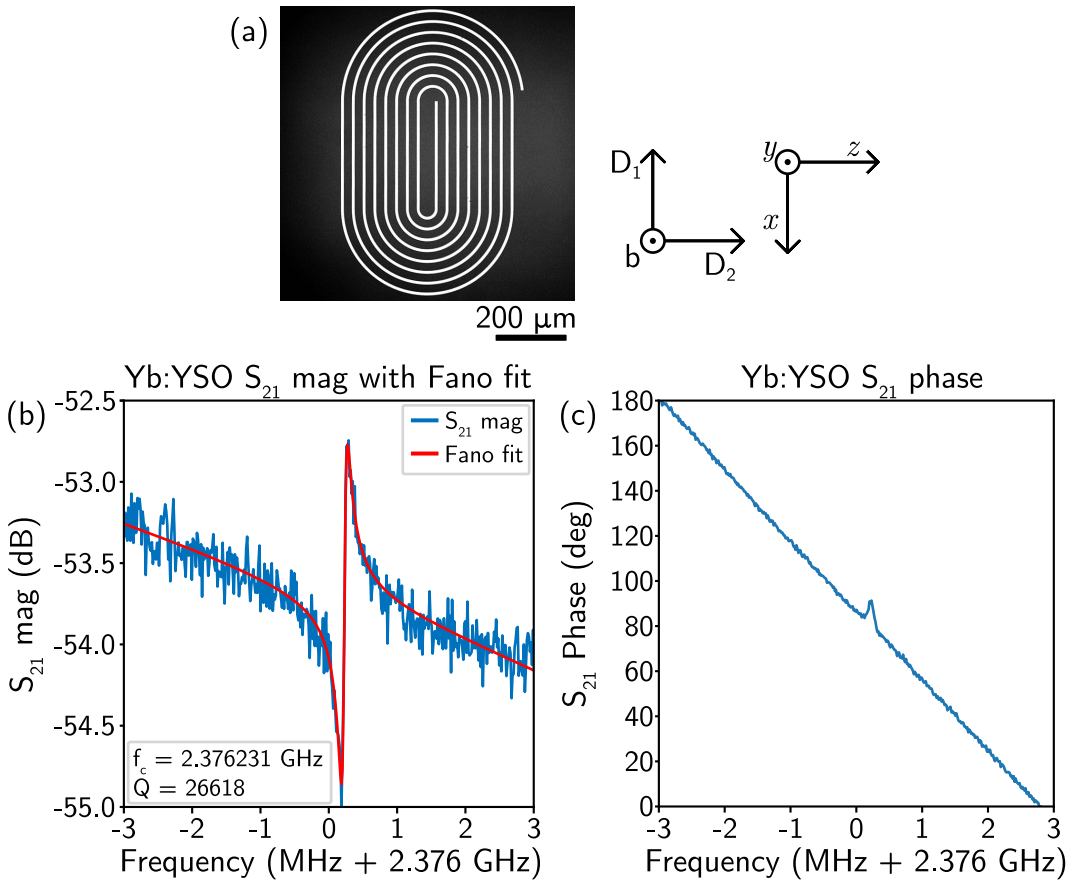

Figure 7.13: (a) Micrograph of the NbN resonator on 50 ppm $^{\text{nat}}$Yb:Y_2SiO_5 substrate. The S_{21} transmission through the cavity for a MW power of −70 dBm into the 3D cavity is shown in (b) magnitude and (c) phase for zero applied magnetic field. A fit to the resonance magnitude $|S_{21}|$ using Eqn. 2.11 yields the centre frequency $f_c = 2.376$ GHz and quality factor $Q = 87\,160$.

yielding a comparable cooperativity to the high-field measurement $C = \frac{g_{\text{ens}}^2}{\gamma_s \kappa_c} = 8.5$. The spin linewidth $\gamma_s/2\pi$ seen here is substantially narrower than that measured at 5 GHz $\gamma_s/2\pi = 3.73$ MHz, due to the decreased $\frac{df}{dB}$. This demonstrates the viability of driving low-field transitions in Yb:Y_2SiO_5 with a superconducting resonator.

7.2.4 Attempted low-frequency ESR

With the coupling between resonator and spin demonstrated at low fields, pulsed experiments were attempted at and around the centre of the spin resonance found in Fig. 7.14 at $B_b = 2$ mT, $f = 2.372$ GHz. When no echo was forthcoming using the same parameters as in 7.1.3, experimental parameters were adjusted including the addition of the 3 W solid-state amplifier (now safe to use within the operational window of the bridge's circulators), modifying length of MW pulses between 4 µs–

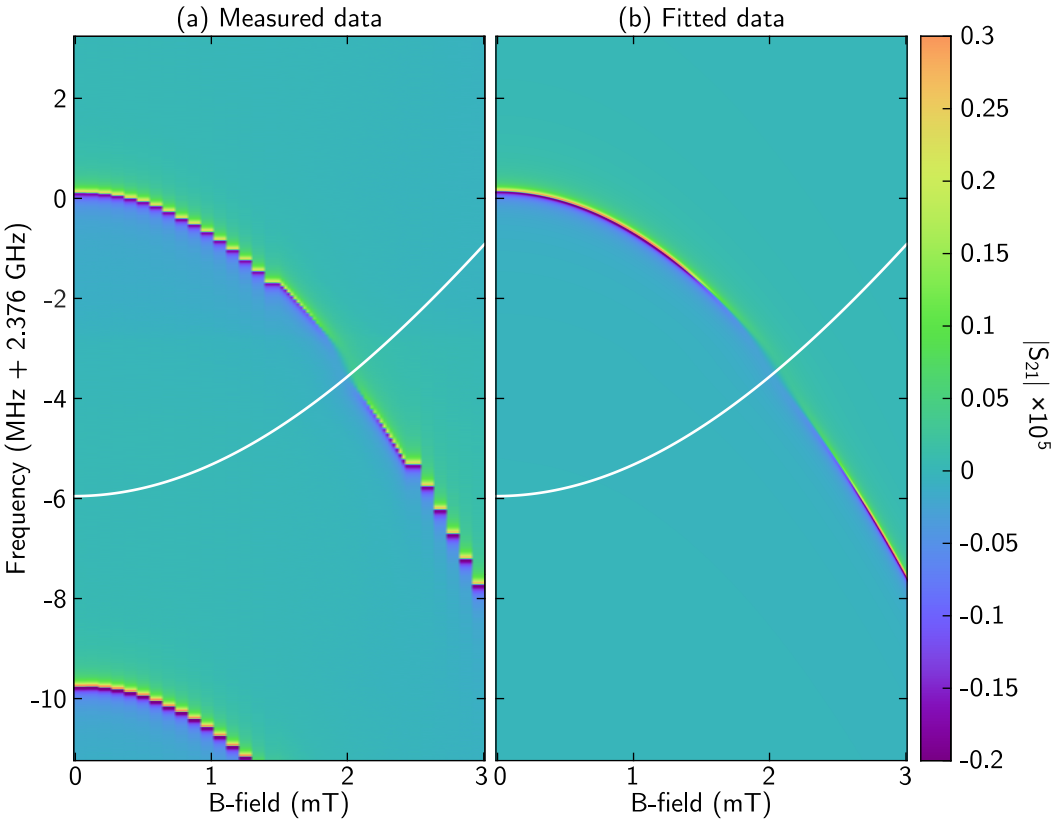

Figure 7.14: Tuning resonator and spin with out-of-plane field. Extracted coupling parameters are $g_{\mathrm{ens}}/2\pi = 450\,\mathrm{kHz}$, $\gamma_{\mathrm{s}}/2\pi = 875\,\mathrm{kHz}$, $\kappa_{\mathrm{c}}/2\pi = 27\,\mathrm{kHz}$, yielding a weak coupling $C = \frac{g_{\mathrm{ens}}^2}{\gamma_{\mathrm{s}}\kappa_{\mathrm{c}}} = 8.5$. The large variation in background transmission, seen in Fig. 7.12, has been subtracted for clarity in this figure but is correctly accounted for in the fit to Eqn. 2.12.

25 µs, increasing and decreasing the shot repetition time, and averaging repeated echo sequences overnight (10^2~10^3 shots). Despite the relative ease of measuring single-shot echoes at high frequency, and observing a spin resonance at this field and frequency in CW, retrieval of an echo proved not possible with this resonator.

With no spin echo, it was not possible to measure coherence times at these frequencies, making the second step of measuring an increased coherence time at the near-ZEFOZ point impossible with the current setup. To realise the experimental limiting factor, consider the measurement setup with the fabricated chip encased within a 3D cavity. The primary purpose of the cavity is to suppress radiative emission from the superconducting resonator by ensuring the lowest frequency cavity mode it can emit to is significantly detuned from that of the resonator. The 5.5 GHz TE_{101} box mode of the cavity meets this criterion for both resonators mea-

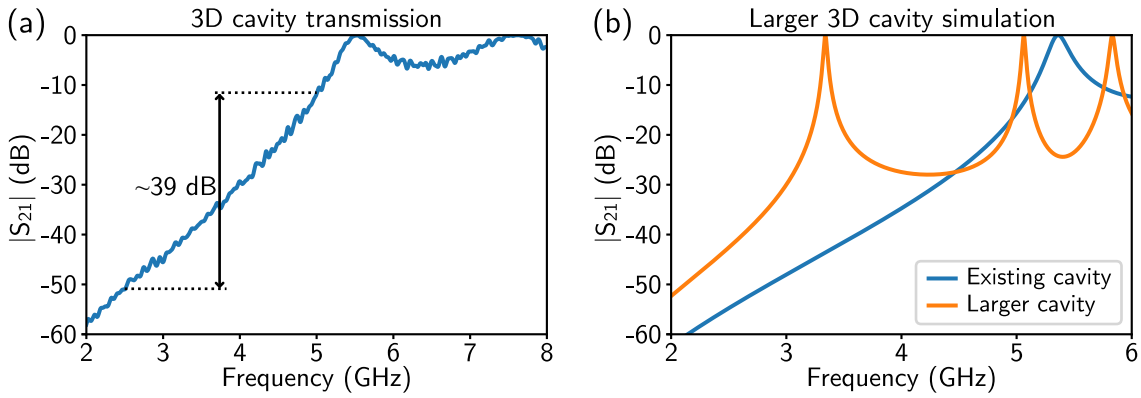

Figure 7.15: (a) Insertion loss in the 3D cavity is significantly greater at 2.5 GHz than at 5 GHz, making driving spins less for a given input power and limiting the effectiveness by which an echo can be read out. (b) CST simulations of a larger 3D cavity, designed to make full use of the space in the LCN fridge sample box, would reduce the fundamental frequency and reduces insertion loss.

sured here. However, the cavity also acts to drive the resonator via the electric field generated by this box mode.

A measurement of transmission through the 3D cavity measured by a VNA is shown in Fig. 7.15(a). The cavity resonance is deliberately broad, but the amplitude of the cavity mode at 2.5 GHz is nonetheless 39 dB weaker than at 5 GHz. This implies the electric field generated in the cavity is similarly weaker, significantly increasing the insertion loss to the superconducting resonator, making it harder to drive the resonator and much less effective at reading out weak echoes. This is further evidenced in the weak resonator prominence at 2.5 GHz, due to a weak coupling between the cavity and resonator.

In short, the 3D cavity is acting as a filter at the low frequencies required for near-ZEFOZ experiments. This can be accounted for when measuring in CW by increasing the (already low) output power and decreasing the measurement bandwidth to increase signal-to-noise. For pulsed measurements however, the 3 W amplifier limits the maximum power that can be sent to the cavity, and the insertion loss between any echo and the output of the cavity cannot be corrected by external modifications to the microwave setup.

A solution would be to build a lower frequency 3D cavity. The dimensions of this cavity were constrained by the requirement to fit within the ⌀36 mm bore of the vector magnet installed in the NPL fridge (see Section 4.3.2). The frame of the sample box used in the LCN fridge is 59 mm wide, supporting a significantly wider and longer box. Extending the size of the cavity to 70 mm × 6 mm × 55 mm creates a fundamental resonant mode TE_{101} with $f_{101} = 3.46$ GHz according to

Eqn. 4.1, much closer to the frequencies needed to drive near-ZEFOZ resonators and decreasing the insertion loss as simulated in Fig. 7.15(b). The higher Q in the simulation of the larger cavity indicates a redesign of the antennae to couple more strongly to the cavity mode, for example by creating a bend in the output antenna to increase its length and bring it closer to the device, may also reduce the insertion loss by broadening the cavity resonance.

7.3 Discussion

We have used methods developed in Chapter 6 to perform CW measurements and pulsed ESR on a sample of 50 ppm $^{\text{nat}}$Yb:Y_2SiO_5, using a NbN spiral resonator fabricated on its surface. Measuring the roadmap of ESR fields as a function of B-field angle enabled the orientation of the crystal with respect to the superconductor plane and magnet axes to be determined. Using the newly built 2 GHz–4 GHz ESR bridge, transitions from the $I = 0$ isotope at 370 mT along D_2 and the $I = \frac{1}{2}$ ^{171}Yb isotope at 370 mT along D_2 were measured to give the respective two-pulse coherence times $T_{2,370} = (571 \pm 22)$ µs and $T_{2,433} = (1170 \pm 90)$ µs.

Using dynamical decoupling sequences CPMG, XY-4, and XY-8, the measurable coherence time for the ^{171}Yb transition was extended up to $T_{2,\text{XY-4}} = (3.28 \pm 0.12)$ ms and $T_{2,\text{XY-8}} = (9.0 \pm 0.5)$ ms, indicating that low-frequency magnetic field noise from the spin environment or measurement setup appears to be limiting two-pulse coherence measurements.

These high-field measurements are motivated by having a baseline to compare against when operating at a near-ZEFOZ point in ^{171}Yb with low $\left|\frac{\mathrm{d}f}{\mathrm{d}B}\right|$. To this end, a plan for coupling low-frequency resonators to these transitions was presented, involving tuning a resonator to the appropriate frequency by applying an out-of-plane field close to the b crystal axis, then applying an in-plane field close to the D_1–D_2 plane to minimise $\left|\frac{\mathrm{d}f}{\mathrm{d}B}\right|$. The first step was successfully demonstrated in Section 7.2.3, with a CW measurement exhibiting a broadening of the resonator linewidth in good agreement with simulation. However a spin echo proved elusive, due to the 3D cavity measurement setup acting as a filter against these frequencies. A new cavity with lower box mode frequencies is proposed to overcome this and enable future measurements in this range.

Chapter 8

Conclusion

This thesis has described the design and fabrication processes involved in creating superconducting resonators on the surface of a Y_2SiO_5 substrate, characterised fabricated resonators and extracted values related to dielectric loss from the interface with the substrate, and used these resonators to perform ESR experiments using rare-earth ions within the crystal.

8.1 Summary

Using Hamiltonian parameters for ^{145}Nd:Y_2SiO_5 and ^{171}Yb:Y_2SiO_5 from the literature, simulations of ESR experiments sweeping magnetic field and angle were developed and presented in Chapter 2. These form an important tool in identifying and understanding experimentally observed transitions. The simulations were developed further to determine the sensitivity of transition frequency to magnetic field, and hence identify 3D magnetic field vectors that exhibit coherence-enhancing near-ZEFOZ transitions in ^{171}Yb:Y_2SiO_5. Site 2 near-ZEFOZ transitions have a smallest field component along the b crystal axis, compatible with the orientation of Y_2SiO_5 samples used for device fabrication in this thesis.

Thin-ring and spiral superconducting resonator geometries were presented and simulated in Chapter 3. Their fabrication with a NbN thin-film on Y_2SiO_5 substrate in the LCN cleanroom was summarised, and their tunability with applied magnetic field characterised. Thin-ring resonators exhibit a continuous tuning of up to 30 MHz with a 5 mT out-of-plane component [121], while the spiral resonators show a tunability of 20 MHz at 3 mT.

To measure the devices at mK temperatures, dilution refrigerators were equipped with coaxial lines and microwave components shown in Chapter 4. Continuous-wave frequency-swept experiments were performed using a VNA, while pulsed microwave experiments use a custom-built ESR spectrometer presented in Section 4.4. For

experiments around 2–4 GHz, required for low-field and near-ZEFOZ experiments with ^{171}Yb, a microwave bridge was designed and constructed specifically for this project in Section 4.4.1.

Continuous-wave measurement

Using a thin-ring NbN resonator fabricated on 10 ppm ^{145}Nd:Y_2SiO_5, installed within a dilution refrigerator at 10 mK, CW measurements of resonator frequency and quality factor were taken in Chapter 5. A resonance at 6.008 GHz was measured to have a quality factor of ~400 000 in the low-power limit where TLS loss is maximal, and by tracking the resonant frequency as a function of temperature the loss-tangent was found to be $\tan\delta = 4 \times 10^{-6}$, comparable to high quality devices on sapphire and silicon. Applying magnetic field brought ^{145}Nd ESR transitions in resonance with the NbN resonator, causing a measurable dispersive frequency shift at magnetic fields in agreement with a roadmap simulating the anisotropic field dependence of ^{145}Nd:Y_2SiO_5. Fitting to the avoided crossing to extract coupling parameters established a high-cooperativity coupling between resonator and spin ensemble with resonator linewidth $\kappa_c/2\pi = 13.3$ kHz, spin linewidth $\gamma_s/2\pi = 5.7$ MHz, and ensemble coupling strength $g_{ens}/2\pi = 1.5$ MHz, with cooperativity $C = \frac{g_{ens}^2}{\kappa\gamma} = 30$.

These results show that fabricating a superconducting resonator on rare-earth doped Y_2SiO_5 can yield a high-quality device with low dielectric losses, and demonstrate that a high-cooperativity coupling between resonator and electron spin can be achieved.

Pulsed spectroscopy of ^{145}Nd:Y_2SiO_5

Pulsed ESR measurements were performed at 13 mK in Chapter 6 using a thin-ring resonator with frequency 8.071 GHz and $Q = 72\,000$, fabricated on on 200 ppm ^{145}Nd:Y_2SiO_5. The resonator–spin coupling for the $m_I = +\frac{7}{2}$ transition was $g_{ens}/2\pi = 5.933$ MHz with a high cooperativity $C = 153$ resulting in an observable vacuum Rabi splitting. Applying $\frac{\pi}{2}$–π two-pulse sequences produced a spin echo which was used to investigate coherence properties of the ^{145}Nd electron spin transition. The appearance of a train of multiple spin echoes separated by the pulse separation time τ was consistently observable; this is due to the high cooperativity between resonator and spin ensemble, together with imperfect refocusing pulses [154].

Two-pulse sequences were used to measure a coherence time $T_2 = (409 \pm 14)\,\mu s$. By sweeping pulse frequency and magnetic field, the avoided crossing between resonator and spin could be resolved by time-domain spectroscopy; measurements of T_2 at various points of the avoided crossing did not conclusively suggest a dependence of T_2 with position on the avoided crossing. A strong dependence of T_2 with temperature indicated spectral diffusion is mostly suppressed at 13 mK due to polarisation of the electron spin, in agreement with theory.

A significant inhomogeneity in B_1 field generated by the thin-ring resonator prevents accurate rotation of the spin magnetisation by application of single-frequency excitation pulses. By exploiting the arbitrary phase control available through use of an AWG to control a VSG, frequency-swept pulses could be used to implement adiabatic fast passage. Using a WURST pulse, an inversion of the magnetisation (a π rotation) could be realised, enabling measurement of T_1 by inversion recovery. An inhomogeneous relaxation time over the spin ensemble due to a spatially varying Purcell enhancement causes the decay curve to exhibit a multiexponential profile; fitting a biexponential yielded two characteristic decay times $T_{1,\mathrm{fast}} = (696 \pm 47)\,ms$ and $T_{1,\mathrm{slow}} = (9.4 \pm 1.2)\,s$. A θ-rotation could be implemented using a BIR-4 sequence, enabling the observation of Rabi oscillations.

A three-pulse stimulated echo sequence can be used to probe the effect of spectral diffusion. This sequence was implemented in Section 6.8, where the fitted spectral diffusion linewidth $\Gamma_{\mathrm{SD}} = (43 \pm 8)\,kHz$ corresponds to a theoretical spin bath temperature of $T = (163 \pm 16)\,mK$. This is consistent with repeated excitation of the spin ensemble faster than $T_{1,\mathrm{slow}}$ causing the spin bath to be out of thermal equilibrium with the dilution fridge at 14 mK. This could be corrected by thermal cycling prior to an experiment, operating with a longer shot repetition time (with a corresponding increase in the length of the experiment), or achieving a greater Purcell-enhanced relaxation to ensure thermal equilibrium.

The suppression of spectral diffusion at 14 mK, confirmed by measuring $T_2(T)$, leaves a residual decoherence rate at base temperature due to effects including instantaneous diffusion. By using a two-pulse sequence with a reduced refocusing rotation θ the limiting coherence time in the absence of instantaneous diffusion should can be inferred. However the data showed no convincing θ dependence, attributable to the strongly inhomogeneous B_1 field causing a change in pulse amplitude to excite a different subvolume of spins rather than reduce the rotation induced on the spin ensemble.

These results establish that a superconducting resonator fabricated on Y_2SiO_5 can be used to perform pulsed ESR spectroscopy on rare-earth spins in the high-

cooperativity coupling regime. Operating in this regime complicates experiments due to the presence of an avoided crossing between the resonator and spin modes, requiring optimisation of both field and frequency to obtain the strongest echo. The consistent observation of an echo train indicates a complex interplay between the field modes of the resonator and spin ensemble, a matter for further analytical and theoretical investigation. The significantly inhomogeneous B_1 field of the resonator results in spatially varying relaxation rates and pulse rotation angles, hindering attempts at performing pulse sequences requiring specific rotation angles and complicating analysis of relaxation dynamics. Adiabatic fast passage enables pre-rotations angles of π or θ (using WURST or BIR-4 respectively), but the length of these pulses prevent their use as part of a refocusing sequence. Increasing the B_1 field homogeneity over the spin ensemble will help mitigate this, through modification of the resonator geometry or using a different spatial distribution of spins (through ion implantation, for example).

Pulsed spectroscopy of ^{171}Yb:Y_2SiO_5

With the capability of pulsed spectroscopy demonstrated with ^{145}Nd, we proceeded to perform time-domain measurements of ^{171}Yb in Chapter 7. A series of NbN devices were fabricated on 50 ppm $^{\text{nat}}$Yb:Y_2SiO_5, this time using a spiral resonator geometry to facilitate reaching frequencies as low as 2 GHz.

Pulsed measurements were performed with a 4.939 GHz resonator, with CW measurements observing strong transitions from the $I = 0$ isotopes and the $I = \frac{1}{2}$ isotope ^{171}Yb. The abundant $I = 0$ isotopes gave a single ESR transition visible with an avoided crossing of coupling strength $g_{\text{ens}}/2\pi = 7.12$ MHz and cooperativity $C = \frac{g_{\text{ens}}^2}{\gamma_{\text{s}}\kappa_{\text{c}}} = 255$, while ^{171}Yb has two transitions, the higher-field of which coupled more weakly with $g_{\text{ens}}/2\pi = 1.20$ MHz and $C = \frac{g_{\text{ens}}^2}{\gamma_{\text{s}}\kappa_{\text{c}}} = 8.5$.

Measuring T_2 with a two-pulse sequence gave a coherence time of $T_2 = (571 \pm 22)$ µs for the $I = 0$ isotopes at 370 mT and $T_2 = (1170 \pm 90)$ µs for the $I = \frac{1}{2}$ ^{171}Yb transition at 433 mT. The increased coherence time of the ^{171}Yb transition is attributable to the more dilute spin density suppressing spectral diffusion. Dynamical decoupling sequences CPMG, XY-4, and XY-8 were also implemented and fits to the resulting decay curves give a T_1-influenced single-exponential decay rate of (95.7 ± 0.4) ms for CPMG, and fast components of a biexponential decay (3.3 ± 0.1) ms and (9.0 ± 0.5) ms for XY-4 and XY-8 sequences respectively.

With the coherence time of high-frequency transitions characterised, an experiment intending to couple low-frequency field-tunable resonators to near-ZEFOZ

transitions in ^{171}Yb:Y_2SiO_5 was presented in Section 7.2.1. CW measurements demonstrated the principle of the experiment, by applying an out-of-plane field to tune a 2.376 GHz resonator down into resonance with the [1-3] transition of ^{171}Yb with $g_{\mathrm{ens}}/2\pi = 450\,\mathrm{kHz}$ and cooperativity $C = \frac{g_{\mathrm{ens}}^2}{\gamma_{\mathrm{s}}\kappa_{\mathrm{c}}} = 8.5$. However an echo could not be acquired due to a greater insertion loss via the 3D cavity at 2.5 GHz than at 5 GHz which had not been accounted for. Modifying the measurement setup to use a larger volume cavity with lower frequency, or modifying the coupling mechanism to drive the resonator directly via a capacitive coupling to the antennae or via a coplanar waveguide should correct this and enable pulses to be applied and echoes read out — though this may also decrease the coupling-limited Q_{c} or allow radiative losses Q_{r}, limiting the achievable overall quality factor Q_{tot}.

8.2 Outlook

This project aims to create a device to complement established superconductor-based quantum technologies by coupling a superconducting resonator to an ensemble of rare-earth spins. This provides an interface compatible with existing technology through which properties of the rare-earth ions can be exploited, such as their long coherence times which can provide a memory for quantum states, or by adding an additional optical cavity to simultaneously access both microwave-frequency electron spin transitions and optical atomic transitions to create a microwave–to–optical transducer. Conversion between these frequencies enables a microwave-frequency quantum computer to communicate via existing optical fibre networks, and provides an interface by which a quantum repeater can store an entangled state — generated by communicating optically with a separate node of a quantum network — in a solid-state electronic medium.

^{171}Yb:Y_2SiO_5 is a good candidate for such a transducer. It has advantageous optical properties with its near-infrared optical transitions which can be excited by single-mode laser diodes [28] and its high oscillator strength enables it to couple efficiently to optical fields [27]. Its near-ZEFOZ properties simultaneously extend coherence time across both optical and microwave transitions [14], benefitting both applications as a memory and a transducer.

Modifying the experimental setup to allow pulsed measurement at 2 GHz would be the first step in demonstrating a near-ZEFOZ coherence enhancement via a superconducting resonator in accordance with the experimental plan of Section 7.2.1. This plan assumes the resonator is to be tuned with a globally applied magnetic field. An alternative would be to use a resonator which is tunable at zero applied

magnetic field — such as SQUID-embedded resonators [96] tunable with local field from a flux line, or by applying a bias current to tune the kinetic inductance [125, 167] — to exploit the ZEFIZEFOZ condition in ^{171}Yb.

This would be a significant step toward a quantum memory for superconducting quantum technologies. By incorporating this alongside a superconducting qubit, or via a bus to a superconducting computer, the resulting hybrid device would combine the fast gate operations of superconducting qubits with the long memory times available with rare-earth doped crystals.

To turn this into an efficient microwave–to–optical transducer would require the addition of an optical cavity to the setup. Mode-matching between the microwave and optical cavities will be an important consideration in combining the two — a potential route to achieve this could combine a circular inductor (as found in 'omega' style microwave resonators [168]) with the TEM_{0i*} so-called 'doughnut mode' of a laser beam, or by directing the path of a laser to be parallel along a straight inductor in order to minimise the cross-section of the superconductor on which the laser is incident.

Appendices

A. EasySpin example

In Chapter 2, and in the later experimental chapters, the MATLAB toolbox EasySpin [86] is used for ESR simulations. Here some code snippets are presented to illustrate the process.

First we set up three `structs`: `Sys`, defining the spin system; `Exp`, containing important experimental parameters; `Opt`, specifying some options for the solver. These are used in conjunction with `resfields` and `resfreqs_matrix` to calculate resonant fields at a fixed frequency, and resonant frequencies at a fixed field, respectively.

Spin system

```
Sys = struct();
Sys.Nucs = '171Yb';
Sys.I = 0.5;
Sys.S = 0.5;
Sys.g = [ 6.072    -1.460    -0.271; % [D1 D2 b] frame
-1.460     1.845    -0.415;
-0.271    -0.415     0.523];
Sys.A = 1e3*[ 4.847    -1.232    -0.244;
-1.232     1.425    -0.203;
-0.244    -0.203     0.618];
% doi:10.1103/PhysRevB.98.195110
```

Experimental parameters

```
Exp = struct();
Exp.Field = 320; %mT, used in resfreqs
Exp.mwFreq =  5; %GHz, used in resfields
Exp.Range = [0 Inf]; %mT (resfields) or MHz (resfreqs)
Exp.CrystalSymmetry = 'C2h'; % YSO is monoclinic C^6_2h spacegroup
Exp.Temperature = 0.020; % K, accounts for polarisation in amplitude
Exp.Mode = 'perpendicular'; % Orientation of microwave field wrt B0
Exp.CrystalOrientation = [0, pi, 0] % ZYZ Euler angle for crystal
    orientation
```

Optional parameters

```
Opt = struct();
Opt.Threshold = 0; % Ignore transitions with amplitude below this
Opt.Transitions = 'all'; % Use this to calculate specific transitions
Opt.Sites = [1 2]; % Simulate both C2h subsites or just one?
```

EasySpin defines the orientation of the crystal or molecule with respect to the lab frame using ZYZ Euler angles, i.e. angles by which the coordinate system should be rotated to achieve an appropriate alignment of the experiment. Conventionally B_0 is directed along the lab z-axis, but we wish to specify the field direction in the local sample frame (for Y_2SiO_5 this is the [D_1, D_2, b] frame). This function `vec2ori` achieves this.

Convert cartesian field to Euler angle

```
function ori = vec2ori(FieldVector)
% vec2ori  Convert cartesian vector to ZYZ orientation for EasySpin
%   ori = vec2ori([x,y,z])
%   For YSO this is [D1,D2,b] frame

FieldVector = FieldVector./norm(FieldVector);

[alpha,beta]=vec2ang(FieldVector);gamma=0; % Convert FieldVector to
    polar angles.
RotM=erot([alpha,beta,gamma]); % Build a rotation matrix from angles.

BVec=RotM(3,:); % Effectively RotM*[0;0;1], as B-field is along lab Z
[alpha1,beta1]=vec2ang(BVec); % Convert BVec into polar coordinates
ori=[alpha1 beta1 0]; % Specify the orientation of the crystal wrt
    magnetic field.
end
```

The `Sys`, `Exp`, and `Opt` structs can then be passed to one of EasySpin's solvers, which uses matrix diagonalisation to calculate the eigenvectors and eigenvalues of the spin Hamiltonian, returning the resonant frequencies (or fields) for the given experiment in `Pos`. It also calculates the transition probabilities (or amplitudes) calculated by Fermi's golden rule [87] in `Int`. The `resfields` and `resfreqs_matrix` solvers differ in their calculated amplitudes by a factor of $\frac{1}{g}$. `Trans` describes the levels each transition of `Pos` and `Int` is between.

Example simulation ramping field along D_2 axis

```
Fields = linspace(0,500,1001); % Ramp field from 0 to 500 mT
FieldAxis = [0, 1, 0];         % Oriented along D2 axis

num_field_points = length(Fields);
num_levels = (2*Sys.I+1)*(2*Sys.S+1);      % Number of spin levels
num_trans = 0.5*num_levels*(num_levels-1); % Number of transitions

Pos_array = NaN(num_trans,num_field_points); % Frequencies
Int_array = NaN(num_trans,num_field_points); % Amplitudes

for n = 1:num_field_points
Exp.Field = Fields(n); % Set field magnitude and orientation
Exp.CrystalOrientation = vec2ori(Fields(n)*FieldAxis);

[Pos,Int,~,Trans] = resfreqs_matrix(Sys,Exp,Opt);

Pos_array(:,n) = Pos; % MHz for resfreqs, mT for resfields
Int_array(:,n) = Int; % (MHz^2/mT^2) for resfreqs (MHz/mT) for
   resfields
end
```

B. 2–4 GHz bridge specifications

	dB
Pre-amp gate switch isolation	−54.8
Post-amp gate switch isolation	−54.7
Acquisition switch isolation	−56.0
LNA gain	+47.8

Table B.1: Measured parameters of active components in the bridge, derived from measurements presented in Table B.2.

		Amplifier		Marker		
Measurement	Mode	Pulse	LNA	Gate	Acq	dB
RF to Port 1	Trans					−1.5
RF to Port 1	Trans	✓				−105
RF to Port 1	Trans	✓		✓		−5.4
RF to Pulse Amp 1	Trans	✓				−57.4
RF to Pulse Amp 1	Trans	✓		✓		−2.6
Pulse Amp 2 to Port 1	Trans	✓				−57.4
Pulse Amp 2 to Port 1	Trans	✓		✓		−2.7
Port 1 to RF	Refl			✓		−14.5
Port 1 to RF	Trans			✓		−16.4
Port 2 to RF	Refl			✓		−110
Port 2 to RF	Trans			✓		−106
Port 1 to IQ mixer	Refl					−41.9
Port 1 to IQ mixer	Refl				✓	+14.4
Port 2 to IQ mixer	Trans					−41.3
Port 2 to IQ mixer	Trans				✓	+15.2
Port 2 to IQ mixer	Trans		✓			+7.7
Port 2 to IQ mixer	Trans		✓		✓	+63.0
Monitor LO to IQ mixer	Trans					−11.7
Monitor Sig to IQ mixer	Trans					−21.6
Monitor RF to IQ mixer	Trans					−11.7

Table B.2: Characterisation of losses, isolation, and gain in the microwave bridge. The position of the front panel switches and status of markers is marked. S_{21} transmission in dB was measured with a VNA at 2 GHz and 4 GHz, the mean of these measurements is shown in the table.

Bibliography

[1] G. E. Moore. "Cramming more components onto integrated circuits". *Proceedings of the IEEE*, (1965) (cit. on p. 13).

[2] M. M. Waldrop. "The chips are down for Moore's law". *Nature* **530** (7589), 144–147, (2016) (cit. on p. 13).

[3] R. P. Feynman. "Simulating physics with computers". *International Journal of Theoretical Physics* **21** (6-7), 467–488, (1982). arXiv: `9508027 [quant-ph]` (cit. on p. 13).

[4] D. Deutsch. "Quantum Theory, the Church-Turing Principle and the Universal Quantum Computer". *Proceedings of the Royal Society A: Mathematical, Physical and Engineering Sciences* **400** (1818), 97–117, (1985) (cit. on p. 13).

[5] J. A. Jones and D. Jaksch. *Quantum Information, Computation and Communication*. Cambridge University Press, 2012 (cit. on pp. 14, 25).

[6] J. M. Raimond, M. Brune, and S. Haroche. "Colloquium: Manipulating quantum entanglement with atoms and photons in a cavity". *Reviews of Modern Physics*, (2001) (cit. on pp. 14, 31).

[7] D. Leibfried, R. Blatt, C. Monroe, and D. Wineland. *Quantum dynamics of single trapped ions*. 2003 (cit. on pp. 14, 31).

[8] B. D. Josephson. "The discovery of tunnelling supercurrents". *Reviews of Modern Physics*, (1974) (cit. on p. 14).

[9] D. I. Schuster. "Circuit Quantum Electrodynamics". PhD thesis. Yale University, 2007 (cit. on p. 14).

[10] M. Kjaergaard et al. "Superconducting Qubits: Current State of Play". *Annual Review of Condensed Matter Physics* **11** (1), annurev–conmatphys–031119–050605, (2020) (cit. on p. 15).

[11] F. Arute et al. "Quantum supremacy using a programmable superconducting processor". *Nature* **574** (7779), 505–510, (2019) (cit. on p. 15).

[12] G. Wolfowicz et al. "Atomic clock transitions in silicon-based spin qubits." *Nature nanotechnology* **8** (8), 561–4, (2013). arXiv: 1301.6567 (cit. on pp. 15, 31).

[13] M. Zhong et al. "Optically addressable nuclear spins in a solid with a six-hour coherence time". *Nature* **517** (7533), 177–180, (2015) (cit. on pp. 15, 20, 31).

[14] A. Ortu et al. "Simultaneous coherence enhancement of optical and microwave transitions in solid-state electronic spins". *Nature Materials* **17** (8), 671–675, (2018). arXiv: 1712.08615 (cit. on pp. 15, 20, 31, 48, 51, 115, 147, 155, 159, 171).

[15] Y. Wang et al. "Single-qubit quantum memory exceeding ten-minute coherence time". *Nature Photonics* **11** (10), 646–650, (2017) (cit. on p. 15).

[16] J. H. Wesenberg et al. "Quantum computing with an electron spin ensemble". *Physical Review Letters*, (2009). arXiv: 0903.3506 (cit. on pp. 15, 18).

[17] Y. Kubo et al. "Hybrid quantum circuit with a superconducting qubit coupled to a spin ensemble". *Physical Review Letters*, (2011). arXiv: 1110.2978 (cit. on pp. 15, 18, 98, 116).

[18] G. Kurizki et al. "Quantum technologies with hybrid systems". *Proceedings of the National Academy of Sciences* **112** (13), 3866–3873, (2015). arXiv: 1504.00158 (cit. on p. 15).

[19] S. Probst. "Hybrid quantum system based on rare earth doped crystals". PhD thesis. KIT, 2015 (cit. on pp. 15, 18, 139, 144).

[20] I. Wisby. "Hybrid rare-earth ion superconductor systems for quantum information processing". PhD thesis. Royal Holloway, 2016 (cit. on pp. 15, 60).

[21] C. Grezes et al. "Towards a spin-ensemble quantum memory for superconducting qubits". *Comptes Rendus Physique* **17** (7), 693–704, (2016) (cit. on p. 15).

[22] C. Grezes et al. "Storage and retrieval of microwave fields at the single-photon level in a spin ensemble". *Physical Review A* **92** (2), 020301, (2015). arXiv: 1504.02220 (cit. on p. 15).

[23] C. O'Brien, N. Lauk, S. Blum, G. Morigi, and M. Fleischhauer. "Interfacing superconducting qubits and telecom photons via a rare-earth-doped crystal". *Physical Review Letters* **113** (6), 1–5, (2014). arXiv: 1402.5405 (cit. on pp. 15, 20).

[24] L. A. Williamson, Y. H. Chen, and J. J. Longdell. "Magneto-optic modulator with unit quantum efficiency". *Physical Review Letters* **113** (20), 1–5, (2014). arXiv: 1403.1608 (cit. on pp. 15, 20).

[25] X. Fernandez-Gonzalvo, Y. H. Chen, C. Yin, S. Rogge, and J. J. Longdell. "Coherent frequency up-conversion of microwaves to the optical telecommunications band in an Er:YSO crystal". *Physical Review A - Atomic, Molecular, and Optical Physics* **92** (6), 1–7, (2015). arXiv: 1501.02014 (cit. on pp. 15, 18, 20).

[26] E. Z. Cruzeiro et al. "Spectral hole lifetimes and spin population relaxation dynamics in neodymium-doped yttrium orthosilicate". *Physical Review B* **95** (20), 205119, (2017). arXiv: 1611.05444 (cit. on pp. 15, 28, 140, 159).

[27] S. Welinski, A. Ferrier, M. Afzelius, and P. Goldner. "High-resolution optical spectroscopy and magnetic properties of Yb3+ in Y2SiO5". *Physical Review B* **94** (15), 155116, (2016) (cit. on pp. 15, 42, 147, 171).

[28] H.-J. Lim, S. Welinski, A. Ferrier, P. Goldner, and J. J. L. Morton. "Coherent spin dynamics of ytterbium ions in yttrium orthosilicate". *Physical Review B* **97** (6), 064409, (2017). arXiv: 1712.00435 (cit. on pp. 15, 29, 130, 142, 144, 147, 157, 171).

[29] A. Tiranov et al. "Spectroscopic study of hyperfine properties in Yb 3 + 171 : Y 2 SiO 5". *Physical Review B* **98** (19), 195110, (2018) (cit. on pp. 15, 20, 42, 46, 147).

[30] J. M. Klinger. "A historical geography of rare earth elements: From discovery to the atomic age". *Extractive Industries and Society*, (2015) (cit. on p. 16).

[31] K. A. Denault et al. "Average and local structure, debye temperature, and structural rigidity in some oxide compounds related to phosphor hosts". *ACS Applied Materials and Interfaces* **7** (13), 7264–7272, (2015) (cit. on pp. 17, 19).

[32] Z. Shoudu et al. "Czochralski growth of rare-earth orthosilicates–Y2SiO5 single crystals". *Journal of Crystal Growth* **197** (4), 901–904, (1999) (cit. on pp. 17, 98).

[33] M. P. Hedges, J. J. Longdell, Y. Li, and M. J. Sellars. "Efficient quantum memory for light". *Nature* **465** (7301), 1052–1056, (2010) (cit. on pp. 17, 18).

[34] G. Dold et al. “High-Cooperativity Coupling of a Rare-Earth Spin Ensemble to a Superconducting Resonator Using Yttrium Orthosilicate as a Substrate”. *Physical Review Applied* **11** (5), 054082, (2019) (cit. on pp. 17, 18, 62, 100, 116).

[35] F. Könz et al. “Temperature and concentration dependence of optical dephasing, spectral-hole lifetime, and anisotropic absorption in Eu3+:Y2SiO5”. *Physical Review B - Condensed Matter and Materials Physics*, (2003) (cit. on p. 17).

[36] ICSD. “The inorganic crystal structure database” (cit. on p. 19).

[37] K. Momma and F. Izumi. “VESTA 3 for three-dimensional visualization of crystal, volumetric and morphology data”. *Journal of Applied Crystallography* **44** (6), 1272–1276, (2011) (cit. on p. 19).

[38] N. C. Carvalho, J.-M. Le Floch, J. Krupka, and M. E. Tobar. “Multi-mode technique for the determination of the biaxial Y 2 SiO 5 permittivity tensor from 300 to 6 K”. *Applied Physics Letters* **106** (19), 192904, (2015). arXiv: `1503.04089` (cit. on pp. 18, 67).

[39] N. Kukharchyk et al. “Photoluminescence of focused ion beam implanted Er3+:Y2SiO5 crystals”. *physica status solidi (RRL) - Rapid Research Letters* **8** (10), 880–884, (2014) (cit. on p. 18).

[40] T. Böttger, C. W. Thiel, Y. Sun, and R. L. Cone. “Optical decoherence and spectral diffusion at 1.5 μm in Er3+: Y2 SiO5 versus magnetic field, temperature, and Er3+ concentration”. *Physical Review B - Condensed Matter and Materials Physics* **73** (7), 1–16, (2006) (cit. on pp. 18, 29, 127, 142).

[41] M. Rančić, M. P. Hedges, R. L. Ahlefeldt, and M. J. Sellars. “Coherence time of over a second in a telecom-compatible quantum memory storage material”. *Nature Physics* **14** (1), 50–54, (2017) (cit. on p. 18).

[42] S. Probst et al. “Three-dimensional cavity quantum electrodynamics with a rare-earth spin ensemble”. *Physical Review B - Condensed Matter and Materials Physics* **90** (10), 1–5, (2014). arXiv: `arXiv:1406.3535v1` (cit. on p. 18).

[43] J. R. Ball et al. “Loop-gap microwave resonator for hybrid quantum systems”. *Applied Physics Letters* **112** (20), 204102, (2018) (cit. on p. 18).

[44] M. Goryachev et al. “Discovery of iron group impurity ion spin states in single crystal Y_2SiO_5 with strong coupling to whispering gallery photons”. *Applied Physics Letters* **106** (23), 232401, (2015) (cit. on pp. 18, 107).

[45] I. Wisby et al. “Coupling of a locally implanted rare-earth ion ensemble to a superconducting micro-resonator”. *Applied Physics Letters* **105** (10), 102601, (2014). arXiv: 1407.5064 (cit. on pp. 18, 59, 98).

[46] S. Probst et al. “Anisotropic rare-earth spin ensemble strongly coupled to a superconducting resonator”. *Physical Review Letters* **110** (15), 1–5, (2013). arXiv: 1212.2856v1 (cit. on pp. 18, 98, 116).

[47] T. Zhong, J. M. Kindem, E. Miyazono, and A. Faraon. “Nanophotonic coherent light–matter interfaces based on rare-earth-doped crystals”. *Nature Communications* **6** (May), 8206, (2015). arXiv: 1507.00977 (cit. on p. 18).

[48] D. I. Schuster et al. “High-cooperativity coupling of electron-spin ensembles to superconducting cavities”. *Physical Review Letters*, (2010). arXiv: 1006.0242 (cit. on pp. 18, 35, 38, 59, 98, 116).

[49] H. Wu et al. “Storage of multiple coherent microwave excitations in an electron spin ensemble”. *Physical Review Letters*, (2010). arXiv: 0908.0101 (cit. on p. 18).

[50] A. Bienfait et al. “Reaching the quantum limit of sensitivity in electron spin resonance”. *Nature Nanotechnology* (December), 10, (2015). arXiv: 1507.06831 (cit. on pp. 18, 79, 98, 100).

[51] C. W. Zollitsch et al. “High cooperativity coupling between a phosphorus donor spin ensemble and a superconducting microwave resonator”. *Applied Physics Letters* **107** (14), 142105, (2015) (cit. on pp. 18, 98, 116).

[52] A. Tkalčec et al. “Strong coupling of an Er3+-doped YAlO3 crystal to a superconducting resonator”. *Physical Review B* **90** (7), 075112, (2014) (cit. on pp. 18, 98, 116).

[53] D. L. McAuslan, J. G. Bartholomew, M. J. Sellars, and J. J. Longdell. “Reducing decoherence in optical and spin transitions in rare-earth-metal-ion-doped materials”. *Physical Review A - Atomic, Molecular, and Optical Physics* **85** (3), 1–9, (2012). arXiv: arXiv:1201.4610v1 (cit. on pp. 20, 31).

[54] J. Binney and D. Skinner. *The Physics of Quantum Mechanics*. 2010 (cit. on p. 23).

[55] A. Abragam and B. Bleaney. *Electron Paramagnetic Resonance of Transition Ions*. 1970, 4, 42, 133–163, 398–406, 417–430, 541–547, 583–599. arXiv: arXiv:1011.1669v3 (cit. on p. 23).

[56] M. Brustolon and E. Giamello. *Electron Paramagnetic Resonance: A Practitioner's Toolkit*. 2008, 1–539. arXiv: arXiv:1011.1669v3 (cit. on p. 23).

[57] D. Griffiths and D. Schroeter. *Introduction to Quantum Mechanics*. 3rd ed. Cambridge University Press, 2018 (cit. on p. 25).

[58] E. L. Hahn. "Spin Echoes". *Physical Review* **80** (4), 580–594, (1950) (cit. on p. 27).

[59] A. Schweiger and G. Jeschke. *Principles of Pulse Electron Paramagnetic Resonance*. Oxford University Press, 2001 (cit. on pp. 27, 28, 30, 66, 128).

[60] S. Agarwal, S. M. H. Rafsanjani, and J. H. Eberly. "Tavis-Cummings model beyond the rotating wave approximation: Quasidegenerate qubits". *Physical Review A - Atomic, Molecular, and Optical Physics*, (2012). arXiv: 1106.0052 (cit. on p. 32).

[61] E. T. Jaynes and F. W. Cummings. "Comparison of Quantum and Semiclassical Radiation Theories with Application to the Beam Maser". *Proceedings of the IEEE* **51** (1), 89–109, (1963) (cit. on p. 32).

[62] C. Grèzes. "Towards a Spin-Ensemble Quantum Memory for Superconducting Qubits". PhD thesis. CEA Saclay, 2015, 1–231 (cit. on p. 32).

[63] C. F. Brennecke. "Collective Interaction Between a Bose-Einstein Condensate and a Coherent Few-Photon Field presented by". PhD thesis. ETH Zürich, 2009. arXiv: 9605103 [cs] (cit. on pp. 32–34).

[64] M. Tavis and F. W. Cummings. "Exact solution for an N-molecule-radiation-field Hamiltonian". *Physical Review*, (1968) (cit. on p. 34).

[65] E. M. Purcell. "Spontaneous Emission Probabliities at Radio Frquencies". *Physical Review* **69**, 674–674, (1946) (cit. on p. 34).

[66] A. Bienfait et al. "Controlling spin relaxation with a cavity". *Nature* **531** (7592), 74–77, (2016). arXiv: 1508.06148 (cit. on pp. 34, 35, 59, 64, 139).

[67] C. J. Wood, T. W. Borneman, and D. G. Cory. "Cavity Cooling of an Ensemble Spin System". *Physical Review Letters* **112** (5), 050501, (2014) (cit. on p. 34).

[68] C. Eichler, A. J. Sigillito, S. A. Lyon, and J. R. Petta. "Electron Spin Resonance at the Level of 1 0 4 Spins Using Low Impedance Superconducting Resonators". *Physical Review Letters* **118** (3), 037701, (2017) (cit. on pp. 35, 64).

[69] K. Sandner et al. “Strong magnetic coupling of an inhomogeneous nitrogen-vacancy ensemble to a cavity”. *Physical Review A* **85** (5), 053806, (2012) (cit. on pp. 35, 37).

[70] C. W. Zollitsch. “Single Excitation Transfer in the Quantum Regime: A Spin-Based Solid-State Approach”. PhD thesis. Technische Universität München, 2016 (cit. on pp. 35, 37).

[71] A. Bärnthaler et al. “Probing decoherence through fano resonances”. *Physical Review Letters* **105** (5), 1–4, (2010). arXiv: 1003.5381 (cit. on pp. 36, 99).

[72] J. Leppäkangas et al. “Resonance inversion in a superconducting cavity coupled to artificial atoms and a microwave background”. *Physical Review A* **99** (6), 063804, (2019) (cit. on pp. 36, 99).

[73] G. Hechenblaikner, M. Gangl, P. Horak, and H. Ritsch. “Cooling an atom in a weakly driven high-Q cavity”. *Physical Review A* **58** (4), 3030–3042, (1998) (cit. on pp. 37, 38).

[74] A. A. Clerk, M. H. Devoret, S. M. Girvin, F. Marquardt, and R. J. Schoelkopf. “Introduction to quantum noise, measurement, and amplification”. *Reviews of Modern Physics* **82** (2), 1155–1208, (2010) (cit. on p. 37).

[75] I. Diniz, S. Portolan, R. Ferreira, J. M. Gérard, P. Bertet, and A. Auffèves. “Strongly coupling a cavity to inhomogeneous ensembles of emitters: Potential for long-lived solid-state quantum memories”. *Physical Review A* **84** (6), 063810, (2011) (cit. on p. 37).

[76] T. Lindström, C. H. Webster, J. E. Healey, M. S. Colclough, C. M. Muirhead, and A. Y. Tzalenchuk. “Numerical simulations of a flux qubit coupled to a high quality resonator”. *Journal of Physics: Conference Series* **97** (1), 012319, (2008) (cit. on p. 37).

[77] E. Abe, H. Wu, A. Ardavan, and J. J. L. Morton. “Electron spin ensemble strongly coupled to a three-dimensional microwave cavity”. *Applied Physics Letters* **98** (25), 3–5, (2011). arXiv: 1106.0507 (cit. on p. 38).

[78] P. F. Herskind, A. Dantan, J. P. Marler, M. Albert, and M. Drewsen. “Realization of collective strong coupling with ion Coulomb crystals in an optical cavity”. *Nature Physics* **5** (7), 494–498, (2009) (cit. on p. 38).

[79] Y. Wang and J. Y. Haw. "Bridging the gap between the Jaynes-Cummings and Rabi models using an intermediate rotating wave approximation". *Physics Letters, Section A: General, Atomic and Solid State Physics* **379** (8), 779–786, (2015). arXiv: 1502.02806 (cit. on p. 40).

[80] A. Baust et al. "Ultrastrong coupling in two-resonator circuit QED". *Physical Review B* **93** (21), 214501, (2016) (cit. on p. 40).

[81] J. Casanova, G. Romero, I. Lizuain, J. J. García-Ripoll, and E. Solano. "Deep Strong Coupling Regime of the Jaynes-Cummings Model". *Physical Review Letters* **105** (26), 263603, (2010) (cit. on p. 40).

[82] F. Yoshihara, T. Fuse, S. Ashhab, K. Kakuyanagi, S. Saito, and K. Semba. "Superconducting qubit–oscillator circuit beyond the ultrastrong-coupling regime". *Nature Physics* **13** (1), 44–47, (2017) (cit. on p. 40).

[83] Y. Jia. "Crystal radii and effective ionic radii of the rare earth ions". *Journal of Solid State Chemistry* **95** (1), 184–187, (1991) (cit. on p. 41).

[84] H. Maier-Flaig. "Electron and nuclear spin properties of 145Neodymium doped Y2SiO5". MA thesis. Karlsrhue Institute of Technology, 2013, 153 (cit. on p. 41).

[85] R. Marino. "Proprietes magnetiques et optiques de cristaux dopes terres rares pour l'information quantitiqe". PhD thesis. Univesite des science et technologies de Lille, 2011, 192. arXiv: arXiv:1011.1669v3 (cit. on p. 41).

[86] S. Stoll and A. Schweiger. "EasySpin, a comprehensive software package for spectral simulation and analysis in EPR". *Journal of Magnetic Resonance* **178** (1), 42–55, (2006) (cit. on pp. 43, 174).

[87] J. Nehrkorn, A. Schnegg, K. Holldack, and S. Stoll. "General magnetic transition dipole moments for electron paramagnetic resonance". *Physical Review Letters*, (2015) (cit. on pp. 45, 46, 175).

[88] J. Bardeen, L. N. Cooper, and J. R. Schrieffer. "Microscopic Theory of Superconductivity". *Physical Review* **106** (1), 162–164, (1957) (cit. on p. 57).

[89] J. F. Annett. *Superconductivity, Superfluids and Condensates*. 2004 (cit. on pp. 57, 58, 60).

[90] W. Meissner and R. Ochsenfeld. "Ein neuer Effekt bei Eintritt der Supraleitfähigkeit". *Die Naturwissenschaften* **21** (44), 787–788, (1933) (cit. on p. 58).

[91] F. London and H. London. "The electromagnetic equations of the supraconductor". *Proceedings of the Royal Society of London. Series A - Mathematical and Physical Sciences*, (1935) (cit. on p. 58).

[92] S. Probst et al. "Shaped pulses for transient compensation in quantum-limited electron spin resonance spectroscopy". *Journal of Magnetic Resonance* **303**, 42–47, (2019) (cit. on p. 58).

[93] J. Zmuidzinas. "Superconducting Microresonators: Physics and Applications". *Annual Review of Condensed Matter Physics* **3** (1), 169–214, (2012) (cit. on p. 59).

[94] D. Bothner et al. "Magnetic hysteresis effects in superconducting coplanar microwave resonators". *Physical Review B - Condensed Matter and Materials Physics* **86** (1), 1–11, (2012). arXiv: 1202.5963 (cit. on p. 59).

[95] A. J. Sigillito et al. "Fast, low-power manipulation of spin ensembles in superconducting microresonators". *Applied Physics Letters* **104** (22), (2014). arXiv: 1403.0018 (cit. on pp. 59, 137).

[96] O. Kennedy et al. "Tunable Nb Superconducting Resonator Based on a Constriction Nano-SQUID Fabricated with a Ne Focused Ion Beam". *Physical Review Applied* **11** (1), 014006, (2019) (cit. on pp. 59, 64, 172).

[97] J. J. Morton and P. Bertet. "Storing quantum information in spins and high-sensitivity ESR". *Journal of Magnetic Resonance* **287**, 128–139, (2018) (cit. on pp. 59, 64, 65).

[98] J. Burnett et al. "Evidence for interacting two-level systems from the 1/f noise of a superconducting resonator." *Nature Communications* **5** (May), 4119, (2014). arXiv: 1311.1655 (cit. on pp. 59–61).

[99] M. R. Vissers, M. P. Weides, J. S. Kline, M. Sandberg, and D. P. Pappas. "Identifying capacitive and inductive loss in lumped element superconducting hybrid titanium nitride/aluminum resonators". *Applied Physics Letters* **101** (2), (2012). arXiv: 1203.5112 (cit. on p. 59).

[100] V. Ranjan et al. "Pulsed electron spin resonance spectroscopy in the Purcell regime", (2019). arXiv: 1909.02443 (cit. on p. 59).

[101] S. E. De Graaf, A. V. Danilov, A. Adamyan, T. Bauch, and S. E. Kubatkin. "Magnetic field resilient superconducting fractal resonators for coupling to free spins". *Journal of Applied Physics* **112** (12), (2012) (cit. on pp. 59, 64).

[102] N. W. Ashcroft and N. D. Mermin. *Solid State Physics*. 1976. arXiv: arXiv:1011.1669v3 (cit. on pp. 60, 62).

[103] T. Lindström, J. E. Healey, M. S. Colclough, C. M. Muirhead, and A. Y. Tzalenchuk. "Properties of superconducting planar resonators at millikelvin temperatures". *Physical Review B - Condensed Matter and Materials Physics* **80** (13), 2–5, (2009). arXiv: arXiv:0905.1481v2 (cit. on pp. 60–62, 102, 103).

[104] J. Burnett, L. Faoro, and T. Lindström. "Analysis of high quality superconducting resonators: consequences for TLS properties in amorphous oxides". *Superconductor Science and Technology* **29** (4), 044008, (2016). arXiv: 1512.02553 (cit. on pp. 60, 61).

[105] S. Ramo, J. R. Whinnery, and T. Van Duzer. *Fields and waves in communication electronics*. Wiley, 1994, 844 (cit. on p. 61).

[106] J. Gao. "The Physics of Superconducting Microwave Resonators". PhD thesis. 2008, 1–141 (cit. on pp. 61, 62).

[107] S. Geaney et al. "Near-Field Scanning Microwave Microscopy in the Single Photon Regime". *Scientific Reports* **9** (1), 12539, (2019) (cit. on p. 61).

[108] J. Wenner et al. "Surface loss simulations of superconducting coplanar waveguide resonators". *Applied Physics Letters* **99** (11), 113513, (2011). arXiv: 1107.4698 (cit. on p. 61).

[109] C. Neill et al. "Fluctuations from edge defects in superconducting resonators". *Applied Physics Letters* **103** (7), 072601, (2013). arXiv: 1306.3718 (cit. on p. 61).

[110] D. Niepce, J. Burnett, M. Gutierrez Latorre, and J. Bylander. "Geometric Scaling of Two-Level-System Loss in Superconducting Resonators". *Superconductor Science and Technology*, (2019) (cit. on p. 61).

[111] P. Macha et al. "Losses in coplanar waveguide resonators at millikelvin temperatures". *Applied Physics Letters* **96** (6), 062503, (2010) (cit. on p. 62).

[112] S. H. Simon. *The Oxford Solid State Basics*. Oxford University Press, 2013 (cit. on p. 62).

[113] J. Kang et al. "On-chip intercalated-graphene inductors for next-generation radio frequency electronics". *Nature Electronics* **1** (1), 46–51, (2018) (cit. on p. 63).

[114] S. K. Yip and J. A. Sauls. "Nonlinear Meissner effect in CuO superconductors". *Physical Review Letters* **69** (15), 2264–2267, (1992). arXiv: 9207021 [cond-mat] (cit. on p. 63).

[115] S. Sridhar, D. H. Wu, and W. Kennedy. "Temperature dependence of electrodynamic properties of YBa2Cu3Oy crystals". *Physical Review Letters* **63** (17), 1873–1876, (1989) (cit. on p. 63).

[116] J. Zmuidzinas. "Superconducting Microresonators: Physics and Applications". *Annual Review of Condensed Matter Physics* **3** (1), 169–214, (2012) (cit. on pp. 63, 64, 101).

[117] C. Kittel. "Introduction to Solid State Physics, 8th edition". *Wiley & Sons, New York, NY*, (2004) (cit. on p. 63).

[118] J. E. Healey, T. Lindström, M. S. Colclough, C. M. Muirhead, and A. Y. Tzalenchuk. "Magnetic field tuning of coplanar waveguide resonators". *Applied Physics Letters* **93** (4), 043513, (2008) (cit. on p. 64).

[119] N. Samkharadze et al. "High-Kinetic-Inductance Superconducting Nanowire Resonators for Circuit QED in a Magnetic Field". *Physical Review Applied* **5** (4), 044004, (2016). arXiv: 1511.01760 (cit. on pp. 64, 65).

[120] M. Xu, X. Han, W. Fu, C. L. Zou, M. H. Devoret, and H. X. Tang. "Frequency-tunable high-Q superconducting resonators via wireless control of nonlinear kinetic inductance". *Applied Physics Letters* **114** (19), 192601, (2019) (cit. on p. 64).

[121] C. W. Zollitsch, J. O'Sullivan, O. W. Kennedy, G. Dold, and J. J. L. Morton. "Tuning high-Q superconducting resonators by magnetic field reorientation". *AIP Advances* **9** (12), 125225, (2019). arXiv: 1909.11020 (cit. on pp. 64–66, 100, 103, 167).

[122] D. Bothner, T. Gaber, M. Kemmler, D. Koelle, and R. Kleiner. "Improving the performance of superconducting microwave resonators in magnetic fields". *Applied Physics Letters* **98** (10), (2011). arXiv: 1101.3185 (cit. on p. 64).

[123] D. Bothner et al. "Reducing vortex losses in superconducting microwave resonators with microsphere patterned antidot arrays". *Applied Physics Letters* **100** (1), 1–4, (2012). arXiv: 1110.6332 (cit. on p. 64).

[124] M. R. Vissers et al. "Frequency-tunable superconducting resonators via nonlinear kinetic inductance Frequency-tunable superconducting resonators via nonlinear kinetic inductance". **062601** (2015), (2016) (cit. on p. 64).

[125] A. A. Adamyan, S. E. Kubatkin, and A. V. Danilov. "Tunable superconducting microstrip resonators". *Applied Physics Letters* **108** (17), 172601, (2016) (cit. on pp. 64, 172).

[126] A. T. Asfaw, A. J. Sigillito, A. M. Tyryshkin, T. Schenkel, and S. A. Lyon. "waveguide microresonators Multi-frequency spin manipulation using rapidly tunable superconducting coplanar waveguide microresonators". **032601**, (2017) (cit. on pp. 64, 65).

[127] M. Sandberg et al. "Tuning the field in a microwave resonator faster than the photon lifetime". *Applied Physics Letters* **92** (20), 203501, (2008) (cit. on p. 64).

[128] A. Palacios-Laloy, F. Nguyen, F. Mallet, P. Bertet, D. Vion, and D. Esteve. "Tunable Resonators for Quantum Circuits". *Journal of Low Temperature Physics* **151** (3-4), 1034–1042, (2008) (cit. on p. 64).

[129] M. Göppl et al. "Coplanar waveguide resonators for circuit quantum electrodynamics". *Journal of Applied Physics* **104** (11), 1–8, (2008). arXiv: 0807.4094 (cit. on p. 64).

[130] S. Weichselbaumer, P. Natzkin, C. W. Zollitsch, M. Weiler, R. Gross, and H. Huebl. "Quantitative modeling of superconducting planar resonators for electron spin resonance". *Physical Review Applied* **12** (2), (2019). arXiv: 1811.02971 (cit. on pp. 65, 66, 70, 147).

[131] T. Polakovic et al. "Room temperature deposition of superconducting niobium nitride films by ion beam assisted sputtering". *APL Materials*, (2018). arXiv: 1803.02417 (cit. on p. 65).

[132] R. Russo et al. "NanoSQUIDs based on niobium nitride films". *Superconductor Science and Technology* **30** (2), 024009, (2017) (cit. on p. 65).

[133] M. David Henry, S. Wolfley, T. Monson, B. G. Clark, E. Shaner, and R. Jarecki. "Stress dependent oxidation of sputtered niobium and effects on superconductivity". *Journal of Applied Physics* **115** (8), 083903, (2014) (cit. on p. 65).

[134] A. J. Annunziata et al. "Tunable superconducting nanoinductors". *Nanotechnology* **21** (44), (2010). arXiv: 1007.4187 (cit. on p. 65).

[135] CST Studio Suite. *CST Microwave Studio* (cit. on pp. 67, 81).

[136] F. Crundwell. "The mechanism of dissolution of minerals in acidic and alkaline solutions: Part II Application of a new theory to silicates, aluminosilicates and quartz". *Hydrometallurgy* **149**, 265–275, (2014) (cit. on p. 71).

[137] D. M. Pozar. *Microwave Engineering*. 4th ed. 2012, 6–158. arXiv: 9809069 [gr-qc] (cit. on p. 79).

[138] D. S. Betts and E. N. Smith. *An Introduction to Millikelvin Technology*. Cambridge University Press, 1989 (cit. on pp. 82–84).

[139] F. Pobell. *Matter and methods at low temperatures*. 3rd ed. Springer, 2007, 1–461 (cit. on pp. 82, 83).

[140] D. J. Cousins et al. "An Advanced Dilution Refrigerator Designed for the New Lancaster Microkelvin Facility". *Journal of Low Temperature Physics* **114** (5/6), 547–570, (1999) (cit. on p. 85).

[141] D. Schaeffer et al. "The cryostat of the CUORE Project, a 1-ton scale cryogenic experiment for Neutrinoless Double Beta Decay Research". *Journal of Physics: Conference Series* **150** (1), 012042, (2009) (cit. on p. 85).

[142] S. Krinner et al. "Engineering cryogenic setups for 100-qubit scale superconducting circuit systems". *EPJ Quantum Technology* **6** (1), 2, (2019) (cit. on p. 87).

[143] E. Kupce and R. Freeman. "Adiabatic Pulses for Wideband Inversion and Broadband Decoupling". *Journal of Magnetic Resonance, Series A* **115** (2), 273–276, (1995) (cit. on pp. 91, 133).

[144] L. A. O'Dell. "The WURST kind of pulses in solid-state NMR". *Solid State Nuclear Magnetic Resonance* **55-56**, 28–41, (2013) (cit. on pp. 91, 132, 133).

[145] C. Bonizzoni, A. Ghirri, and M. Affronte. "Coherent coupling of molecular spins with microwave photons in planar superconducting resonators". *Advances in Physics: X* **3** (1), 1435305, (2018) (cit. on pp. 98, 116).

[146] L. Faoro and L. B. Ioffe. "Quantum two level systems and kondo-like traps as possible sources of decoherence in superconducting qubits". *Physical Review Letters* **96** (4), 1–5, (2006). arXiv: 0510554 [cond-mat] (cit. on p. 102).

[147] Y. Kubo et al. "Strong coupling of a spin ensemble to a superconducting resonator". *Physical Review Letters*, (2010). arXiv: arXiv : 1006 . 0251v3 (cit. on p. 116).

[148] S. Putz et al. “Protecting a spin ensemble against decoherence in the strong-coupling regime of cavity QED”. *Nature Physics* **10** (10), 720–724, (2014) (cit. on p. 116).

[149] S. Weichselbaumer, C. W. Zollitsch, M. S. Brandt, R. Gross, and H. Huebl. “Echo trains in pulsed electron spin resonance of a strongly coupled spin ensemble”. *arXiv*, (2018). arXiv: 1809.10116 (cit. on pp. 116, 131).

[150] C. Kutter, H. P. Moll, J. Van Tol, H. Zuckermann, J. C. Maan, and P. Wyder. “Electron-spin echoes at 604 GHz using far infrared lasers”. *Physical Review Letters* **74** (15), 2925–2928, (1995) (cit. on p. 127).

[151] S. Takahashi, R. Hanson, J. Van Tol, M. S. Sherwin, and D. D. Awschalom. “Quenching spin decoherence in diamond through spin bath polarization”. *Physical Review Letters* **101** (4), (2008). arXiv: 0804.1537 (cit. on pp. 127, 128, 130).

[152] S. Probst, H. Rotzinger, A. V. Ustinov, and P. A. Bushev. “Microwave multimode memory with an erbium spin ensemble”. *Physical Review B* **92** (1), 014421, (2015) (cit. on pp. 127, 128, 130).

[153] A. Blank. “A new approach to distance measurements between two spin labels in the >10 nm range”. *Physical Chemistry Chemical Physics*, (2017) (cit. on pp. 128, 130).

[154] K. Debnath, G. Dold, J. J. L. Morton, and K. Mølmer. “Self-stimulated pulse echo trains from inhomogeneously broadened spin ensembles”. *arXiv*, (2020). arXiv: 2004.01116 (cit. on pp. 131, 132, 168).

[155] J. P. Gordon and K. D. Bowers. “Microwave Spin Echoes from Donor Electrons in Silicon”. *Physical Review Letters* **1** (10), 368–370, (1958) (cit. on p. 131).

[156] J. G. Powles. “The Adiabatic Fast Passage Experiment in Magnetic Resonance”. *Proceedings of the Physical Society* **71** (3), 497–500, (1958) (cit. on p. 132).

[157] C. Hardy, W. Edelstein, and D. Vatis. “Efficient adiabatic fast passage for NMR population inversion in the presence of radiofrequency field inhomogeneity and frequency offsets”. *Journal of Magnetic Resonance (1969)* **66** (3), 470–482, (1986) (cit. on p. 132).

[158] M. Garwood and Y. Ke. “Symmetric pulses to induce arbitrary flip angles with compensation for rf inhomogeneity and resonance offsets”. *Journal of Magnetic Resonance (1969)* **94** (3), 511–525, (1991) (cit. on p. 135).

[159] M. Garwood and L. DelaBarre. “The return of the frequency sweep: Designing adiabatic pulses for contemporary NMR”. *Journal of Magnetic Resonance* **153** (2), 155–177, (2001) (cit. on p. 135).

[160] P.-Y. Li et al. “Hyperfine Structure and Coherent Dynamics of Rare-Earth Spins Explored with Electron-Nuclear Double Resonance at Subkelvin Temperatures”. *Physical Review Applied* **13** (2), 024080, (2020) (cit. on p. 140).

[161] G. Wolfowicz and J. J. Morton. “Pulse techniques for quantum information processing”. *eMagRes* **5** (4), 1515–1528, (2016) (cit. on pp. 144, 157).

[162] CIAAW. *Isotopic compositions of the elements*. 2015 (cit. on p. 152).

[163] S. Meiboom and D. Gill. “Modified Spin-Echo Method for Measuring Nuclear Relaxation Times”. *Review of Scientific Instruments* **29** (8), 688–691, (1958) (cit. on p. 156).

[164] A. M. Souza, G. A. Alvarez, and D. Suter. “Robust dynamical decoupling for quantum computing and quantum memory.” *Physical review letters* **106** (24), 240501, (2011) (cit. on p. 157).

[165] T. Gullion, S. Louis, and D. B. Baker. “New, Compensated Carr-Purcell Sequences”. *Journal of Magnetic Resonance* **484**, 479–484, (1990) (cit. on p. 157).

[166] M. A. Ali Ahmed, G. A. Álvarez, and D. Suter. “Robustness of dynamical decoupling sequences”. *Physical Review A* **87** (4), 042309, (2013) (cit. on p. 157).

[167] A. J. Sigillito, A. M. Tyryshkin, T. Schenkel, A. A. Houck, and S. A. Lyon. “All-electric control of donor nuclear spin qubits in silicon”. *Nature Nanotechnology* (August), 1–6, (2017) (cit. on p. 172).

[168] B. S. Miller et al. “Spin-enhanced nanodiamond biosensing for single-molecule diagnostics”. *In preparation*, (2020) (cit. on p. 172).

List of acronyms and abbreviations

AWG	Arbitrary Waveform Generator
BIR	B_1-insensitive rotation
CW	Continuous wave
dBm	decibel-milliwatts ($\mathrm{dBm} = 10 \log_{10} \mathrm{mW}$)
ESR	Electron Spin Resonance
HWHM/FWHM	Half-width/Full-width at half-maximum
LNA	Low Noise Amplifier
LO	Local Oscillator
MW	Microwave
NISQ	Noisy intermediate-scale quantum
QED	Quantum electrodynamics
REI	Rare-earth ions
RF	Radio Frequency
TLS	Two-level systems
VNA	Vector Network Analyser
VSG	Vector Signal Generator
WURST	Wideband, uniform rate, smooth truncation
YSO	Yttrium Orthosilicate
ZEFIZEFOZ	Zero field, zero first-order zeeman transition
ZEFOZ	Zero first-order zeeman transition